Magnetocaloric effect and critical behaviour near the magnetic phase transition temperature in rare-earth compounds

By

Mboukam Jean Jules

A Thesis presented in fulfillment of the requirements for the degree of Master of Science at the University of the Western Cape

Department: Physics and Astronomy

Faculty: Natural Science

Supervisor(s):

Prof. M.B. Tchoula Tchokonté, University of the Western Cape

Co-Supervisor(s):

Dr. B.M. Sondezi, University of Johannesburg

June 18, 2018

Declaration

I declare that this dissertation is my own independently researched work conducted in the Physics Department of the University of the Western Cape, Bellville, South Africa. It is being submitted for the degree of Master of Science, and it is the first time this is being submitted for this degree.

. . . . .

Mboukam Jean Jules

Acknowledgements

First at all, I would like to express my profound gratitude to my supervisor, Prof. M.B. Tchoula Tchokonté, who helped me to manage this master's project, for all his advice and encouragement, for his constant availability, and for having made me benefit from his great understanding of the complex subtleties relating to the high requirements in this domain of Strongly Correlated Electrons Systems and who was always enthusiastic and energetic to propose new directions of work.

I would like to thank my co-supervisor, Dr. B.M. Sondezi, for believing in me and her availability of conducting experiments at the Physics laboratory of the University of Johannesburg.
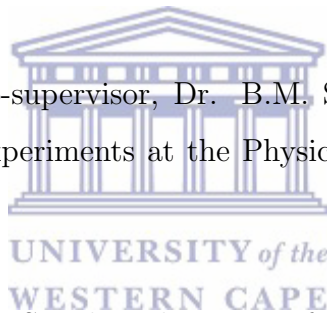
I say big thanks to Prof. A.M. Strydom the owner of the Strongly Correlated Electrons Systems laboratory of the Physics department of University of Johannesburg, for accepting me in his laboratory for experiments. By the same occasion I thank Prof. D. Kaczorowski for the magnetic measurements he has done on my compounds.

I would like to thank and dedicate this work to my parents Mr. Mboukam Samuel and Semou Yvette as well as my brothers, sisters and Noubactep family who believe in me and always encourage me to succeed.

I say big thanks to Dr. A.K.H. Bashir, Mr Bako, Djoumessi Fobasso Redrisse and Tedonkeng Francis for their advices and helps.

I would like to thank the University of the Western Cape as well as the Physics Department and its staff for the opportunity they gave me to study in this prestigious institution.

Research publications and Conference presentations

1. Research publications

- **J.J. Mboukam**, B.M. Sondezi, M.B. Tchoula Tchokonté, A.K.H. Bashir, A.M. Strydom, D. Britz, and D. Kaczorowski, Magnetocaloric effect and other low–temperature properties of Pr_2Pt_2In; In press Physica B: Condensed Matter.

- M.B. Tchoula Tchokonté, **J.J. Mboukam**, B.M. Sondezi, A.K.H. Bashir, A.M. Strydom, D. Britz, and D. Kaczorowski, Critical behavior study around the ferromagnetic phase transition in Pr_2Pt_2In; In press Physica B: Condensed Matter.

- M.B. Tchoula Tchokonté, **J.J. Mboukam**, A.K.H. Bashir, B.M. Sondezi, A.M. Strydom, K.R. Kumar, and D. Kaczorowski, Electrical resistivity and thermodynamic properties of the ferromagnet Nd_2Pt_2In; In press Journal of Alloys and Compounds.

- M.B. Tchoula Tchokonté, **J.J. Mboukam**, A.K.H. Bashir, B.M. Sondezi, A.M. Strydom, K.R. Kumar and D. Kaczorowski, Magnetocaloric effect and its implementation in critical behavior study of Nd_2Pt_2In compound: Submitted to the International Workshop on New Materials and Crystal Growth.

- M.B. Tchoula Tchokonté, **J.J. Mboukam**, A.K.H. Bashir, B.M. Sondezi, A.M. Strydom and D. Kaczorowski, Complex magnetic behavior in $RE_8Pd_{24}Ga$ (RE = Gd, Tb and Dy) compounds: Submitted to AIP Advance Journal.

2. Conference presentations

- United Kingdom–South Africa workshop (Low-dimensional nanomaterials) at the University of Cape Town: 2 - 3 May 2017.

  1. M.B. Tchoula Tchokonté, **J.J. Mboukam**, B.M. Sondezi, A.K.H. Bashir, A.M. Strydom, D. Britz, and D. Kaczorowski, Magnetocaloric effect and critical behaviour study around the para-to-ferromagnetic phase transition temperature in Pr_2Pt_2In.

- 62nd Annual conference of the South African Institute of Physics at Stellenbosch University: 3 - 7 July 2017.

  1. **J.J. Mboukam**, B.M. Sondezi, M.B. Tchoula Tchokonté, A.K.H. Bashir, A.M. Strydom, R.K. Kumar, and D. Kaczorowski, Electrical resistivity and the thermodynamic properties of the ferromagnet Nd_2Pt_2In.

  2. M.B. Tchoula Tchokonté, **J.J. Mboukam**, B.M. Sondezi, A.K.H. Bashir, A.M. Strydom, R.K. Kumar and D. Kaczorowski, Critical behaviour at the paramagnetic to ferromagnetic phase transition in Nd_2Pt_2In.

- International conference on Strongly Correlated Electron Systems (SCES): 17 - 21 July 2017 in Clarion congress hotel, Prague, Czech Republic.

  1. M.B. Tchoula Tchokonté, **J.J. Mboukam**, B.M. Sondezi, A.K.H. Bashir, A.M. Strydom, Britz, D. and D. Kaczorowski, Critical behaviour study around the para–to-ferromagnetic phase transition in Pr_2Pt_2In.

  2. **J.J. Mboukam**, B.M. Sondezi, M.B. Tchoula Tchokonté, A.K.H. Bashir, A.M. Strydom, D. Britz, and D. Kaczorowski, Magnetocaloric effect and other low-temperature properties of Pr_2Pt_2In.

iv

Abstract

Rare-earth intermetallic compounds continue to draw considerable attention, due to their fundamental importance in understanding physical properties and potential applications based on a variety of phenomena. The focus of this project is to employ two family of rare-earth intermetallic compounds: RE_2Pt_2In (RE = Pr, Nd) and $RE_8Pd_{24}Ga$ (RE = Gd, Tb, Dy) ternary intermetallic systems as a model candidate to uncover the underlying ground state properties that result in a strong coupling between the conduction electron and the $4f$-electron of the rare-earth ions.

The present thesis report on the magnetocaloric effect, the critical behaviour study around the magnetic phase transition temperature and other low-temperature properties of RE_2Pt_2In (RE = Pr, Nd) and $RE_8Pd_{24}Ga$ (RE = Gd, Tb, Dy). The start of the research project was focused on sample synthesis using arc-furnace melting and sample characterization using X-ray powder diffractometer D8 Advance with Cukα radiation. The elemental composition and homogeneity of the prepared samples was checked by scanning electron microscopy (SEM), energy dispersion spectroscopy (EDS) and microprobe detection. The physical and magnetic properties investigated included: electrical resistivity ($\rho(T)$), heat capacity ($C_p(T)$), magnetic susceptibility ($\chi(T)$), magnetization ($M(\mu_0 H)$), and isothermal magnetization ($M(\mu_0 H, T)$). Magnetocaloric effect was estimated from $M(\mu_0 H, T)$. All these properties were measured using the physical property measurement system (PPMS) and the magnetic property measurement system (MPMS) both from Quantum Designs.

The results of $\rho(T)$, $\chi(T)$ and $C_p(T)$ indicate that both compounds Pr_2Pt_2In and Nd_2Pt_2In order ferromagnetically below $T_C = 9$ K and 16 K, respectively. In the ordering state, $\rho(T)$ and $C_p(T)$ data for both Pr_2Pt_2In and Nd_2Pt_2In compounds are dominated by magnon contribution with an energy gap of about $\Delta_R = 13(1)$ K and 8(2) K and

$\Delta_C = 7.6(3)$ K and $6.0(3)$ K, respectively. Above T_C, $\rho(T)$ variations of Pr and Nd compounds are characteristic of electron-phonon interaction in the presence of the s-d interband scattering, while $C_p(T)$ follows the standard Debye formula with the Debye temperature $\theta_D = 155.0(3)$ K and $152.44(2)$ K for Pr_2Pt_2In and Nd_2Pt_2In, respectively. In the case of Nd_2Pt_2In, the $4f$-electron specific heat shows a Schottky-type anomaly around 60 K associated with crystal-electric-field with energy splitting $\Delta_1 = 145(7)$ K and $\Delta_2 = 195(13)$ K of the Nd^{3+}-ion $(J = 9/2)$ multiplet, that we associated with the first and second excited state of Nd^{3+}-ion. On the other hand, $\chi(T)$ data at high temperature for all the investigated compounds follow the Curie-Weiss relation giving an effective magnetic moment close to that expected for the RE^{3+}-ion. The magnitude of the magnetocaloric effect estimated from the isothermal magnetization for selected investigated compounds are similar to the values reported for most rare-earth based intermetallics. Characteristic behaviour of the isothermal magnetic entropy change maximum points out to a second-order character of the magnetic transition. The critical behaviour study at the paramagnetic to ferromagnetic phase transition in Pr_2Pt_2In and Nd_2Pt_2In has been investigated by means of isothermal magnetization. The Arrott-plots confirm the second-order character of the ferromagnetic phase transition for both compounds. The derived critical exponent values obtained for Pr_2Pt_2In are close to those expected for a 3D-Ising ferromagnet and Nd_2Pt_2In are close to both 3D-Ising and 3D-Heisenberg ferromagnet.

For $RE_8Pd_{24}Ga$ family of compounds, the results of $\rho(T)$, $\chi(T)$ and $C_p(T)$ indicate antiferromagnetic phase transition for RE = Gd and Dy and complex magnetic behaviour for RE = Tb at low-temperatures. Above the ordering temperature, $\rho(T)$ show normal metallic behaviour for all three compounds, while $C_p(T)$ follows the standard Debye formula above their respective magnetic transition temperature with the Debye temperature $\theta_D = 238.886(7)$ K, $230.26(4)$ K and $233.20(2)$ K for RE = Gd, Tb, Dy, respectively.

The work in this thesis is presented as follows:

Chapter 1 presents the introduction and an overview of rare-earth intermetallic compounds. This is followed by the definition, preparation and metallurgical aspects of RE intermetallic compounds and ends with a motivation of the work carried out in this thesis.

Chapter 2 presents various theoretical concepts, which have been used to analyse and

interpret the experimental results discussed in this thesis. These are among others: the different magnetic interactions which allow to generate magnetism in intermetallic compounds, the different kinds of magnetism present in compounds, the spin wave theory, the critical behaviour, the mean field theory as well as the concepts of magnetocaloric effect. The theoretical concepts of the physical and magnetic properties of rare-earth intermetallic compounds are also presented in this chapter.

In chapter 3, the experimental methods used in this study are presented. Sample synthesis, characterization and measurement techniques are discussed.

Chapter 4 and 5 report the experimental results obtained for the tetragonal system RE_2Pt_2In and the cubic series of compounds $RE_8Pd_{24}Ga$, respectively. A brief discussion of the results studied in these families of compounds is also presented.

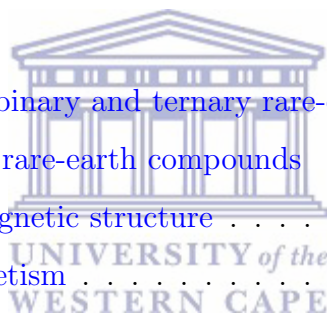Chapter 6: presents the conclusion of the thesis and further works.

Contents

Contents

Contents

UNIVERSITY *of the*

WESTERN CAPE

List of Figures

UNIVERSITY *of the*

WESTERN CAPE

List of Tables

Chapter 1

Introduction

1.1 Overview of rare-earth intermetallic compounds

[1, 2]

The group of lanthanide comprises the elements with atomic number 57 - 71 in the periodic table. In nature, these elements are always found together and are taken together in general with yttrium. It has become natural to call the elements consisting of the lanthanide and yttrium, the rare-earth elements.

The outer electron shell determining the number and nature of the valences is much the same for these 15 elements. The same for their atomic or metallic radii which differ by the order of only a few per cent. These similarities lead to the same chemical properties. As a result of that it presents considerable difficulties in separating these elements from each other. Furthermore, the chemical similarity leads to more or less uniform behaviour when the rare-earth metals are combined with other metals. In other words, one can say that if one member of the group forms an intermetallic compound of a given composition and crystal structure, all the other members will act in the same way. In contrast to the chemical properties, the physical properties may vary remarkably within such a series of isotropic compounds. The $4f$-electron shell of the rare-earth elements are gradually filling up from 0 - 14; as a result, spin and orbital moment will show a large variation as one proceeds from La compound to the corresponding Lu compound. This situation offers the possibility of studying theoretical models in which spin and orbital moment occur as parameters under a wide variety of different conditions.

1

1.1. Overview of rare-earth intermetallic compounds

The family of compounds formed between rare-earth and $3d$-transition metals is of particular interest in this research project and the total number of these compounds is enormous. Examples are the binary intermetallic compounds where the combination of one rare-earth element and $3d$-element give rise to more than ten different compounds and the ternary intermetallic compound where the one rare-earth element, one $3d$-element and one element of the p-block give rise to a large number of compounds. The majority of investigations of rare-earth-transition compounds reported in the literature so far, deal with the magnetic properties of these compounds and other few physical properties of compounds were reported in order to obtain a good understanding of the nature of the magnetic interactions. In the binary and ternary rare-earth compounds, the magnetic properties are determined by the rare-earth moments. The transition metals, except for Mn do not carry magnetic moments. These materials have a metallic character and the interatomic distance between the rare-earth are fairly large. The magnetic interaction between the highly localized $4f$-electrons is realized by their conduction electrons mediating in an exchange interaction, and the effect of crystal-electric-field acting on the $4f$-electrons. In rare-earth intermetallic compounds, exchange interactions between rare-earth moments are mediated by spin polarization of conduction electrons. This mechanism leads to long-range exchange interaction with an oscillatory dependence of the interaction strength on the distance between the moments and is known as the Ruddermann-Kittel-Kasuya-Yosida (RKKY) interaction. Intermetallic compounds in which the rare-earth partner bears no magnetic moment such as La, Lu, Y and tetravalent Ce have received much attention since they provide a good opportunity to investigate the origin and the nature of the $4f$-electron magnetism.

In recent years, interest in intermetallic compounds between rare-earth and transition metals has increased rapidly from the discovery that several of its members can be used as magnetic refrigerant for magnetic refrigeration and as a starting material for permanent magnets of outstanding quality. Interest in magnetic refrigeration is increasing rapidly as an environment-friendly alternative to conventional vapor-cycle refrigeration [3].

1.2 Definition, preparation and metallurgical aspects of rare-earth intermetallic compounds

[1]

When two metals A and B are alloyed, three possibilities exist. First of all, the two metals may not mix in the solid state, in which case A and B are present as separate phases. Such a situation occurs if the heat of mixing is distinctly positive. Secondly, the two metals may form a solid solution of the metals A and B which is not much different from the liquid mixture. Its physical properties most often agree with those expected on the basis of a linear interpolation between the properties of the parent materials. Thirdly, the alloying of the two metals lead to the formation of intermetallic compounds which are characterized by well defined stoichiometric compositions such as AB, A_3B, AB_2, AB_5 etc. In an ideal case, the A and B atoms are not distributed at random but are arranged in the crystallographic unit cell at defined positions, being different for A and B atoms. Its physical properties need not have anything in common with the physical properties of the composing elements.

For the synthesis of most of the intermetallic compounds, the stoichiometric proportions of the starting materials are melted together either in an arc-furnace or a levitation or induction furnace on a crucible (Al_2O_3, ThO_2, MgO, Cu). Since rare-earth elements react readily with crucible materials at elevated temperatures, heating in a resistance furnace is less satisfactory. The melt will contain additional impurities from crucible beside the impurities incorporated in the crucible. For instance, Al impurity leads to a deficient in rare-earth concentration. After cooling the sample from liquid state to solid state, the sample is not always single phase but may consist of a mixture of several intermetallic compounds. This situation is closely related with the phase relationship of the corresponding RE-M p phase diagram.

1.3 Motivation

In the field of engineering, sustainable development has become a large focus as climate

3

change and carbon emission both become more pressing issues. As modern technologies improve, so does the need for sustainability, which is defined by the Environmental Protection Agency (EPA) as creating and maintaining the conditions under which humans and the natural world can exist in productive harmony to support present and future generations [4]. Creating sustainability solutions is a challenge with which modern engineers are faced.

One challenge that engineers currently face within the realm of sustainability is refrigeration. Although it is an issue that goes unnoticed by most people, traditional refrigeration systems are harmful to the environment. It is predicted that by the year 2030 refrigeration systems and air conditioning will account for 13% of carbon gas emissions [5]. In brief, traditional refrigeration is not sustainable and change is necessary.

As refrigeration becomes an urgent problem in consideration to global warning and carbon emissions, engineers are looking for alternative methods of refrigeration which show much more promise than traditional cooling systems. One of these methods that is being currently researched, is magnetocaloric refrigeration. As opposed to typical refrigeration that uses harmful chemical refrigeration agents, magnetocaloric refrigeration utilizes the application and removal of a magnetic field in order to change the temperature of specific materials with magnetocaloric properties in order to achieve a desired cooling effect.

Magnetic refrigeration is a revolutionary, efficient, environmentally friendly cooling technology, which is on the threshold of commercialization. The magnetic rare-earth materials are utilized as the magnetic refrigerants in most cooling devices and for many cooling applications, the $Nd_2Fe_{14}B$ permanent magnets are employed as the source of the magnetic field [6].

Research on magnetic refrigeration based on magnetocaloric effect has attracted much attention nowadays due to its higher efficiency and eco-friendly concerns over the conventional gas compression method. It has been also demonstrated to be a very promising alternative to conventional vapor-cycle refrigeration due to its potential savings and alleviation of the environmental concerns [3, 7, 8]. Therefore, it has aroused worldwide interest

in the search and development of new magnetic refrigerants with a large magnetocaloric effect which is considered to be the most important requirement of the industrial application near temperature helium liquefaction [9]. A variety of prototype materials involving second-order and first-order magnetic transition have been investigated theoretically and experimentally in an attempt to achieve a large magnetocaloric effect [10, 11, 12, 13, 14, 15]. In view of this challenge within the realm of sustainability, the present research project is mainly focused on the search of magnetic rare-earth intermetallic compounds with large magnetocaloric effect.

UNIVERSITY *of the*
WESTERN CAPE

Chapter 2

Theoretical concepts

2.1 Magnetic properties of binary and ternary rare-earth compounds

[1, 16]
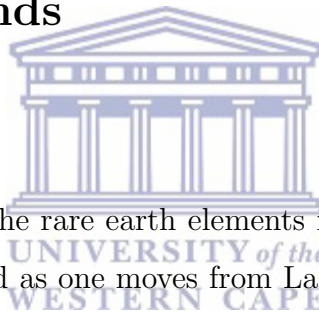
A well-known property of the rare earth elements is their incomplete $4f$ shell which becomes progressively more filled as one moves from La $(4f^0)$ to Lu$(4f^{14})$. The unpaired electron in this $4f$ shell completely determines the physical properties of the rare-earth elements and compounds. These $4f$ shells are deep inside the atom and close to the nucleus. Furthermore, they are well shielded by the $5s^25p^6$ shell. As a result of that, they remain unaffected by their environment and the chemical properties of the rare-earth are almost the same. The wave function of the $4f$ shell is of small radial extent giving a localized character to the $4f$ electrons. All rare-earth elements give rise to the same type of compound when combined with other metals to form binary or ternary compounds. Exceptions are Ce, Eu and Yb. The other rare-earth elements are present in the trivalent state in metal systems, the three elements Ce, Eu and Yb generally adopt different valences. For instance, Ce most often tends to be tetravalent and Eu and Yb divalent.

Spin (S), orbital (L) and total angular (J) momentum of the single rare-earth ions are determined by Hund's rules. The corresponding quantum number are gathered in table 2.1 together with the spectroscopic splitting factor g_J, values of $g_J[J(J+1)]^{1/2}$ and $g_J J$. The

two latter quantities completely determine the magnetic behaviour in the paramagnetic and magnetically ordered regime, respectively. In most models, the magnetic coupling between two localized moments is proportional to $\vec{S}_i.\vec{S}_j$. In this case, the spin coupling remains unchanged within a class of isostructural rare-earth compounds and the ordering temperature are predictable to scale as $(g-1)^2 J(J+1)$.

Table 2.1: Ionic properties of rare-earth elements with their splitting factors and their theoretical magnetic moments.

RE-ion	Ground term	S	L	J	g_J	$g_J[J(J+1)]^{1/2}$	$g_J J$
La^{3+}	$4f^0$ $^1S_0$	0	0	0	—	0	0
Ce^{3+}	$4f^1$ $^2F_{5/2}$	1/2	3	5/2	6/7	2.54	2.14
Pr^{3+}	$4f^2$ $^3H_4$	1	5	4	5/4	3.58	3.20
Nd^{3+}	$4f^3$ $^4I_{9/2}$	3/2	6	9/2	8/11	3.62	3.28
Pm^{3+}	$4f^4$ $^5I_4$	2	6	4	3/5	2.68	2.40
Sm^{3+}	$4f^5$ $^6H_{5/2}$	5/2	5	5/2	2/7	0.84	0.72
Eu^{3+}	$4f^6$ $^7F_0$	3	3	0	0	0	0
Gd^{3+}	$4f^7$ $^8S_{7/2}$	7/2	0	7/2	2	7.94	7
Tb^{3+}	$4f^8$ $^7F_6$	3	3	6	3/2	9.72	9
Dy^{3+}	$4f^9$ $^6H_{15/2}$	5/2	5	15/2	4/3	10.63	10
Ho^{3+}	$4f^{10}$ $^5I_8$	2	6	8	5/4	10.60	10
Er^{3+}	$4f^{11}$ $^4I_{15/2}$	3/2	6	15/2	6/5	9.59	9
Tm^{3+}	$4f^{12}$ $^3H_6$	1	5	6	7/6	7.57	7
Yb^{3+}	$4f^{13}$ $^2F_{7/2}$	1/2	3	7/2	8/7	4.54	4
Lu^{3+}	$4f^{14}$ $^1S_0$	0	0	0	—	0	0

2.2   Origin of magnetism in rare-earth compounds

[17, 18, 19, 20, 21]

The magnetism of rare-earth compound originates from the rare-earth ion. One of the fundamental properties of an electron (beside that it carries a charge) is that it has a magnetic dipole moment, i.e. it behaves like a tiny magnet, producing a magnetic field. This dipole moment originated from the more fundamental property of the electron that has quantum mechanical spin. Owing to its quantum nature, the spin of the electron can be in one of only two states; with the magnetic field either pointing "up" or "down". Ferromagnetism originates mainly from the spin of the electron, although there is also

7

2.2. Origin of magnetism in rare-earth compounds

a contribution from the orbital angular momentum of the electron around the nucleus. Briefly, the magnetic moment of a free atom originates from three principal sources:

- The spin angular momentum associated with an electron.

- The orbital angular momentum as a result of movement of the electron around the nucleus.

- The change in the orbital momentum induced by an applied magnetic field.

The first two give paramagnetic contributions to magnetization and the third gives a diamagnetic contribution. Materials made of atoms with filled electron shells have a total dipole moment of zero (see table 2.1), because the electrons all exist in pairs with opposite spin. Every electron's magnetic moment is cancelled by the opposite moment of the second electron in the pair. Only an atom with unpaired spins can have a net magnetic moment, thus ferromagnetism only occurs in materials with partially filled shells. The unpaired spins (which also include angular momentum) tend to align in parallel to an external magnetic field, an effect called paramagnetism. Ferromagnetism involves an additional phenomenon; however in a few substances the dipoles tend to align spontaneously leading to a spontaneous magnetization, even when there is no applied magnetic field.

In summary, Magnetism arises in rare-earth compounds from the open $4f$ shell with a variation of spin and orbital moments. The electronic configuration of the rare-earth elements in the solid is $[X_e]4f^n(5d6s)^3$, except for the divalent Eu and Yb. This series of rare-earth elements shown in table 2.1 is characterized by a successive filling of the $4f$ shell with increasing atomic number from 0 to 14. It is almost completely localized within the occupied $5s$ and $5p$ orbitals and remains atomic-like even in the solid state. As a result of that, the $4f$ electrons are not directly involved in the chemical properties of the atoms. The increasing screening of the core potential with the degree of occupancy of the $4f$ causes a decrease of the ionic radius. Therefore, the rare-earth are a series of chemically very similar elements that differ by their ionic radius and their magnetic properties. Magnetism arises from the open $4f$ shell, with a systematic variation of spin and orbital moments across the series. Rare-earth compounds are subjected to the strong coulomb interaction to which are added the effects of spin-orbit coupling, the crystalline-field and the exchange interactions.

8

2.2.1 Overview on magnetic structure

As mentioned above, localized magnetism arises from the open $4f$ shell of rare-earth ions which are completely localized within the $5s$ and $5p$ orbitals. The magnetism of the rare-earth compounds is mainly governed by the Hund's rule. Already the elemental metals exhibit a rich variety of magnetism phenomena. While Gd and divalent Eu exhibit pure spin magnetism ($L = 0$, $J = S = 7/2$), Dy and Ho carry the largest total moments of all elements. Due to the strong localization of the $4f$ electrons, the direct overlap of the wave function of these $4f$ electrons is a negligible contribution to the inter-atomic coupling, which is rather dominated by the indirect RKKY interaction in the metals [17, 22]. The $4f$-$4f$ coupling mechanism is due to a direct intra-atomic exchange interaction between the $4f$ electrons and the conduction electrons which then mediate the coupling between the $4f$ electrons of different lattice sites. This exchange interaction will be discussed in the next section.

The rare-earth compounds exhibit magnetic behaviour primarily as a result of unpaired $4f$-electrons. In physics, several different types of magnetism are distinguished and the type of magnetic behaviour exhibited is divided into several categories such as diamagnetism, paramagnetism, ferromagnetism, ferrimagnetism, antiferromagnetism, canted ferromagnetism, helical spin array, ferromagnetism energy band etc. In the present thesis, an overview of these different types of magnetic behaviour of only the diamagnetism, paramagnetism, ferromagnetism, ferrimagnetism and antiferromagnetism will be presented.

2.2.1.1 Diamagnetism

Diamagnetism is a quantum mechanical effect that occurs in all materials. Diamagnetism is exhibited by all materials when subjected to an applied magnetic field. Diamagnetic materials are repelled by a magnetic field. Indeed an applied magnetic field creates an induced magnetic field in the opposite direction, causing a repulsive force. The common treatment of diamagnetism of atoms and ions make use of the Lamor theorem which state that: in a magnetic field the motion of the electrons around a central nucleus is, to

the first order in applied magnetic field, B, the same as a possible motion in the absence of B except for the superposition of a precession of the electron with angular frequency: $\omega = eB/2m$, e and m being the charge and the mass of the free electron, respectively [23].

In diamagnetic materials, all electrons are paired and the total magnetic moment is zero. The applied field tends to deform orbitals so that the motion of electrons creates a magnetic field which opposes the external field, this decreases the magnetic field within the material. The diamagnetic behaviour gains its origin from the induction associated with the orbital motion due to paired electrons [24]. Therefore, the magnetic induction increases linearly with the power of the external field. This phenomenon is a weak form of magnetism and in most cases, other phenomena completely overshadow this contribution because those phenomena are more powerful. So to see the diamagnetic behaviour, it is important to eliminate other magnetic phenomena as ferromagnetism or antiferromagnism [25]. Generally, the magnetic susceptibility of diamagnetic materials is negative with a magnitude of the order of -10^{-5}. In most materials diamagnetism is a weak effect which can only be detected by sensitive laboratory instruments. The magnetic susceptibility of diamagnetic materials normally depends only very weakly on temperature and is almost temperature independent from room temperature and below.

2.2.1.2 Paramagnetism

In contrast to diamagnetic materials, paramagnetic, ferromagnetic, ferrimagnetic, and antiferromagnetic materials are attracted by a magnetic field. Substances are considered paramagnetic when there is an intrinsic non-zero magnetic moment on each of their atoms, which is independent of the applied magnetic field. There is also no dipole moment and the electron spins are randomly oriented in the absence of a magnetic field. When a magnetic field is applied, and the unpaired electrons of the substance are aligned in the direction of the applied field, it is considered to be ferromagnetic. In paramagnetic and ferromagnetic materials, the weak diamagnetic force is overcome by the attractive force of magnetic dipoles in the material. The magnetic susceptibility of paramagnetic materials is always positive with an order of magnitude of 10^{-4}.

2.2.1 . Overview on magnetic structure

2.2.1.3 Ferromagnetism

Ferromagnetism is the basic mechanism by which certain materials (such as ions) form permanent magnets, or are attracted by magnets. Materials are only ferromagnetic below their corresponding Curie temperature. Ferromagnetic materials are magnetic in the absence of an applied magnetic field. When the field is absent, the material has spontaneous magnetization (also called the saturation magnetization) which is a result of the ordered magnetic moments; that is, for ferromagnetism, the spins are symmetric in that they are aligned in the same direction creating a permanent magnetic field. The magnetic interactions are held together by exchange interactions; otherwise thermal disorder would overcome the weak interactions of magnetic moments. Below the Curie temperature (T_C), the electron spins are aligned and parallel, causing spontaneous magnetization (figure 2.1). Above the Curie temperature, the material is paramagnetic, as the atoms lose their ordered magnetic moments when a material undergoes a phase transition [26]. Ferromagnetism is the strongest type of magnetism: it is the only one that typically creates a force strong enough to be felt, and is responsible for the common phenomena of magnetism in magnets encountered in everyday life. Permanent magnets (materials that can be magnetized by an external magnetic field and remain magnetized after the external field is removed) are either ferromagnetic or ferrimagnetic, as are the materials that are noticeably attracted to them. Only a few substances are ferromagnetic e.g. Fe, Ni and Co including most of their alloys and some rare-earth compounds. Ferromagnetism is very important in industry and modern technology (magnetic refrigeration) and is the basis of many electrical and electro-mechanical devices [17]. Ferromagnetism is a property not just of the chemical make-up of a material, but of its crystalline structure and microstructure. There are ferromagnetic metal compounds whose constituent elements are not themselves ferromagnetic, called Heusler compounds, named after Fritz Heusler. On the contrary, there are non-magnetic compounds, such as stainless steel, composed almost exclusively of ferromagnetic elements. Amorphous (non-crystalline) ferromagnetic metallic compounds can be made by very rapid quenching (cooling) of a liquid compound. These materials have an advantage in that their properties are nearly isotropic; these results in low coercitivity, low hysteresis loss, high permeability and high electrical resistivity [17]. These properties made these materials good candidates for magnetic refrigeration. One such typical material is a transition metal-

11

metalloid compound made from about 80% transition metal (e.g. Fe, Co or Ni) and a metalloid (e.g. B, C, Si, Al or P) [17]. A new class of exceptionally strong ferromagnet are the rare-earth magnets, which forms part of the investigations presented in this thesis. They contain rare-earth elements that are known for their ability to carry large magnetic moments in well localized $4f$-orbitals.
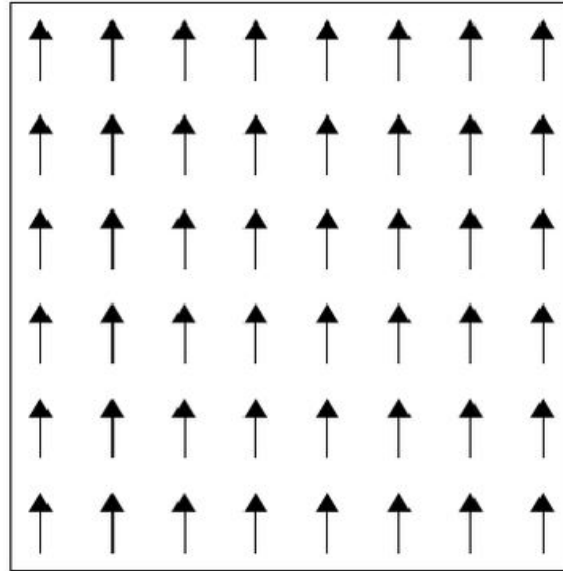
Figure 2.1: Ferromagnetic representation of spins aligned in the same direction.

In many ferromagnetic crystals, the saturation magnetization at $T = 0$ K does not correspond to the parallel alignment of the magnetic moments of the constituent paramagnetic ions, even in crystals for which the paramagnetic ions have their normal magnetic moments [23]. For instance, in the magnetite Fe_3O_4 or $FeO - Fe_2O_3$, the ferri (Fe^{3+}) ions are in the state with spin $S = 5/2$ and zero orbital moment, which means each ion should contribute 5 μ_B to the saturation moment. On the other hand, the ferrous (Fe^{2+}) ions have spin of $S = 2$ and should contribute 4 μ_B, neglecting the residual orbital moment contribution. Thus, the effective number of Bohr magnetons per Fe_3O_4 formula unit should be about 14 if all spins were parallel but the observed value is 4.1. This shortfall is understood if the moments of Fe^{3+} ions are antiparallel to each order, therefore the observed moment arise from Fe^{2+} ion [23].

2.2.1.4 Ferrimagnetism

The term ferrimagnetism, was coined originally to describe the ferrite type ferromagnetic spin order such as in figure 2.2. Ferrimagnetic materials are only ferrimagnetic below the Curie temperature. They are magnetic in the absence of an applied magnetic field and are made up of two different ions with moments directed antiparallel to each other. When a magnetic field is absent the material has a spontaneous magnetism which is the result of ordered magnetic moments; that is, for ferrimagnetism one ion's magnetic moments aligned facing in one direction with certain magnitude and the other ion's magnetic moments are aligned facing in the opposite direction with a different magnitude (figure 2.2). As the magnetic moments are of different magnitude in opposite direction, there is still a spontaneous magnetization and a magnetic field is present [27]. Similar to ferromagnetic materials the magnetic interactions are held together by exchange interactions. The orientation of moments however are antiparallel which results in net magnetic moments by subtracting their momentum from one another [27]. The magnetization and magnetic susceptibility behaviour of ferrimagnetic materials are similar to that of the ferromagnetic materials. In general, ferrimagnetic materials are poor conductors compared to ferromagnetic materials but useful in applications when a material with a minimum spontaneous magnetization is required to operate at high frequencies like in the transformer devices with no significant Eddy current.
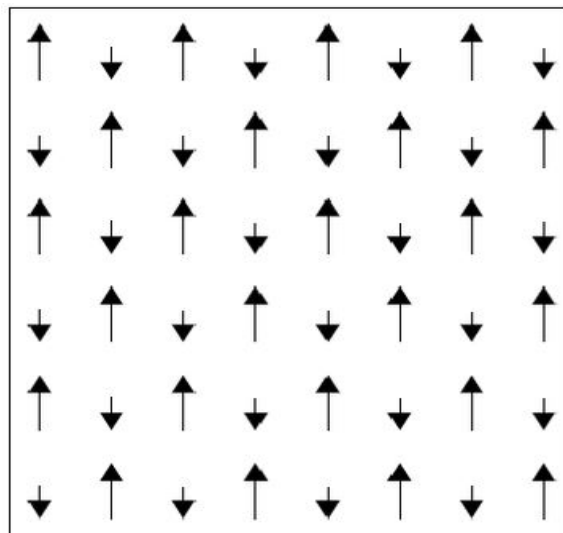
Figure 2.2: Ferrimagnetic representation of spins aligned in opposite directions with difference in magnitude.

2.2.1.5 Antiferromagnetism

In antiferromagnet, the spin are ordered in an antiparallel arrangement with zero net moment at temperature below the ordering or the Néel temperature T_N. An antiferromagnet is a special case of a ferrimagnet for which both magnetic moments have equal saturation magnetization. Materials are only antiferromagnetic below their corresponding Néel temperature (T_N). This is similar to the Curie temperature as above T_N the material undergoes a phase transition and becomes paramagnetic. The material has equal magnetic moments aligned in opposite directions (figure 2.3) resulting in a zero magnetic moment and a net magnetism of zero at all temperatures below T_N. Antiferromagnetic materials are weakly magnetic in the absence or presence of an applied magnetic field. Similar to ferromagnetic and ferrimagnetic materials the magnetic interaction are held together by exchange interactions preventing thermal disorder from overcoming the weak interactions of magnetic moment. When disorder occurs it is at T_N [27].
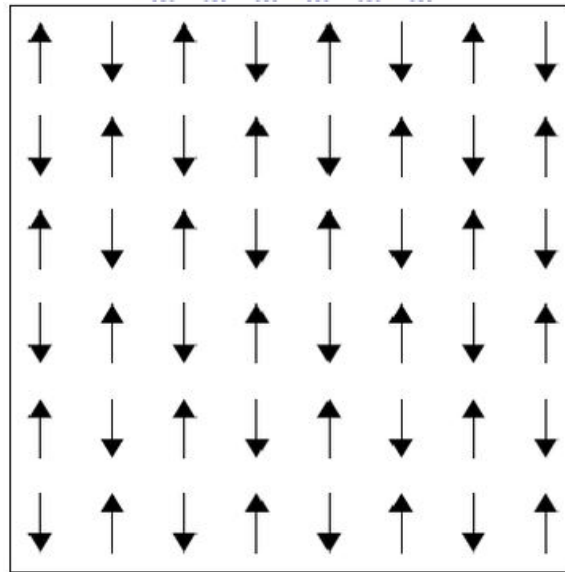
Figure 2.3: Antiferromagnetic representation of spins aligned in opposite directions with same magnitude.

2.2.2 Theory of magnetism

2.2.2.1 Paramagnetism and the Curie-law

Paramagnetism is the simplest type of magnetism in which the magnetization is reversible. For low levels of magnetization, the magnetization of paramagnets follows what is known as Curie's law, at least approximately. This law indicates that the magnetic susceptibility of paramagnetic materials is inversely proportional to their temperature, i.e. materials become more magnetic at lower temperatures. The mathematical expression of the Curie law is:

$$M = \chi H = \frac{C}{T}H, \tag{2.1}$$

where H is the applied magnetic field and C is a material-specific Curie constant. Curie's law is valid under the commonly encountered conditions of low magnetization ($\mu_B H \leq k_B T$, where μ_B is the Bohr magneton and k_B is the Boltzmann constant), but does not hold in the high/low temperature regime where saturation of magnetization occurs ($\mu_B H \geq k_B T$) and magnetic dipole are all aligned with the applied magnetic field. When the dipole are aligned, increasing the external magnetic field will not increase the total magnetization since there can be no further alignment. For paramagnetic ion with non-interacting magnetic moments with total angular momentum J, the Curie constant, C, is related to the individual ions magnetic moments through the relation:

$$C = \frac{N_A}{3k_B}\mu_{\text{eff}} \quad \text{where} \quad \mu_{\text{eff}} = g_J \mu_B \sqrt{J(J+1)}. \tag{2.2}$$

The parameter μ_{eff} is interpreted as the effective magnetic moment per paramagnetic ion. N_A is the Avogadro number and g_J is the gyromagnetic ratio also known as the Landé g-factor defined as follows:

$$g_J = 1 + \frac{J(J+1) + S(S+1) - L(L+1)}{2J(J+1)}, \tag{2.3}$$

with S and L representing the total electron spin and the total orbital momentums,

15

respectively. The origin of the observed magnetic behaviour results from electron spin and orbital motion and it becomes clear from equation 2.1 to 2.3 how the magnetic behaviour is directly related to the electron configuration of the magnetic ions. For the compounds investigated in this thesis, only the rare-earth elements contribute to the magnetism or carry a magnetic moment with good agreement between the theoretical and experimental μ_{eff} values.

2.2.2.2   Curie-Weiss law

The Curie-Weiss law is a simple model derived from mean-field approximation, this mean it works well for the materials with temperature T much greater than their corresponding Curie or Néel temperature, $T \gg T_{\text{C}}$ or T_{N}; however it fails to describe the magnetic susceptibility, χ, in the immediate vicinity of the Curie or Néel point because of local fluctuation between atoms [28]. The Curie-Weiss law is an adapted version of the Curie law. It holds particularly at high temperature where there is known spontaneous interaction between neighboring unpaired electrons (systems with minimal interaction). For systems with interaction, paramagnetic behaviour is observed but at low enough temperatures the magnetic moment may order. The Curie or Néel point is seen as a phase transition between a ferromagnet or antiferromagnet and a paramagnet. The word paramagnet merely refers to the linear response of the system to an applied magnetic field. Therefore, a modification is made to the Curie law which incorporates a parameter, θ, to indicate the strength of the interaction between the unpaired f-electrons, and known as the Curie-Weiss law:

$$\chi_{CW}(T) = \frac{N\mu_{\text{eff}}^2}{3K_{\text{B}}\left(T - \theta_{\text{P}}\right)}, \tag{2.4}$$

where θ_{P} is the Weiss temperature. The sign of θ_{P} depends on whether ferromagnetic or antiferromagnetic interactions dominate and it is rarely exactly zero, except in the dilute, isolated cases. The paramagnetic Curie-Weiss description above T_{C} or T_{N} is a rather different interpretation of the word paramagnet as it does not imply the absence of interactions, but rather that, the magnetic structure is random in the absence of an external magnetic field. Usually, ferromagnetic substances show very large susceptibilities compared to para-

magnetic substances and deviate from Curie-Weiss law below a ferromagnetic temperature T_{C}. This deviation results from the parallel alignment of the magnetic moments which eventually saturate at a very low-temperature. On the other hand, substances which order antiferromagnetically typically possess smaller χ values than paramagnetic substances at low-temperatures. The transition to antiferromagnetic order occurs below T_{N} as a result of disorder i.e. exchange interactions, which couple the magnetic moments and aligns in the antiparallel manner. Both the Curie and Curie-Weiss law cannot describe the susceptibility behaviour below T_{C} or T_{N}.

2.2.2.3 Exchange interactions

i) Direct interaction

Magnetism is a macroscopic phenomenon that at microscopic level occurs due to exchange interactions, whose typical range, or more simply length scale, is determined by the spatial extent of the quantum mechanical wave function [29]. Confinement of these wave functions for example; the presence of a surface leads to many unusual magnetic phenomena [30]. The mechanism of spin alignment is not magnetic in origin; it is essentially the effect of the Pauli exclusion principle tending to keep parallel spins apart and known as exchange interaction. The interaction is a result of the fact that the wave function of two electrons must be antisymmetric under the exchange of all electron coordinates, space and spin:

$$\psi(\vec{r}_1, \vec{s}_1; \vec{r}_2, \vec{s}_2) = -\psi(\vec{r}_2, \vec{s}_2; \vec{r}_1, \vec{s}_1). \tag{2.5}$$

From this relation, it follows that the wave function vanishes when the coordinates of two electrons are identical: $\vec{s}_1 = \vec{s}_2, \vec{r}_1 = \vec{r}_2$. The overall antisymmetry of the wave function therefore tends to keep electrons of parallel spin apart so that the expectation of the coulomb repulsion energy $e^2/4\pi\varepsilon_0|\vec{r}_1 - \vec{r}_2|$ of both electrons is reduced for parallel spin than that of antiparallel spin. This represents the exchange interaction between the two electrons and can be expressed in the form $J_{12}\vec{s}_1.\vec{s}_2$, which correspond to the Coulomb energy of the parallel spin state being $2J_{12}$ smaller that of the antiparallel spin state. It result from this interpretation that $J_{12} > 0$ for ferromagnetic alignment of spins and

2.2.2 . Theory of magnetism

$J_{12} < 0$ for antiferromagnetic alignment of spins. Exchange interaction between the electrons of the same atoms explain Hund's rule. On the other hand, Coulomb interaction between two electrons on different atoms depends on their relative spin orientation as a result of the antisymmetry of the wave function. The resulting exchange energy decreases rapidly with increasing distance between the two atoms. This type of interaction just discussed is known as direct interaction which cannot explain magnetic ordering in rare-earth metals due to the small overlap of the $4f$ wave functions on neighboring atoms.

ii) Indirect interaction: Rudderman-Kittel-Kasuya-Yosida interaction

Another type of interaction is the indirect exchange process observed in the rare-earth metals. This indirect exchange interaction also leads to a coupling between spins of the same form as in the direct exchange interaction: $-J_{12}\vec{s}_1.\vec{s}_2$. In this case, J_{12} alternates in sign and decreases in magnitude with increasing distance between the atoms. The RKKY interaction refers to the interaction of the localized moments themselves through a spin density oscillation of the RKKY-type. This interaction results from the limited spatial extent of the $4f$ wave function of adjacent rare-earth centres which may turn out to be a negligible contribution to the inter-atomic coupling. Interaction between them can only be possible via polarized conduction electrons and leads to a magnetic ordering of $4f$ moments at low-temperatures. In contrast to the $3d$ metals, the $3d$ wave functions are spatially more extended and one can expect to find direct interaction provided that the atoms are close enough together or in an appropriate concentrated state. The mechanism of RKKY interaction is that the interaction between localized magnetic moment of the $4f$ ion and the spin of the conduction electron causes a spin polarization of the conduction band, creating an oscillating spin density wave [31]. The RKKY interaction for the magnetic exchange is described by the Hamiltonian:

$$H_{RKKY} = J_{RKKY}^{ij}\vec{S}_i.\vec{S}_j, \qquad (2.6)$$

where $\vec{S}_i$ and $\vec{S}_j$ are the total spins of the localized $4f$ electrons located at i and j position, respectively and separated by a distance $\vec{r}_{ij}.J_{RKKY}^{ij}$ is the coupling constant found to be

2.2.2 . Theory of magnetism

in the form [19, 32]:

$$J_{\text{RKKY}}^{i,j} = 6\pi Z J^2 N\left(E_{\text{F}}\right)\left(\frac{sin\left(2k_{\text{F}}r_{ij}\right)}{\left(2k_{\text{F}}r_{ij}\right)^4} - \frac{cos\left(2k_{\text{F}}r_{ij}\right)}{\left(2k_{\text{F}}r_{ij}\right)^3}\right), \tag{2.7}$$

with Z being the number of conduction electrons per atom, k_{F} the Fermi wave number, $N(E_{\text{F}})$ is the density of state at the Fermi level and J is the exchange integral defined according to the Schrieffer-Wolff transformation [33] as follows:

$$J = -\frac{|V_{sf}|^2}{|\varepsilon_{4f} - \varepsilon_{\text{F}}|}; \tag{2.8}$$

V_{sf} is the hybridization matrix element between the $4f$ electrons and the conduction band so $|V_{sf}|^2$ will describe the strength of the hybridization between the itinerant conduction electrons and the localized $4f$ electrons; $\varepsilon_{4\text{f}}$ denotes the position of the $4f$ energy level relative to the Fermi energy level ε_{F}. The negative sign indicates that the coupling between the conduction electrons and the local moment is antiparallel. The RKKY exchange coefficient J_{RKKY}^{ij}, oscillates from positive to negative as the separation of ions changes and has the damped oscillatory nature. Therefore, depending upon the separation, r_{ij} between a pair of ions, their magnetic coupling can be ferromagnetic or antiferromagnetic. The energy scale connected to the RKKY interaction is given by:

$$K_{\text{B}}T_{\text{RKKY}} \propto J^2 N\left(E_{\text{F}}\right). \tag{2.9}$$

2.2.2.4   Spin wave theory

[27, 34]

There are several reasons why researchers want to know the elementary excitations of ordered magnets. Some of these are: (i) experiments measure them and (ii) they determine thermal behaviour (at low-temperature) such as the specific heat, the resistivity or the reduction of the order parameter by thermal fluctuations.

Spin waves are the analog for magnetically ordered systems of lattice waves in solid sys-

2.2.2 . Theory of magnetism

tems; just like the quantized lattice wave is called a "phonon" and a quantized spin wave is called "magnon". This section illustrates the determination of the low-temperatures thermal behaviour of the heat capacity, magnetization and electrical resistivity relevant in this thesis.

A classical mechanical calculation of the low lying excited states of a chain of ferromagnetically aligned spins, assumed that the spins behave as classical angular momentum. This calculation is similar to that used to calculate the lattice vibrations in a solid system. Considering only the nearest neighbor exchange interaction and using the Heisenberg Hamiltonian:

$$H = -\sum_i \sum_{j \neq i} J_{ij} \vec{S}_i . \vec{S}_j, \tag{2.10}$$

(J_{ij} is the exchange interaction between the total spin momentums S_i and S_j of the i and j atoms) the exchange energy of the nth spin in the chain is given by:

$$E_n = -2J\vec{S}_n . \left(\vec{S}_{n-1} + \vec{S}_{n+1} \right), \tag{2.11}$$

where $2J$ is the nearest neighbor exchange interaction. From the equation of motion of the nth spin with some approximations, the dispersion relation of the spin waves is given by:

$$\hbar\omega_k = 4JS(1 - cos(ka)), \tag{2.12}$$

with k the wave vector and a the lattice spacing.

A quantum mechanical approach to the calculation of the spin waves also yields to the same dispersion relation given by equation 2.12, however, as we might expect from the analogy with lattice vibration, the energy of a mode of wave number k is quantized and can only take the value:

$$E_n = \left(n + \frac{1}{2} \right) \hbar\omega_k. \tag{2.13}$$

From the dispersion relation given by equation 2.12, the magnon energy ε as k tends to

2.2.2 . Theory of magnetism

zero, leads to a quadratic dependence of ε in the form:

$$\varepsilon = \hbar\omega_k = 2JSak^2. \tag{2.14}$$

The contribution of the spin waves to the heat capacity of ferromagnet materials at low temperature is then obtained using the number of spin wave modes with wave number between k et $k + dk$ and the number of mode with frequency between ω and $\omega + d\omega$. The energy associated with each mode is related to the average number of magnons at temperature T given by the Bose-Einstein distribution function. Thus, the contribution of the magnons to the total energy is given by:

$$E = E_0 + \frac{V}{4\pi^2}\left(\frac{\hbar}{2JSa^2}\right)^{3/2}\left(\frac{k_{\mathrm{B}}T}{\hbar}\right)^{5/2}\int_0^\infty \frac{x^{3/2}}{e^x - 1}dx, \tag{2.15}$$

where E_0 is the zero point energy, V is the volume of the crystal and $x = \hbar w/k_{\mathrm{B}}T$. Equation 2.15 leads to the spin wave contribution to the heat capacity at low temperatures in the form:

$$C_{\mathrm{M}} = \frac{dE}{dT} \propto k_{\mathrm{B}}T^{3/2}. \tag{2.16}$$

Similar to the heat capacity, the magnetization can be expressed in the form:

$$M = M_{\mathrm{s}}\left[11 - \frac{1}{NS4\pi^2}\left(\frac{k_{\mathrm{B}}T}{2JSa^2}\right)^{3/2}\int_0^\infty \frac{x^{1/2}}{e^x - 1}dx\right], \tag{2.17}$$

where $M_{\mathrm{s}} = Ng\mu_{\mathrm{B}}S$ is the saturation magnetization and the integral give a constant number. It follows from equation 2.17 that the magnetization decreases as $T^{3/2}$ from its saturation value is much better with the experimentally observed behaviour than those predicted by the mean-field theory.

For an anisotropy ferromagnet material, the magnon dispersion relation is given in the limit of small wave number k in the form [34]:

$$\omega_k = \Delta + Dk^2, \tag{2.18}$$

where Δ accounts for an anisotropy gap and D is the spin wave stiffness. The electrical resistivity resulting from the scattering of conduction electron due to the spin wave modes

21

2.2.2 . Theory of magnetism

is given by:

$$\rho_{\mathrm{M}} = \frac{A}{k_{\mathrm{B}}T} \int \frac{\omega}{\sinh^2\left(\omega/2k_{\mathrm{B}}T\right)} d\omega \int k^3 \, \mathrm{Im}\chi(k,\omega) dk, \tag{2.19}$$

where $A = (1/3\hbar)(4\pi m G^2/ne)$ with m, e, and n being the mass, charge and number of conduction electrons per unit volume, respectively. G is the coupling constant between the conduction electrons and the rare-earth moments. The imaginary part of the transverse dynamic susceptibility, $\mathrm{Im}\chi(k,\omega)$, associated with the spin waves is given by:

$$\mathrm{Im}\chi\left(k,\omega\right) = \pi\left[\delta\left(\omega - E_k\right) + \delta\left(\omega + E_k\right)\right], \tag{2.20}$$

with E_k the energy of the magnetic excitation responsible for the scattering of the conduction electrons. In the isotropic ferromagnet case $\Delta = 0$ (gapless dispersion in k-space) one obtains $\rho_{\mathrm{M}} \sim T^2$. For anisotropy ferromagnetic materials or when a symmetry lifting external magnetic field is applied, there is a gap in the spectrum and the resistivity can be obtained for $k_{\mathrm{B}}T \ll \Delta$, given by [35]:

$$\rho_{\mathrm{M}}\left(T\right) = a\Delta_{\mathrm{FM}}T\left[1 + 2\frac{k_{\mathrm{B}}T}{\Delta_{\mathrm{FM}}}\right] exp\left(-\frac{\Delta_{\mathrm{FM}}}{k_{\mathrm{B}}T}\right), \tag{2.21}$$

where a is a constant which depends on the materials. The spin wave contribution to the heat capacity at low-temperatures expected for an energy gapped ferromagnetic spin wave is given by:

$$C_{\mathrm{M}}\left(T\right) \approx \gamma T + BT^{3/2} exp\left(-\frac{\Delta_{\mathrm{FM}}}{k_{\mathrm{B}}T}\right), \tag{2.22}$$

where γ is the Sommerfeld coefficient and B a constant that defines the stiffness of the sample.

For antiferromagnetic materials, Yamada and Takada [36] suggest a new expression of the transverse dynamic susceptibility, $\mathrm{Im}\chi(k,\omega)$ associated with spin waves given by:

$$\mathrm{Im}\chi\left(k,\omega\right) = \frac{\pi}{\varepsilon_k}\left[\delta\left(\omega - \omega_k^+\right) + \delta\left(\omega + \omega_k^-\right)\right] \tag{2.23}$$
$$\omega_k^{\pm} = -\mu_{\mathrm{eff}}H \pm \varepsilon_k,$$

22

with:

$$\varepsilon_k = \frac{1}{2}\left(\omega_k^+ - \omega_k^-\right) = \left(\Delta^2 + Dk^2\right)^{1/2}. \tag{2.24}$$

The resistivity then follows:

$$\rho_{\mathrm{M}}(T) \approx b\Delta_{\mathrm{AFM}}^2 \left(\frac{k_{\mathrm{B}}T}{\Delta_{\mathrm{AFM}}}\right)^{1/2} exp\left(-\frac{\Delta_{\mathrm{AFM}}}{k_{\mathrm{B}}T}\right) \times$$
$$\left[1 + \frac{2}{3}\left(\frac{k_{\mathrm{B}}T}{\Delta_{\mathrm{AFM}}}\right) + \frac{2}{15}\left(\frac{k_{\mathrm{B}}T}{\Delta_{\mathrm{AFM}}}\right)^2\right], \tag{2.25}$$

where b is a constant. The spin wave contribution to the heat capacity at low temperatures expected for an energy gapped antiferromagnetic spin wave having the same dispersion relation given by equation 2.24 takes the form [37]:

$$C_{\mathrm{M}}(T) = \Delta_{\mathrm{AFM}}^{7/2}T^{1/2}exp\left(-\frac{\Delta_{\mathrm{AFM}}}{k_{\mathrm{B}}T}\right) \times$$
$$\left[1 + \frac{39}{20}\left(\frac{k_{\mathrm{B}}T}{\Delta_{\mathrm{AFM}}}\right) + \frac{51}{32}\left(\frac{k_{\mathrm{B}}T}{\Delta_{\mathrm{AFM}}}\right)^2\right]. \tag{2.26}$$

2.2.3 Crystal electric field effect and Schottky anomaly

Crystal electric field results from the surrounding electrons and ions in the crystal. In a compound, a $4f$-ion is exposed to a crystal-electric-field, which reflects the symmetry at the rare-earth ion site. This crystal-electric-field completely or partially lifts the degeneracy of the $4f$ free-ion ground state multiplet $(2J + 1)$, J being the total angular momentum. It should be noted that the ground state of a free-ion or atom with a partially filled $4f$ shell can be derived using Hund's rule. Ground state multiplets generally denote the lowest lying multiplets in the presence of a crystal-electric-field. The resulting number of multiplets is determined by the local crystal symmetry and their relative energy levels depends on the exact form and magnitude of the crystal-electric-field.

In rare-earth compounds, crystal-electric-fields are likely responsible for the magnetocrystalline anisotropy, but may themselves cause the splitting of the $(2J + 1)$-fold degenerate manifold. The crystal-electric-field splitting affects many physical properties. For a system with a first excited level at $k_{\mathrm{B}}T_{\Delta_{\mathrm{CEF}}}$ ($T_{\Delta_{\mathrm{CEF}}}$ denotes the temperature correspond-

ing of the crystal-electric-field) above the ground state, only the lowest lying multiplet has a high probability of occupancy for $T \ll T_{\Delta_{\text{CEF}}}$. Therefore, the properties of the system are determined by the ground state multiplet. With increasing temperature, the state above the ground state becomes populated. The corresponding increase of entropy shows up as an extra contribution to the $4f$-electron specific heat of the system in the region $T_{\Delta_{\text{CEF}}}$, in the form of Schottky anomaly, expressed for m number of levels in the form:

$$
C_{\text{Sch}}(T) = \frac{R \sum_{i=0}^{m} g_i \left(\frac{\Delta_i}{T}\right)^2 exp(-\frac{\Delta_i}{T})}{\left[\sum_{i=0}^{m} g_i \left(-\frac{\Delta_i}{T}\right)\right]^2} \times
$$
$$
\left[\sum_{i=0}^{m} g_i exp(-\frac{\Delta_i}{T}) - \sum_{i=0}^{m} g_i (\frac{\Delta_i}{T})^2 exp(-\frac{\Delta_i}{T})\right], \tag{2.27}
$$

where level i with degeneracy of g_i is situated at an energy Δ_i above the ground state. The change of the effective moment with increasing occupancy of higher energy levels becomes evident in the magnetic susceptibility. Transport properties reflect the enhanced scattering on crystal-electric-field excitation around $T_{\Delta_{\text{CEF}}}$. In the case of the temperature variation of the electrical resistivity, crystal-electric-field is sometimes characterized by a broad curvature at high temperatures around $T_{\Delta_{\text{CEF}}}$.
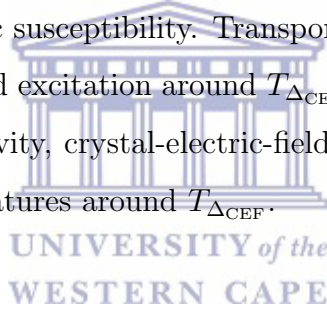
2.3 Critical behaviour

The description of magnetic transition in the vicinity of critical temperature can be made through the use of critical exponents. It is a matter of expressing the quantities studied according to the relevant quantities of the system in accordance with a power law. In magnetic systems, the most relevant critical exponents correspond to the temperature dependence of the spontaneous magnetization and magnetic field dependence of magnetization value at the Curie temperature. Depending on the type of model, the value of the exponents are different. According to the scaling hypothesis, for second order phase transition, the spontaneous magnetization M_{s} below T_{C}, inverse initial susceptibility $\chi_0^{-1}(T)$ above T_{C} and magnetization M at T_{C} follow the power-law dependence [38]:

$$
M_{\text{s}}(T) = M_0 \left(-t\right)^{\beta}; \quad t{<}0, \tag{2.28}
$$

2.3. Critical behaviour

$$\chi_0^{-1}(T) = \Gamma(-t)^\gamma; \quad t>0 \tag{2.29}$$

$$M = XH^{1/\delta}; \quad t = 0, \tag{2.30}$$

where $t = (T - T_{\mathrm{C}})/T_{\mathrm{C}}$ is the reduced temperature, M_0, Γ and X are the critical amplitudes. The magnetic equation of states relating to the variables $M(\mu_0 H, t)$, $\mu_0 H$ and T can be obtained using the scaling hypothesis and can be expressed as:

$$M(\mu_0 H, t) = |t|^\beta f_\pm \left(\frac{\mu_0 H}{t^{\beta+\gamma}}\right), \tag{2.31}$$

where $f_+(T > T_{\mathrm{C}})$ and $f_-(T < T_{\mathrm{C}})$ are regular analytic functions. Equation 2.31 implies that for true scaling relations and right choice of β, γ and δ, the scaled $M/|t|^\beta$ plotted as a function of $\mu_0 H/|t|^{\beta+\gamma}$ reveals that the magnetic isotherms in the vicinity of T_{C} fall into two individual branches, one for $T < T_{\mathrm{C}}$ and the other for $T > T_{\mathrm{C}}$. However, the critical exponents often show various systematic trends or crossover phenomena as one approaches T_{C} [39, 40, 41]. This occurs if the magnetic system is governed by various competing couplings and/or disorders. In that case, it is useful to introduce the temperature-dependent effective critical exponents, β_{eff} and γ_{eff} for $t \neq 0$. It can be mentioned that effective exponents are nonuniversal properties and they are defined as [38]:

$$\beta_{\mathrm{eff}}(t) = \frac{d[\ln M_{\mathrm{s}}(t)]}{d \ln(t)} \gamma_{\mathrm{eff}}(t), \tag{2.32}$$

$$\gamma_{\mathrm{eff}}(t) = \frac{d\left[\ln \chi_0^{-1}(t)\right]}{d(\ln t)}. \tag{2.33}$$

- In the asymptotic limit $t \longrightarrow 0$, the effective exponents approach the universal critical (asymptotic) exponent.

- In the critical regime (asymptotic limit) where $\chi \sim (T - T_{\mathrm{C}})^\gamma$, γ_{eff}, is defined as $\lim_{t\to 0} \gamma_{\mathrm{eff}} = \gamma$.

- At high temperatures (mean-field theory, $T \longrightarrow \infty$) where we can establish the Curie-Weiss law, $\chi = C/(T - T_{\mathrm{C}})$, γ_{eff} is defined as $\lim_{t\to 0} \gamma_{\mathrm{eff}} = 1$.

2.3.1 Mean-field theory

[42]

The mean-field theory is one of the main tools of finding the critical temperature of magnetic materials below the paramagnetic phase transition. This theory usually applies to a spontaneous magnetization and on the inverse initial susceptibility respectively, just below and above the critical temperature. From this, the mean-field theory could be defined as an approximation of treating a full system of interacting particles, it is a useful approach which gives a qualitative prediction of the behaviour at the phase transition [43]. So, in Physics there are some complicated equations to solve and therefore require some approximations to get the right solutions. Some researchers like Ising and Heisenberg, found the tools to overcome these difficulties via the mean-field theory model. From interactions studied above and the fact that atoms are a set of spins $(\pm\frac{1}{2})$, the simplest approach to consider, according to the interactions between spins is to take into account the average exchange felt by a particular spin (i) due to all the other spins in atom [44]. This is the essence of the mean-field theory. In this system, spins are connecting to the nearest neighbors of the specific spin (i) by the Hamiltonian [42, 45]:

$$\delta H_i = S_i \left[J \sum_\delta S_{i+\delta} \right] - \vec{\mu}_i H = -\vec{\mu}_i H_{\text{eff}}, \tag{2.34}$$

which includes the coupling term of the spin to the external field with H_{eff} the effective magnetic field defined as: $H_{\text{eff}} = -\frac{J}{g\mu_{\text{B}}} \sum_\delta S_{i+\delta} + H$.

In mean-field theory, the term S_i is replaced by the average of the neighboring operators $<S_{i+\delta}>$, so, the effective magnetic field becomes [42]:

$$H_{\text{eff}} = -\frac{Jn}{(g\mu_{\text{B}})^2} M, \tag{2.35}$$

where $M = <\mu>$ is the magnetization and n is the number of nearest neighbors atoms. In an effective magnetic field, the magnetization takes the form of [42]:

$$M\gamma S B \left(\beta\gamma S H_{\text{eff}} \right) = \gamma S B \left(\beta\gamma S \left[-\frac{Jn}{(g\mu_{\text{B}})^2} M \right] \right), \tag{2.36}$$

where γ and β are constants and $B(x)$ is the Brillouin function (with $x = \beta\gamma S H_{\text{eff}}$). This

26

nonlinear equation can be solved for a given H. So, to get the critical temperature for example, this equation will be solved for $H = 0$ and the $B(x)$ will be expanded for small value of x. Then equation 2.36 above becomes:

$$M = -\gamma S B \left(\frac{nJ}{\gamma T_{\mathrm{C}}} M \right) \approx -\gamma S \frac{S+1}{3S} \frac{nJ}{\gamma T_{\mathrm{C}}} M; \qquad (2.37)$$

$$\Rightarrow T_{\mathrm{C}} = -\frac{S(S+1)}{3} nJ. \qquad (2.38)$$

In this theory, T_{C} is of the same order with the interaction energy $|J|$. Below T_{C}, the variation of the magnetization near the transition is proportional to T as follows: $M \sim (T - T_{\mathrm{C}})^{1/2}$. Just above T_{C} the inverse magnetic susceptibility is also proportional to T as $\chi_0^{-1} \sim (T - T_{\mathrm{C}})$. The exponents 1/2 and 1 are characteristic of the disappearance of the order parameter near the transition of the classical mean-field theory model [46, 47].

2.3.2 The Ising model

The Ising model is a crude model for ferromagnetic compounds that takes the lattice of magnetic moments into account [48, 49]. It can be derived from quantum mechanics through several considerations, educated guesses and rough simplifications. This theory on the studies of phase transition (which take place when a small variation of a parameter such as temperature or applied magnetic field changes the state of a system) was discovered by Ernest Ising in 1920 [50]. The spontaneous magnetization of ferromagnetic compounds is the original purpose of this model. In this regard, two cases are well-established [42, 48, 49, 51, 52]:

- in the absence of interactions, the spin are in paramagnetic state and trying to align with an applied field. The Hamiltonian in this particular approximation is:

$$H_{\mathrm{P}} = \sum g\mu_{\mathrm{B}} B \vec{\sigma}, \qquad (2.39)$$

with $\sigma = \pm\frac{1}{2}$ being the value of the spin and B is the applied magnetic field.

- by considering the interactions between neighboring spins i and j, the Hamiltonian

takes the form of:

$$H_{\text{int}} = -\frac{J}{2} \sum_{i \neq j} \sigma_i \sigma_j. \tag{2.40}$$

The Ising model put together these two cases [42]:

$$H_{\text{Ising}} = -\frac{J}{2} \sum_{i \neq j} \sigma_i \sigma_j + \sum g\mu_{\text{B}} B \vec{\sigma}. \tag{2.41}$$

Looking at this latter equation, Ising proposed some approximations to solve it by using the mean-field theory. This theory is based on treating exactly one spin at a time and average over all of the properties of the surrounding spins and makes the assumption that, the mean-field for all spins is the same (so that the result must be self-consistent) [46]. By focusing on one spin i, the factor $1/2$ cancels and the average Hamiltonian over the lattice volume becomes [42, 53]:

$$H_i = -J\sigma_i \sum <\sigma_j> + g\mu_B B \sigma_i, \tag{2.42}$$

where, $<\sigma_j>$ is the average value of neighboring spins in the lattice. Suppose $<\sigma_j> = n <\sigma_i>$, where n is the number of the nearest neighbor spin. The self-consistent approximation reveals $<\sigma_j> = <\sigma_i>$ for every spin j and it follows [42, 53]:

$$H_i = \left(-Jn<\sigma_i> + g\mu_{\text{B}} B\right) \sigma_i. \tag{2.43}$$

In the absence of an external field, the energy depending on the average value of neighboring spins is [42]:

$$E_{\sigma i} = \pm\frac{1}{2} = \pm\frac{Jn}{2}<\sigma_i>. \tag{2.44}$$

From the point of view of statistical mechanics, the partition function Z could be stated as [42, 54]:

$$Z = e^{\beta Jn<\sigma_i>/2} - e^{-\beta Jn<\sigma_i>/2}, \tag{2.45}$$

28

2.3.2 . The Ising model

with:

$$<\sigma_i> = \frac{1}{2}\frac{e^{\beta Jn<\sigma_i>/2} - e^{-\beta Jn<\sigma_i>/2}}{e^{\beta Jn<\sigma_i>/2} - e^{-\beta Jn<\sigma_i>/2}} \approx \frac{1}{2}\tanh\left(\frac{\beta Jn<\sigma_i>}{2}\right), \qquad (2.46)$$

where $\beta = 1/k_B T$. By solving the self-consistency equation for $<\sigma_i>$, the magnetization of the material can be determined from the plotted graph $y = <\sigma_i>$ and $(1/2)\tanh(\beta Jn<\sigma_i>/2)$. When T is small, it leads to the spontaneous magnetization and the transition point from paramagnetic to ferromagnetic region which can be found by looking at the slope of the given curves for a small value of $<\sigma_i>$.

For a small value of x, $\tanh(x) \approx x \Rightarrow (1/2)\tanh(\beta Jn<\sigma_i>/2) \approx \beta Jn<\sigma_i>/4$, so, if $\beta Jn/4 < 1$ two lines intersect at $<\sigma_i> = 0$ and if $\beta Jn/4 > 1$, the lines will intersect again at non zero values of $<\sigma_i>$ and the critical temperature T_C occurs when $\beta Jn/4 = 1$ or $Jn/4k_B T_C = 1$, so, the critical temperature found takes the expression [42]:

$$T_C = \frac{Jn}{4k_B}. \qquad (2.47)$$

Considering the system at temperatures above the phase transition point the magnetization and the magnetic susceptibility, respectively become [42]:

$$M = \frac{N(E)\mu_B^2 B}{k_B T}, \qquad (2.48)$$

where $N(E)$ is the density of spins with energy E related to the magnetic susceptibility by:

$$\chi = \lim_{B \to 0} \mu_0 \frac{\partial M}{\partial B} = \frac{\chi_{\text{Curie}}}{1 - \frac{T_C}{T}}. \qquad (2.49)$$

Around T_C, the inverse magnetic susceptibility (just above T_C) and the spontaneous magnetization (just below T_C) are proportional to T as follows $\chi_0^{-1} \sim (T - T_C)^\gamma$ and $M_0 \sim (T - T_C)^\beta$, respectively with $\gamma = 1.241$ and $\beta = 0.325$. The exponents γ and β are characteristic of the disappearance of the order parameter near the transition of the classical 3D-Ising model [46, 47].
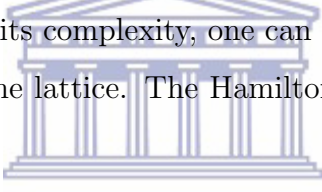
2.3.3   The Heizenberg model

[38, 55]

In the Heisenberg model of the mean-field theory, the main idea is the fact that it exists as an exchange interaction with a coupling constant λ between the magnetic moments of spins S_i and S_j located on different sites i and j. In this particular case, the exchange energy can be expressed as:

$$E_{\text{ex}} = -2J_{ij}S_i.S_j, \tag{2.50}$$

where J_{ij} is the exchange parameter. The negative sign conforms to the agreement that if $J_{ij} >0$ the configuration in which the spins S_i and S_j are parallel is privileged. In the opposite case ($J_{ij} <0$), the antiparallel alignment of spins is favoured. So, in order to easily solve equation 2.50 according to its complexity, one can assume that $J_{ij} = 0$ except when site i and j are neighboring of the lattice. The Hamiltonian for the entire system in this case then takes the expression:

$$H_{\text{ex}} = -\sum_{i=1}^{n}\sum_{j=1}^{n} J_{ij}S_iS_j - g\mu_{\text{B}}\sum_{i=1}^{n} S_i.H, \tag{2.51}$$

where H is the applied magnetic field. The mean-field approximation to the Heisenberg Hamiltionian of equation 2.51 is one of the largest classes of cluster approximations [56]. In this case, one only treats the interactions among the spins within a cluster exactly, whereas for the remaining spins in the system (in the z-direction) one can suppose $S_{iz} = <S_z>$ and $S_{ix} = S_{iy} = 0$. For the molecular field approximation, one chooses the cluster to consist of a single spin, so that the Hamiltonian becomes:

$$H_i = \left(-2\sum_{j} J_{ij}<S_z> - g\mu_{\text{B}}H\right) S_{iz}. \tag{2.52}$$

Equation 2.52 describes a single spin situated in a magnetic field of magnitude:

$$H_{\text{eff}} = 2\left(\frac{\sum_j J_{ij}}{g\mu_{\text{B}}}\right) <S_z> + H = 2\left(\frac{\sum_j J_{ij}}{(g\mu_{\text{B}})^2}\right) M + H, \tag{2.53}$$

30

with the coupling constant $\lambda = 2 \left(\sum_j J_{ij}/(g\mu_{\mathrm{B}})^2 \right)$. So, the relation between the critical temperature, the Curie constant C and λ is given by:

$$T_{\mathrm{C}} = \lambda C = \frac{2}{3k_{\mathrm{B}}} S(S+1) \sum_j J_{ij}. \tag{2.54}$$

For the case of nearest neighbors interactions ($J_{ij} = J$ only when site j is one of the q sites that are nearest neighbors of site i), $\sum_j J_{ij} = qJ$ (q being the coordination number) and T_{C} in this case could be written as follows:

$$T_{\mathrm{C}} = \frac{2}{3k_{\mathrm{B}}} qJS(S+1). \tag{2.55}$$

In this Heisenberg model, the disconcerting aspect about equation 2.55 is that it predicts two lattices with the same value of q. For instance, the simple cubic lattice is predicted to have the same value of T_{C} as the plane triangular lattice.

The spontaneous magnetization below T_{C} and the inverse magnetic susceptibility are proportional to T_{C}. i.e. $M_{\mathrm{s}} \sim (T-T_{\mathrm{C}})^{\beta}$ and $\chi_0^{-1} \sim (T-T_{\mathrm{C}})^{\gamma}$ with $\beta = 0.365$ and $\gamma = 1.386$. The exponents β and γ are characteristic of the disappearance of the order parameter near the transition of the classical 3D-Heisenberg model [46, 47].

2.4 Phase transition

All thermodynamic systems are characterized by a certain number of physical parameters, called variables of state such as the density or the magnetization. If the metal has the magnetic properties, it is evident that these variables strongly depend on the conditions applied to the system, in particular the temperature, the pressure, and the applied magnetic field. From this dependence emerges a fundamental property of matter, which is the possibility of seeing one of these parameters of state undergoing sudden variation on the macroscopic scale. This is what is called a "phase transition". There are two main types of transitions (first and second order), which are distinguished by the existence or not, of the variation of entropy during the transition from one phase to another at constant temperature and pressure. The first order phase transition is characterized by a discontinuity of at least one first derivative of the appropriate potential such as the entropy at the transition point. Then comes the transition of higher order which is characterized by the continuity

of all the first derivatives of the potential. Nevertheless, a great majority of them are of the second order, that is to say, that some second order derivatives are discontinuous as it is in the case of the specific heat at constant pressure [57].

2.4.1   Landau theory of second-order phase transition

The Landau theory of second order phase transition is based on the existence of order parameter (the spontaneous magnetization is the order parameter of the transition), thus, the value characterizes the phase present in the considered system. At high temperature this parameter is zero. At low-temperatures, a spontaneous symmetry break occurs at about the critical point and the order parameter takes a non-zero value in the ordered phase. At the vicinity of the critical point, Landau suggests developing the free energy of the system in power of order parameter. From this development, Landau comes out with the value of the critical exponents known as the mean-field model. In this model, the succession of the phases when the temperature increases is understood by a competition between the internal energy U (which favor order in the system) and the entropy S (source of disorder) in the free energy G and in which the minimum value of the order parameter denotes the thermodynamic equilibrium [54, 57, 58].

2.5   Magnetocaloric effect

2.5.1   Introduction and background

The first observation of the magnetocaloric effect dates back to almost 136 years (1881), when Warburg observed it in iron. So, in the years 1926 - 1927, the idea of using adiabatic demagnetization to reach a very low-temperature has been proposed, independently by Debye and Giauque [59, 60]. The magnetocaloric effect is defined as the change in temperature of certain magnetic materials due to the variation of an applied magnetic field. One of the most important applications of this effect, is the magnetic refrigeration which is based on the results in the heating of a material during its magnetization and its cooling during its demagnetization process. So, in a conventional refrigeration system, a gas is used, which leads to its heating and then its cooling. Similarly, the studies of

the magnetocaloric effect in rare-earth compounds has great importance in magnetism in order to improve the quality of magnetic refrigeration. In addition to refrigeration, the magnetocaloric effect applies to several areas of technology such as electronic devices, air conditioners and heat pumps.

2.5.2 Magnetocaloric effect principle

To describe the magnetocaloric effect, a paramagnetic or a ferromagnetic spin system close to its transition temperature has to be considered. The entropy of the system can be described by the entropy relative to the magnetic order of the system (magnetic entropy) and that related to the temperature of the system (lattice entropy, electronic entropy). The application of an external field aligns the spin moments at the origin disorder by the thermal agitation as is shown in figure 2.4:
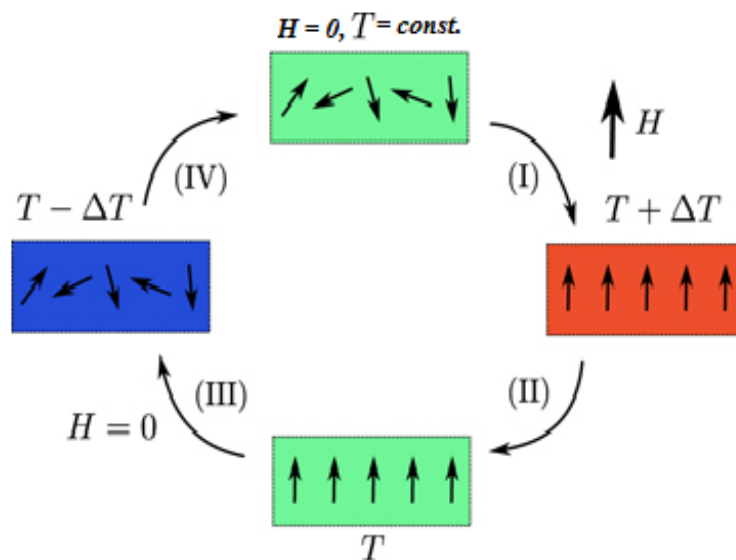
Figure 2.4: Schematic representation of the basic processes of the magnetocaloric effect.

In most cases, the electronic and lattice contribution of the entropy are independent of the magnetic field. In the isothermal process shown in figure 2.4 above, the variation of the magnetic entropy is ΔS_{M}, whereas, if the operation is performed without heat exchange with the outside (adiabatic process), the electronic and lattice entropy increase in order to maintain the entropy of the unchanged system. The increasing of entropy leads to a heating of the system and therefore to an increase of the temperature. If the process is reversible, an adiabatic demagnetization will cause a decrease in temperature up to its initial value [61]. For the antiferromagnetic system, the application of an external

field destroys the antiparallel arrangement of the magnetic moments and therefore the disorder increases. The magnetocaloric effect generally passes through extrema (minimum or maximum) at the transition temperature. It requires an important magnetic moment to have a significant magnitude. In fact, during the isothermal magnetization process, the total magnetic entropy change ΔS_{H} of the magnetic system due to the external applied field H is given as:

$$\Delta S_{\mathrm{M}}(T, H) = \int_{H_0}^{H_1} \left(\frac{\partial M(T, H)}{\partial T} \right)_H dH. \tag{2.56}$$

Since $\partial M / \partial T$ has its maximum around the transition temperature, a large value of the magnetocaloric effect is expected near the transition temperature. In fact the maximum theoretical molar magnetic entropy variation of a material is given by its magnetic contribution [62]:

$$\Delta S_{\mathrm{M}}{}^{max} = R \ln (2J + 1), \tag{2.57}$$

where R is the gas constant and J is the total angular momentum of the magnetic ion.

2.5.3 Thermodynamic approach of magnetocaloric effect

The entropy of magnetic materials at constant pressure depends on the applied magnetic field H and the temperature T. The thermodynamic entropy relation can be written as the sum of three contributions (magnetic, lattice and electronic contribution), viz:

$$S(T, H) = S_{\mathrm{M}}(T, H) + S_{\mathrm{lat}}(T) + S_{\mathrm{el}}(T). \tag{2.58}$$

When a variation of a magnetic field is applied (from H_0 to H_1), adiabatic process and reversible process state that the total entropy of the system remains constant and the system undergoes an increase in temperature and a decrease in the magnetic entropy ΔS_{M}. The increase in temperature ΔT_{ad} can be evaluated as the isentropic difference of $S(T)$ curves to H_0 and H_1 as in figure 2.5 [11] where the difference between the entropy curves at H_0 and H_1 at a given temperature corresponds to the variation of the magnetic entropy ΔS_{M}.
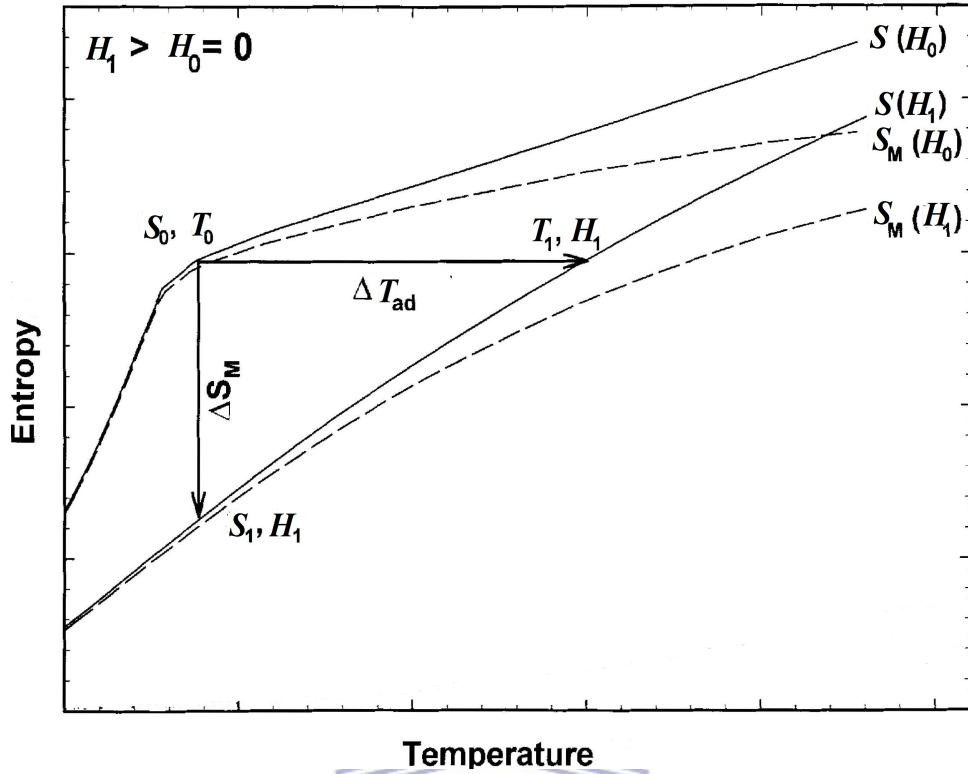
Figure 2.5: Diagram presenting the different processes of the magnetocaloric effect. Solid green line represents the total entropy in two different magnetic fields ($H_0 = 0$ and $H_1 > 0$), the dotted lines show the electronic and lattice contributions to the entropy (non-magnetic) and the dashed lines show the magnetic entropy in the two fields. The horizontal red arrows shows ΔT_{ad} and the vertical arrow shows ΔS_M, when the magnetic field is changed from H_0 to H_1.

So, the variation of the adiabatic temperature ΔT_{ad} and the variation of the magnetic entropy ΔS_M represents the two physical quantities allowing to quantify the magnetocaloric effect. This variation of both quantities are determined by the physical measurements of the magnetization or the heat capacity. The thermodynamic relationship that links ΔT_{ad} and ΔS_M are:

- Variation of magnetic entropy ΔS_M and the magnetization M. The thermodynamic properties of a magnetic system where the pressure is constant and where the temperature and the applied field H is varying, are described by the free Gibbs energy G:

$$G\left(P, H, T\right) = U + PV - \mu_0 MH - TS, \tag{2.59}$$

where U is the internal energy of the system, V is the volume of the sample, μ_0 is the

2.5.3 . Thermodynamic approach of magnetocaloric effect

permeability of the vacuum and S is the entropy. The differentiation of G gives:

$$dG\left(P, H, T\right) = dU + PdV - \mu_0 M dH - TdS + VdP - \mu_0 H dM - SdT. \qquad (2.60)$$

If these three parameters (P, H and T) are not constant , this becomes:

$$dG(P, H, T) = \left(\frac{\partial G}{\partial P}\right)_{H,T} dP + \left(\frac{\partial G}{\partial H}\right)_{P,T} dH + \left(\frac{\partial G}{\partial T}\right)_{H,P} dT. \qquad (2.61)$$

From the equations 2.60 and 2.61, it emerges the first thermodynamic principle:

$$dU = TdS + \mu_o H dM - PdV, \qquad (2.62)$$

and equation 2.61 becomes:

$$dG\left(P, H, T\right) = VdP - \mu_0 M dH - SdT. \qquad (2.63)$$

From these last equations, the equation of states is described as:

$$V = \left(\frac{\partial G}{\partial H}\right)_{H,T} ; \quad \mu_0 M = \left(\frac{\partial G}{\partial H}\right)_{P,T} ; \quad S = -\left(\frac{\partial G}{\partial T}\right)_{P,H} . \qquad (2.64)$$

The partial derivative of these three equations of states lead to Maxwell equations:

$$\mu_0 \left(\frac{\partial M}{\partial T}\right)_{P,H} = -\frac{\partial}{\partial T}\left(\left(\frac{\partial G}{\partial T}\right)_{P,T}\right)_{P,H} = -\frac{\partial}{\partial H}\left(\left(\frac{\partial G}{\partial T}\right)_{P,H}\right)_{P,T} = \left(\frac{\partial S}{\partial H}\right)_{P,T} . \quad (2.65)$$

The variation of the entropy associated with the magnetocaloric effect at constant pressure and at constant temperature can be determined by:

$$\int_{H_0}^{H_1} \mu_0 \left(\frac{\partial G}{\partial T}\right)_{P,H} dH = \int_{H_0}^{H_1} \mu_0 \left(\frac{\partial S}{\partial H}\right)_{P,T} dH = \Delta S\left(T, H_0 \longrightarrow H_1\right), \qquad (2.66)$$

$\Rightarrow$

$$\Delta S\left(T, H_0 \longrightarrow H_1\right) = \mu_0 \int_{H_0}^{H_1} \left(\frac{\partial G}{\partial T}\right)_{P,H} dH. \qquad (2.67)$$

This variation of the entropy is called change of magnetic entropy ΔS_{M}

36

2.5.3 . Thermodynamic approach of magnetocaloric effect

- Variation of ΔS_{M}, Δ_{ad} and heat capacity C_{p}:

The quantity ΔS_{M} is connected to the quantity of heat which can be transferred from T_0 to T_1 (heating process) from the equation:

$$q = \int_{T_0}^{T_1} \Delta S_{\mathrm{M}} \left(T, H_0 \longrightarrow H_1\right) dT, \tag{2.68}$$

the derivative of the entropy in respect to the variables T, H, P gives:

$$S = S\left(P, H, T\right) \Rightarrow dS = \left(\frac{\partial S}{\partial T}\right)_{H,T} dP + \left(\frac{\partial S}{\partial H}\right)_{P,T} dH + \left(\frac{\partial S}{\partial T}\right)_{P,H} dT. \tag{2.69}$$

The heat capacity at constant pressure and constant field is defined as:

$$C_{P,H} = T\left(\frac{\partial S}{\partial T}\right)_{P,H}. \tag{2.70}$$

If the system is at constant pressure, the differentiation of Maxwell equation above (equation 2.69) becomes:

$$dS = \mu_0 \left(\frac{\partial M}{\partial T}\right)_{P,H} dH + \frac{C_{P,H}}{T} dT. \tag{2.71}$$

In this latter equation (equation 2.71), if $\mathrm{d}\,T = 0$, then $dH \neq 0$. And if the integration of ΔS_{M} varies from H_0 to H_1, it will be clear that the variation of the entropy will be higher. This occurs around the critical temperature of a magnetic compound. For a given magnetic filed, the entropy can be determined from the heat capacity as follows [11]:

$$dS = \frac{C_{P,H}}{T} dT \Rightarrow \Delta S\left(T, H\right) = \int_{T_0}^{T_1} \frac{C_{P,H}}{T} dT. \tag{2.72}$$

So, the variation of the entropy due to $\Delta H = H_1$ - H_0 can be written as:

$$\Delta S\left(T, H_0 \longrightarrow H_1\right) = \int_{T_0}^{T_1} \frac{C_{P,H_0} - C_{P,H_1}}{T} dT. \tag{2.73}$$

By considering $\mathrm{d}S = 0$ (adiabatic process) the expression of the temperature variation

becomes [11]:

$$dT = -\frac{T}{C_{P,H}} \mu_0 \left(\frac{\partial M}{\partial T}\right)_{P,H} dM$$

$$\Rightarrow \Delta T\left(H_0 \longrightarrow H_1\right) = -\int_{H_0}^{H_1} \frac{T}{C_{P,H}} \mu_0 \left(\frac{\partial M}{\partial T}\right)_{P,H} dH. \tag{2.74}$$

Moreover, by considering all these equations, some information about the behaviour of the magnetocaloric effect in compounds can be figured out:

- Magnetization at a constant field in both paramagnetic and ferromagnetic materials decreases with increasing temperature i.e. $(\partial M / \partial T)_H < 0 \Rightarrow \Delta S_{\mathrm{M}}(T, \Delta H) < 0$.

- In ferromagnetic compounds, the absolute value of the derivative of magnetization with respect to temperature, $|(\partial M/\partial T)_H|$ is maximum at T_{C} and therefore $|\Delta S_{\mathrm{M}}(T, \Delta H)|$ should show a peak at $T = T_{\mathrm{C}}$.

The magnetocaloric effect is thus a very multiform property (different order/disorder transition, diversity of transition), which can be divided into various categories. Firstly, we can distinguish the magnetocaloric effect following: (i) the order of the transition: second order transition or first order transition (ii) the sign of magnetocaloric effect (normal or standard), as in the case of ferromagnetic materials with heating at the adiabatic application of the field, or inversely with the cooling (antiferromagnetic-ferromagnetic, respectively). From a point of view of magnetocaloric effect application, all types of materials (anti, ferro, paramagnetic) could be useful in a magnetic refrigeration system, air-conditioning and electronic devices.

2.6 Physical and magnetic properties

This section illustrates the theory of the physical and magnetic properties investigated in this thesis. These properties include: the electrical resistivity, the heat capacity, the magnetic susceptibility and magnetization.

2.6.1 Electrical resistivity

2.6.1 . Electrical resistivity

In general, transport properties in materials are governed by the free charge electrons (conduction electrons). Thus, knowledge of the density of the free electrons, the energy associated with free electrons and the paths they follow in a material are of great importance for the study of transport properties in particular, the electrical resistivity relevant in the present thesis. The free electrons in metals obey the Fermi-Dirac statistic. The Fermi surface separates the unoccupied state above the Fermi level to the occupied state below the Fermi level. As a result of that, the electrons near the Fermi surface govern the transport properties of a given material.

Transport properties in metals arise from scattering of conduction electrons from different sources. These sources can be:

- The presence of impurities can either be accidental, deliberate in the crystals or an imperfections in the crystals. The resistivity and thermal conductivity resulting from this scattering process are dominated at low-temperatures. The resistivity associated with this scattering process is known as residual resistivity, ρ_0 and is temperature-dependent.

- The vibration of the ions in the crystals around their fixed positions due to quantized lattice phonons. The effect increases largely as the temperature increases and it dominates at high temperatures. The resistivity associated with this scattering process is known as the phonon resistivity, ρ_{ph} and is temperature-dependent.

- The perfect magnetic order in ferromagnetism or antiferromagnetism as the temperature is decreasing below their Curie or Néel temperature. The resistivity associated with this scattering process is known as the magnetic resistivity, ρ_M and is dependent on the temperature.

- The localized magnetic moments of $4f$ or $5f$ atoms in diluted or concentrated Kondo systems, heavy fermion materials, intermediate valence and spin fluctuation systems. It is noted that this scattering process is irrelevant for materials under investigation in the present thesis.

- The electrons themselves, but for normal metals this effect is negligible and at high temperature electron-electron interaction is also negligible due to the dominant electron-phonon interaction [23]

39

2.6.1 . Electrical resistivity

Apart from the electron-electron scattering process, the transport properties such as electrical resistivity, $\rho(T)$, thermoelectric power, $S(T)$ and thermal conductivity, $\lambda(T)$ may be described using the linearised Boltzmann equation [63, 64] and can be expressed as follows:

$$\frac{1}{\rho(T)} = e^2 K_0; \quad S(T) = -\frac{K_1}{|e| \, T K_0}; \quad \lambda(T) = \frac{1}{T} \left(K_2 - \frac{K_1^2}{K_0} \right).$$ (2.75)

The integrals K_n are given by:

$$K_n = \frac{K_F^2}{3\pi^2 m} \int \varepsilon_k^n \tau(\varepsilon_k) \left(-\frac{\partial f_k}{\partial \varepsilon} \right) d\varepsilon_k,$$ (2.76)

where K_F is the wave vector at the Fermi surface, f_k the Fermi-Dirac distribution function, $\tau(\varepsilon_k)$ the relaxation time and ε_k the energy of the conduction electrons in a state k. Once the relaxation time is determined, the difference in transport properties can be obtained.

i) Linear approximation

The electrical resistivity of most materials changes with temperature. If the change in temperature ($\Delta T = T - T_0$) is too small, a linear approximation is used and it is written in the form:

$$\rho(T) = \rho_0 \left[1 + \alpha(T - T_0) \right],$$ (2.77)

where α denotes the temperature coefficient of resistivity, T_0 is a fixed reference temperature, usually taken at room temperature and ρ_0 is the resistivity at temperature T_0. The parameter α is an empirical parameter obtained from the fit of measurement data. Because the linear fitting is only an approximation, α is different for different reference temperatures. As a result of that, it is often to specify the temperature that α was measured at with a suffix, such as $\alpha 10$, and the relationship only holds in a range of temperatures around the reference [65]. For temperatures over a large temperature range, $\rho(T)$ deviates from linearity and a more detailed analysis and understanding should be required.

ii) Electrical resistivity of materials

The resistivity of metals originates from the contribution of different scattering processes than an electron suffers along its motion in a crystal. If the rates of collisions from these different scattering mechanisms are taken independently as first approximation, therefore this leads to Mathiessen's rule according to which the total resistivity is given by:

$$\rho(T) = \rho_0 + \rho_{\mathrm{ph}} + \rho_{\mathrm{M}}(T). \tag{2.78}$$

The sum of the first two terms is the total resistivity for a nonmagnetic material while the sum of the three terms is the total resistivity for a magnetic material.

As mentioned above, ρ_0 arises from the scattering of free electrons by stationary imperfections, defects or impurities in the crystal. This contribution to the total resistivity is a sensitive measure of the perfection of a specimen. In current practice, ρ_0 specifies the overall purity and perfection of a metal crystal. This is done by quoting the ratio of the resistivity at room temperature to that of the resistivity near zero temperature as $RRR = \rho_{300K}/\rho_{2K}$. In general, imperfections of a specimen have a great effect on the residual resistivity. The reduction of imperfections of a specimen can be achieved by heat treatment of the specimen at a sufficiently high temperature for a period of time. The value of ρ_0 of a metal directly dependent to its impurity concentration. Some materials lose all electrical resistivity at sufficiently low-temperatures, due to an effect known as superconductivity. At finite temperature, the thermal vibration of ions around their equilibrium position, produces departures from the perfect regularity of the ideal crystal and hence leads to scattering. This thermal vibration is known as phonons and give rise to electron-phonon scattering. The procedure for calculating the scattering probability due to phonons as a function of temperature is namely to find the number of available states into which an electron may be scattered and the number of suitable phonons available for scattering [66]. For an electron in a spherical Fermi surface, however, the density of available states is practically independent of the energy of the electron compared with the Fermi energy but depends strongly on the occupation probability [66]. The resulting temperature

2.6.1 . Electrical resistivity

dependence of the phonon resistivity is given by the Bloch-Grüneissen formula [67]:

$$\rho\left(T\right) = A\left(\frac{T}{\theta_{\mathrm{R}}}\right)^n \int_0^{\theta_{\mathrm{R}}/T} \frac{x^n}{\left(e^x - 1\right)\left(1 - e^{-x}\right)} dx, \tag{2.79}$$

where A is a constant that depends on the velocity of electrons at the Fermi surface, the Debye radius (the Debye radius also called the Debye length in plasma and electrolytes is a measure of a charge carrier's net electrostatic effect in solution and how far its electrostatic effect persists.) and the number density of electrons in metals as well as the strength of electron-phonon coupling. θ_{R} is the Debye temperature as obtained from resistivity measurements and matches closely with the values of Debye temperature obtained from heat capacity measurements [68]. n is an integer that depends upon the nature of interaction:

- $n = 5$ implies that the resistivity is due to scattering of electrons by phonons (as it is for simple metals)

- $n = 3$ implies that the resistivity is due to $s - d$ inter-band scattering (as in the case for transition metals)

- $n = 2$ implies that the resistivity is due to the electron-electron interaction.
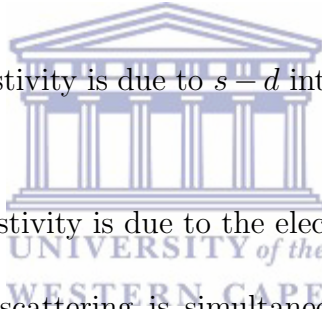
If more than one source of scattering is simultaneously present, Matthiessen's rule must be applied, that the total phonon resistivity can be approximated by adding up several different terms, each with the appropriate value of n. At high temperatures and low-temperatures, equation 2.79 can be approximated by:

$$\rho_{\mathrm{ph}} \propto \left(\frac{T}{\theta_{\mathrm{R}}}\right) \quad (T \gg \theta_{\mathrm{R}}); \quad \rho_{\mathrm{ph}} \propto \left(\frac{T}{\theta_{\mathrm{R}}}\right)^5 \quad (T \ll \theta_{\mathrm{R}}). \tag{2.80}$$

The magnetic contribution ρ_{M}, relates to the scattering associated with magnetic $4f$ ions. As mentioned above, ordered magnetism can be ferromagnetism, antiferromagnetism, ferrimagnetism or helical ordering as observed in heavy rare-earth metals. In magnetically ordered materials, no scattering of conduction electrons is observed when T tends to zero. As T approaches the ordering temperature, T_{ord}, an increase of the spin-disorder scattering is observed and reaches its maximum value above the ordering temperature (paramagnetic region). The calculation of the resistivity in the paramagnetic region was found to be

2.6.1 . Electrical resistivity

independent of the temperature and expressed in the form [69, 70, 71]:

$$\rho_{\mathrm{M}} = (T{>}T_{\mathrm{ord}}) = \frac{3\pi n m^*}{2\hbar e^2 E_{\mathrm{F}}} |\Gamma|^2 (g_J - 1)^2 J (J + 1),\qquad(2.81)$$

where m^* is the effective electron mass, E_{F} is the Fermi energy, e is the electron charge, n is the number of atoms per unit volume and Γ is the measure of the strength of the $s - f$ interaction.

At low-temperatures, below the ordering region, $T{<}T_{\mathrm{ord}}$, the magnetic resistivity, ρ_{M} originates from the interaction of conduction electrons with the magnetic spin system (spin wave). This contribution added to the phonon resistivity, which is reasonably well described by the Bloch theory [67], varying at T^5 at low-temperatures and as T above the Debye temperature. It is difficult however to estimate the magnitude of the spin wave scattering. As the work in this section is entirely concerned with spin wave scattering, it would simplify the problem considerably if the phonon contribution to the measured resistivity could be estimated in some way and subtracted from the experimental curve. Vonsovski [72] appears to have been the first person to recognize that an additional contribution to the resistivity would occur in ferromagnetic materials as a result of the exchange interaction between the conduction electron and localized magnetic moment often called the $s - f$ interaction. Following that, Turov [73] used spin wave treatment to show that the $s - f$ interaction leads to a contribution $\rho_{\mathrm{M}} \sim T^2$ at low-temperatures. Later on, Kasuya [69] suggested a qualitative description of the temperature dependence of ρ_{M}. Representing the $s - f$ interaction by a molecular field, he obtained an expression which describes the main features of the variation of ρ_{M} from low-temperatures to temperatures above T_C. A similar approach was suggested by de Gennes and Friedel [70] who examined the effects of short-range order around T_C. Later on, Kasuya [74] used a spin wave description of the interaction to derive a low-temperature expression for ρ_{M}. Assuming a spin wave dispersion relation of the form $\omega(q) \sim q^2$, he obtained:

$$\rho_{\mathrm{M}}(T) = \frac{\pi^2}{8} \frac{V m}{n e^2} \frac{J^2(0)}{\hbar E_{\mathrm{F}}} (g_J - 1)^2 j \left(\frac{k_{\mathrm{B}} T}{k_{\mathrm{F}} J(0)} \right)^2,\qquad(2.82)$$

where $J(0)$ is a parameter which describes the strength of the $s - f$ interaction, g_J is the Landé g factor, j is the total angular momentum quantum number of each magnetic atom,

E_F is the Fermi energy of the conduction electrons and V and n are respectively the volume and the number of atoms in the crystal. The same result was obtained by Mannari [75] using a slightly different method.

For antiferromagnetic materials, several authors [76, 77, 78] obtained a T^4 dependence of ρ_M at low-temperatures using the antiferromagntic magnon spectrum dispersion $\omega(q) \sim q$. Yamada and Takada [79] suggest the calculation of the electrical resistivity of antiferromagnetic metals due to electron-magnon scattering on the $s-f$ model in the low-temperatures region by the use of the variational approach to the Boltzmann equation. They obtained the temperature variation of ρ_M in the form:

$$\rho_{\mathrm{M}}(T) = \begin{cases} \sim T^5, & \text{for } \Delta \ll T \ll T_N \\ \sim T exp\left(-\frac{\sqrt{T_N \Delta}}{T}\right), & \text{for } T \ll T_N, \Delta \end{cases}, \tag{2.83}$$

where Δ is the anisotropy energy of the spin system. More discussions on spin wave theory is given in subsection 2.2.2.4 above.

2.6.2   Heat capacity

1. The measurements of the heat capacity in this work are done at constant pressure, therefore the term C_P will be used throughout the thesis.

2. The heat capacity of metals results from various contributions. These are the: electronic contribution, C_e, the lattice or phonon contribution, C_{ph}, the magnetic contribution, C_M and the Schottky contribution, C_{Sch}, and the nuclear contribution, C_{nucl}. The total heat capacity is then given by adding all the contributions and can be written as:

$$C_{\mathrm{p}}(T) = C_{\mathrm{e}}(T) + C_{\mathrm{ph}}(T) + C_{\mathrm{M}}(T) + C_{\mathrm{nucl}}(T). \tag{2.84}$$

The phonon contribution is well described by the Debye model given in the form [19]:

$$C_{\mathrm{ph}} = C_{\mathrm{D}}(T) = 9nR \left(\frac{T}{\theta_{\mathrm{D}}}\right)^3 \int_0^{\theta_{\mathrm{D}}/T} \frac{x^3 e^x}{(e^x - 1)^2} dx, \tag{2.85}$$

44

2.6.2 . Heat capacity

with $x = (\hbar\omega)/(k_B T)$. n is the number of atoms per formula unit, R is the gas constant and θ_D is the characteristic Debye temperature. At low-temperatures the integral give a constant and $C_{ph}(T)$ follows a T^3 power law:

$$C_D(T) = \frac{12\pi^4}{5} nR \left(\frac{T}{\theta_D}\right)^3. \tag{2.86}$$

In a few cases, the phonon contribution is also described by both the Debye and Einstein models, with the Einstein model given in the form [19]:

$$C_E(T) = 3nR \left(\frac{\theta_E}{T}\right)^2 \frac{e^{\frac{\theta_E}{T}}}{\left(e^{\frac{\theta_E}{T}} - 1\right)^2}, \tag{2.87}$$

where θ_E is the Einstein temperature. The resulting phonon contribution described by the two models can be approximated by the formula [80]:

$$C_{ph}(T) = kC_D(T) + (1+k)C_E(T). \tag{2.88}$$

The parameter k is a mutual weight of phonon modes of the two models.

At high temperatures, Dulong and Petit predicted the heat capacity of metals to be a constant $3nR$. This can be explained by the equipartition theorem, for which each atom can be considered as an independent oscillator. This high temperature constant heat capacity is often used to inspect whether the sample structure and the number of atoms per formula units is consistent with the measured and classical limit of heat capacity. Experimental results of the phonon heat capacity of magnetic materials are obtained from their homologue non-magnetic La, Y, Lu based compounds.

The electronic heat capacity dominates at very low-temperatures and follows a linear behaviour with temperature:

$$C_e(T) = \gamma T, \tag{2.89}$$

where γ is the electronic or Sommerfeld coefficient. It should be noted that in metals, only electrons close to the Fermi level, contribute to the heat capacity. Therefore, the electronic coefficient γ is proportional to the density of state at the Fermi level, $N(E_F)$, which in

2.6.2 . Heat capacity

turn is related to the effective mass of the conduction electrons given in the form [64]:

$$\gamma = \frac{2}{3}\pi^2 k_{\mathrm{B}}^2 N\left(E_{\mathrm{F}}\right) = \frac{1}{3}k_{\mathrm{B}}^2 \frac{m^* k_{\mathrm{F}}}{\hbar}^3, \tag{2.90}$$

where k_{F} is the Fermi wave number. It should be mentioned that, C_{e} is one of the most important contributions used to identify heavy-fermion systems. Thus for non-magnetic materials the total heat capacity at low-temperatures can be approximated by the formula:

$$C_{\mathrm{p}}(T) = \gamma T + \beta T^3. \tag{2.91}$$

For magnetic materials, the magnetic excitations contribute to the total heat capacity, C_{M}. This contribution is described well by the formula that accounts for scattering of conduction electrons on ferromagnetic or antiferromagnetic spin waves with energy gap Δ in magnon spectrum (see section 2.2.2.4: spin wave theory). Another property associated with the magnetic contribution, C_{M}, to the total heat capacity is the $4f$-electron magnetic entropy, S_{M}. This property is defined by the relation:

$$S_{\mathrm{M}}(T) = \int_0^T \frac{C_{\mathrm{M}}(T')}{T'} dT', \tag{2.92}$$

S_{M} illustrates the degeneracy of the system. Owing to the weak interaction between the local magnetic moment of the rare-earth ions, each ion possesses an intrinsic total angular momentum J, and the ground state will be $(2J + 1)$ fold degenerate. As the temperature increase all the states above ground state are populated and the magnetic entropy saturate to a constant value given by:

$$S_{\mathrm{M}} = R\ln(2J + 1). \tag{2.93}$$

Another contribution to the total heat capacity is the Schottky term which describes the overall crystal-electric-field, responsible for the splitting of the ground state into different energy levels. As a result of this, an ion can occupy different energy levels (see section 2.2.3 above) giving rise to a Schottky anomaly which manifests itself by a broad maximum on the $C_{\mathrm{M}}(T)$ curve and a tendency to be zero at low and high temperatures. This broad maximum superimposes on the lattice and other contributions [80]. In the case of two energy levels ε_0 and ε_1 and with a degeneracy g_1 and g_2, the resulting Schottky term is

defined as follows:

$$S_{\text{Sch}}(T) = R \left(\frac{\Delta}{T} \right)^2 \left(\frac{g_0}{g_1} \right) \frac{e^{\frac{\Delta}{T}}}{\left(1 + \frac{g_0}{g_1} e^{\frac{\Delta}{T}} \right)^2}, \tag{2.94}$$

where $\varepsilon_1/k_{\text{B}}$ is the energy separation between the ground state and the first excited state. A general expression of the Schottky term for n energy levels and degeneracy is given in section 2.2.3, equation 2.27.

The last contribution is the nuclear heat capacity, C_{nucl}, originating from the rare earth nuclear Schottky anomaly which is enhanced due to the hyperfine interaction. This contribution can be expressed by a $C_{\text{nucl}} \propto 1/T^3$, since the high temperature tail of the nuclear specific heat follows [28]:

$$\frac{C_{\text{nucl}}(T)}{R} = \frac{I(I+1)g_{\text{N}}^2 \mu_{\text{N}}^2 (1+K^2)}{3k_{\text{B}}^2} \left(\frac{B_{\text{eff}}}{T} \right)^2,$$
$$K = \frac{\chi A}{j J \mu_{\text{B}} g_{\text{N}} \mu_i \text{N}} \tag{2.95}$$

where B_{eff} is the effective magnetic field acting on the rare-earth nuclei, I is the nuclear spin (e.g. $I = 5/2$ for Pr), g_{N} is the gyromagnetic coefficient for the rare-earth atom (e.g. 13 MHz/T for Pr), μ_{N} is the nuclear magnetic moment of the rare-earth atom and $K \propto \chi$ is the enhancement factor which is proportional to the magnetic susceptibility. K also expresses the hyperfine interaction. This contribution is characterized by an increase $C_{\text{p}}(T)$ with decreasing temperature well below the ordering temperature, T_{C} or T_{N}.

2.6.3 Magnetization and magnetic susceptibility(see also section 2.2.2)

A material is magnetized in the presence of a magnetic field, B. The overall magnetization of a system of N moments per unit volume is given by [27]:

$$M = N \frac{\sum_{J_z=-J}^{+J} -g\mu_{\text{B}} B J_z \, exp \left[-\frac{g\mu_{\text{B}} J_z}{k_{\text{B}} T} \right]}{\sum_{J_z=-J}^{+J} exp \left[-\frac{g\mu_{\text{B}} J_z}{k_{\text{B}} T} \right]}, \tag{2.96}$$

where J is the total angular momentum and g is the Landé g-factor. To evaluate the magnetization it is convenient to express it in terms of the partition function of the dipole

47

2.6.3 . Magnetization and magnetic susceptibility(see also section 2.2.2)

moment, Z given in the form:

$$M = -\frac{N k_{\mathrm{B}} T^2}{B} \frac{1}{Z} \left(\frac{\partial Z}{\partial T}\right)_{\mathrm{B}} = -\frac{N k_{\mathrm{B}} T^2}{B} \left(\frac{\partial \ln Z}{\partial T}\right)_{\mathrm{B}}. \tag{2.97}$$

$$Z = \sum_{J_z = -J}^{+J} exp\left[-\frac{g \mu_{\mathrm{B}} B J_z}{k_{\mathrm{B}} T}\right]$$

The calculation of Z leads to the formula of the magnetization given in the form:

$$M = N g \mu_{\mathrm{B}} J B_J(x), \tag{2.98}$$

where $x = (g\mu_{\mathrm{B}} B J) / (k_{\mathrm{B}} T)$ is a dimensionless measure of the magnetic field and $B_J(x)$ is the Brillouin function defined as follows:

$$B_J(x) = \frac{2J+1}{2J} \coth\left[\left(\frac{2J+1}{2J}\right) x\right] - \frac{1}{2J} \coth\left(\frac{x}{2J}\right). \tag{2.99}$$

From this relation it is clear that the behaviour of the magnetization is similar to that $B_J(x)$ which increases linearly at low fields and tends to the saturation magnetization $N g \mu_{\mathrm{B}} J$ at high fields, which correspond to maximum possible alignment of the dipole moments with the field. For $x \ll 1$, $B_J(x)$ can be approximated in the form:

$$B_J(x) \approx \frac{(J+1)}{3J} x, \tag{2.100}$$

so that, the low fields magnetization be approximated as follows:

$$M(B) = \frac{N g^2 \mu_{\mathrm{B}}^2 J(J+1)}{3 k_{\mathrm{B}} T} B. \tag{2.101}$$

Recalling that B is a local magnetic field of the rare-earth ion which is usually different from the applied magnetic field, the magnetic susceptibility can be obtained from equation 2.101. Therefore one obtains:

$$\chi(T) = \frac{\mu_0 M}{B} = \frac{N g^2 J(J+1) \mu_{\mathrm{B}}^2 \mu_0}{3 k_{\mathrm{B}} T}, \tag{2.102}$$

where μ_0 is the permeability of the free space or vacuum. The effective magnetic moment

48

2.6.3 . Magnetization and magnetic susceptibility(see also section 2.2.2)

is then defined as:

$$\mu_{\text{eff}} = g \left[J \left(J + 1 \right) \right]^{1/2} \mu_{\text{B}}.$$ (2.103)

Equation 2.102 is known as the Curie law for a paramagnet, which states that the susceptibility is inversely proportional to the absolute temperature and be written in the form:

$$\chi(T) = \frac{C}{T}$$ (2.104)
$$C = \frac{N g^2 J(J + 1)\mu_{\text{B}}^2 \mu_0}{3 k_{\text{B}}}.$$

C is known as the Curie constant. For ferromagnetic and antiferromagnetic materials, the Curie law is modified by the Curie-Weiss relationship (see section 2.2.2).

UNIVERSITY *of the*
WESTERN CAPE

Chapter 3

Experimental techniques

3.1 Introduction

This chapter presents the manner in which all the processes and methods were used in obtaining the results. The details of synthesizing the compounds as well as their characterization with respect to their crystal structure studied are extensively described. The description of equipment used to get different results on such RE-based compounds will be discussed.

3.1.1 Procedure of samples preparation

Polycrystalline samples of RE_2Pt_2In and $RE_8Pd_{24}Ga$ and their non-magnetic La-analogs were prepared using the arc-furnace. The synthesis by arc-furnace involves the melting of pure elements together using arc plasma. For compounds containing unstable elements like Pr and La, extra care was taken. The RE-elements were etched in a 50:50 nitric acid: deionized water solution. This was done to ensure that the thin alkaline oxide layer is removed from the surface of the element. The etched elements were then rinsed and dried in acetone. The purities of all elements used in this study are listed in table 3.1. Stoichiometric quantities of all elements were carefully weighed to the accuracy of 0.0002 g for a starting sample mass of 2.0 g. The elements were then placed together in a copper crucible water cooled system in an arc furnace having an ingot of titanium-getter. This

3.1.1 . Procedure of samples preparation

latter element is added in order to absorb any impurity in the chamber during the melting process. The chamber (see figure 3.1) has been closed hermetically and a high vacuum degassing eliminates atmospheric gasses that might be inside the chamber. The chamber was flushed with argon (Ar) seven times, before a high vacuum was established. The elements were melted together into a button which was over-turned three times to ensure homogeneity. Water was allowed to continuously flow under the copper hearth during the melting process. The arc plasma which generated the flame in the chamber to melt the samples was provided from the inverter system manufactured by Thermamax; model *TSA*-400*D*. The melted samples were then weighed and mass loss was determined, and obtained to be about 1% for all compounds.

Table 3.1: purity of the starting elements given in wt. %.

Element	Purity(wt.%)
La	99.99
Pr	99.90
Nd	99.99
Gd	99.99999
Tb	99.99
Dy	99.99
Pt	99.95
Pd	99.99
In	99.999
Ga	99.99

Figure 3.1: The figure showing the arc-furnace chamber, with the titanium and the starting elements placed in the appropriate copper crucible.

51

3.2 Sample characterisation

The microstructure and chemical composition of all the synthesized samples were investigated by scanning electron microscopy (SEM) and energy dispersive spectroscopy (EDS). The quality of the samples was checked by X-ray powder diffraction at room temperature using a Bruker D8 Advance diffractometer (figure 3.3) with a CuKα radiation ($\lambda = 1.540698$Å). The room temperature crystallographic structures were determined by analysing the X-ray powder diffraction spectrum using the cell and intensity least square (CAILS)-Pawley and Rietveld refinements method from TOPAS ACADEMIC programme.

3.2.1 Energy Dispersive Spectroscopy (EDS)

The energy dispersive spectroscopy analysis has been performed using Field Emission Gun Scanning Electron Microscope (FEGSEM) Auriga (see figure 3.2) in order to obtain the chemical composition of the starting elements. The energy dispersive spectroscopic analysis usually involves the generation of an X-ray spectrum from the entire scan area of the scanning electron microscopy. To perform this, the samples were all mounted on a sample holder aluminium stub with carbon sticky tapes and were inserted in FEGSEM. In the Detector Secondary Electron (DSE) the samples were magnified 100 times, the Electron High Tension (EHT) was set at 20 kV and the working distance was around 9.2 mm. Images were analysed and recorded using an energy dispersive spectroscopy software Aztec Energy.
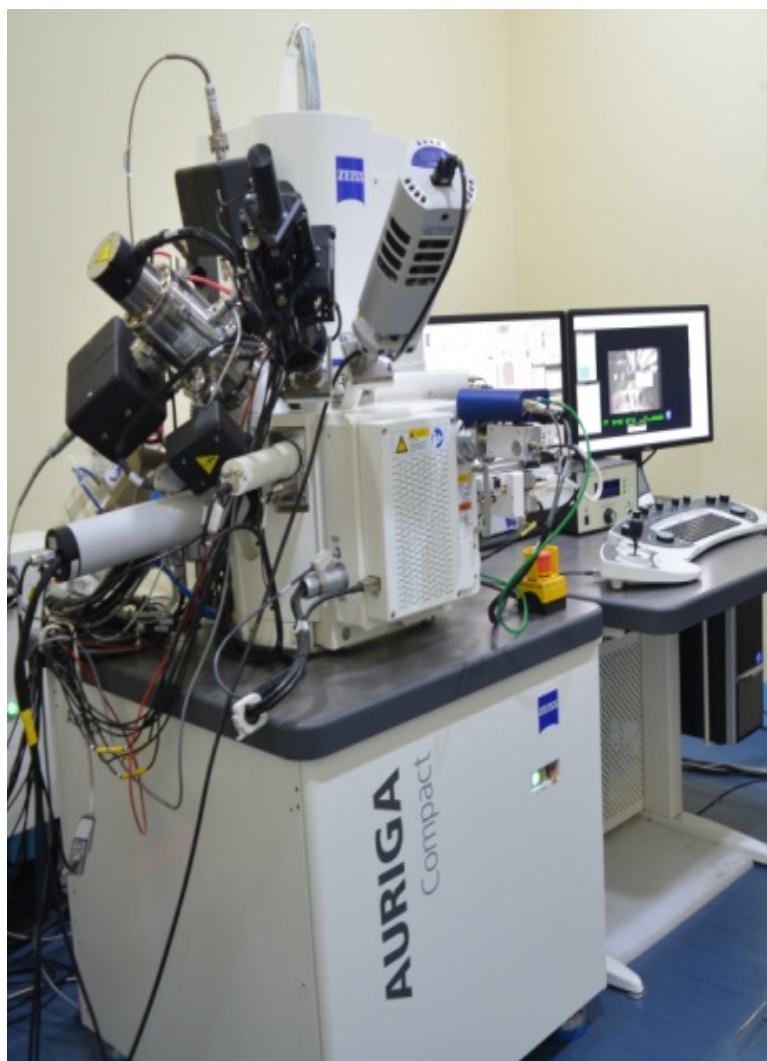
Figure 3.2: Photograph of Field Emission Gun Scanning Electron Microscope.

3.2.2 X-ray diffraction

X-ray diffraction is a powerful technique of obtaining the structural information of substances. For this, the sample needs to be grain powder in order to produce an important signal and therefore a strong intensity. Small pieces of samples cut from the button have been collected, crushed and ground in an agate mortar, in order to have a fine powder specimen. The powdered sample was then placed on a glass slide mounted at the middle of the diffractometer of figure 3.3. The sample holder was made from a polyvinyl chloride (PVC) glass, which is an amorphous material (ensuring that the scattering X-ray that is produced is not a coherent signal and can be easily subtracted from the measured data).

3.2.2 . X-ray diffraction

Figure 3.3: Photograph of diffractometer D8 Advance.

So, to perform the measurements, X-ray beams were directed onto the surface of the crystal, the waves (with a wave vector $\vec{K}_t$) are partially transmitted and partially reflected ($\vec{K}_s$) by the crystals. For elastic scattering, $|K_t| = |K_s| = \dfrac{2\pi}{\lambda}$ must be satisfied. The appearance of peaks or the X-ray diffraction spectra in the range of $0° \leq 2\theta \geq 90°$ appeared. This means that the reflected waves on the plane of atoms or crystals are in phase and implies that there is equality between the angle of incident and the scattering angle. On the other hand, this means that the positive interference of diffracted X-ray beams occurs when the Bragg condition is satisfied:

$$n\lambda = 2d_{hkl}\sin(\theta), \tag{3.1}$$

where n (an integer) is the diffraction order, λ is the wavelength of the X-ray beams, θ is the angle between the incident X-ray and the surface of the crystal, d_{hkl} is the interplanar distance.

54

The diagram depicting a schematic representation of Bragg law is presented in figure 3.4:
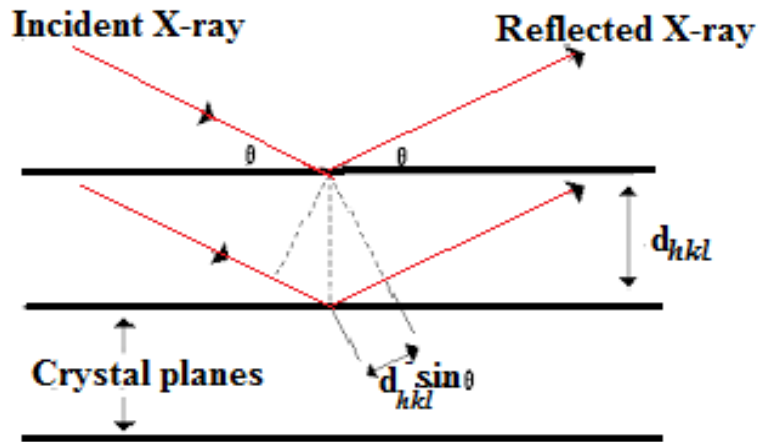
Figure 3.4: Cross section of the incident and reflected X-ray beams on the surface of a powdered sample: Bragg's law.

3.2.2.1 Cell and Intensity Least Square (CAILS)-Pawley and Rietveld refinement method

[81, 82, 83]

The CAILS-Pawley refinement method provides information about the lattice parameters of the crystal structure. In this refinement method, only cell parameters, peak width parameters and integrates intensities are refined. CAILS refinement is independent of the atomic position parameters (or structural model) and only depends on the space group symmetry. Furthermore, in the CAILS method the intensities of all diffraction peaks vary independently.

The Rietveld refinement method also depends on the space group symmetry, but is different for the CAILS method. The difference is in the sense that not only the parameters as in the CAILS method are refined but the intensities of all peaks vary dependently and the full structure are refined such as the atomic coordinates, the site occupancy, the isotropic displacement parameters as well as the interatomic distances.

3.2.2.2 Criteria of fit

The Rietveld refinement method uses selected parameters to considerably reduce the difference between experimental pattern (observed data, y_o) and a model based on the hypothesized crystal structure and instrumental parameters (calculated pattern, y_c). The use of full profile fitting and crystallographic constraints (lattice parameters and space groups to constrain peak positions, crystal structure to constrain peak intensities) are carefully considered. The Rietveld analyses the whole diffraction pattern by including the profile fitting, the refinement of the structure parameters from diffraction data (lattice parameters, atomic positions and site occupancies). TOPAS ACADEMIC is a graphics based profile analysis program built around a non-linear least squares fitting [84, 85]. The quality of the fit is defined by the refined agreement indices of the sample. These are referenced [84]:

- R-pattern (R_p) and R-pattern background corrected (R'_p): It is an indicator of the goodness of fits (GOF) given by:

$$R_p = \frac{\sum |Y_{o,m} - Y_{c,m}|}{\sum |Y_{o,m}|}, \quad R'_p = \frac{\sum |Y_{o,m} - Y_{c,m}|}{\sum |Y_{o,m} - Gkg_m|}; \tag{3.2}$$

- R-weighted pattern (R_{wp}) and R-weighted pattern background corrected (R'_{wp}): It is a measure of the GOF, calculated point by point and weighted by a standard deviation of the data, given by:

$$R_{wp} = \sqrt{\frac{\sum w_m (Y_{o,m} - Y_{c,m})^2}{\sum w_m Y_{o,m}^2}}, \quad R'_{wp} = \sqrt{\frac{\sum w_m (Y_{o,m} - Y_{c,m})^2}{\sum w_m (Y_{o,m} - Bkg_m)^2}}; \tag{3.3}$$

- R-expected (R_{exp}) and R-expected background corrected (R'_{exp}): It is an expected value of R_{wp}, given by:

$$R_{exp} = \sqrt{\frac{\sum M - P}{\sum w_m Y_{o,m}^2}} \quad R'_{exp} = \sqrt{\frac{\sum M - P}{\sum w_m (Y_{o,m} - Bkg_m)^2}}; \tag{3.4}$$

- the goodness of fit (GOF) based on statistics is expressed by:

$$GOF = \chi^2 = \frac{R_{wp}}{R_{exp}}; \tag{3.5}$$

- R-Bragg (R_{B} or intensity factor): It is a measure of the quality of the structural model related to the peak shape and not the area. It is given by:

$$R_{\mathrm{B}} = \frac{\sum |I_{o,k} - I_{c,k}|}{\sum |I_{o,k}|}; \tag{3.6}$$

- and finally the Durbin-Watson parameter (DW) d: It is a measure of the fit model, given by [86, 87]:

$$DW = d = \frac{\sum_{m=2}^{\mathrm{M}} (\Delta Y_m - \Delta Y_{m-1})}{\sum_{m=1}^{\mathrm{M}} (\Delta Y_m)^2}, \tag{3.7}$$
$$\Delta Y_m = Y_{0,m} - Y_{c,m},$$

where $Y_{o,m}$ and $Y_{c,m}$ are the observed and calculated data respectively at data point m, Bkg_m is the background at data point m, M and P are respectively the number of data points and parameters, w_m the weighting given to data point m, $I_{o,k}$ and $I_{c,k}$ are the observed and calculated intensities of the kth reflection.
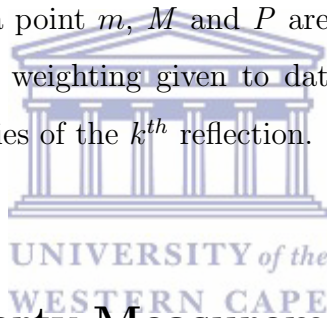
3.3 Physical Property Measurement System (PPMS)

The PPMS manufactured by Quantum Design (USA) allows the physical property measurement (electrical resistivity, heat capacity, thermal transport option, magnetoresistivity) of compounds at the temperature range of 400 K - 1.8 K with an applied field up to 9 T and it can also be measure down to 50 mK by inserting the Helium-3 (^{3}He) cryogenic system, which is also from the same manufacturer. In this equipment, the magnet is in axial solenoid configuration, with the center of the magnet corresponding to the sample position. However, the PPMS can also allow the measurement of magnetic properties by using the vibrating sample magnetometer (VSM) techniques. In these techniques, the magnetic field and ramp rate are determined by the magnetic power supply. All physical properties (resistivity and specific heat) results reported in this work were measured on the PPMS shown in figure 3.5 [88]:
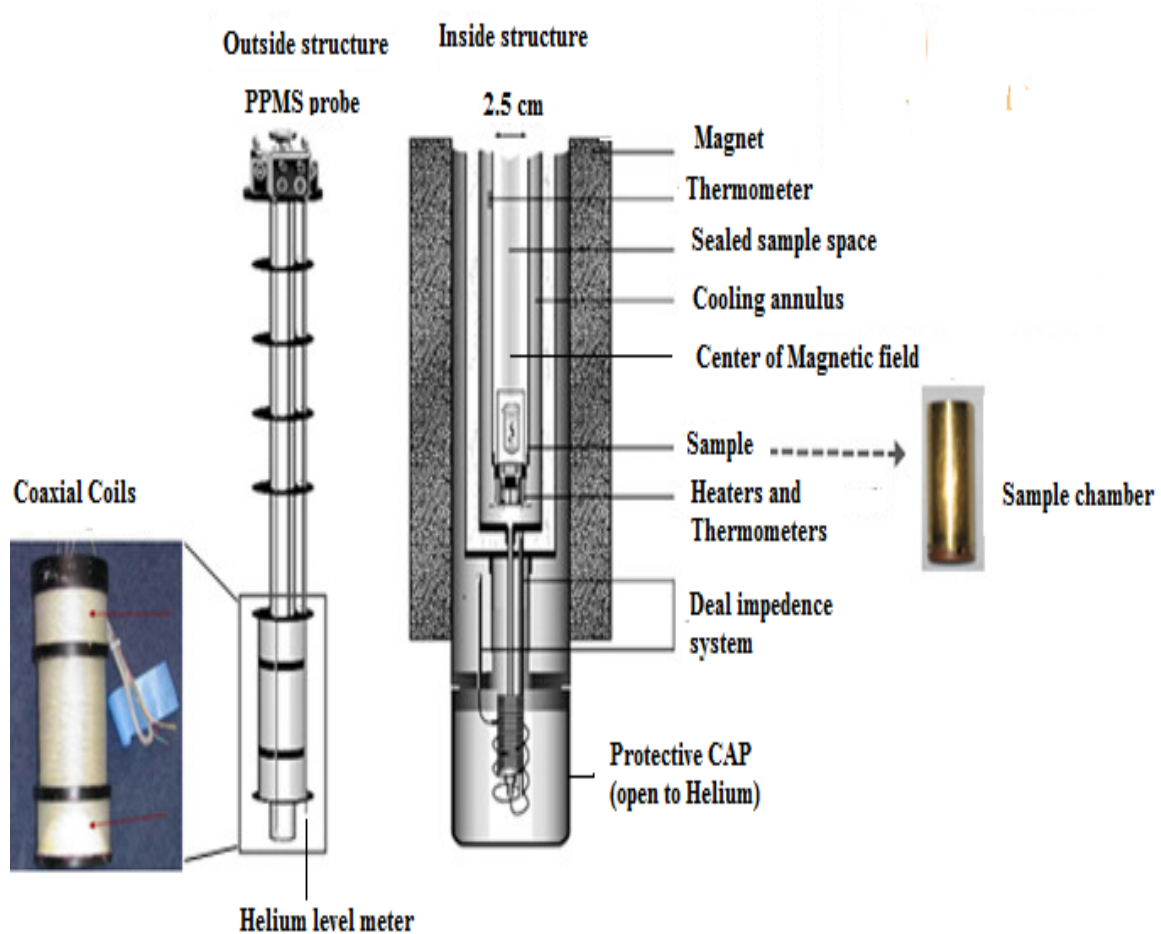
Figure 3.5: Cross section of Physical Properties Measurements System (PPMS).

3.3.1 Electrical resistivity

A rectangular bar sample was mounted on an AC resistivity puck which caters for two samples. Before mounting the sample on the puck, the surface of the puck was firstly cleaned with ethanol then the kapton tape was cut and placed on its surface to electrically insulate the samples from the puck. The four point probe technique as presented in figure 3.6 was used. In this technique, 2 current contacts attached at the side of the sample pass the current through the sample, while 2 voltage contacts were attached at the surface of the sample, measuring the potential difference drop across a section of the sample. The contacts were made with 50 μm of diameter gold wires with purity of 99.99 wt. % and were attached to the sample using spot welding techniques. These samples were then fixed on the puck using GE vanish glue and was left for a while to dry. This special glue was used for its properties of keeping contact at very low temperatures and avoids the possibility of sample detachment during the measurement process. All samples were spot welded in this

58

manner as depicted in this figure:
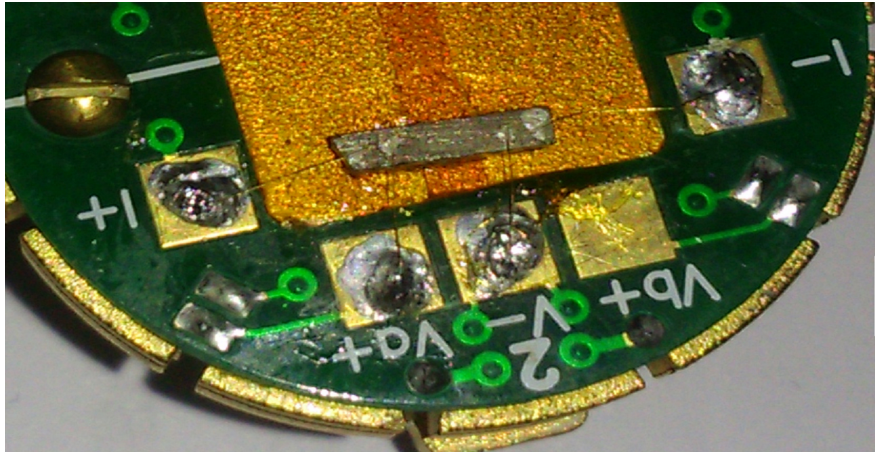
Figure 3.6: Photograph of a sample mounted on channel 2 using spot welding techniques for the electrical resistivity measurements.

The prepared samples were loaded into the PPMS. The typical excitation current 4500 μA was used for Helium-4 (^{4}He) direct current resistivity measurements under the frequency of 17 Hz. The potential difference between the gold wires fixed on the sample is used to automatically measure the resistance and consequently the resistivity ($\rho(T)$) of the sample. All $\rho(T)$ measurements were done in the temperature range 300 K down to 100 K at the cooling rate of 1.5 K/min, from 99 K to 11 K at the rate of 1 K/min in 90 steps and from 10 K to 1.8 K at 0.5 K/min in 41 steps. This sequence was applied on all the electrical resistivity measurements in this work.

3.3.2   Specific heat

Specific heat measurements carried in temperature range 300 K - 1.8 K were performed on a Quantum Design PPMS which operates according to the thermal relaxation calorimetry method. They were run at constant pressure and changes in sample volume were negligible according to the change rate of the measured temperature. These measurements were first done by mounting the Apiezon N grease on the specific heat puck (sapphire specimen holder) in order to ensure good thermal contact and was loaded onto the PPMS. The specific heat measurements of the grease plus puck (Addenda measurements) were carried out before each measurement. The appropriate sequence was set and was run at

59

3.3.2 . Specific heat

the same range of temperature as the data would be recorded. The addenda measurement was followed by a sample measurement where a typical sample mass used was between 9 mg - 11 mg. This was deposited on the Apiezon N grease to ensure a good signal noise ratio as shown in the schematic representation of the heat capacity puck in figure 3.7 [88]. This measurement of the heat capacity first uses a heating period which is followed by a cooling period, after which the capacity option fits the entire temperature response of the sample platform to a model that accounts for the thermal relaxation of the sample platform to the bath temperature and the relaxation between the sample platform and the sample itself. Moreover, the specific heat measurements were done, with the heat pulse of around 1% of the current puck temperature. The contribution of the platform and sample gives the total specific heat. This latter contribution is determined from a "$two-\tau$" model which simulates the effect of heat flowing between the sample and the platform, and the effect of heat flowing between the platform and the puck. The contribution of the grease and platform to the total specific heat was determined by a separate measurement using a one-τ model fitting:

$$C_{\text{total}} \frac{dT_{\text{p}}}{dT} = -K_{\text{w}}(T - T_{\text{b}}) + P(t), \tag{3.8}$$

with:

$$\tau = C_{\text{total}}/K_{\text{w}}, \tag{3.9}$$

where τ is the relaxation time and K_{w} is the thermal conductance of the supporting wires, T_{b} is the constant related to puck temperature and $P(t)$ is the heater power.
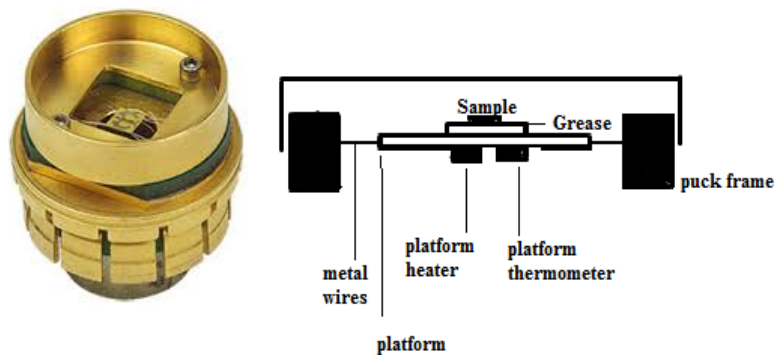
Figure 3.7: [4]He specific heat puck and its schematic representation of the platform.

3.4 Magnetic Property Measurement System (MPMS)

The magnetic properties studied, were measured using MPMS which is also from the same manufacturer as PPMS equipment, as seen in figure 3.8 [89]. This equipment has three main modes of measurements, namely the reciprocating sample option (RSO), alternative current (AC), and direct current (DC) measurements methods. In DC method, two Josephson junction (that consists of two weakly coupled superconducting electrodes) are connected parallel onto two superconductors with an insulating gap in between. If the gap is thin enough, electron pairs can tunnel from one superconductor across the gap to the other superconductor, by means of quantum tunnelling, a resistanceless current flows across the insulator.

The MPMS measures the magnetic properties such as magnetic susceptibility and magnetization with a field range of up to 7 T produced by a highly uniform axial solenoid magnet. Moreover, the working frequency in this system is given as $\omega_j = 2\pi V/\Phi_0$, where Φ_0 is the magnetic flux quantum and V is the applied voltage [89, 90].

The magnetic properties studied in this thesis were performed using DC option measurements. Here, the magnetometer is very accurate so as to easily detect a high magnetic moment of diamagnetic, paramagnetic, ferromagnetic and antiferromagnetic magnetic materials.
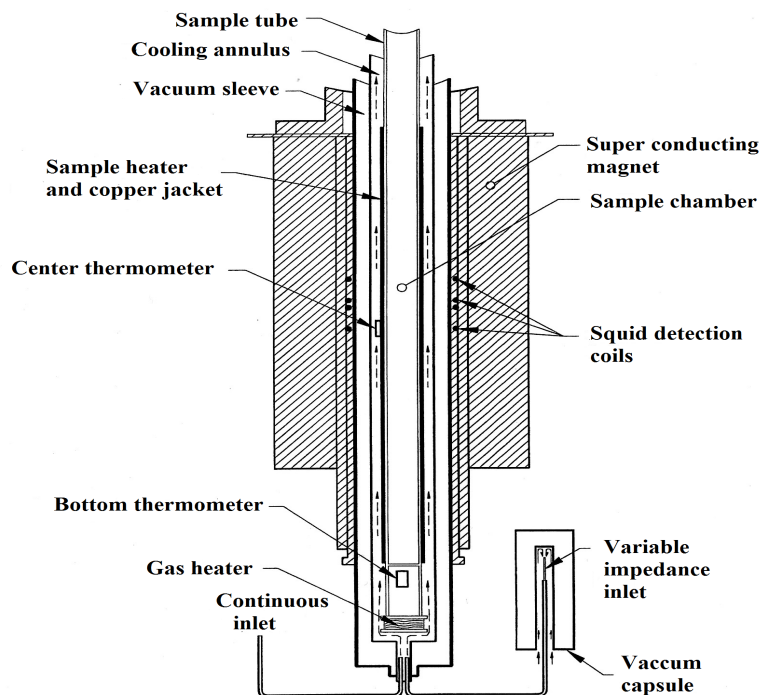
Figure 3.8: Schematic representation of Magnetic Properties Measurement Syspem (MPMS).

61

3.4.1   Magnetic measurements

The measurement consists of oscillating the sample through superconducting detection coils at a constant speed with a chosen amplitude of 4 cm with an oscillation frequency of 0.5 Hz at a given temperature and in a homogeneous magnetic field. When the sample is moving within the coils, the magnetization of the space within the coils changes, thereby inducing an electrical current in the detection coils. This induced current is not attenuated and any change in magnetic flux produces a proportional change of current in the detection circuit according to Faraday's principle ($\nabla \times$ E = - $\frac{\partial B}{\partial t}$). However, the maximum value of the induced voltage corresponds to the time when the sample is in the center of the pick up coils and this centering is done prior to the measurement. The coils are inductively coupled to a superconducting quantum interference device (SQUID), through a flux gate transformer. Therefore, by moving the sample on either side of the detection coils, an integration of the magnetic field is realized and the flux transformer is used to transmit the signal to SQUID [89, 91]. From the phase difference across the junction of the SQUID, the magnetic moment in emu (electromagnetic unit) is obtained from the SQUID response. The amplitude of the measured signal is proportional to the magnetization of the sample. These measurements can be carried out by varying the temperature (magnetic susceptibility measurements) or maintaining the temperature constant, and vary the applied magnetic field (magnetization measurements). Samples were put in a 1 cm straw which was placed at the middle of the uncut straw as shown in figure 3.9. This uncut straw serves as the sample holder and has a diamagnetic signal which is linear in field.

Figure 3.9: Picture showing sample mounted in the straw for the magnetization and magnetic susceptibility measurements on MPMS.

Chapter 4

Results and Discussion: RE$_2$Pt$_2$In (RE = Pr, Nd)

4.1 Literature review and introduction

Recently, a group of ternary Ce-based rare-earth compounds with the composition Ce$_2$T$_2$M (T = 3d-, 4d-, 5d-transition elements; M = In, Sn, Pb) crystallizing in the primitive tetragonal structure of the Mo$_2$FeB$_2$-type (an ordered derivative of the U$_3$Si$_2$-type structure) was reported [92, 93]. The proximity of the 4f level to the Fermi level generates unusual ground state properties, such as heavy fermion, intermediate valence, magnetic ordering, superconducting or Kondo insulator. Magnetic measurements of this group of compounds indicated that the physical property was mainly governed by the 4f-d hybridization [92]. For the family of compounds Ce$_2$T$_2$In in particular, it was reported that the ground state changes from a nonmagnetic to a well localized magnetic regime [92]. For the compounds Ce$_2$Ni$_2$In and Ce$_2$Rh$_2$In, the magnetic susceptibility data shows a broad maximum at high temperatures, a signature of intermediate valence (IV) systems [92, 93, 94]. Magnetic measurements of Ce$_2$Pt$_2$In suggest that this compound is strongly temperature-dependent with no magnetic ordering down to 1.7 K [92, 95] whereas, the compounds Ce$_2$Cu$_2$In and Ce$_2$Pd$_2$In order antiferromagnetically below T_N = 5.5 K and 3.2 K, respectively. Ce$_2$Au$_2$In orders ferromagnetically below T_C = 4.0 K and undergo spin rearrangement of the Ce magnetic moment above T_C at 4.3 K [92, 93, 95]. Similarly, Ce$_2$Pd$_2$Sn order ferromagnetically below T_C = 4.2 K. The electrical resistivity, $\rho(T)$ results confirm the IV behaviour of Ce$_2$Ni$_2$In and Ce$_2$Rh$_2$In compounds while the remaining

ternary compounds in the family of Ce_2T_2In was found to be determined by an interplay of Kondo and crystal-electric-field effect [92]. In the case of Ce_2Ni_2Sn compounds, $\rho(T)$ results are characteristic of Kondo behaviour with a Kondo temperature $T_K = 9$ K [93]. Antiferromagnetic order was observed for the Ce_2Pd_2Pb at $T_N = 6.2$ K with a second-order phase transition involving a reduction in the effective moment observed at $T = 120$ K of Ce ion [93].
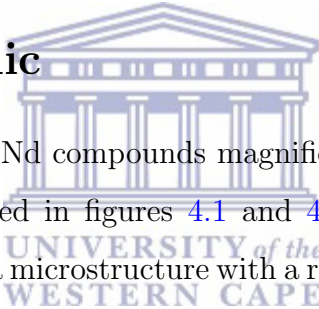
During the writing of this report, no ferromagnet has been observed or reported up to now in the actinide-based 2:2:1 compounds [96, 97]. Few ferromagnets up to date in the family of rare-earth based 2:2:1 compounds were found [93, 95, 98].

The study of critical behaviour of the second-order magnetic phase transitions is amongst the valuable tools to study the appropriateness of the double exchange mechanism to describe the magnetism of the compound. Furukawa and Motome [99] show theoretically that the 3D-Heisenberg model is compatible with the double exchange mechanism. We found it interesting to undertake the study of the critical behaviour near the paramagnetic-ferromagnetic phase transition in Pr_2Pt_2In and Nd_2Pt_2In compounds. This was done through isothermal magnetization measurements around the transition temperature T_C as well as magnetic susceptibility. On the other hand, magnetic refrigeration based on magnetocaloric effect of solid state substances has been proven to bear many advantages over conventional gas-compression refrigeration techniques, like higher efficiency and environmental features [3, 8]. Currently, intense research is being carried out to identify suitable magnetic materials for their use in refrigeration technology. Although magnetocaloric effect is an intrinsic property of all magnetic materials, especially alloys and compounds of rare-earth metals, they are expected to show enhanced, field-tunable magnetic entropy change. This is mainly because of intrinsically large molar magnetic entropy values associated with tripositive rare-earth ions [100]. Furthermore, the magnetic moments corresponding to $4f$-electrons of the rare-earth are larger than those of a typical $3d$-electron system by a factor of 2 [100]. Magnetocaloric effect is characterized by an adiabatic change in temperature (ΔT_{ad}) and an isothermal magnetic entropy change, ΔS, arising from the application or removal of magnetic field under adiabatic conditions. The physics of magnetocaloric effect gets enriched by correlated spin-lattice degree of freedom [100]. It has

been observed that many materials with first or second-order phase transition exhibit large magnetocaloric effect, but at the same time magnetic hysteresis reduces the cooling efficiency. Hence, materials with large magnetocaloric effect and negligible hysteresis are good candidates for applications in magnetic refrigeration. Prominent examples of such systems are $Gd_5(Si, Ge)_4$ [101], MnAs [14, 102] and Ni_2MnGa [103]. The search for new heavy rare-earth intermetallic compounds prospective for magnetic refrigeration application is presently one of the key topics in modern materials science [104, 105, 106].

The results of X-ray diffractometer, energy dispersive spectroscopy, crystal structure, electrical resistivity, magnetic susceptibility, magnetization, heat capacity, critical behaviour, magnetocaloric effect obtained on polycrystalline compounds Pr_2Pt_2In and Nd_2Pt_2In are presented and discussed in this chapter.

4.2   Crystallographic

The micrographs of Pr and Nd compounds magnified at 50 μm taken from scanning electron macroscope are presented in figures 4.1 and 4.2 respectively. The micrograph images of both compounds show a microstructure with a region of slightly different darkness. Furthermore, they are characterized by a smooth surface. The results of this analysis implied that the entire samples were homogeneous which indicate that the dissimilar regions should be attributed to crystallites with different crystallographic orientation. The quantitative energy dispersive spectroscopy measurents over the surface area of each sample indicate the sample elemental composition normalized to the rare-earth content to be: $Pr_2Pt_{1.980(2)}In_{0.953(2)}$ and $Nd_2Pt_{1.970(2)}In_{0.945(2)}$ which are roughly close to the 2:2:1 composition. The small offsets of the atomic ratios are ascribed to the small mass loss that occurs during sample synthesis.

4.2. Crystallographic
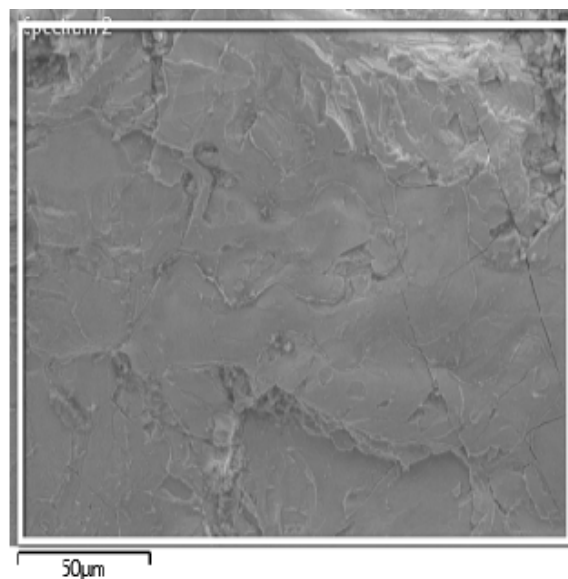
Figure 4.1: Cross section micrograph of scanning electron macroscope done on Pr_2Pt_2In with a scale of $50\mu m$.
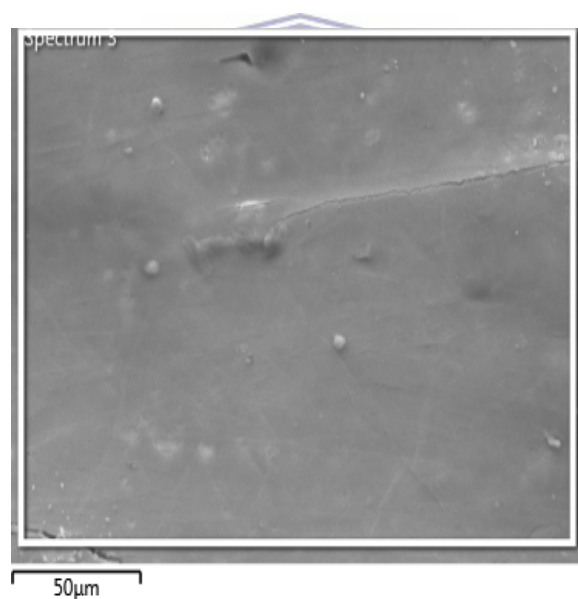
Figure 4.2: Cross section micrograph of scanning electron macroscope done on Nd_2Pt_2In with a scale of $50\mu m$.

Figures 4.3a, 4.4a, 4.5a displayed X-ray diffractograms obtained for La, Pr and Nd compounds together with Rietveld full-profile least squares refinement fits to the data. X-ray diffraction study revealed single-phase characters of all three compounds and confirms the tetragonal Mo_2FeB_2-type structure (an ordered derivative of the U_3Si_2-type structure) with space group P4/mbm-D_{4h}^5, No. 127). In this structure, the RE atoms occupy the crystallographic $4h$ sites; Pt atoms occupy the 4g site and In atoms occupy the 2a sites. The resulting tetragonal crystal structure is depicted in figure 4.6 and the atomic coordi-

nates are listed in table 4.1. In the refinement process, the site occupancy fraction (S.O.) as well as the isotropic displacement parameter (Beq) of all atoms were kept fixed (fully occupied). The phase density value obtained amounts to 22.0(1) g/cm^3; 20.695 g/cm^3 and 21.152(8) g/cm^3 for La$_2$Pt$_2$In, Pr$_2$Pt$_2$In and Nd$_2$Pt$_2$In respectively. These values are of the same order of magnitude which indicates the same phase density for all three compounds. The room temperature lattice parameters and the unit cell volume are gathered in table 4.1. These values are in good agreement with the literature data [92, 94]. The observed relationship $V_{\text{La}_2\text{Pt}_2\text{In}} > V_{\text{Pr}_2\text{Pt}_2\text{In}} > V_{\text{Nd}_2\text{Pt}_2\text{In}}$, confirms the lanthanide concentration between La and Nd. The final refined agreement indices as defined in chapter 3, subsection 3.2.2.2, for La$_2$Pt$_2$In, Pr$_2$Pt$_2$In, Nd$_2$Pt$_2$In are gathered in table 4.2. The observed values of R_{B} indicate that the structural model may be correct. However, in order to check the quality of the Rietveld refinement, the X-ray diffraction patterns of all three compounds was refined on the basis of the CAILS-Pawley refinement method using the same space group, P4/mbm-D_{4h}^5, (No. 127, see figures 4.3b, 4.4b, 4.5b). As mentioned in chapter 3, subsection 3.2.2.1, the CAILS refinement method is different from the Rietveld refinement method in the sense that only cell parameters, peak width parameters and integrated intensities are refined. Furthermore, the CAILS refinement method does not involve the atomic position parameters or the structural model and only depends on the space group symmetry. In the CAILS method the intensities of all peaks vary independently. The value of the agreement indices obtained from the CAILS refinement are also listed in table 4.2. It is observed that these values are of the same order of magnitude with that obtained from the Rietveld refinement discussed above. This observation indicates that the χ^2 and R-factors are not due to an incorrect structural model. A more detailed analysis of the refinement for both methods reveals that the observed peak shape is different from the peak calculated using three phase peak-type functions for classical analytical full pattern fitting. However, the peak shapes are still not well fitted, which may be due to strain or chemical inhomogeneity or high defect density in the sample. The overall diffraction patterns show that all three compounds are largely single-phase with no impurities.
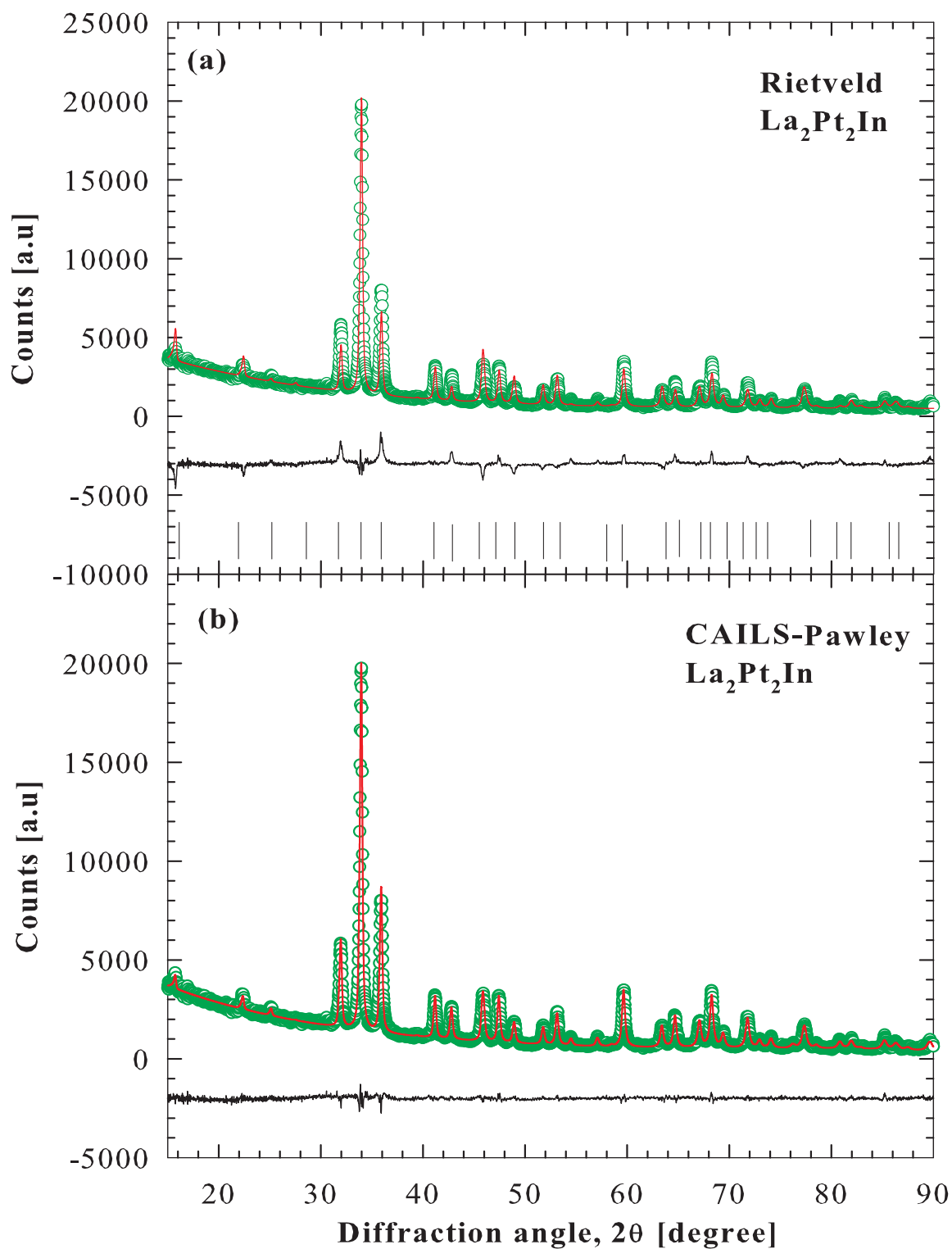
Figure 4.3: The X-ray diffraction pattern (green symbols) of La$_2$Pt$_2$In collected at room temperature and its Rietveld (a) and Pawley (b) refinement (red curves). The bottom black curves are the difference between the experimental and calculated patterns. The vertical ticks in (a) represent the Bragg's reflections.
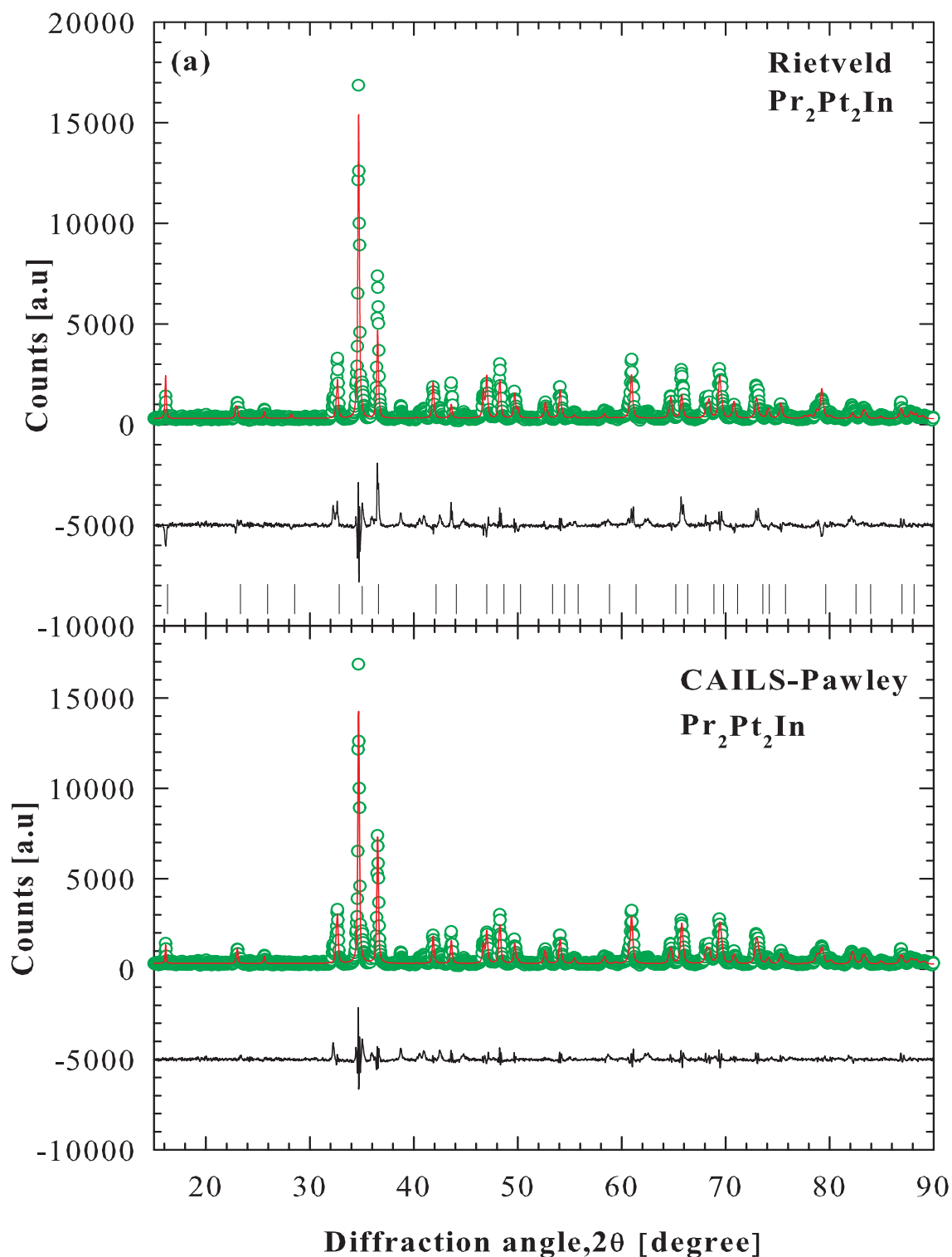
Figure 4.4: The X-ray diffraction pattern (green symbols) of Pr_2Pt_2In collected at room temperature and its Rietveld (a) and Pawley (b) refinement (red curves). The bottom black curves are the difference between the experimental and calculated patterns. The vertical ticks in (a) represent the Bragg's reflections.
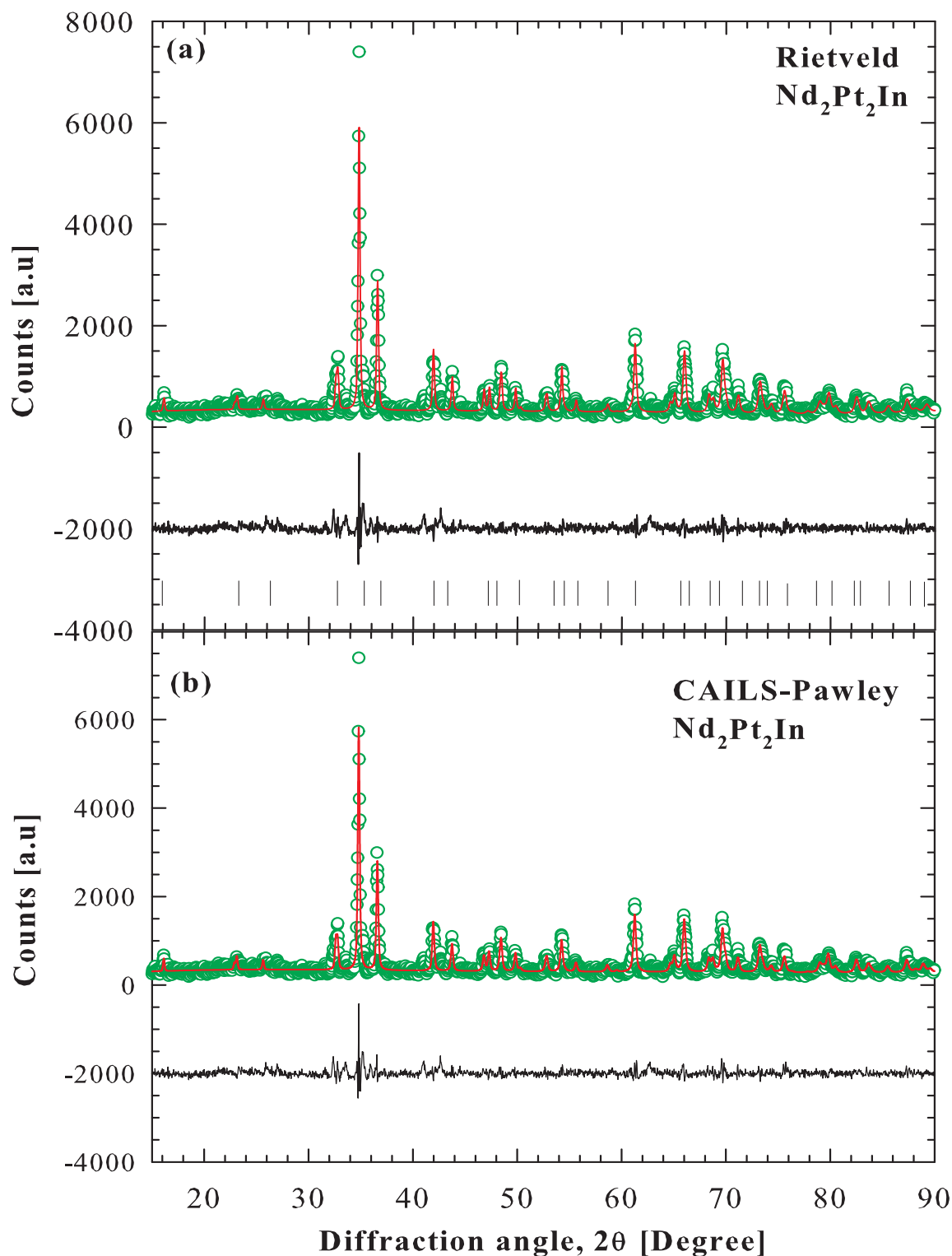
Figure 4.5: The X-ray diffraction pattern (green symbols) of Nd_2Pt_2In collected at room temperature and its Rietveld (a) and Pawley (b) refinement (red curves). The bottom black curves are the difference between the experimental and calculated patterns. The vertical ticks in (a) represent the Bragg's reflections.
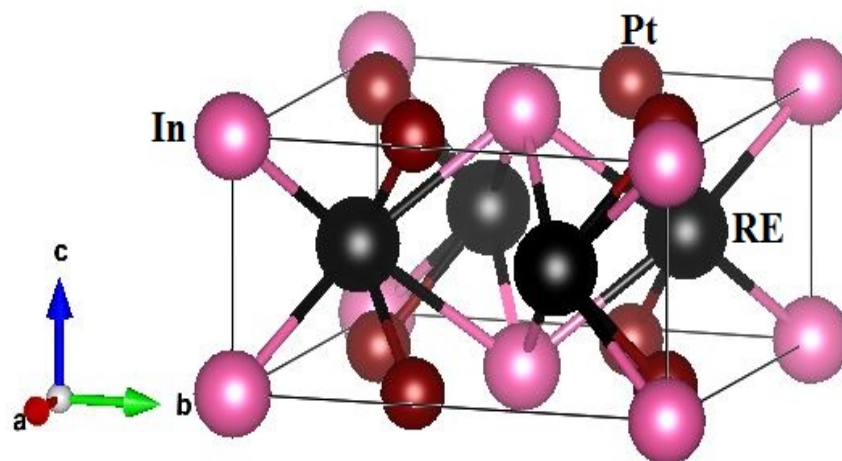
Figure 4.6: The tetragonal unit cell of RE_2Pt_2In. The pink, brown and black balls represent In, Pt and Pr atoms, respectively.

Table 4.1: Atomic coordinates derived for RE_2Pt_2In from the Rietveld refinement. The site occupancies S.O. = 1 and the isotropic displacement parameters $B_{eq} = 1$ were assumed.

Atom	Wyckoff site	x	y	z	a(Å)	c(Å)	V(Å³)
La	4h	0.683(1)	x+1/2	0.5	7.8524(5)	3.9365(3)	242.72(4)
Pt	4g	0.127(1)	x+1/2	0			
In	2a	0	0	0			
Pr	4h	0.683(1)	x+1/2	0.5	7.7694(6)	3.8634(4)	233.66(4)
Pt	4g	0.127(1)	x+1/2	0			
In	2a	0	0	0			
Nd	4h	0.683(1)	x+1/2	0.5	7.7576(9)	3.8383(5)	230.990(3)
Pt	4g	0.127(1)	x+1/2	0			
In	2a	0	0	0			

71

Table 4.2: R-factors obtained from the Rietveld and Pawley refinement methods in X-ray powder diffraction data analysis of RE$_2$Pt$_2$In, with RE = La, Pr and Nd.

discrepancy factors-Rietveld	La$_2$Pt$_2$In	Pr$_2$Pt$_2$In	Nd$_2$Pt$_2$In
R_{wp} [%]	9.546	9.071	7.285
R_{exp} [%]	2.441	2.191	2.211
R_{p} [%]	6.741	7.511	5.637
χ^2	3.910	4.429	3.401
DW	0.213	0.615	0.259
R_{B} [%]	8.574	8.226	4.775
discrepancy factors-Pawley			
R_{wp} [%]	16.679	18.381	16.039
R_{exp} [%]	2.422	4.168	4.716
R_{p} [%]	9.904	13.976	12.566
χ^2	3.886	4.410	3.295
DW	0.078	0.765	1.097

4.3   Pr$_2$Pt$_2$In

4.3.1   Electrical resistivity

The electrical resistivity measurements were done on a bar-shaped specimen of typical dimension 1×1×6 mm^3. The temperature dependence of the electrical resistivity, $\rho(T)$, of Pr$_2$Pt$_2$In is displayed in figure 4.7. The compound shows metallic conductivity with some bending of the $\rho(T)$ curve characteristic of s-d interband scattering. Based on the Matthiessen's rule, this experimental data was described in the framework of Bloch-Grüneisen-Mott function [107, 108]:

$$\rho\left(T\right) = \left(\rho_0 + \rho_0^{\infty}\right) + 4k\theta_{\mathrm{R}}\left(\frac{T}{\theta_{\mathrm{R}}}\right)^5 \times$$

$$\int_0^{\frac{\theta_{\mathrm{R}}}{T}} \frac{x^5}{\left(e^x - 1\right)\left(1 - e^{-x}\right)}dx - \alpha T^3, \tag{4.1}$$

where ρ_0 represents the residual resistivity due to static imperfections in the sample, ρ_0^{∞} is the spin-disorder resistivity, the second term accounts for the electron-phonon scattering processes and the third term describes the scattering of conduction electrons into a narrow d-band (interband Mott scattering). The constant k and α are related to the strength of

72

4.3.1 . Electrical resistivity

the electron-phonon and the *s-d* interactions respectively, whereas, θ_R is a characteristic energy scale of lattice vibrations, a rough measure of the Debye temperature in the system. The least squares fit of equation 4.1 to the experimental $\rho(T)$ data (solid red curve figure 4.7a main panel) yielded: the sum of the residual and the spin-disorder resistivity $\rho_0 + \rho_0^\infty = 44.5(2)$ $\mu.\Omega.\text{cm}$, the Debye resistivity temperature $\theta_R = 193.8(6)$ K, the electron-phonon coupling constant $k = 674.3(4)$ $\mu\Omega.\text{cm}.\text{k}^{-3}$ and the inter-band scattering coefficient $\alpha = 5.61(1)$ $\times 10^{-7}$ $\mu\Omega.\text{cm}.\text{K}^{-3}$. The inset to figure 4.7a displays an expanded view of the low-temperature $\rho(T)$ data. At $T_C = 9$ K, the electrical resistivity shows a sudden drop marking an onset of the ferromagnetically ordered state, also observed in heat capacity and the magnetic susceptibility (see section 4.3.2 and 4.3.3).
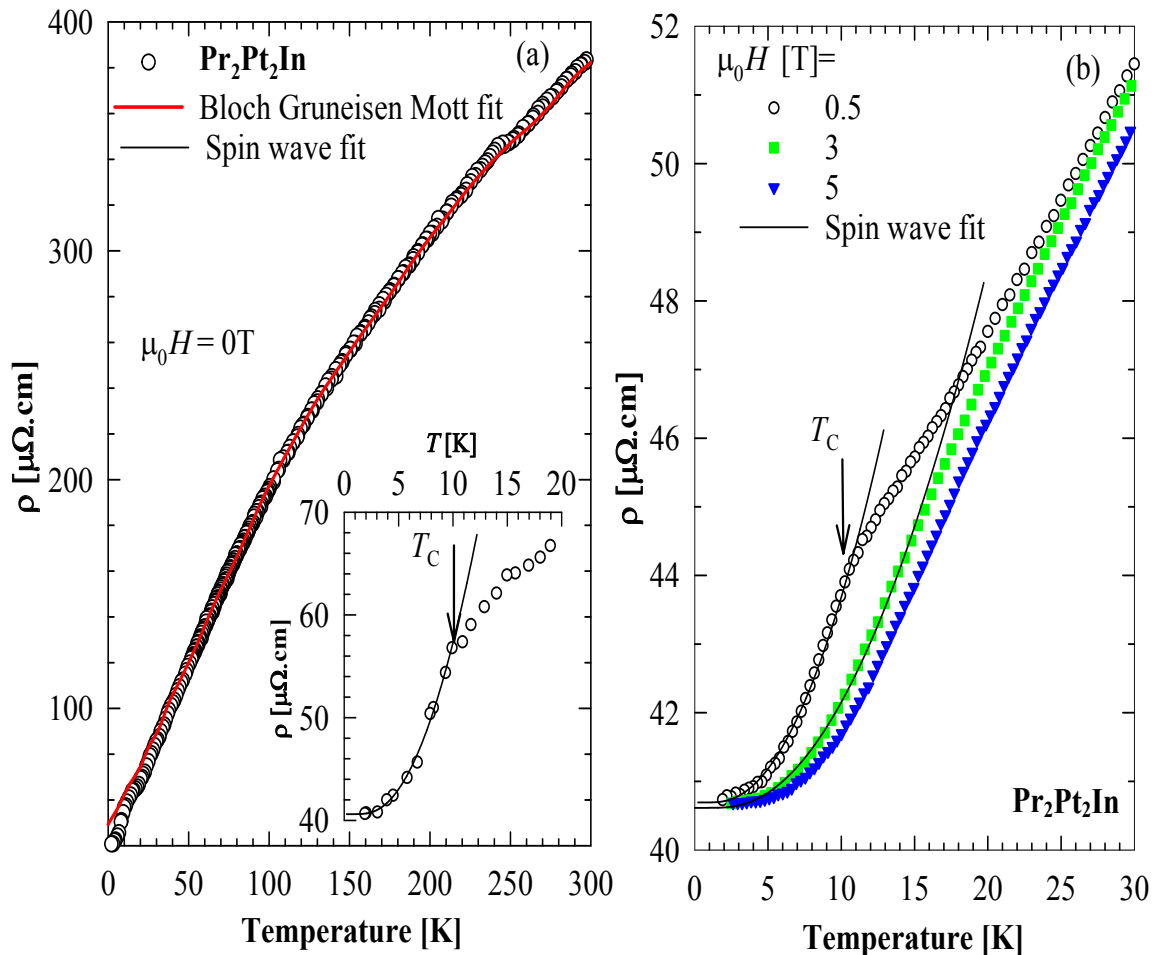
Figure 4.7: (a) Temperature variation of the electrical resistivity, $\rho(T)$, of Pr_2Pt_2In measured in 0 T. The solid red curve through the data points is the least squares fit of equation 4.1 to the experimental data. The inset displays the low-temperatures $\rho(T)$ data in 0 T. The black solid curve represents the least squares fit of equation 4.2 to the experimental data. (b) displays the low-temperatures $\rho(T)$ of Pr_2Pt_2In measured in a field of 0.5; 3 and 5 T. The black solid curves represent the least squares fits of equation 4.2 to the experimental data. The arrows indicate the position of T_C.

73

4.3.1 . Electrical resistivity

Figure 4.7b shows the low-temperature electrical resistivity data of Pr_2Pt_2In $\rho(T)$ measured in an external magnetic field of 0.5, 3, 5 T. The application of magnetic field shifts the phase transition to high temperatures, as expected for ferromagnet materials. In 5 T, the ferromagnetic anomaly is not discernible on the $\rho(T)$ curve. As can be inferred from figure 4.7b (see also the inset of figure 4.7a), in the ordered state, the $\rho(T)$ variations measured in 0 and finite applied magnetic field can be well described by the formula that accounts for scattering conduction electrons on ferromagnetic spin-wave excitations with an energy gap Δ_R in magnon spectrum [34]:

$$\rho(T) = \rho_0 + A\Delta_R T \left[1 + 2\frac{T}{\Delta_R}\right] exp\left(-\frac{\Delta_R}{T}\right), \tag{4.2}$$

where A is a prefactor that determines the stiffness of the sample. The least squares fits of equation 4.2 to the experimental data yielded the parameters gathered in table 4.3. Combining the results of the performed evaluations of the zero-field resistivity (equation 4.1 and equation 4.2), the spin-disorder resistivity can be derived to be $\rho_0^\infty = 4.0(3)$ $\mu\Omega$cm, with the transition temperature at $T_C = 9$ K.

Table 4.3: The parameters derived from the analysis of the low-temperatures electrical resistivity data of Pr_2Pt_2In.

$\mu_0 H$ [T]	ρ_0 [$\mu\Omega$.cm]	A [$\mu\Omega$cm/K^2]	Δ_R [K]
0	40.6(3)	0.13(7)	8(2)
0.5	40.69(4)	0.021(8)	7(1)
3	40.61(3)	0.010(3)	8.1(9)

The magnetic phase transition manifests itself as a pronounced feature in the temperature derivative of the resistivity, $d\rho/dT$. In accordance with the criterion given by Sato *et al* in [109], the value of T_C can be defined as a midpoint of the anomaly in the $d\rho/dT$ curve as shown in figure 4.8.

74
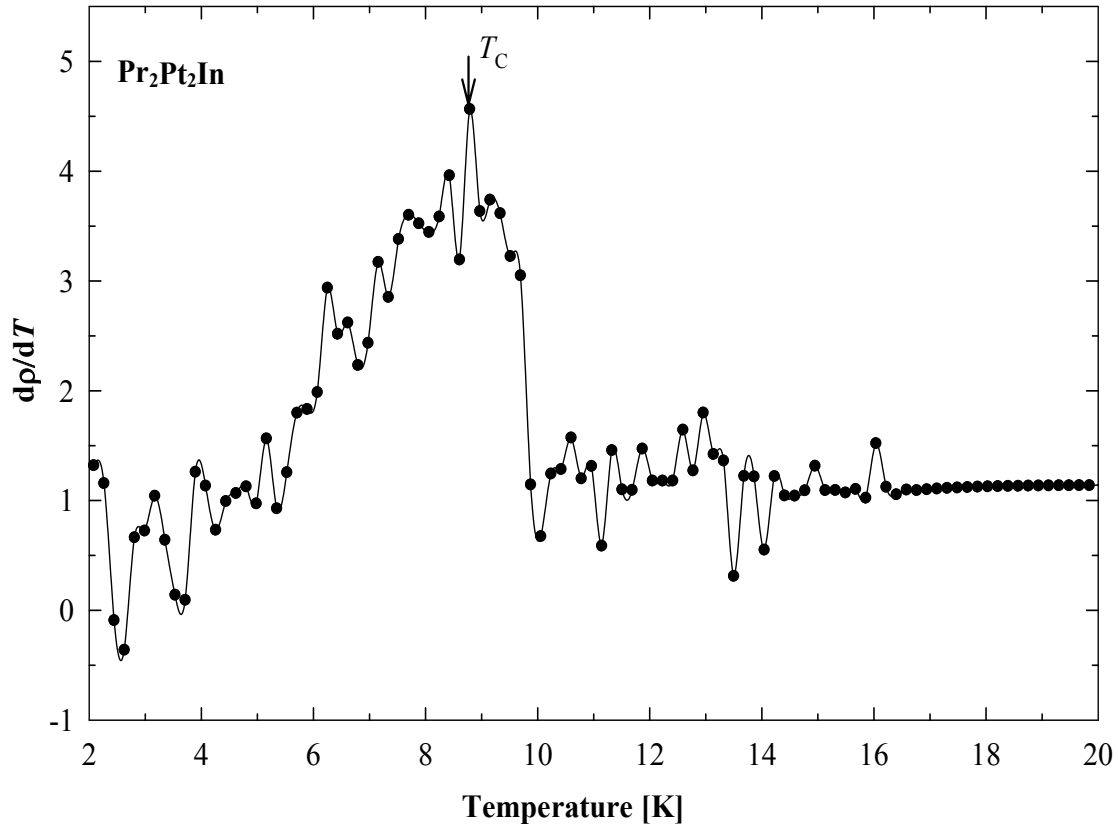
Figure 4.8: The temperature derivative, $d\rho/dT$, as a function of temperature. The arrow indicates the critical temperature T_C associated with the maximum in the curve.

4.3.2 Heat Capacity

The temperature variation of the specific heat, $C_p(T)$, of Pr_2Pt_2In is depicted in figure 4.9. At room temperature, the specific heat attains a value of 131 J/mole.K, close to the Dulong-petit limit $3nR = 124.7$ J/mole.K ($n = 5$ is the number of atoms per formula unit, R stands for the gas constant). In the paramagnetic state, $C_p(T)$ can be approximated by the standard Debye formula:

$$C_p(T) = \gamma T + 9nk_B \left(\frac{T}{\theta_D}\right)^3 \int_0^{\theta_D/T} \frac{x^4 e^x}{(e^x - 1)^2} dx, \tag{4.3}$$

where γ is the Sommerfeld coefficient and θ_D is the Debye temperature. The least squares fit of equation 4.3 to the experimental data yielded $\gamma = 1.7(1)$ J/mole.K^2 and $\theta_D = 155.0(3)$ K. The value of θ_D is similar to those reported for other members of the RE_2Pt_2In series [92]. It is fairly close to the value of θ_R derived from the electrical resistivity data of Pr_2Pt_2In.

75

The low-temperatures, $C_p(T)$ data of Pr_2Pt_2In, measured in 0 magnetic field, 2 and 5 T, are displayed in the inset of figure 4.9. $C_p(T)$ data shows a λ-shape anomaly at $T_C = 9$ K that correspond to the second order phase transition from the paramagnetic state to the ferromagnetic state one, in line with the Arrott-plots analysis(see section 4.3.4). The observed T_C value in 0 magnetic field agree with the results obtained from the electrical resistivity (see section 4.3.1) and the magnetic susceptibility studies (see section 4.3.3) studies. Typical for ferromagnetic materials, the specific heat peak marking the onset of the magnetically ordered state shifts to higher temperatures with an increase in the magnetic field strength. In 5 T, the peak disappears, in accordance with the behaviour of the electrical resistivity measured at the same field (see above).
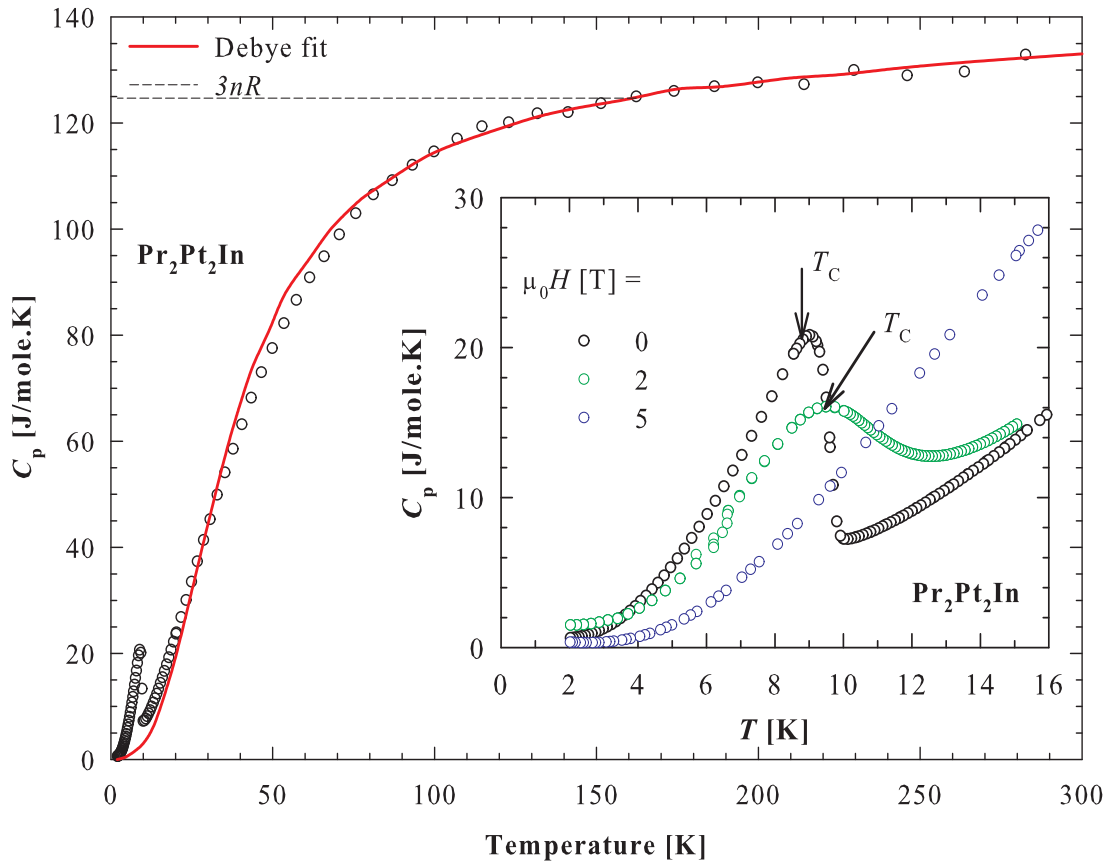
Figure 4.9: Temperature variation of the heat capacity, $C_p(T)$ of Pr_2Pt_2In measured in 0 magnetic field. The solid red curve is the least squares fit of equation 4.3 to the experimental data. The solid dash line represents the Dulong-petit value $3nR = 124.7$ J/mole.K. The inset shows an expanded view of the low-temperatures $C_p(T)$ data. The arrows indicate the position of T_C of Pr_2Pt_2In taken in 0 and in applied field of 2 and 5 T.

Figure 4.10 displays the magnetic $4f$-electron contribution to the total specific heat, $C_{4f}(T)$ of Pr_2Pt_2In in 0 and 2 T, obtained by subtracting the phonon contribution that was assumed to be the same as in the isostructural compound La_2Pt_2In (see section 4.4.2).

As depicted in the figure, below T_C the $C_{4f}(T)$ data measured in 0 magnetic field can be described by the formula:

$$C_{4f}(T) = \gamma T + BT^{3/2} exp\left(-\frac{\Delta_C}{T}\right), \tag{4.4}$$

that takes into account the electronic term and the magnon contribution with an energy gap, Δ_C, in the ferromagnetic spin-wave spectrum (B is a constant associated with the stiffness of the sample). The parameters obtained by least squares fitting are: the Sommerfeld coefficient $\gamma = 0.09(4)$ J/mole.K^2, $B = 1.42(3)$ J/mole.K^2, $\Delta_C = 6.0(3)$ K in 0 T. The value of Δ_C is close to T_C, and very similar to the values of Δ_R derived from the low-temperatures $\rho(T)$ data.

At high temperatures, $C_{4f}(T)$ measured in 0 magnetic field (figure 4.10a) shows a broad hump around 20 K that can be attributed to crystal-electric-field effect.
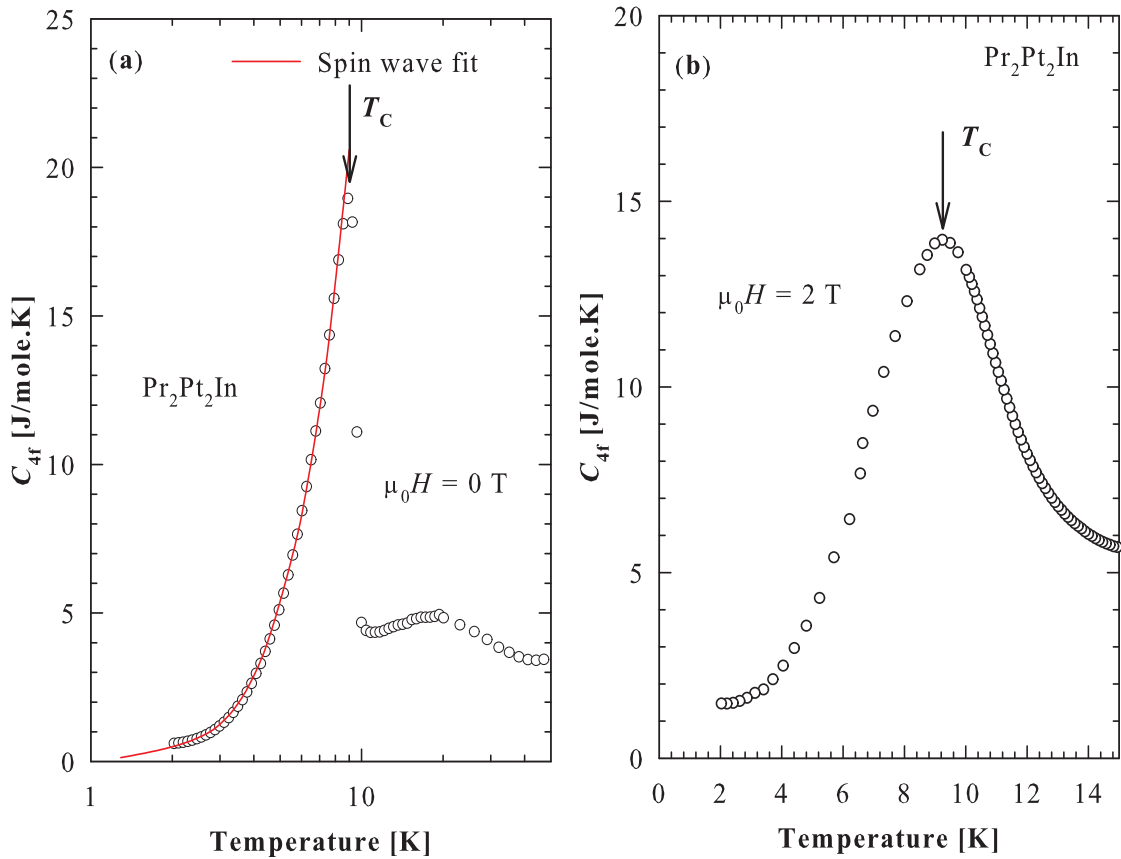
Figure 4.10: Temperatures variation of the $4f$ contribution to the total heat capacity, $C_{4f}(T)$ of Pr$_2$Pt$_2$In measured in (a) 0 and (b) 2 T. The solid red curve is the least squares fit of the spin-wave dispersion relation (equation 4.4) to the $C_{4f}(T)$ data measured in 0 magnetic field. The arrows indicate the position of T_C.

The $4f$-electron magnetic entropy was calculated from the integration:

$$S_{4f}(T) = \int_0^T \frac{C_{4f}(T')}{T'} dT', \tag{4.5}$$

and the results are presented in figure 4.11. The entropy attains the value of $R\ln 2$ appropriate for a well isolated doublet very close to T_C.
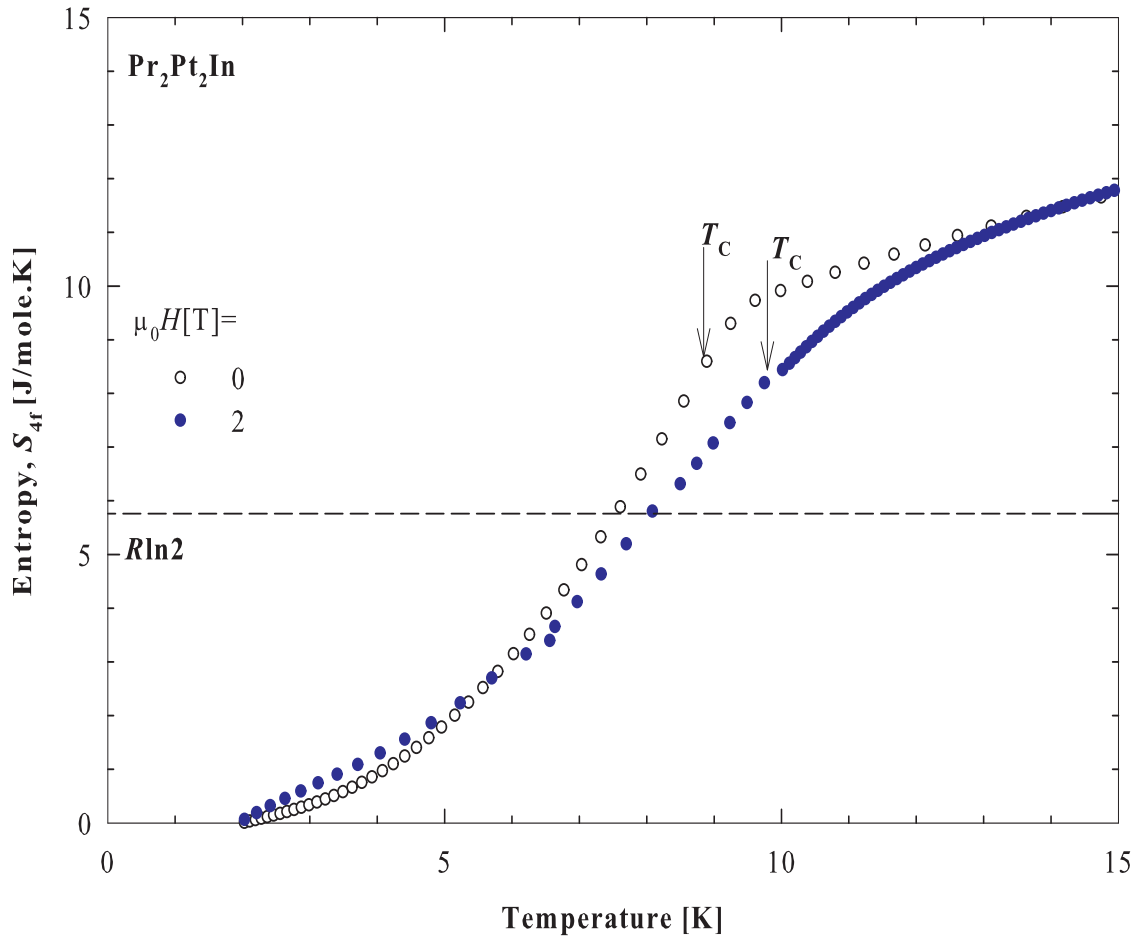
Figure 4.11: Temperature variation of the $4f$-electron magnetic entropy $S_{4f}(T)$ of Pr_2Pt_2In measured in 0 and 2 T. The arrows indicate the position of T_C. The horizontal dash line marks the value $R\ln 2 = 5.76$ J/mole.K expected for the doublet ground state.

4.3.3 Magnetic susceptibility and magnetization

Figure 4.12 shows the inverse magnetic susceptibility, $\chi^{-1}(T)$ measured in the field of 0.1 T in the temperature range 400 K - 1.7 K. It is observed that $\chi^{-1}(T)$ data follows the Curie-Weiss relationship above 150 K:

$$\chi^{-1}(T) = \frac{3k_B(T - \theta_P)}{N_A \mu_{eff}^2}, \tag{4.6}$$

78

where the parameters have their usual meaning (see chapter 2). Least squares fit on $\chi^{-1}(T)$ data to equation 4.6 gives the values of the effective magnetic moment, $\mu_{\text{eff}} = 3.61(2)\mu_{\text{B}}/\text{Pr}$ and the Weiss temperature constant, $\theta_{\text{p}} = 20.1(4)$ K. The observed value of μ_{eff} is very close to that expected for the free Pr^{3+} ion; $\left(g_J\sqrt{j(j+1)} = 3.58\mu_{\text{B}}\right)$ and indicates a development of well localized magnetic moments in $\text{Pr}_2\text{Pt}_2\text{In}$. The positive value of θ_{P} reveals the ferromagnetic ground state of $\text{Pr}_2\text{Pt}_2\text{In}$. Below 150 K, $\chi^{-1}(T)$ deviate distinctly from the Curie-Weiss behaviour which is likely due to magnetocrystalline anisotropy or to thermal depopulation of crystal-electric-field split Pr $4f^2$-state.
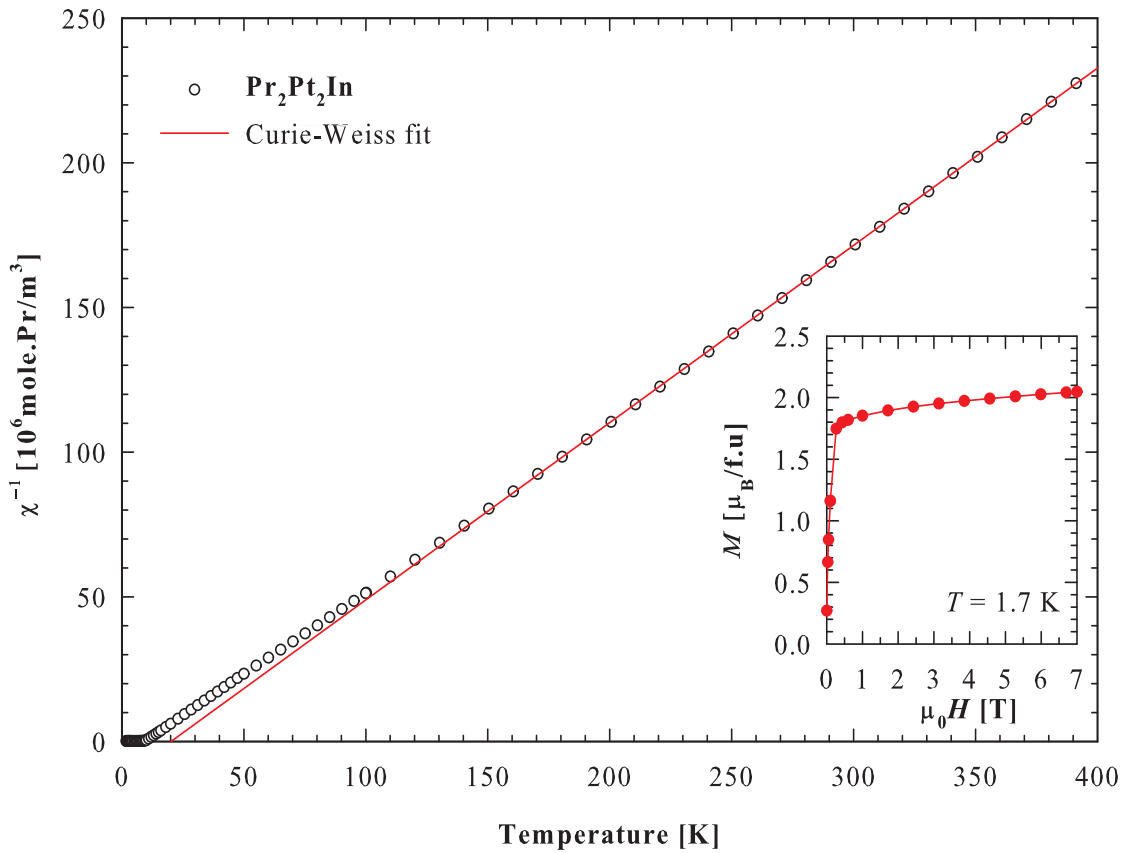
Figure 4.12: Temperature variation of the inverse magnetic susceptibility, $\chi^{-1}(T)$, of $\text{Pr}_2\text{Pt}_2\text{In}$ measured in a field of 0.1 T. The red solid line is least squares fit of the Curie-Weiss relation equation 4.6 to the experimental data above 150 K. The inset displays the magnetic field variation of the magnetization in $\text{Pr}_2\text{Pt}_2\text{In}$ taken at 1.7 K.

The inset of figure 4.12 shows the field dependence of the magnetization, $M(\mu_0 H)$ for $\text{Pr}_2\text{Pt}_2\text{In}$ measured at 1.7 K. The shape of $M(\mu_0 H)$ is typical for ferromagnetic materials. In a field stronger than 0.5 T, one observes a saturation at a value $M_{\text{s}} = 2.05\ \mu_{\text{B}}/\text{Pr}^{3+}$, which is smaller than the theoretical value ($g_J J = 3.2\ \mu_{\text{B}}$) calculated for a free Pr^{3+}-ion. This reduction can be attributed to the crystal-electric-field effect as well as to magnetic

4.3.3 . Magnetic susceptibility and magnetization

anisotropy.

Figure 4.13a shows the low-temperatures $\chi(T)$ data for the Pr_2Pt_2In. $\chi(T)$ data shows an abrupt rise characteristic of ferromagnetic materials. The magnetic phase transition temperature was estimated at the midpoint of the abrupt rise in the $\chi(T)$ curve and accurately taken at the minimum of the derivative of $\chi(T)$ curve as indicated in figure 4.13b by the vertical arrow at $T_C = 9$ K.
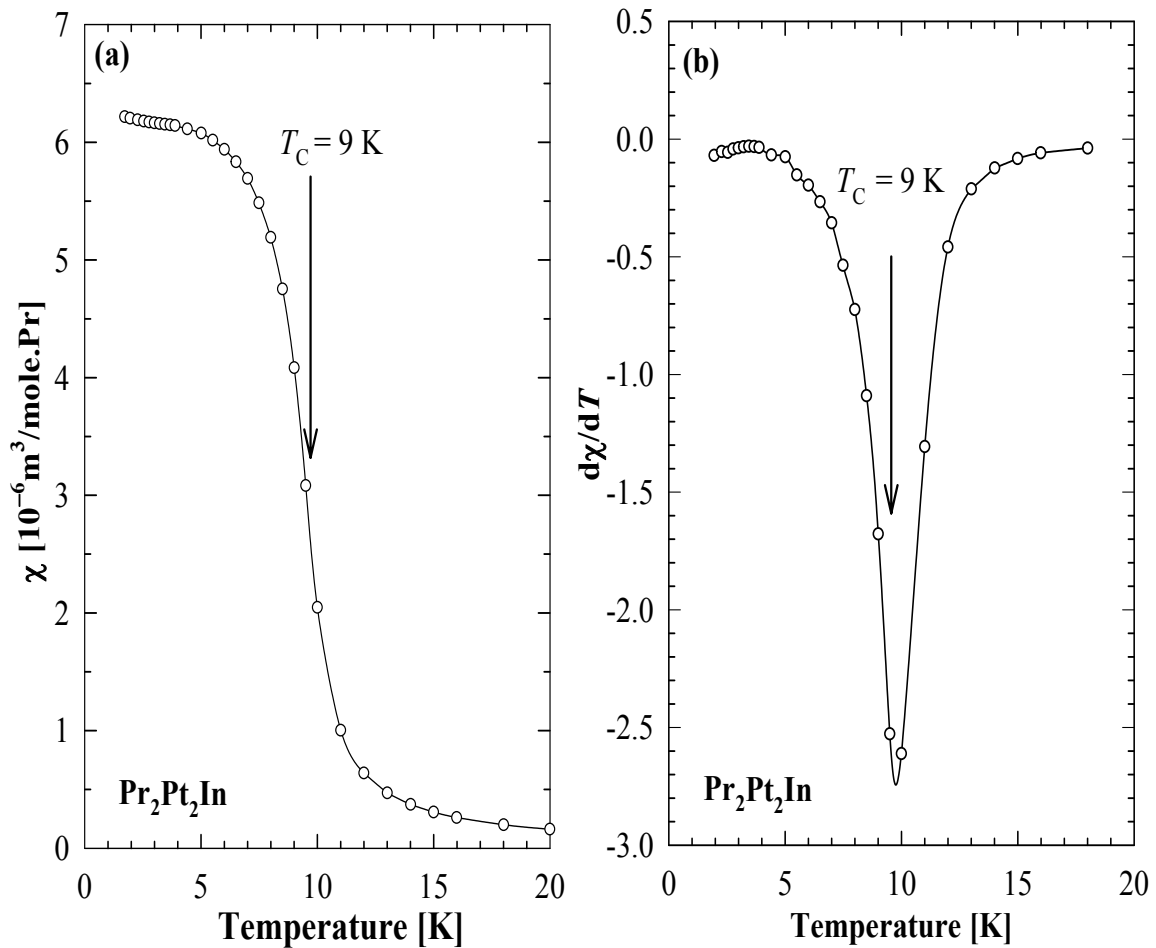
Figure 4.13: (a) The low-temperatures $\chi(T)$ data of Pr_2Pt_2In in the ferromagnetic region, measured in field of 0.1 T. The arrow indicates the ferromagnetic transition temperature T_C taken at the midpoint of the abrupt rise in the $\chi(T)$ curve. (b) $d\chi(T)/dT$ curve with the arrow indicating the position of T_C taken at the minimum of $d\chi(T)/dT$ curve.

4.3.4   Critical behaviour study around the magnetic phase transition in Pr₂Pt₂In

4.3.4.1   Arrott-plots

Figure 4.14 shows the standard Arrott-plot M^2 vs. $\mu_0 H/M$ for the magnetization isotherms taken in the temperature range 8 K - 11.2 K in step of 0.2 K.
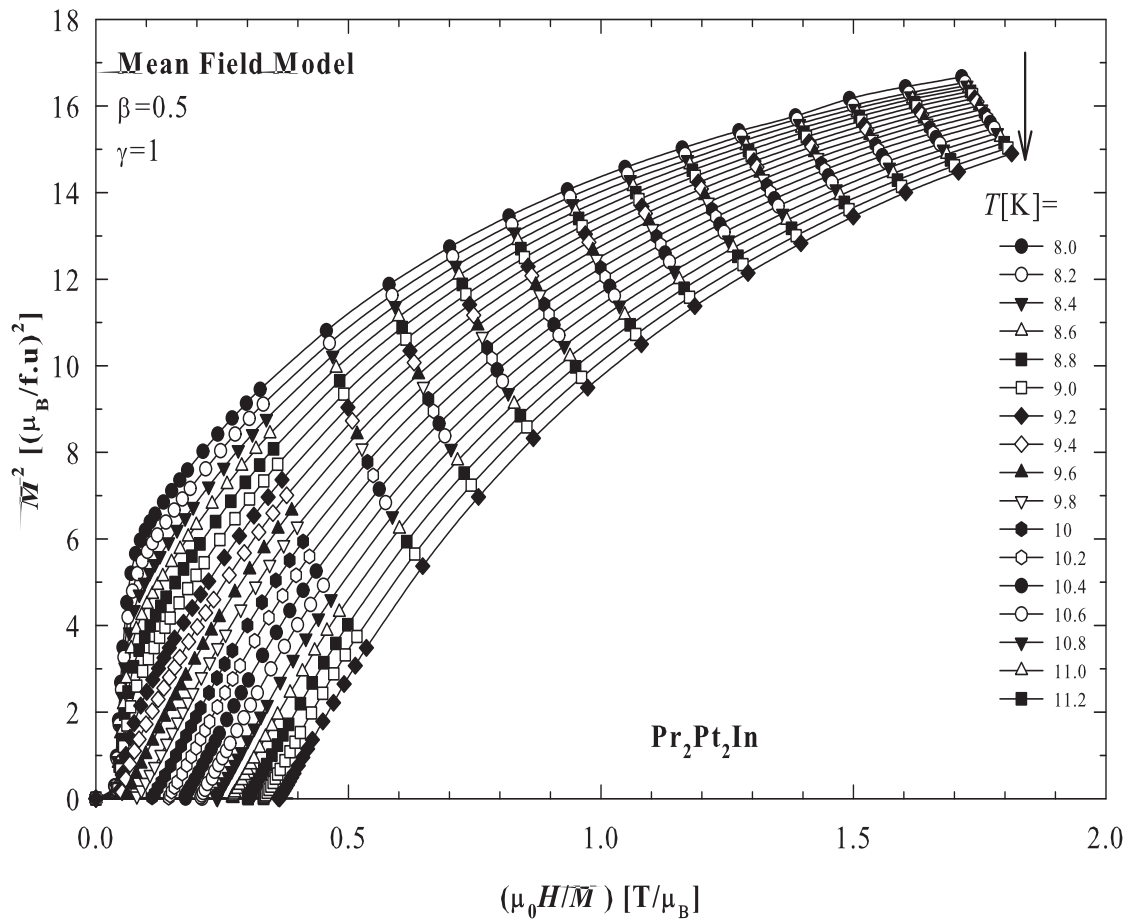
Figure 4.14: The standard Arrott-plot for the mean-field model M^2 vs. $\mu_0 H/M$ of isotherms collected around T_C for Pr₂Pt₂In.

Apparently, all the isotherms deviated from linearity even in a strong magnetic field, which indicates that a mean-field description of the magnetic exchange interactions in Pr₂Pt₂In is not appropriate. In the entire temperature interval examined, the isotherms have positive slopes, which indicates a second-order nature of the transition [110]. In order to evaluate the critical exponent, and thus the class of universality to which Pr₂Pt₂In

4.3.4 . Critical behaviour study around the magnetic phase transition in Pr_2Pt_2In

compound might belong, we have used the modified Arrott-plots given by [111]:

$$\left(\frac{\mu_0 H}{M}\right)^{1/\gamma} = a\frac{(T - T_C)}{T} + bM^{1/\beta}. \tag{4.7}$$

As starting trial values of β and γ, the values predicted within the 3D-Ising model (β = 0.325, γ = 1.241) and the 3D-Heisenberg (β = 0.365, γ = 1.386) were applied. Linear fittings of the experimental data points at high fields provides quantitative information when comparing their slopes for each universality class. The deviation of each slope with respect to the average values for both models was compared and pointed out to be good for the 3D-Ising model. Thus, the 3D-Ising critical exponents has been taken as the starting point from which an iterative process was carried out similar to references [51, 112]. The result of this treatment is presented in figure 4.15.
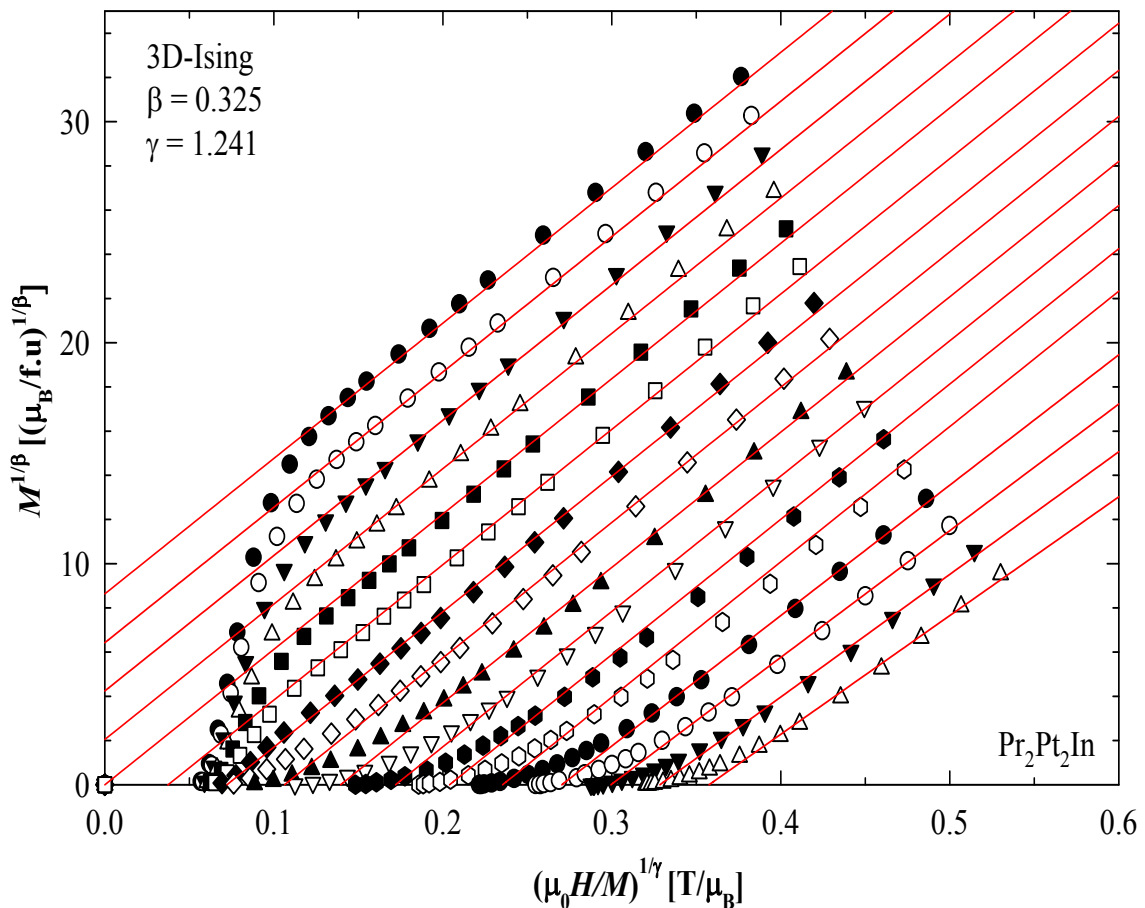
Figure 4.15: Modified Arrott-plots using the critical exponent of the 3D-Ising model. The solid red lines are the linear fits, according to equation 4.7.

Following the theory of ferromagnetism, it is observed from figure 4.15 that in weak

4.3.4 . Critical behaviour study around the magnetic phase transition in $\mathbf{Pr_2Pt_2In}$

magnetic fields, the data exhibit a downward curvature as they are averaged over domains which are magnetized in different directions [113]. In the next step, an iterative process was used, similar to that described in reference [51]. A linear extrapolation of the isotherms in figure 4.15 gave $(M_s)^{1/\beta}$ and $\left(\chi_0^{-1}\right)^{1/\gamma}$ as intercepts on the $(M)^{1/\beta}$ and $(\mu_0 H/M)^{1/\gamma}$ axes, respectively. The obtained values of $M_s(T)$ and $\chi_0^{-1}(T)$ are plotted in figure 4.16. They were evaluated using the formulas [38]:

$$M_{\mathrm{s}}(T) = M_0 \left(-\frac{T - T_{\mathrm{C}}}{T_{\mathrm{C}}} \right)^{\beta} \qquad (T < T_{\mathrm{C}}), \tag{4.8}$$

$$\chi_0^{-1}(T) = \Gamma \left(\frac{T - T_{\mathrm{C}}}{T_{\mathrm{C}}} \right)^{\gamma} \qquad (T > T_{\mathrm{C}}), \tag{4.9}$$

where M_0 and Γ are the critical amplitudes. The least squares fit of equation 4.8 to the M_{s} data yielded $\beta = 0.325(3)$ and $T_{\mathrm{C}} = 8.80(3)$ K, while the least squares fit of equation 4.9 to the $\chi_0^{-1}(T)$ data gave $\gamma = 1.058(3)$ and T_{C} 8.814(3) K. These new values of the critical exponents were used to construct other modified Arrott-plots similar to those shown in figure 4.15. The process was repeated until convergence was reached and the final values of the critical exponents were $\beta = 0.324(2)$, $\gamma = 1.15(2)$. Remarkably, these values are close to those predicted within the 3D-Ising model, and smaller than the critical exponents derived in the 3D-Heisenberg model ($\beta = 0.365$, $\gamma = 1.386$).

4.3.4 . Critical behaviour study around the magnetic phase transition in Pr$_2$Pt$_2$In
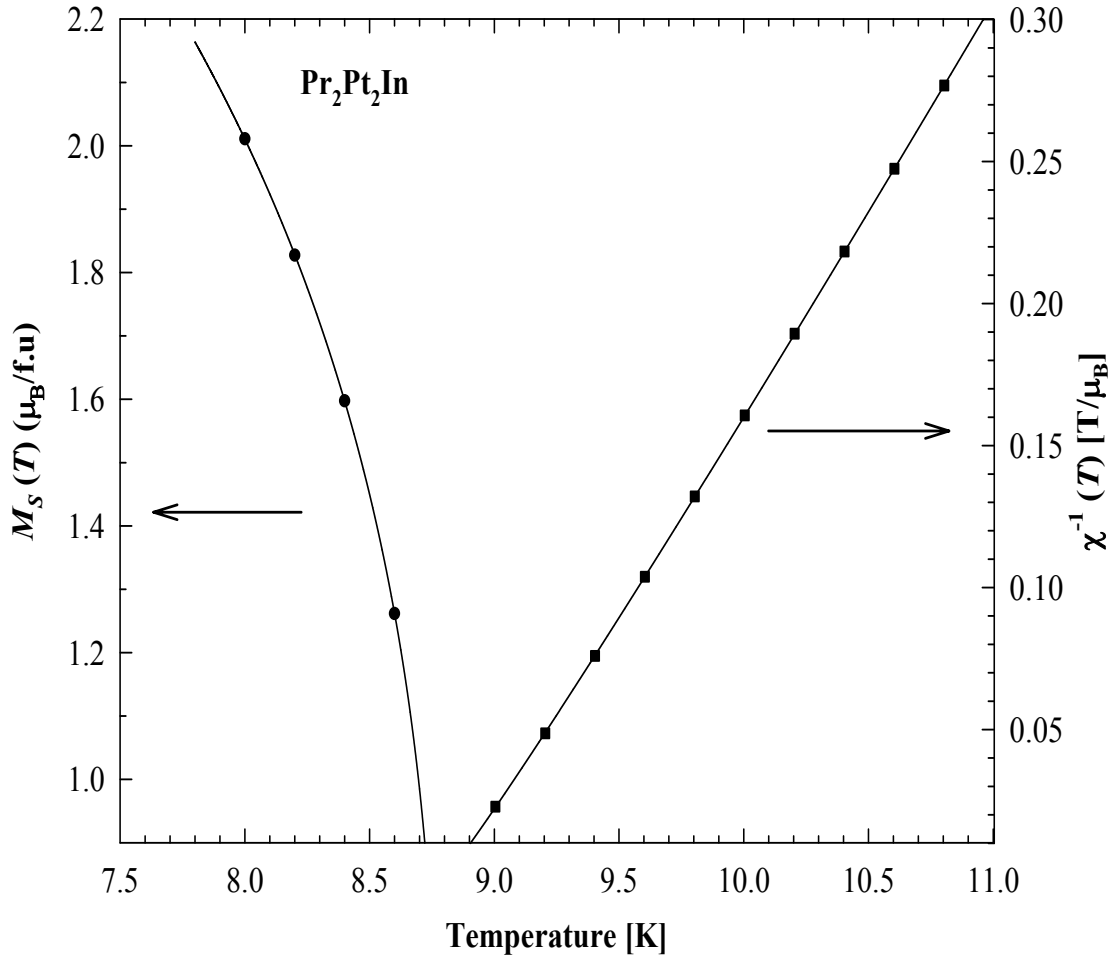
Figure 4.16: Temperature variation of the spontaneous magnetization, $M_\mathrm{s}(T)$ (left axis), and the reciprocal initial susceptibility, $\chi_0^{-1}(T)$ (right axis), derived from the modified Arrott-plots shown in figure 4.15. The solid curves are least squares fits using equations 4.8 and 4.9.

4.3.4.2 Kouvel-Fisher

Another approach applied to the magnetization data of Pr$_2$Pt$_2$In in order to obtain accurate values of the critical exponents was the scaling analysis developed by the Kouvel and Fisher [114, 115]. The experimental $M_\mathrm{s}(T)$ and $\chi_0^{-1}(T)$ data were fitted by the Kouvel-Fisher equations [115, 116]:

$$\frac{M_\mathrm{s}(T)}{dM_\mathrm{s}(T)/dT} = \frac{T - T_\mathrm{C}}{\beta}, \tag{4.10}$$

$$\frac{\chi_0^{-1}(T)}{d\chi_0^{-1}(T)/dT} = \frac{T - T_\mathrm{C}}{\gamma}. \tag{4.11}$$

As displayed in figure 4.17, both plots are straight lines with their slopes being equal

4.3.4 . Critical behaviour study around the magnetic phase transition in $\mathbf{Pr_2Pt_2In}$

to $1/\beta$ and $1/\gamma$, respectively, and their intercepts with the temperature axis defines T_C. From those straight line fits, the estimated critical exponents and T_C were: $\beta = 0.323(6)$, $T_C = 8.8$ K (from equation 4.10) and $\gamma = 1.054(3)$ and $T_C = 8.4(3)$ K (from equation 4.11). All these critical exponents estimated from the various techniques are gathered in table 4.4, together with the theoretically predicted values of the different models. Apparently, the Kouvel-Fisher analysis led to the results very similar to those obtained from the modified Arrott-plots.
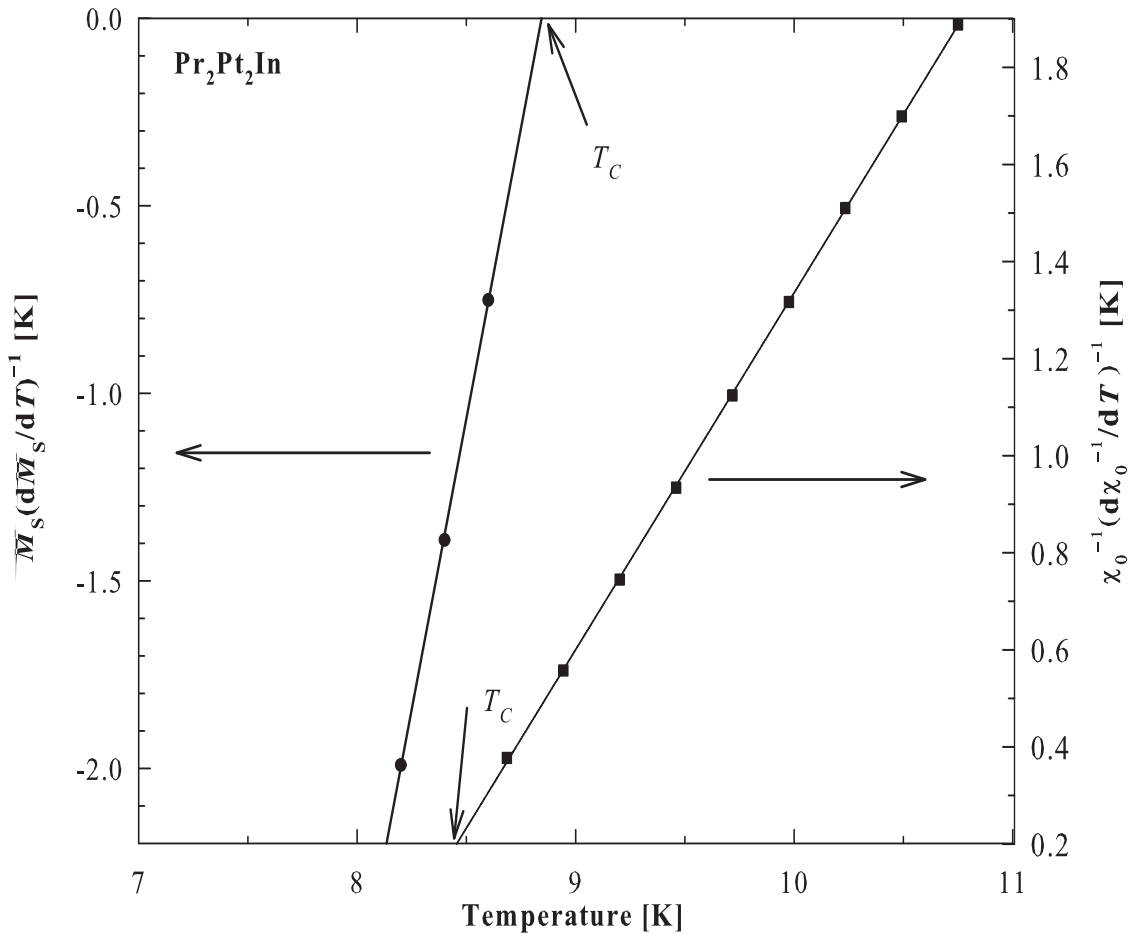
Figure 4.17: Kouvel-Fisher plot of spontaneous magnetization $M_s(T)$ (left axis) and the inverse initial susceptibility $\chi_0^{-1}(T)$ (right axis). The straight lines are the least squares fits of the data points using equations 4.10 and 4.11.

4.3.4.3 Critical isotherm analysis and scaling law

The critical isotherm exponent δ can be determined directly from the critical isotherm given by:

$$M(\mu_0 H, T_C) = X(\mu_0 H)^{1/\delta}, \tag{4.12}$$

85

4.3.4 . Critical behaviour study around the magnetic phase transition in Pr_2Pt_2In

where X is the critical amplitude. Figure 4.18a (main panel) shows the magnetic field dependence of the magnetization in Pr_2Pt_2In measured at $T_C = 8.8$ K. As apparent from the inset to this figure, the plot $\log M$ vs. $\log(\mu_0 H)$ is a straight line with its slope being equal to $1/\delta$. The derived value of critical exponent is $\delta = 4.54(4)$.
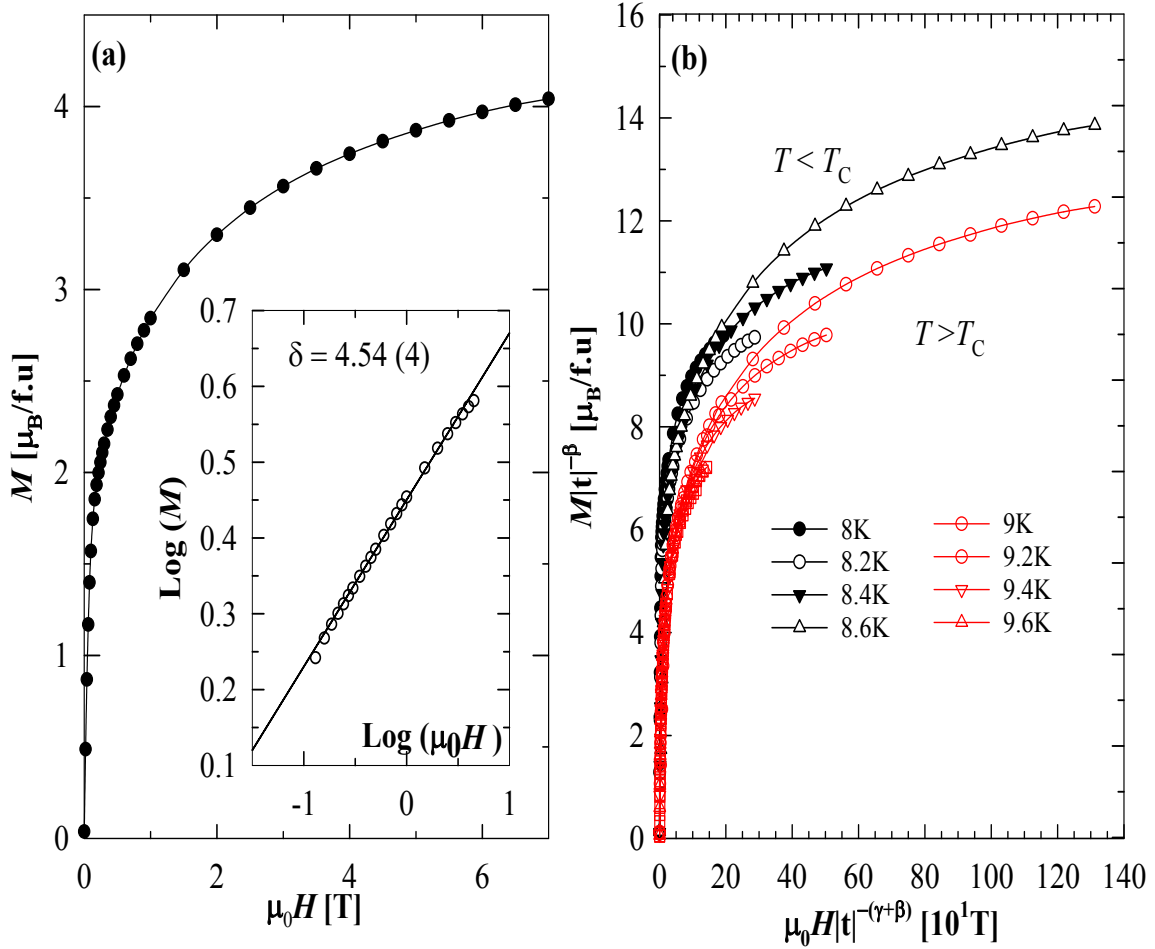
Figure 4.18: (a) Field variation of the critical isotherm, $M(\mu_0 H, T_C = 8.8$ K) for Pr_2Pt_2In. The inset shows the data with log-log representation. The straight line is the linear fit using equation 4.12. (b) The renormalized magnetization in Pr_2Pt_2In plotted as a function of the renormalized field (see equation 4.14). The isotherms in two separate branches correspond to temperature T_C and above T_C.

The exponent δ can also be calculated using the Widom scaling relationship [116, 117]:

$$\delta = 1 + \frac{\gamma}{\beta}. \tag{4.13}$$

Applying the values of β and γ derived from the modified Arrott-plots one obtained $\delta = 4.26(4)$, while using the critical exponents from the Kouvel-Fisher plots one got $\delta = 4.26(7)$. All the critical exponent values (β, γ and δ) obtained using different methods

4.3.5 . Isothermal magnetization and magnetocaloric effect

match reasonably well, which proves internal consistency of all the analysis performed.

Finally, it will be interesting to investigate the validity of our results obtained by checking if the critical exponents can reproduce the equation of states given by:

$$M(\mu_0 H, t) = |t|^\beta f_\pm \left(\frac{\mu_0 H}{t^{\beta+\gamma}} \right), \tag{4.14}$$

where f_+ and f_- are the regular functions for $T < T_C$ and $T > T_C$ respectively, and $t = (T - T_C)/T_C$ is the reduced temperature. As can be inferred from figure 4.18b, using the critical exponents β and γ and the critical temperature T_C, derived within the different methods applied, one obtains a collapse of the data representing the region below and above T_C into two distinct curves, in line with the expected scaling behaviour. The critical exponents obtained in this work for Pr_2Pt_2In are gathered in table 4.4, together with the theoretical predicted values of the different models, it is clear that the values found for this compound do not match with the conventional mean-field theory and they are slightly smaller than those of the isotopic 3D-Heisenberg model. Apparently, the ferromagnetic transition in Pr_2Pt_2In can be ascribed to the 3D-Ising universality class.

Table 4.4: Values of the critical exponents β, γ and δ derived for Pr_2Pt_2In from the modified Arrott-plots, the Kouvel-Fisher model and the critical isotherm. The values of δ for modified Arrott-plots and the Kouvel-Fisher model have been calculated from the Widom scaling. The theoretical values for various models are also given for the sake of comparison.

Material	Ref.	Technique	β	γ	δ
Pr_2Pt_2In	This work	Modified Arrott-plots	0.325(3)	1.058(3)	4.26(4)
	This work	Kouvel-Fisher	0.323(6)	1.054(3)	4.26(7)
	This work	Critical isotherm			4.54(4)
Mean-Field model	[47]	Theory	0.5	1.0.	3.0
3D-Heisenberg model	[47]	Theory	0.365	1.386	4.80
3D-Ising mode	[47]	Theory	0.325	1.241	4.82

4.3.5 Isothermal magnetization and magnetocaloric effect

Figure 4.19 depicts the field variations of the isothermal magnetization, $M(\mu_0 H, T)$ in Pr_2Pt_2In, measured in an applied field of up to 7 T in the temperature range 4 K - 20 K in a step of 2 K. The compound exhibits a behaviour typical of ferromagnet in the ordered state. At $T = 4$ K, $M(\mu_0 H)$ reaches a saturation value of 2.05 μ_B per Pr^{3+}-ion,

4.3.5 . Isothermal magnetization and magnetocaloric effect

i.e. much smaller than the theoretical value of $gJ = 3.2$ μ_B expected for a free Pr^{3+}-ion. This reduction can be attributed to crystal-electric-field effect and/or magnetic anisotropy.
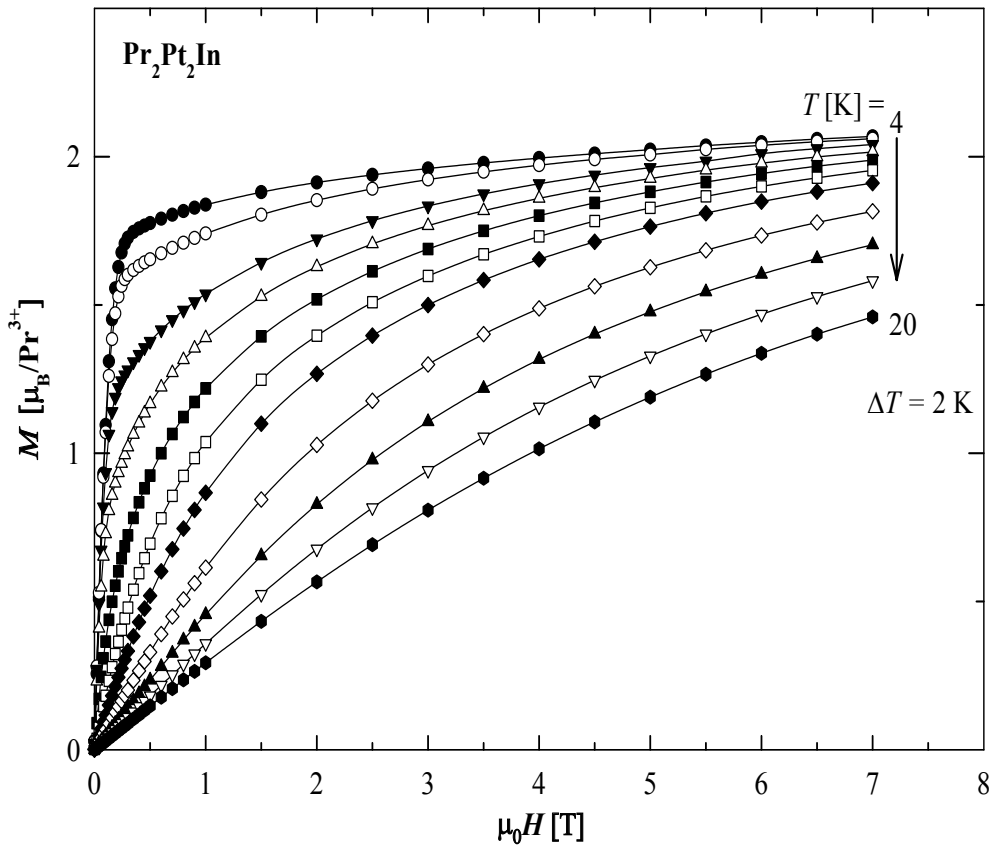
Figure 4.19: Isothermal magnetization curves, $M(\mu_0 H, T)$ of Pr_2Pt_2In measured in the vicinity of the Curie temperature $T_C = 9$ K.

The magnetocaloric effect in Pr_2Pt_2In can be estimated from the $M(\mu_0 H, T)$ data using the Maxwell relation:

$$\Delta S_M (\mu_0 H, T) = \int_0^{\mu_0 H} \left(\frac{\partial M(\mu_0 H', T)}{\partial T} \right)_{\mu_0 H} d(\mu_0 H'). \tag{4.15}$$

Figure 4.20a shows the isothermal magnetic entropy change $(-\Delta S_M(T))$ as a function of temperature, for several values of the magnetic field changes. For the compound investigated, magnetocaloric effect is positive in the whole temperature range covered, consistent with the ferromagnetic ordering. Around T_C, the $-\Delta S_M$ curves form broad maxima, the magnitude of which gradually increases with an increase in the field change, reaching 7.44 J/(kg.K) for a field change of 7 T. This value is similar to those of some magnetocaloric materials with second-order ferromagnetic phase transitions such as TbCoA having $T_C = 70$ K, $-\Delta S_M^{max} = 10.5$ J/kg.K [104], $Er(Co_{0.85}Si_{0.15})_2$ with $T_C = 60$ K,

4.3.5 . Isothermal magnetization and magnetocaloric effect

$-\Delta S_{\mathrm{M}}^{max} = 8$ J/(kg.K) [118].

In order to investigate the nature of the phase transition in Pr_2Pt_2In, the maximum value of $-\Delta S_{\mathrm{M}}^{max}$ at T_{C} was plotted in figure 4.20b as a function of $h^{2/3}$, where h is the reduced field ($h = (\mu_0 H)\mu_{\mathrm{B}}/k_{\mathrm{B}}T_{\mathrm{C}}$). It should be noted that magnetic materials with second-order phase transitions generally follow the relationship [106]:

$$-\Delta S_{\mathrm{M}}^{max} = -kM_{\mathrm{s}}(0)h^{2/3} - S(0,0), \tag{4.16}$$

where k is a constant, $M_{\mathrm{s}}(0)$ is the saturation magnetization and $S(0,0)$ is a reference parameter which cannot be equal to zero [106]. Fitting equation 4.16 to the $-\Delta S_{\mathrm{M}}^{max}$ data (solid line in figure 4.20b) yielded the following values: $S(0,0) = $ -0.5(3) J/kg.K and $kM_{\mathrm{s}}(0)$ = 2.3(1) J/kg.K. The sign of $S(0,0)$ is negative, which is expected for a second-order phase transition [119, 120]. Furthermore, the linear behaviour of $-\Delta S_{\mathrm{M}}^{max}$ vs. $h^{2/3}$ indicates strong localization of the magnetic moments [121].

In order to verify the value of the entropy change maximum (- $\Delta S_{\mathrm{M}}^{max}$) obtained from the isothermal magnetization, ($M(\mu_0 H,T)$), the evaluation of this quantity was performed by calculating the magnetic entropy change directly from a calorimetric measurement of the field dependence of heat capacity by the integration:

$$\Delta S_{\mathrm{M}}(T, \mu_0 H) = \int_0^T \frac{C_{\mathrm{M}}(T', \mu_0 H) - C_{\mathrm{M}}(T', 0)}{T'} dT', \tag{4.17}$$

where $C_{\mathrm{M}}(T, \mu_0 H)$ and $C_{\mathrm{M}}(T, 0)$ are the value of the magnetic contribution to the total heat capacity of Pr_2Pt_2In measured in field and 0 magnetic field respectively. As mentioned earlier, this magnetic contribution was obtained by subtracting the phonon contribution that was assumed to be the same as in the isostructural compound La_2Pt_2In (see section 4.4.2) to that of Pr_2Pt_2In. The results of $-\Delta S_{\mathrm{M}}^{max}$ obtained from heat capacity measured for a field change of 5 T are shown in figure 4.21. It is observed from figure 4.20a and 4.21 that the shape of $-\Delta S_{\mathrm{M}}^{max}$ estimated from $M(\mu_0 H,T)$ and $C_{\mathrm{M}}(T, \mu_0 H)$ are similar. Furthermore, $-\Delta S_{\mathrm{M}}(T)$ obtained from $C_{\mathrm{M}}(T, \mu_0 H)$, reaches a maximum value of 6.45 J/mole.K at 9 K for a field change of 5 T. This value corroborated with the value of 6.93 J/mole.K observed from $-\Delta S_{\mathrm{M}}(T)$ curve obtained from $M(\mu_0 H,T)$ for the same field

change of 5 T.
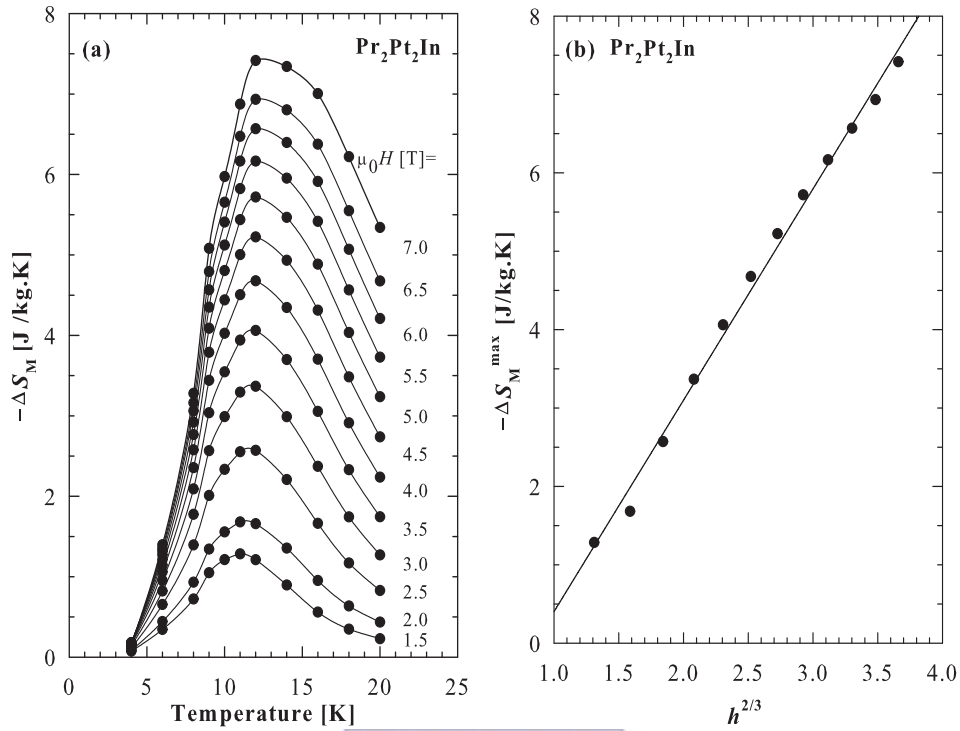
Figure 4.20: (a) Temperature dependencies of the isothermal magnetic entropy change, $-\Delta S_{\mathrm{M}}(T)$, in Pr_2Pt_2In measured with different field changes in steps of 0.5 T. (b) The maximum isothermal magnetic entropy change at T_{C} as a function of reduced field $h^{2/3}$ (see text for definition). The solid line is the least squares fit to the experimental data using equation 4.16.
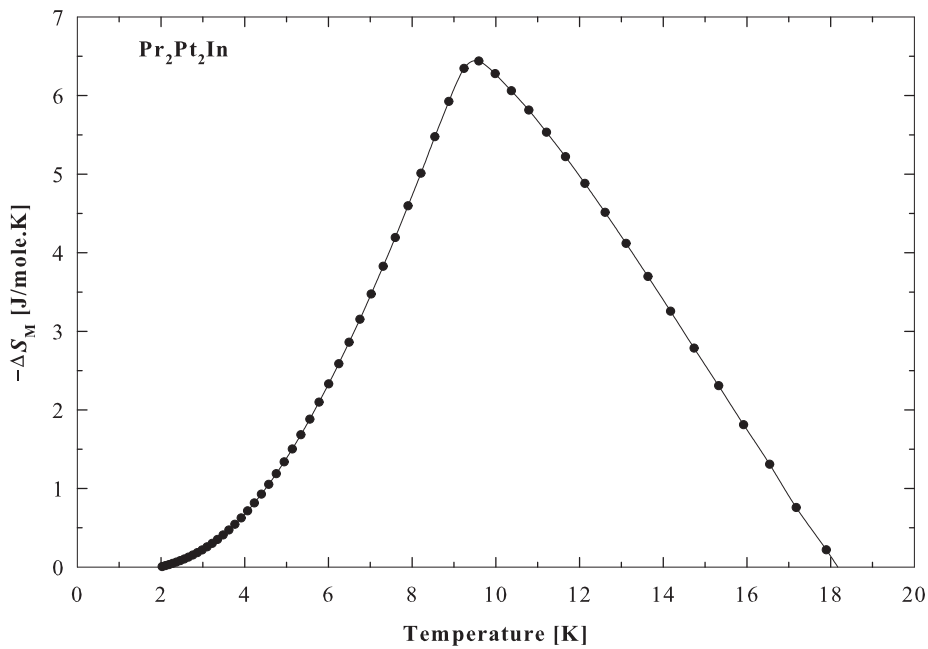
Figure 4.21: Temperature dependence of the magnetic entropy change at 5 T calculated from $C_{\mathrm{M}}(T, \mu_0 H)$.

90

4.4   Nd$_2$Pt$_2$In

4.4.1   Electrical resistivity

The temperature dependence of the electrical resistivity, $\rho(T)$ of the Nd$_2$Pt$_2$In is shown in figure 4.22a. The compound shows metallic conductivity at high temperatures with some bending of the $\rho(T)$ curves characteristic of s-d interband scattering and/or crystal-electric-field effect. This behaviour of $\rho(T)$ is similar to $\rho(T)$ of the homologue compound Pr$_2$Pt$_2$In (see section 4.3.1) and several other rare-earth intermetallic compounds such as La$_3$NiGe$_2$ [122]. General for the Nd-bearing compounds, the crystal-electric-field is predominant in the electrical resistivity [123, 124], and a simple analysis of the Bolch-Grüneissen-Mott relationship [107, 108] of equation 4.1 is not possible. The bottom inset of figure 4.22a displays an expanded view of the low-temperatures $\rho(T)$ data of Nd$_2$Pt$_2$In. $\rho(T)$ shows a sudden drop at $T_{\mathrm{C}} = 16$ K, signalling an onset of ferromagnetically ordered state, as confirmed by the $C_{\mathrm{p}}(T)$ and $\chi(T)$ results (see sections 4.4.2 and 4.4.3). Similar to the Pr$_2$Pt$_2$In compound, the observed decrease of the electrical resistivity with decreasing temperature in the magnetically ordered state in Nd$_2$Pt$_2$In, results from gradual reduction of scattering conduction electrons on magnetic moments. The magnetic phase transition in Nd$_2$Pt$_2$In manifest itself as a pronounced anomaly in the temperature derivative of the resistivity $\mathrm{d}\rho(T)/\mathrm{d}T$ (see figure 4.23). The value of T_C was estimated according to Sato criterion [109], which is at the midpoint of the anomaly in the $\mathrm{d}\rho(T)/\mathrm{d}T$ curve as indicated by the arrow in figure 4.23.

The low-temperatures $\rho(T)$ data of Nd$_2$Pt$_2$In measured in an external magnetic field of 0.5 T and 5 T are shown in figures 4.22b and 4.22c respectively. It is observed that the application of magnetic field shifts T_{C} to higher temperatures as expected for ferromagnet. Below T_{C}, $\rho(T)$ behaviour is governed by the scattering of conduction electrons on ferromagnetic spin-wave excitations with an energy gap (Δ_{R}) in the magnon spectrum and can be described by the equation 4.2. The values of the parameters resulting from the least squares fits of equation 4.2 to the experimental $\rho(T)$ data below T_{C} are listed in table 4.5. The fits of $\rho(T)$ data are shown by the solid red curves in figures 4.22b and 4.22c and also at the bottom inset of figure 4.22a.
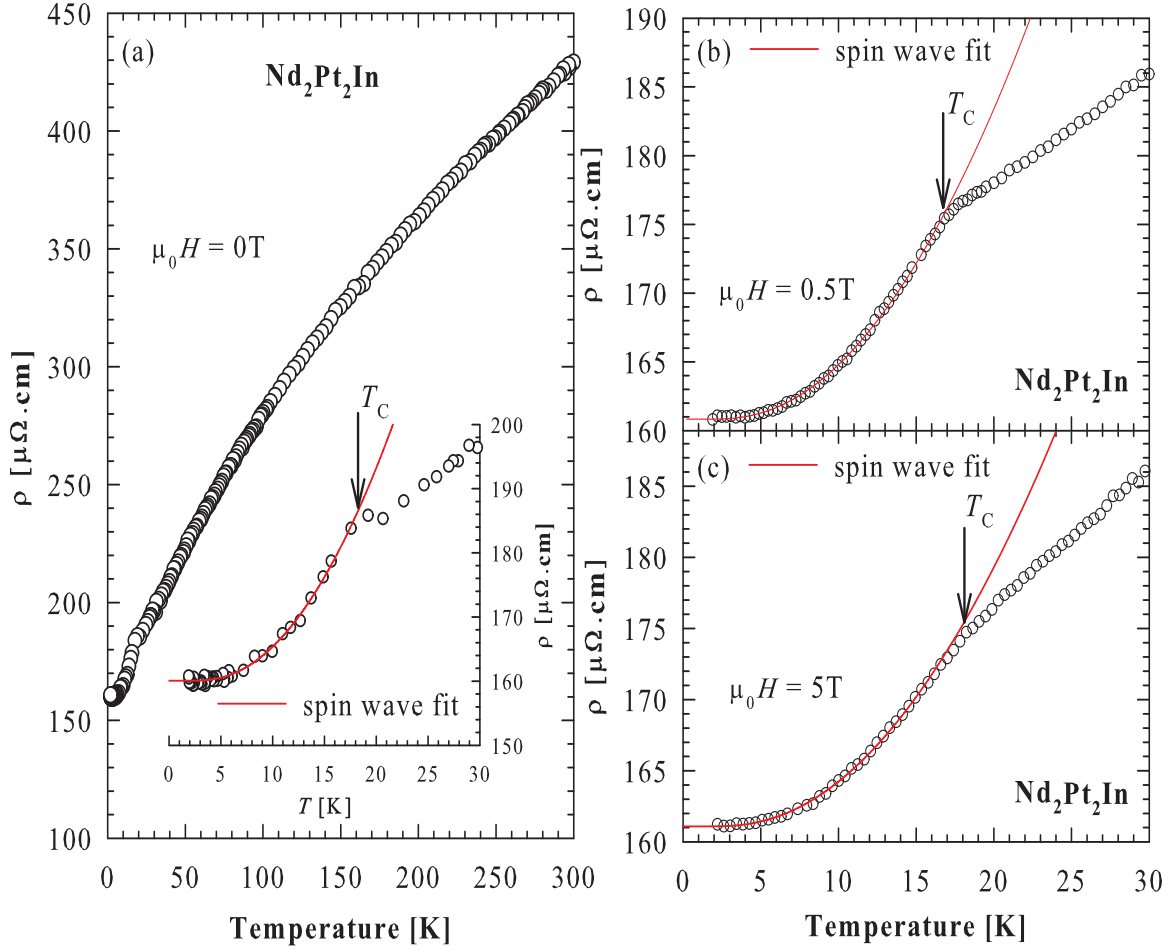
Figure 4.22: (a) Temperature variation of the electrical resistivity, $\rho(T)$ of Nd_2Pt_2In measured in 0 magnetic field. The inset displays the low-temperatures $\rho(T)$ data with the red solid curve representing the least squares fit of the spin-wave dispersion relation 4.2. The arrow indicates the position of T_C. (b) and (c) The low-temperatures $\rho(T)$ data measured in a magnetic field of 0.5 and 5 T, respectively the solid red curves are the least squares fits of the spin-wave dispersion relation 4.2 and the arrows indicate the position of T_C.

Table 4.5: Electrical resistivity parameters of Nd_2Pt_2In derived from the low-temperatures least squares fits of equation 4.2 to the measured data.

μ_0H [T]	ρ_0 [$\mu\Omega$.cm]	A [$\mu\Omega$cm/K^2]	Δ_R [K]
0	160.9(9)	0.06(2)	13(1)
0.5	160.83(5)	0.038(5)	10.9(6)
5	161.09(5)	0.031(4)	11.4(7)
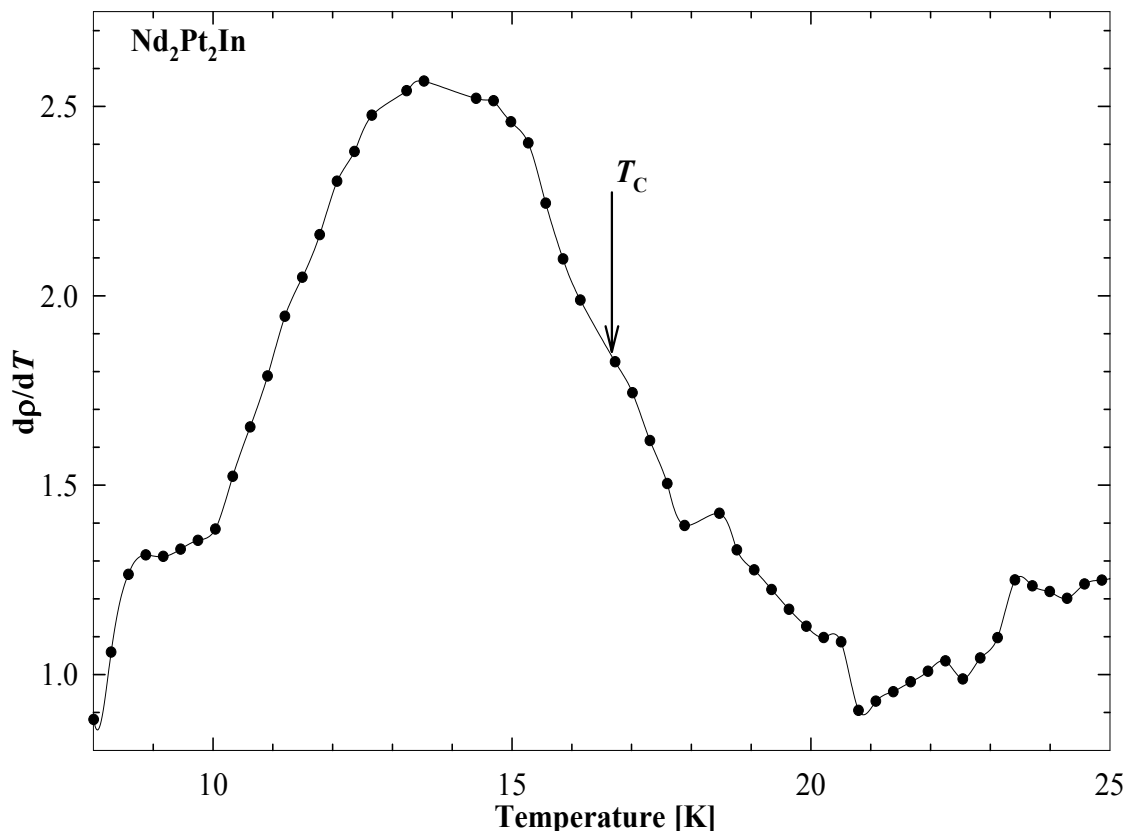
Figure 4.23: The temperature variation of the derivative of the electrical resistivity, $d\rho/dT$. The arrow indicates the position of the critical temperature T_C taken at the midpoint of the anomaly in $d\rho/dT$.

4.4.2 Heat capacity

The temperature dependencies of the specific heat, $C_p(T)$ of Nd_2Pt_2In and the non-magnetic reference compound La_2Pt_2In are displayed in figure 4.24 measured in the temperature range 1.8 K - 300 K in 0 magnetic field. For La_2Pt_2In compound, $C_p(T)$ varies monotonically with no anomaly down to 1.8 K, while for the magnetic Nd_2Pt_2In compound, $C_p(T)$ exhibits a λ-type anomaly at low-temperatures characteristic of the second-order magnetic phase transition, in line with the magnetocaloric effect analysis (see section 4.4.5). The sharp peak amounting to 35 J/mole.K on the $C_p(T)$ data is found at $T_C = 16$ K in agreement with the value observed in the $\rho(T)$ data. At room temperature, $C_p(T)$ data of La_2Pt_2In reach the value of Dulong-Petit, $3nR = 124.7$ J/mole.K ($n = 5$ is the number of atoms per formula unit, R stands for the gas constant), while $C_p(T)$ data of Nd_2Pt_2In attains this value around 170 K. In the whole temperature range measured, the $C_p(T)$ data

4.4.2 . Heat capacity

of La_2Pt_2In can be described by the Debye-Einstein model equation [125]:

$$C_p(T) = \gamma T + 9nR(1-d)\left(\frac{T}{\theta_D}\right)^3 \int_0^{\theta_D/T} \frac{x^4 e^x}{(e^x-1)^2}dx +$$
$$3nRd\left(\frac{\theta_E}{T}\right)^2 \frac{e^{\theta_E/T}}{(e^{\theta_E/T}-1)^2}, \tag{4.18}$$

where d is a number of Einstein modes, the first term represents the electronic contribution with γ being the Sommerfeld coefficient and the second and third terms are the standard Debye and Einstein expressions for the phonon contribution with θ_D and θ_E being the Debye and Einstein temperatures, respectively. The least squares fit of equation 4.18 to the experimental data (note the blue solid line in figure 4.24) yielded the following parameters: $\gamma = 0.0092(1)$ J/(mole.K^2), $\theta_D = 190.3(5)$ K, $\theta_E = 69.8$ (7) K and $d = 0.2$. The value of θ_D obtained for this compound is similar to those reported for the other members of the RE_2Pt_2In series [92, 126]. On the other hand, the least squares fit on $C_p(T)$ data of Nd_2Pt_2In using the Debye equation 4.3 yielded the following parameters: $\theta_D = 152.44(2)$ K; $\gamma = 1.197(1)$ J/(mole.K^2). The value of θ_D obtained for this compound is very close to the value of $155.0(2)$ K obtained for Pr_2Pt_2In. The similarity of θ_D suggests the same lattice vibration in both compounds as a result of the same order of magnitude of their atomic masses.

The inset (a) of figure 4.24 displays the plot of C_p/T^3 *v*s. T for La_2Pt_2In which exhibits a local maximum near T_{max} of about 14 K. This maximum indicates the presence of an Einstein contribution in the $C_p(T)$ data of La_2Pt_2In. From the relation $\theta_E \approx 5T_{max}$, one can estimate the value of θ_E to be about 70 K, which is in good agreement with the analysis in terms of equation 4.18.

The low-temperatures $C_p(T)$ data of Nd_2Pt_2In measured in 0 magnetic field and 2 and 3 T, are displayed in the inset (b) of figure 4.24. Typical for ferromagnets, the specific heat peak marking the onset of the ordered state shifts to higher temperatures with increasing the magnetic field strength. In 3 T, the peak vanishes, similar with the behaviour of $\rho(T)$ measured in field above 5 T (see section 4.4.1).

Figures 4.25a and 4.25b display the magnetic $4f$-electron contribution to the total specific $C_{4f}(T)$ of Nd_2Pt_2In measured in 0 and 2 T, obtained by subtracting the phonon contribution that was assumed to be the same as in the isostructural compound La_2Pt_2In. No mass correction was done in this process since the atomic mass of La and Nd are almost

close relatives of each other. Similar to Pr_2Pt_2In compound, as shown in the figures, below T_C, the $C_{4f}(T)$ data of Nd_2Pt_2In can be approximated using equation 4.4, that represents a sum of the electronic term and the ferromagnetic magnon contribution with energy gap Δ_C in the spin-wave spectrum (B is a constant associated with the stiffness of the sample). The parameters obtained by least squares fitting (solid red curves) in figure 4.25a and 4.25b are listed in table 4.6. The values of Δ_C are smaller than T_C and roughly half the values of Δ_R obtained from the low temperatures $\rho(T)$ data.
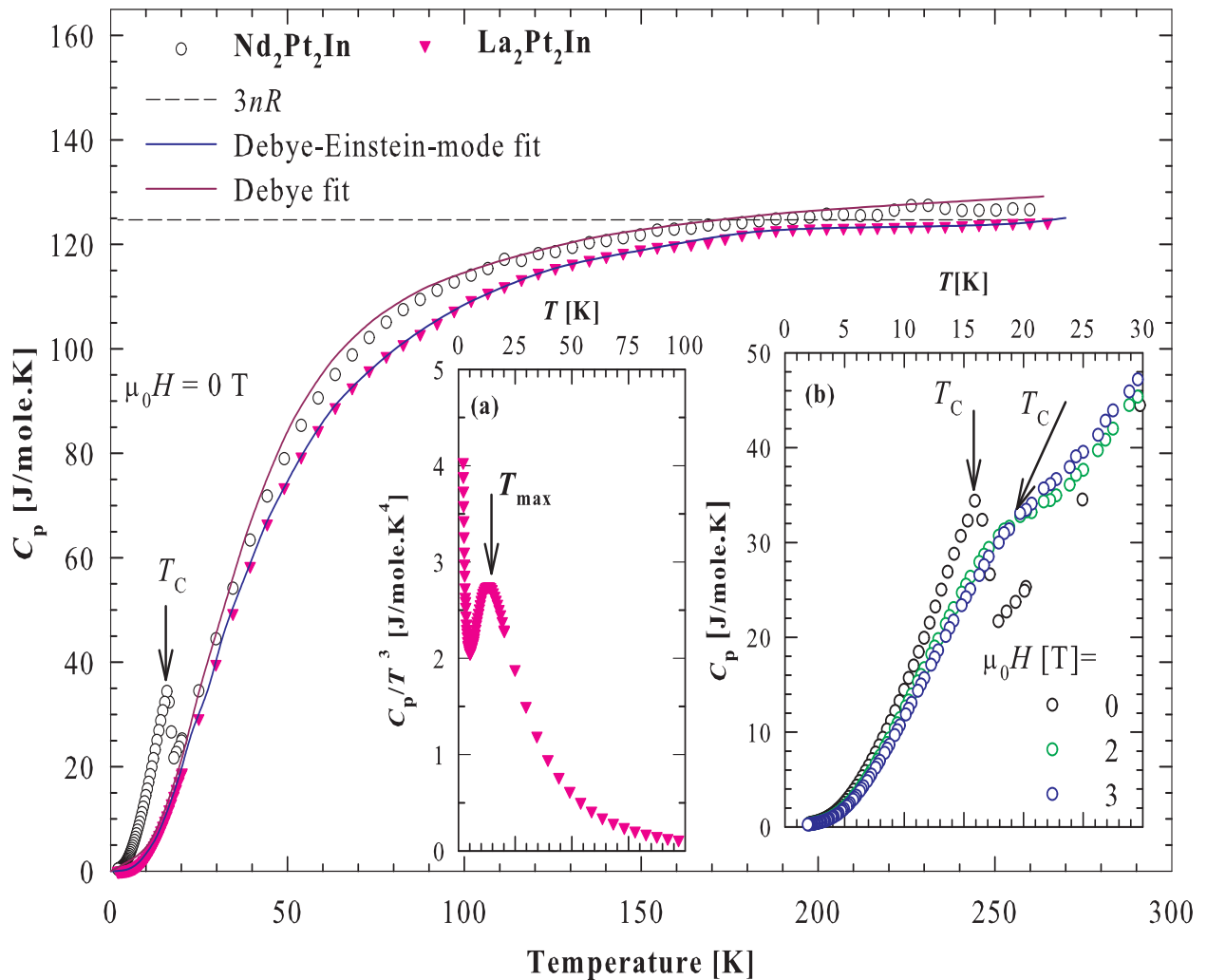
Figure 4.24: (main panel) Temperature variations of the heat capacity, $C_p(T)$ of Nd_2Pt_2In and La_2Pt_2In measured in 0 magnetic field. The solid blue curve is the least squares fit of the Debye-Einstein model (equation 4.18) and the dark brown curve is the least squares fit of the standard Debye formula (equation 4.3) to the experimental data. The arrow in the main panel indicates the position of T_C. The inset (a) shows the specific heat data of La_2Pt_2In plotted as C_p/T^3 vs. T with the arrow indicating the position of a local maximum that provides an estimation of the Einstein temperature. The inset (b) shows an expanded view of the low-temperatures $C_p(T)$ data. The arrows indicate the position of T_C of Nd_2Pt_2In taken in 0 magnetic field and applied magnetic field of 2 and 3 T.

4.4.2 . Heat capacity

In a tetragonal symmetry, the crystal-electric-field will split the tenfold degenerate ground-state multiplet $^4I_{9/2}$ of the Nd^{3+} ion into three doublets with the two higher doublets at energy separation Δ_1 and Δ_2 from the ground state ($\Delta_0 = 0$ K). It is observed from figure 4.25a that $C_{4f}(T)$ exhibits a broad maximum centered around 60 K, characteristic of a Schottky-type anomaly. This thermal dependence of the Schottky-type anomaly ascribed to a crystal-electric-field can be described by the standard formula for Schottky heat capacity which is given by:

$$
C_{Sch}(T) = R \left[g_0 g_1 \left(\frac{\Delta_1}{T} \right)^2 e^{-\frac{\Delta_1}{T}} + g_0 g_2 \left(\frac{\Delta_2}{T} \right)^2 e^{-\frac{\Delta_2}{T}} + g_1 g_2 \left(\frac{\Delta_1 - \Delta_2}{T} \right)^2 e^{-\frac{\Delta_1 + \Delta_2}{T}} \right]
$$

$$
\times \left[\frac{1}{g_0 + g_1 e^{-\frac{\Delta_1}{T}} + g_2 e^{-\frac{\Delta_2}{T}}} \right]^2 , \tag{4.19}
$$

where R is the constant gas, Δ_1 and Δ_2 are the splitting energy level between the ground state and the first excited state and between the ground state and the second excited state. The constants, g_0, g_1 and g_2 represent the degeneracies of the ground state, first excited state and the second excited states, respectively. The analysis of the Schottky peak in $C_{4f}(T)$ in the paramagnetic region based on equation 4.19 displayed in figure 4.25a (green solid curve) using degeneracy $g_0 = g_1 = g_2 = 2$. The calculated energy separation are $\Delta_1 = 145(7)$ K for the first excited state and $\Delta_2 = 195(13)$ K for the second excited state. The corresponding $4f$-electron magnetic entropy $S_{4f}(T)$ was calculated by integrating $C_{4f}(T)/T$. The plots of $S_{4f}(T)$ for Nd_2Pt_2In compound are shown in figure 4.26 for both 0 and 2 T. The entropy attains the value of Rln2 appropriate for a well isolated doublet, at temperature around 10 K for 0 T and 12 K for 2 T which are fairly close to T_C.
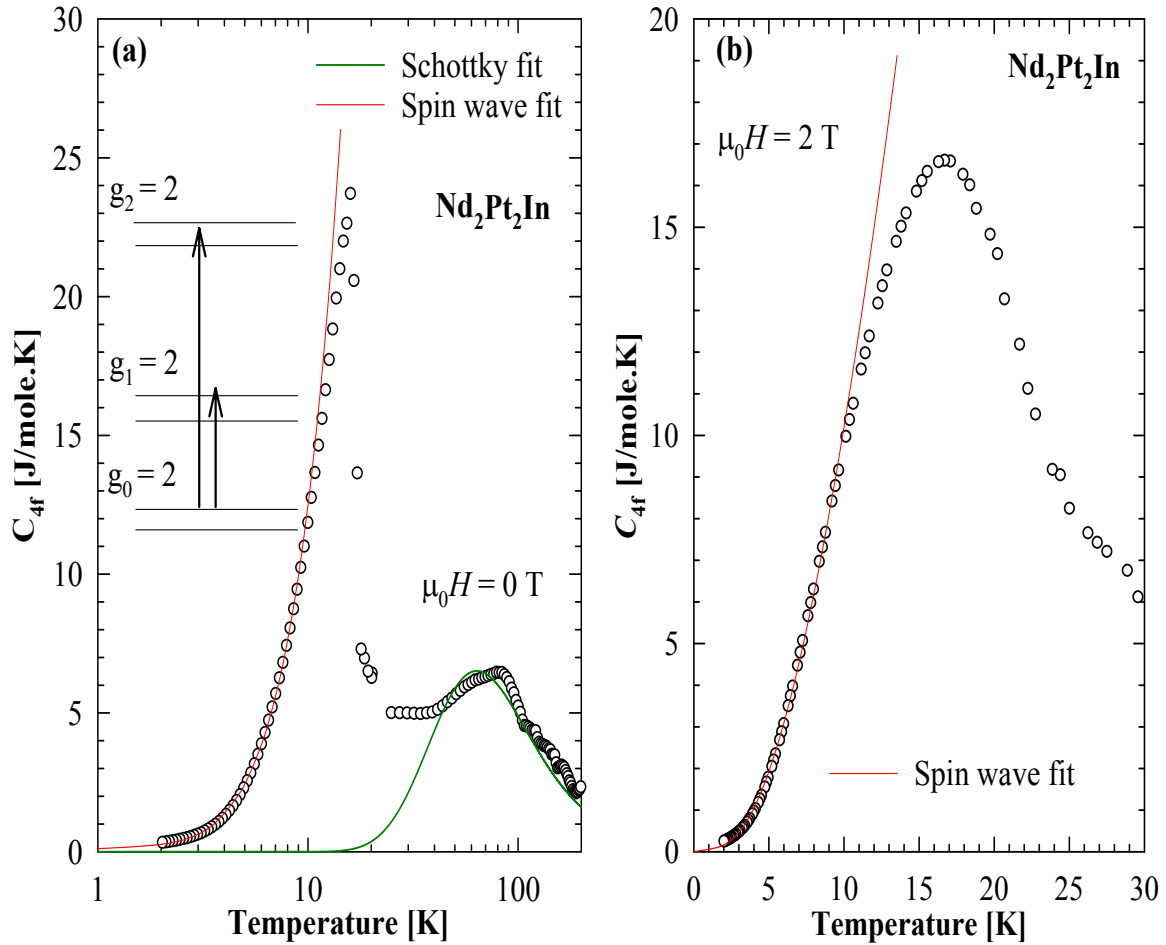
Figure 4.25: (a) The temperature variations of the $4f$-electron contribution to the total heat capacity, $C_{4f}(T)$ of Nd$_2$Pt$_2$In measured in (a) 0 magnetic field and (b) 2 T. The solid red curves are least squares fits of the spin-wave dispersion relation (equation 4.4) to the $C_{4f}(T)$ data. The solid dark green curve in (a) is the least square fit of the Schottky anomaly (equation 4.19) to the $C_{4f}(T)$ data with energy scheme as inset.

Table 4.6: Heat capacity data of Nd$_2$Pt$_2$In obtained from the low-temperatures least square fits of equation 4.4 to the measured data.

μ_0H [T]	γ [J/mole.K^2]	B [J/mole.K$^{5/2}$]	Δ_C[K]
0	0.055(6)	0.39(1)	7.6(3)
2	0.030(5)	0.32(1)	7.3(4)

97
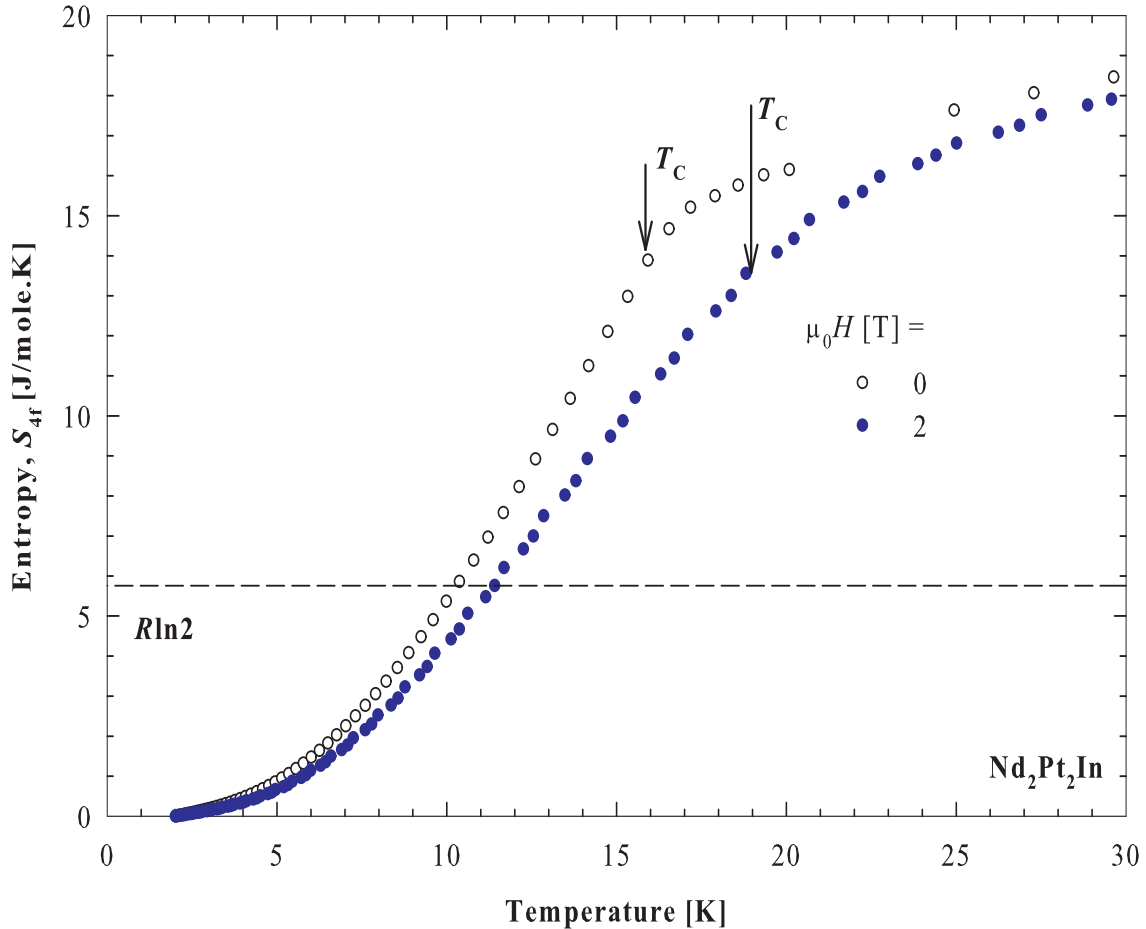
Figure 4.26: The temperature variations of $4f$-electron magnetic entropy S_{4f} of Nd_2Pt_2In measured in 0 magnetic field (black symbols) and in 2 T (blue symbols). The horizontal dash line marks the value of $R\ln2 = 5.76$ J/mole.K expected for the double ground state.

4.4.3 Magnetic susceptibility and magnetization

The temperature variation of the inverse magnetic susceptibility, $\chi^{-1}(T)$ measured in an applied field of 0.1 T in the temperature range 1.7 K - 400 K for the Nd_2Pt_2In compound is shown in figure 4.27. It is observed that $\chi^{-1}(T)$ data follow the Curie-Weiss law (equation 4.6) above 100 K. The least squares fit of the Curie-Weiss relation yielded the effective moment $\mu_{\text{eff}} = 3.61(2)$ μ_B/Nd and the Weiss temperature constant $\theta_p = 17(1)$ K. The observed μ_{eff} value is very close to that expected for the free Nd^{3+}-ion $\left[g_J \left(J(J+1)\right)^{1/2} = 3.62 \ \mu_B\right]$, indicating that only the localized $4f$ shells are contributing towards the magnetic properties. The positive value of θ_p signifies the presence of ferromagnetic exchange interactions in the compound. Deviation from the Curie-Weiss law at lower temperatures can be attributed to magnetic ordered and/or crystal-electric-

98

4.4.3 . Magnetic susceptibility and magnetization

field effects.
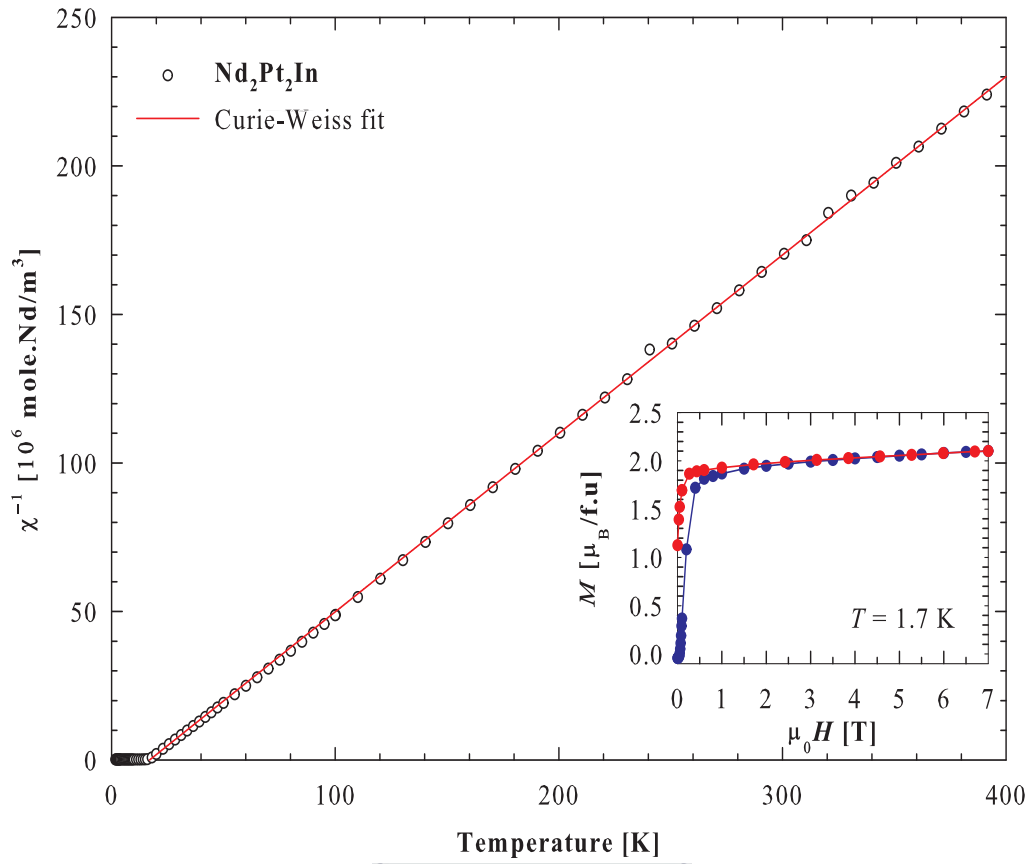
Figure 4.27: Temperature variation of the inverse magnetic susceptibility, $\chi^{-1}(T)$ of Nd_2Pt_2In measured in a magnetic field of 0.1 T in the temperature range 1.7 K - 400 K. The solid red line is the Curie-Weiss fit using equation 4.6 to the experimental data above 100 K. The inset displays the magnetic field variation of the magnetization, $M(\mu_0H)$, in Nd_2Pt_2In, measured at 1.7 K in increasing (blue symbols) and decreasing (red symbols) magnetic field.

The magnetic field dependence of the magnetization, $M(\mu_0H)$, measured for Nd_2Pt_2In at 1.7 K, is showing in the inset of figure 4.27. The shape of $M(\mu_0H)$ is typical for ferromagnetic materials. In a field stronger than 0.5 T, $M(\mu_0H)$ saturates at a value $M_s = 2.12$ μ_B/Nd-ion, which is smaller than the theoretical value for trivalent Nd ($g_JJ = 2.72$ μ_B), likely due to a combined effect of crystal-electric-field and magnetic anisotropy.

Figure 4.28a displays the low-temperatures magnetic susceptibility $\chi(T)$ data. $\chi(T)$ exhibits a behaviour characteristic of a ferromagnet but deviates from saturation below 5 K. The phase transition temperature was estimated at the midpoint of the abrupt rise in the $\chi(T)$ curve that corresponds to the minimum in the $d\chi(T)/dT$ curve at $T_C = 17$ K. Below T_C, $\chi(T)$ data shows a broad maximum around 5 K which could be attributed to spin reorientation at the temperature of the second magnetic transition at T_t or to another magnetic phase to an antiferromagnetic order below T_t. This second magnetic

phase transition is accurately obtained from $\mathrm{d}\chi/\mathrm{d}T$ curve taken at the maximum at $T_\mathrm{t} = 2.7$ K. A similar behaviour of the low-temperatures $\chi(T)$ data was observed in $\mathrm{Ho_2Au_2In}$ below $T_\mathrm{C} = 20(1)$ K [127]. This observation was ascribed to a spin reorientation at the second magnetic transition temperature of 7.0(5) K [127]. More recently, Giovannini *et al.* [128] investigated the effect of nonstoichiometry on the transition from ferromagnetism to antiferromagnetism in the ternary indides $\mathrm{Ce_{1.95}Pd_{+2x}In_{1-x}}$ and $\mathrm{Ce_{2+x}Pd_{1.85}In_{1-x}}$. They reported that the ternary indides crystallize in the parent $\mathrm{Mo_2FeIn_2}$ structure with space group P/mbm and form two branches of solid solutions due to different substitutional mechanisms which have a strong influence on the magnetic properties. Their observations indicate that in the Pd-rich branch, indium vacancies at the $2a$ site are compensated by an excess of Pd located at an additional $4e$. This excess of Pd favours antiferromagnetism. On the other hand, in the Ce-rich branch, the excess of Ce replaces indium atoms at the $2a$ sites and the excess of Ce induces ferromagnetism [128]. It is likely that our sample forms two branches of solid solutions. One branch with excess of Pt which favors antiferromagnetism and the branch with excess of Ce which induces ferromagnetism. Such observation was also present in $\mathrm{Ho_2Au_2In}$ compound [127] but was not present in the study of $\mathrm{Pr_2Pt_2In}$ compound discussed in section 4.3.3.
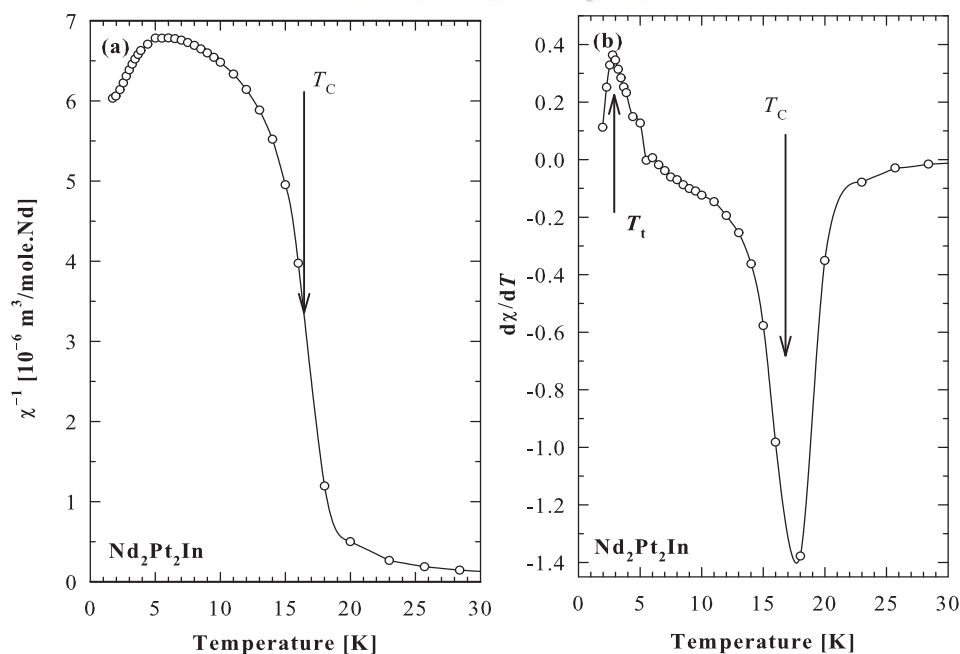
Figure 4.28: (a) The low-temperatures $\chi(T)$ data of $\mathrm{Nd_2Pt_2In}$ in the ferromagnetic region, measured in field of 0.1 T. The arrow indicates the ferromagnetic transition temperature T_C taken at the midpoint of the abrupt rise in the $\chi(T)$ curve. (b) $\mathrm{d}\chi(T)/\mathrm{d}T$ curve with the arrows indicating the positions of T_C and T_t taken at the minimum and maximum of $\mathrm{d}\chi(T)/\mathrm{d}T$ curve respectively.

100

4.4.4 Critical behaviour study around the ferromagnetic phase transition in Nd_2Pt_2In

4.4.4.1 Arrott-plots

Figure 4.29 presents the standard Arrott-plots for the mean-field theory model of Nd_2Pt_2In, M^2 $vs.$ μ_0H/M for the magnetization isotherms taken in temperature range 6 K - 24 K in the step of 0.5 K. Similar to Pr_2Pt_2In, it is observed that all isotherms deviate from linearity at high field, which also indicate that no long-range transitions are responsible for ferromagnetic transition and the mean-field description of the exchange interactions are not present in Nd_2Pt_2In. Following the Banerjee's criterion [110], the positive slope of the curves confirm the second order nature of the transition.

The most effective method of determining the critical temperature, and also the critical exponents is that of the modified Arrott-plots. The same approach used for Pr_2Pt_2In was used to determine the universality class of the Nd_2Pt_2In. In this process, both critical exponents of the 3D-Ising and 3D-Heisenberg models was used. In both cases, there is an apparent linearity and furthermore, the deviation of the slopes with respect to the average value goes from -2.5% to 1.3% for the 3D-Ising model and -2.2% to 1.5% for the 3D-Heisenberg model. This range of deviation for both models are closely similar, suggesting that the ferromagnetic behaviour of Nd_2Pt_2In is between the 3D-Ising and the 3D-Heisenberg models. Thus, both the Ising and Heisenberg exponents have been used separately as a starting point from which an iterative process has been carried out as described previously (see section 4.3.4). The results of this approach are shown in figures 4.30a and 4.30b for 3D-Heisenberg and 3D-Ising models respectively. Following the theory of ferromagnetism and similar to Pr_2Pt_2In, it is observed from figures 4.30a and 4.30b that in weak magnetic fields the data shows a downward curvature as they are averaged over domains which are magnetized in different directions [113].
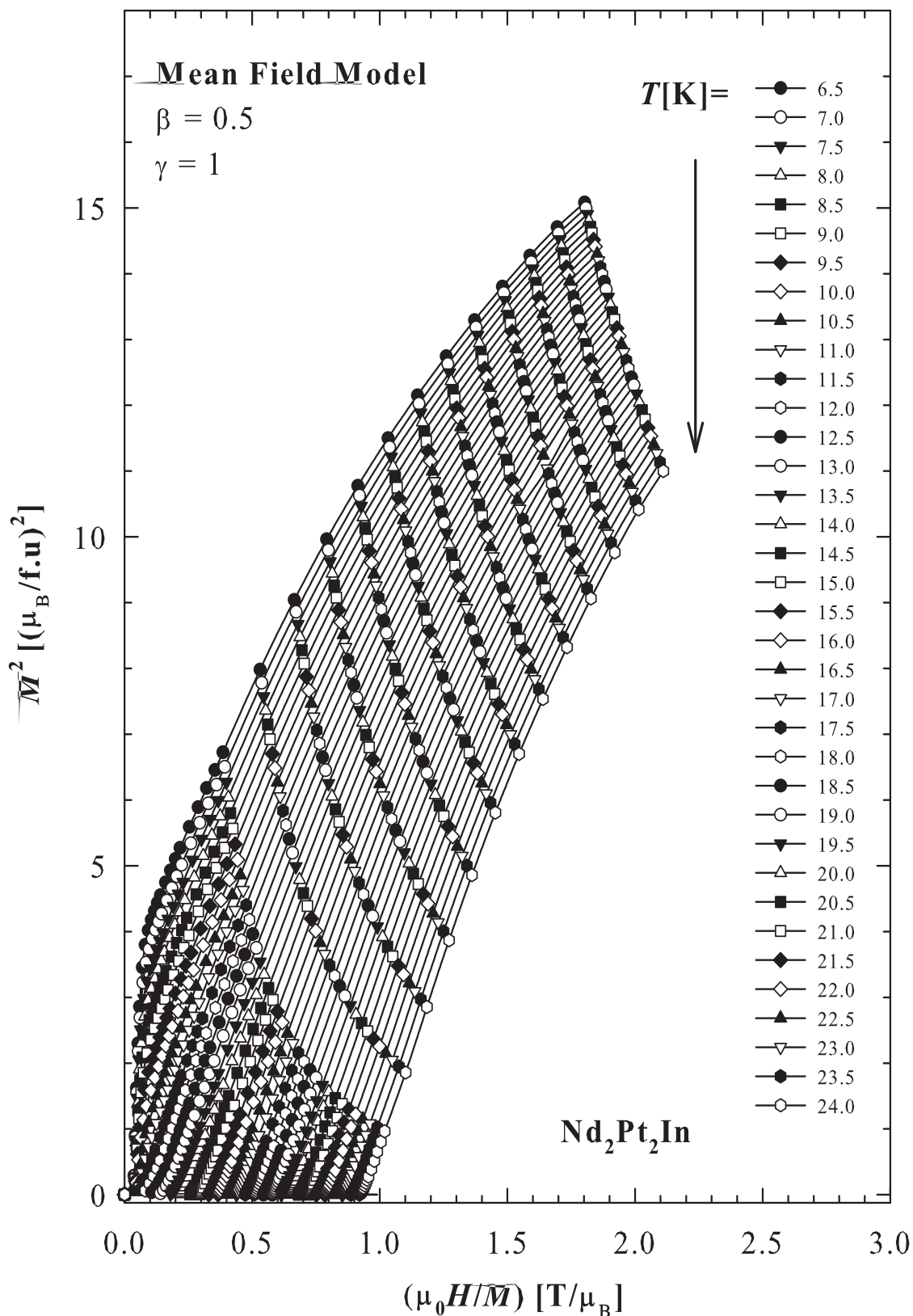
Figure . 4.29: The standard Arrott-plots for the mean-field model M^2 *vs.* $\mu_0 H/M$ of isotherms collected around T_C for Nd$_2$Pt$_2$In.

4.4.4 . Critical behaviour study around the ferromagnetic phase transition in $\mathbf{Nd_2Pt_2In}$
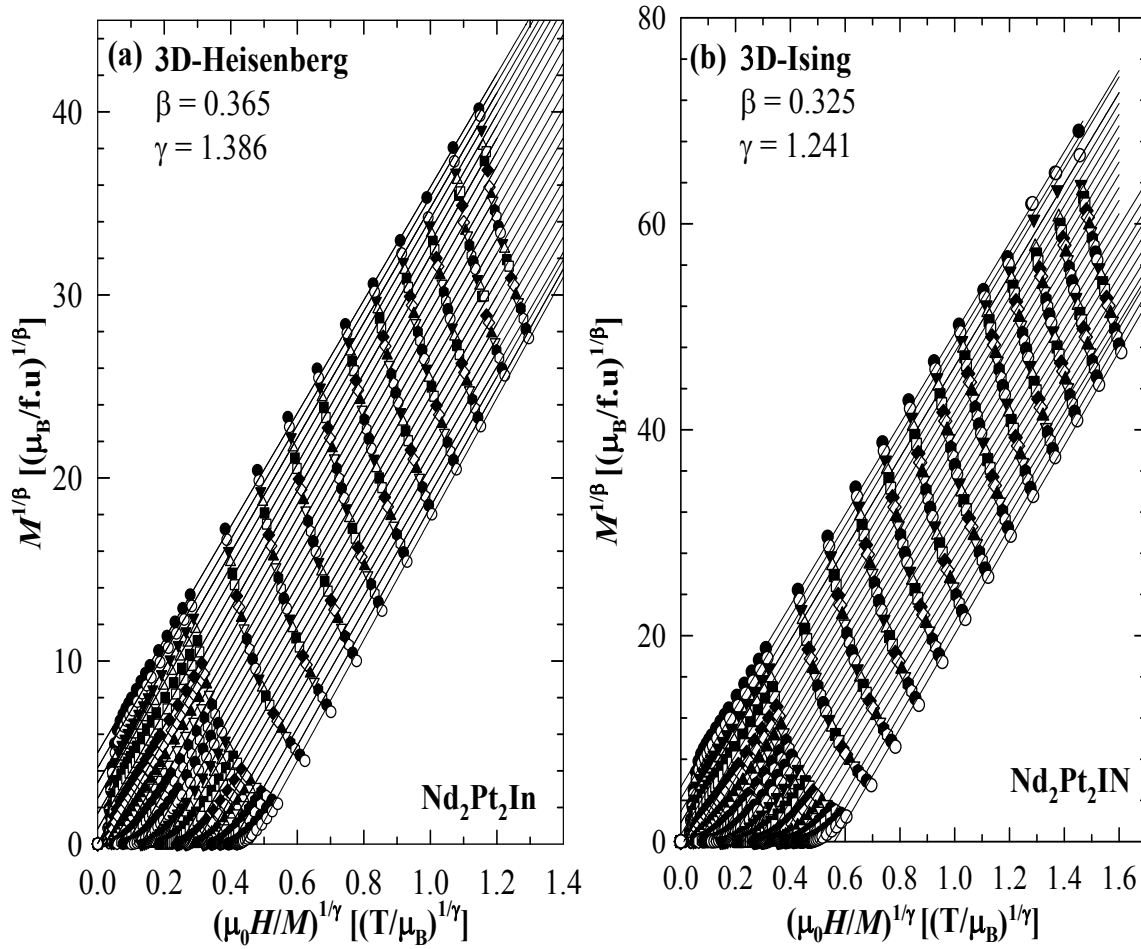
Figure 4.30: Modified Arrott-plots using the critical exponent of the (a) 3D-Heisenberg and (b) 3D-Ising model. The solid black lines are the linear fits using equations 4.7.

In the next step, an iterative process was used as described earlier (see section 4.3.4). A linear extrapolation of the isotherms at high fields in figures 4.30a and 4.30b gave $(M_s)^{1/\beta}$ and $(\chi_0^{-1})^{1/\gamma}$ as intercepts on the $(M)^{1/\beta}$ and $(\mu_0 H/M)^{1/\gamma}$ axes respectively for both models. These values of $(M_s)^{1/\beta}$ and $(\chi_0^{-1})^{1/\gamma}$ are plotted in figures 4.31a and 4.31b and independently fitted to equations 4.8 and 4.9 respectively to give new values of β and γ. These values are again used to construct the modified Arrott-plots similar to figures 4.30a and 4.30b. The process is repeated until convergence is reached and the stable values of β and γ with the best parallelism are obtained. The final values of the critical exponents were: $\beta = 0.366(3)$ and $\gamma = 1.48(2)$ and $\beta = 0.33(1)$ and $\gamma = 1.22(9)$ for the 3D-Heisenberg and the 3D-Ising models respectively. Remarkably, these values are close to both theoretical values of the 3D-Heisenberg and 3D-Ising models.

4.4.4 . Critical behaviour study around the ferromagnetic phase transition in Nd$_2$Pt$_2$In
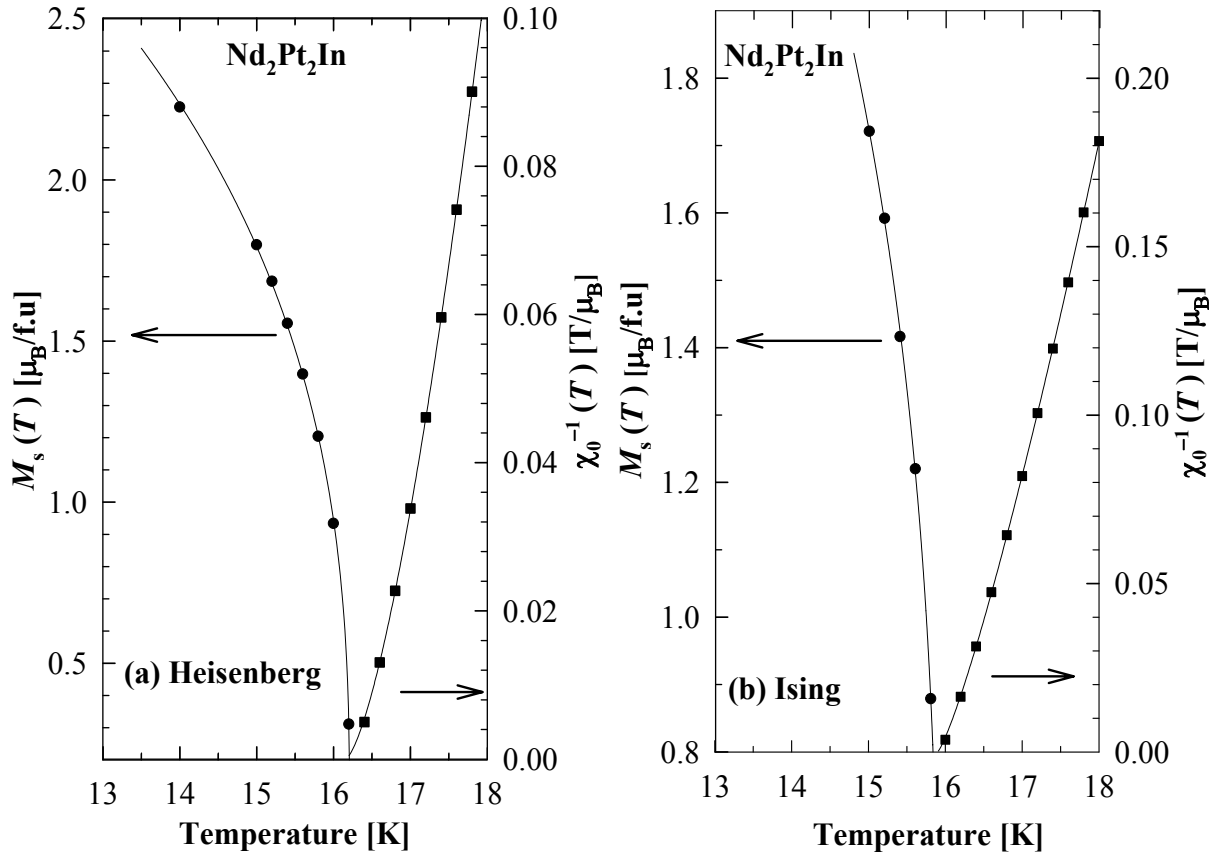
Figure 4.31: Temperature variations of the spontaneous magnetization, $M_s(T)$ (left axis) and the reciprocal initial susceptibility, $\chi_0^{-1}(T)$ (right axis) derived from the modified Arrott-plots, for the (a) 3D-Heisenberg and (b) 3D-Ising models. The solid curves are least squares fits using equations 4.8 and 4.9.

4.4.4.2 Kouvel-Fisher method

The next step in the scaling analysis is the use of the Kouvel-Fisher method to obtain more accurately the critical exponents and the critical temperature [115, 116]. The values of $M_s(T)$ and $\chi_0(T)$ obtained from the modified Arrott-plots are used to fit the Kouvel-Fisher equations 4.10 and 4.11 [115, 116]. $M_s(dM_s/dT)^{-1}$ and $\chi_0^{-1}(d\chi_0^{-1}/dT)^{-1}$ have a linear behaviour with respect to temperature with slopes $1/\beta$ and $1/\gamma$, respectively. One of the advantages of this method is that no prior knowledge of T_C is required as the intercept of such fitted straight lines on temperatures axis gives the value of T_C. The Kouvel-Fisher plot is shown in figures 4.32a and 4.32b for the 3D-Heisenberg and 3D-Ising model, respectively. The straight lines fitting yielded the estimated critical exponents and temperature values of $\beta = 0.350(3)$, $T_C = 16.2$ K, $\gamma = 1.48(2)$ and $T_C = 16.1(2)$ K for the 3D-Heisenberg model and $\beta = 0.33(1)$, $T_C = 16.0$ (6) K, $\gamma = 1.24(1)$ and $T_C = 15.9(3)$ K for the 3D-Ising model respectively. From these results, it has been reasonably found that

4.4.4 . Critical behaviour study around the ferromagnetic phase transition in Nd_2Pt_2In

both methods (Arrott-plots and Kouvel-Fisher-plots) agreed with each order.
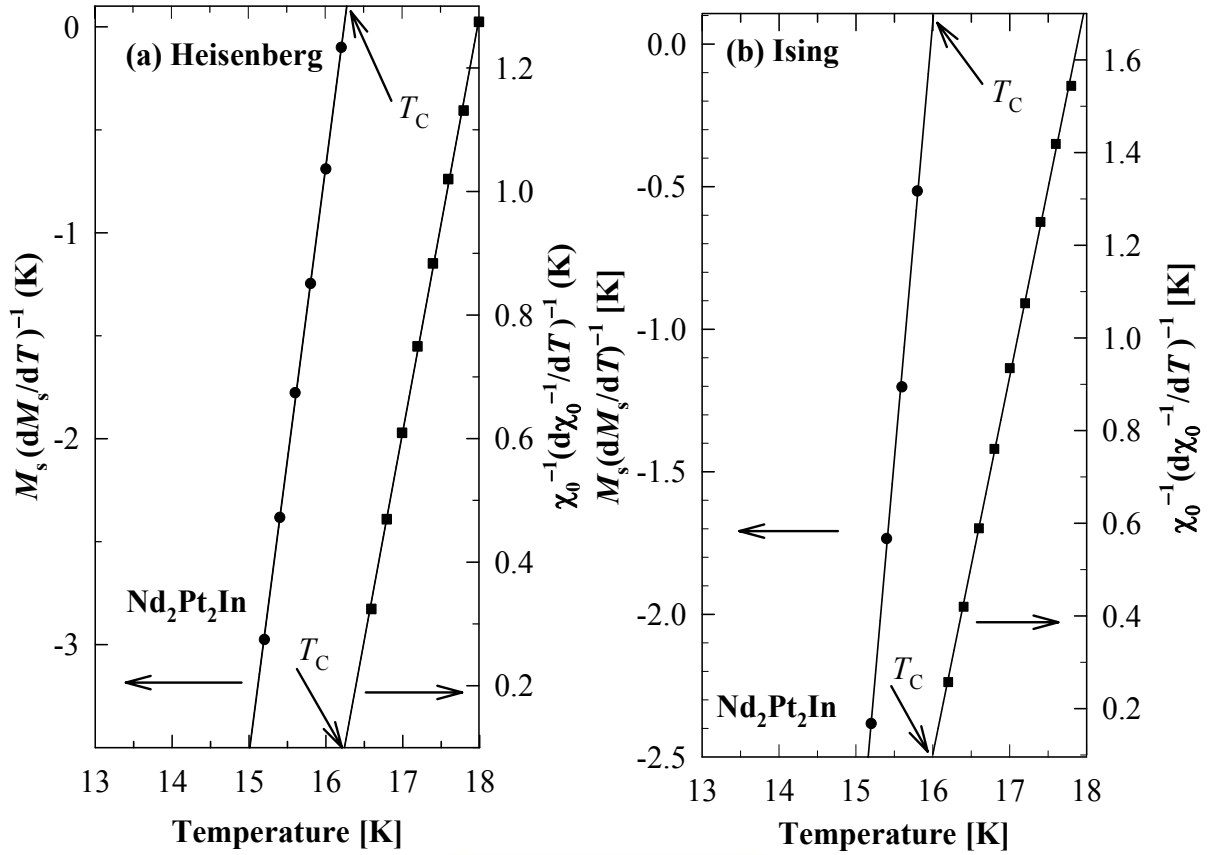
Figure 4.32: Kouvel-Fisher plots of spontaneous magnetization $M_s(T)$ (left axis) and the inverse initial susceptibility $\chi_0^{-1}(T)$ (right axis) for Nd_2Pt_2In. The straight lines least squares fits of the data points to equations 4.10 and 4.11 for both the (a) 3D-Heisenberg and (b) 3D-Ising models.

4.4.4.3   Critical isotherm analysis and scaling law

Similar to Pr_2Pt_2In, the critical exponent δ for the Nd_2Pt_2In can be obtained directly from the critical isotherm given by equation 4.12. Figures 4.33a and 4.33b display the magnetic field dependence of the magnetization in Nd_2Pt_2In measured at $T_C = 16.2$ K for the 3D-Heisenberg and at $T_C = 15.9$ K for the 3D-Ising models. The slope of $M(\mu_0 H, T_C)$ in both models confirmed the ferromagnetic nature of Nd_2Pt_2In. As evident from the insets of these figures, the plots $\log(M)$ $vs.$ $\log(\mu_0 H)$ are straight lines with the slopes being equal to $1/\delta$. The straight lines fitting give $\delta = 4.90(9)$ and $4.00(2)$ for the 3D-Heisenberg and 3D-Ising models, respectively. Using the Widom scaling relationship relating the critical exponents β and γ (equation 4.13), δ can also be calculated. Taking the values of β and γ obtained from the modified Arrott-plots, one obtained $\delta = 5.04(9)$ and from the Kouvel-Fisher plots, one obtained $\delta = 5.23(9)$ for the 3D-Heisenberg model. Using the critical

4.4.4 . Critical behaviour study around the ferromagnetic phase transition in Nd_2Pt_2In

exponent of the 3D-Ising model, one obtained for the modified Arrott-plots $\delta = 4.7(1)$ and 4.8(1) for the Kouvel-Fisher plots. All these values match reasonably well, which proves internal consistency of all the analysis performed. Comparison of these values to the theoretical value of the 3D-Heisenberg and 3D-Ising models, one can easily conclude that the obtained critical exponents from various techniques are in between those theoretically predicted for 3D-Heisenberg and 3D-Ising models.
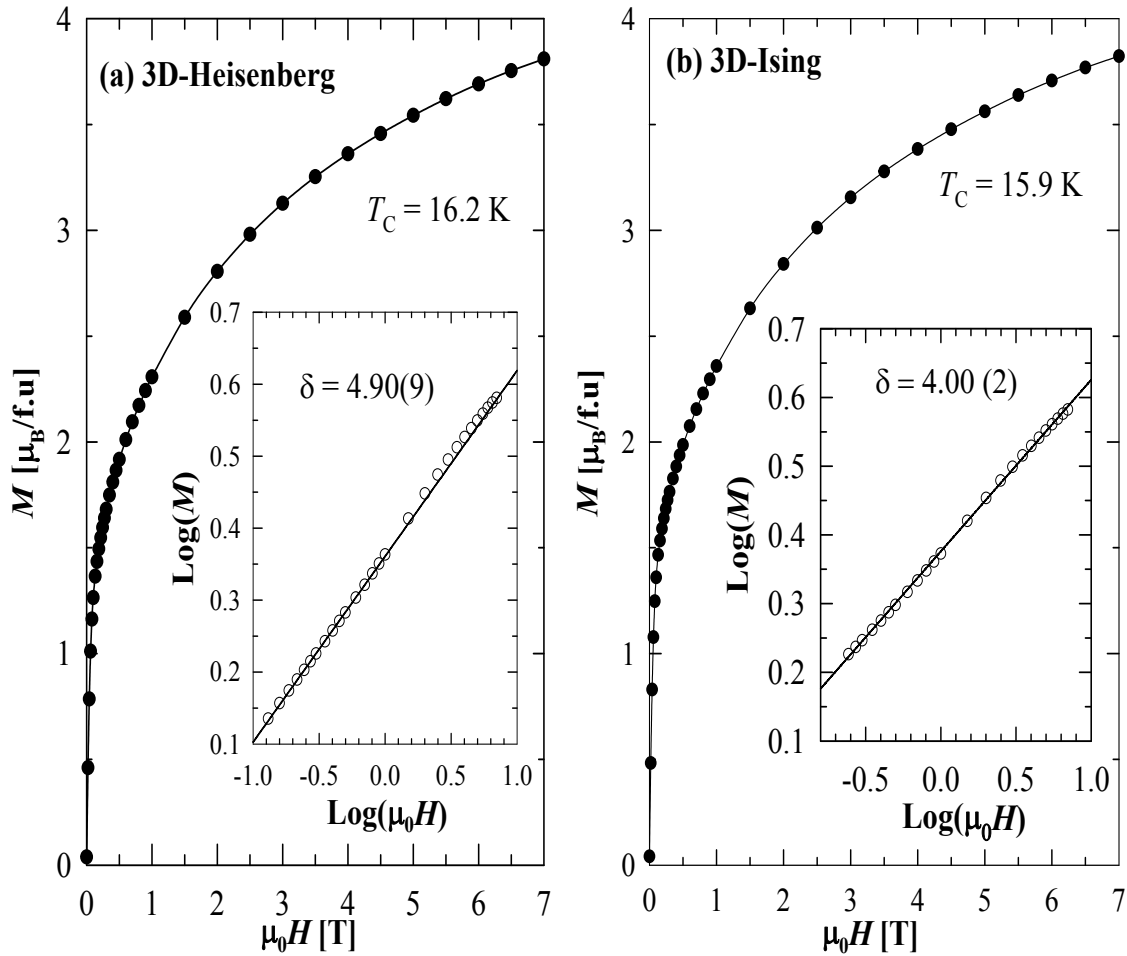
Figure 4.33: Field variation of the critical isotherm, (a) $M(\mu_0 H, T_C = 16.2$ K) and $M(\mu_0 H, T_C = 15.9$ K) for Nd_2Pt_2In. The insets show the data with log-log representation. The straight lines are the fits using equation 4.12.

Finally, it is useful to investigate the validity of the results by checking if the critical exponents can reproduce the equation of states given by equation 4.14. As can be observed from figures 4.34a and 4.34b using the critical exponents β, γ and the critical temperature T_C derived within the different methods applied for the (a) 3D-Heisenberg and (b) 3D-Ising models, one obtains a collapse of the data representing the regions below and above T_C into two distinct curves, in line with the expected scaling behaviour. The insets of these

4.4.4 . Critical behaviour study around the ferromagnetic phase transition in $\mathbf{Nd_2Pt_2In}$

figures show the same plots on a log-log scale to furthermore illustrate the collapse of the data into two different branches, below and above T_C. The critical exponents obtained in this work for Nd_2Pt_2In are gathered in table 4.7 for the 3D-Heisenberg model and 4.8 for the 3D-Ising model. It is clear that the value found for this compound does not match with the conventional mean-field theory and are between the isotropic 3D-Heisenberg and the 3D-Ising models.
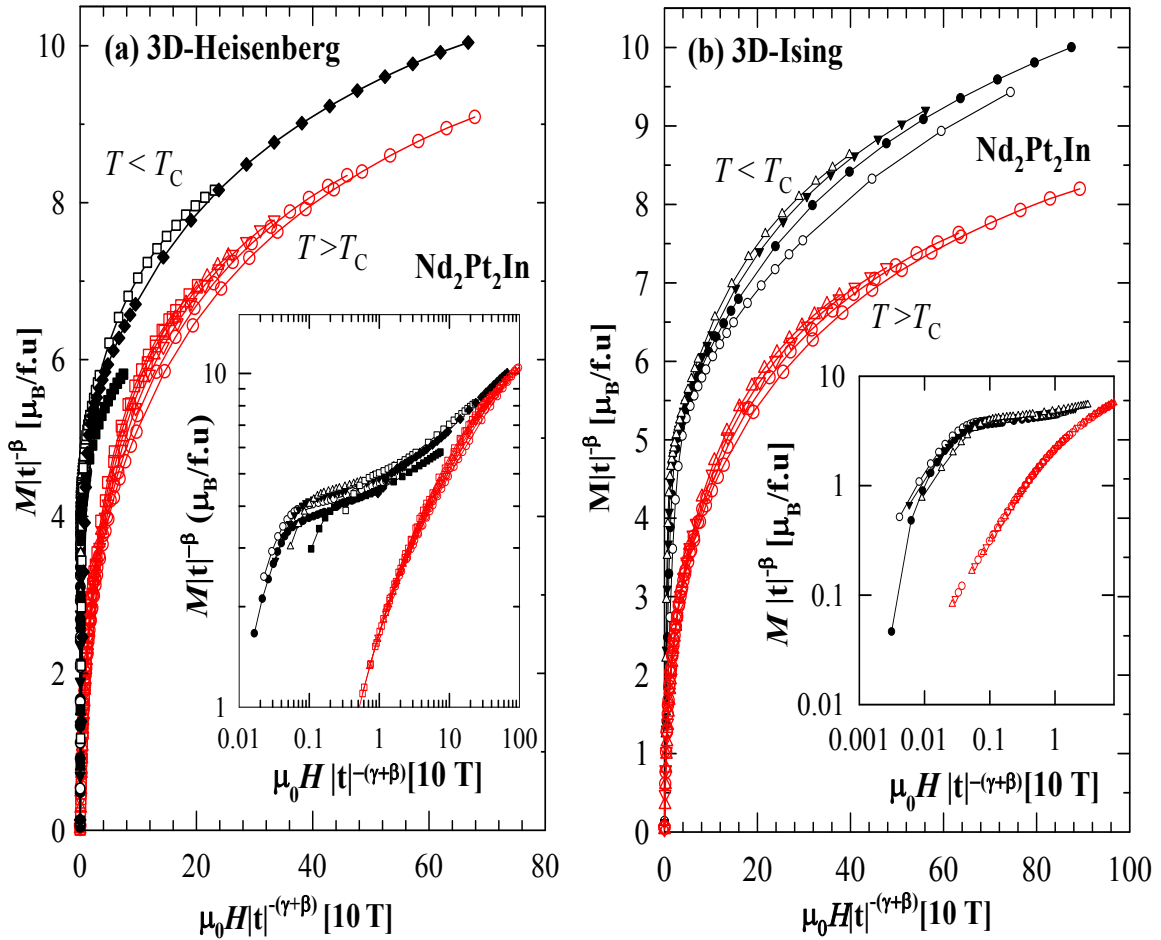
Figure 4.34: The renormalized magnetization in Nd_2Pt_2In plotted as a function of the renormalized field following equation 4.14 with (a) $T_C = 16.2$ K for the 3D-Heisenberg model and (b) $T_C = 15.9$ K for 3D-Ising model. The plots show the collapse into two distinct separate branches below and above T_C. The insets show the same plots on a log-log scale.

Table 4.7: (3D-Heisenberg model). Values of the critical exponents β, γ and δ as estimated from the modified Arrott-plots, the Kouvel-Fisher model and the critical isotherm for the Nd_2Pt_2In. The values of δ for modified Arrott-plots and the Kouvel-Fisher model have been calculated from the Widom scaling. The theoretical values for various models are also given for reasons of comparison.

Material	Ref.	Technique	β	γ	δ
Nd_2Pt_2In	This work	Modified Arrott-plots	0.366(3)	1.48(2)	5.04(9)
	This work	Kouvel-Fisher	0.350(3)	1.48(2)	5.23(9)
	This work	Critical isotherm			4.90(9)
Mean-Field model	[47]	Theory	0.5	1.0	3.0
3D-Heisenberg model	[47]	Theory	0.365	1.386	4.80
3D-Ising model	[47]	Theory	0.325	1.241	4.82

Table 4.8: (3D-Ising model). Values of the critical exponents β, γ and δ as estimated from the modified Arrott-plots, the Kouvel-Fisher model and the critical isotherm for the Nd_2Pt_2In. The values of δ for modified Arrott-plots and the Kouvel-Fisher model have been calculated from the Widom scaling. The theoretical values for various models are also given for reasons of comparison.

Material	Ref.	Technique	β	γ	δ
Nd_2Pt_2In	This work	Modified Arrott-plots	0.33(1)	1.226(9)	4.7(1)
	This work	Kouvel-Fisher	0.33(1)	1.24(1)	4.8(1)
	This work	Critical isotherm			4.00(2)
Mean-Field model	[47]	Theory	0.5	1.0	3.0
3D-Heisenberg model	[47]	Theory	0.365	1.386	4.80
3D-Ising model	[47]	Theory	0.325	1.241	4.82

4.4.5 Isothermal magnetization and magnetocaloric effect

The isothermal magnetization, $M(\mu_0 H, T)$ in Nd_2Pt_2In measured in applied magnetic fields up to 7 T in the temperature range 4 K - 30 K in a step of 2 K is displayed in figure 4.35. The compound exhibits a behaviour typical for ferromagnets in the ordered state. In the paramagnetic state, $M(\mu_0 H, T)$ curves are linear in weak fields and deviate from linearity with a downward curvature in strong fields. In 7 T, the magnetization decreases with increasing temperature from 2,05 to 1.25 μ_B.

Magnetocaloric effect refers to the change of the magnetic entropy (ΔS_M) that can be calculated from the magnetization isotherm using the Maxwell relation (equation 4.15). Figure 4.36a shows $-\Delta S_M(T)$ in Nd_2Pt_2In as a function of temperature for different field changes. Clearly, magnetocaloric is positive in the whole temperature range, consistent

4.4.5 . Isothermal magnetization and magnetocaloric effect

with the ferromagnetic ordering and strong ferromagnetic correlations in the paramagnetic state. Around T_C, the $-\Delta S_M(T)$ curves exhibit broad maxima, the magnitude of which gradually increases with an increase in the field change, reaching 6.25 J/(kg.K) for a field change of 7 T. This value is of the same order of magnitude with the value obtained in Pr_2Pt_2In compound and is comparable to those reported for various promising magnetic refrigerant materials in this temperature range [104, 118].
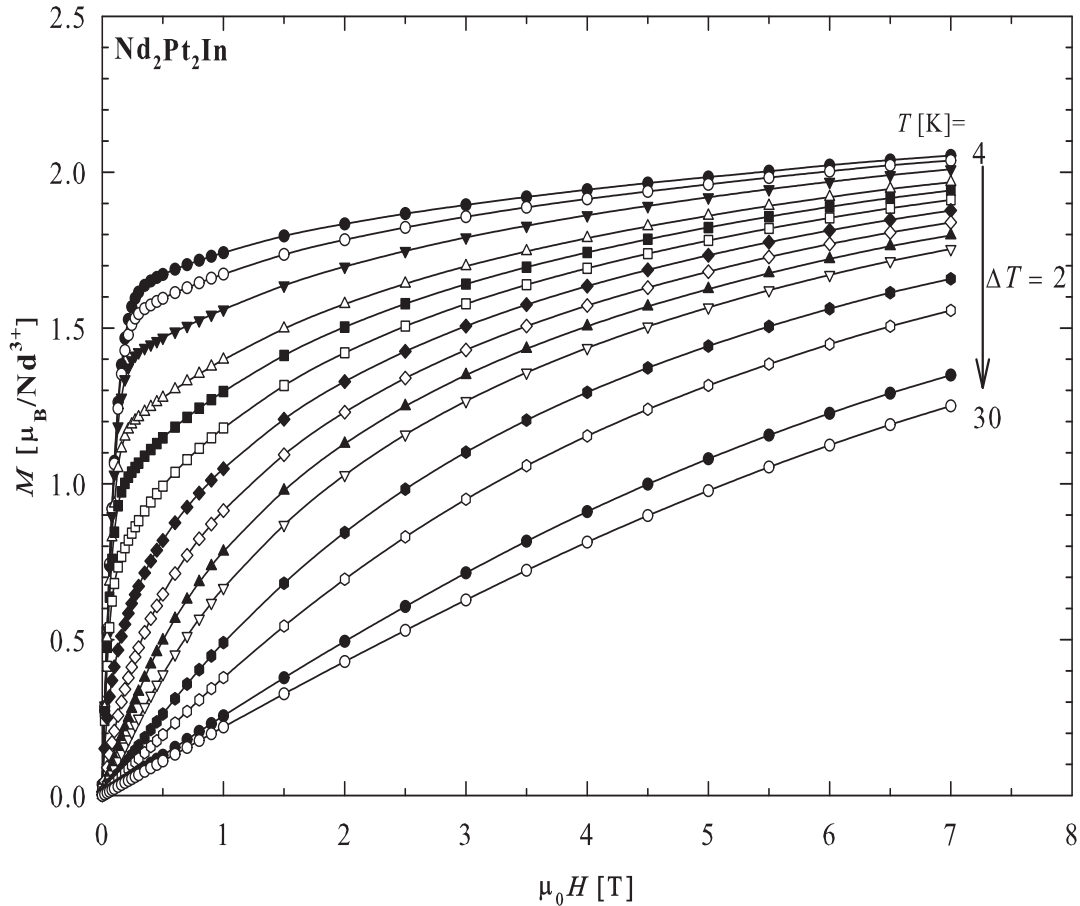
Figure 4.35: Isothermal magnetization curves $M(\mu_0 H, T)$ of Nd_2Pt_2In measured in magnetic field up to 7 T at temperatures between 4 to 30 K with a step of 2 K.

To further investigate the nature of the phase transition in Nd_2Pt_2In compound, the maximum values of $-\Delta S_M^{max}$ at T_C were plotted in figure 4.36b as a function of $h^{2/3}$, where $h = (\mu_0 H \mu_B) / (k_B T_C)$ is the reduced field. For magnetic materials with second-order phase transition, ΔS_M^{max} generally follow the relationship [106]:

$$\Delta_M^{max} = -S(0,1)h^{2/3} - S(0,0), \tag{4.20}$$

where $S(0,1)$ is a parameter proportional to the saturation magnetization $M_s(0)$ and $S(0,0)$ is a non-zero reference parameter [106]. Fitting equation 4.20 to $-\Delta S_M^{max}$ data (note the solid black line) in figure 4.36b yielded the values: $S(0,1) = 2.25(4)$ J/(kg.K) and S(0,0) = - 1.6(1) J/(kg.K). Similar to the Pr_2Pt_2In, negative sign of $S(0,0)$ is expected for a second-order phase transition [119, 120]. Furthermore, the linear behaviour of $-\Delta S_M^{max}$ vs. $h^{2/3}$ suggest strong localization of the magnetic moment in this compound [121].
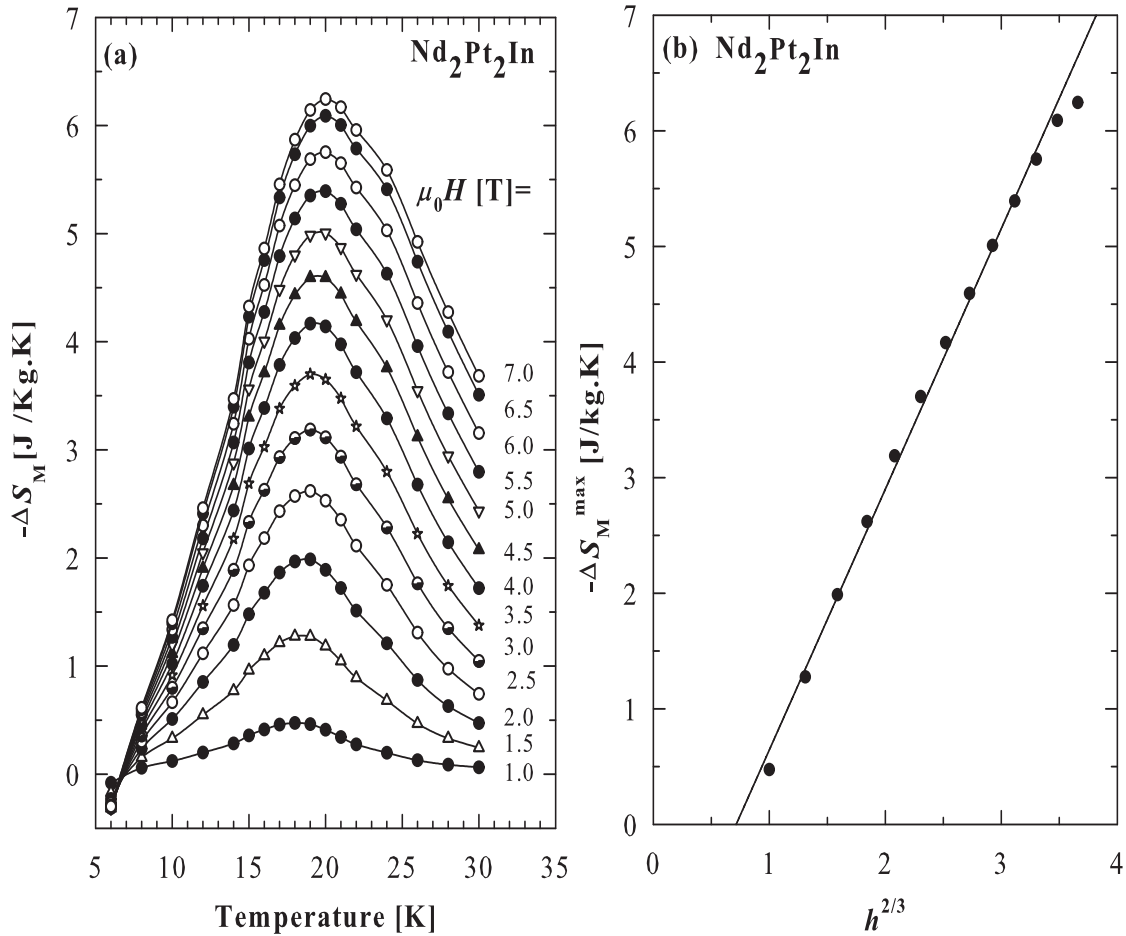
Figure 4.36: (a) Temperature dependencies of the isothermal magnetic entropy change, $-\Delta S_M(T)$, measured for Nd_2Pt_2In with different field changes in steps of 0.5 T. (b) The maximum isothermal magnetic entropy change at T_C as a function of reduced field $h^{2/3}$ (see text for definition). The solid line is the least squares fit of equation 4.20 to the experimental data.

4.4.6   Summary

X-ray diffraction studies indicate the tetragonal Mo_2FeB_2-type crystal structure with space group P4/mbm, No. 127 for Pr and Nd compounds. Studies of $\rho(T)$, $C_p(T)$ and $\chi(T)$ indicate ferromagnetic ordered state below $T_C = 9$ K and 16 K for Pr and Nd compounds, respectively. The ferromagnetic phase transition has a second-order nature

4.4.6 . Summary

for both compounds. Below T_C, both $\rho(T)$ and $C_p(T)$ data can be well described with the ferromagnetic spin-wave with energies gap $\Delta_R = 8(2)$ K and $\Delta_C = 6.0(3)$ K for Pr compound and $\Delta_R = 13(1)$ K and $\Delta_C = 7.6(3)$ K for Nd compound. $C_p(T)$ data of La_2Pt_2In can be well described by the Debye-Einstein model, while $C_p(T)$ of both Pr and Nd compounds, in the paramagnetic state are described by the standard Debye formula. Still in the paramagnetic state, $\rho(T)$ data of Pr_2Pt_2In compound can be well described by the Bloch-Grüneisen-Mott relationship. $\chi(T)$ data at high temperatures follow the Curie-Weiss relation for both compounds given effective magnetic moments close to that expected from Pr^{3+}- and Nd^{3+}-ion. And a positive Weiss temperature, θ_P confirming the ferromagnetic exchange interactions between the Pr moments and between the Nd moments. Critical behaviour studies for Pr_2Pt_2In ascribed the compound to belong to the 3D-Ising universality class, while these studies for Nd_2Pt_2In ascribed the compounds to belong between the 3D-Heisenberg and the 3D-Ising universality class. Magnetocaloric effect and Arrott-plots confirm the second-order phase transition for both compounds. The maximum values of the magnetocaloric effect for both compounds can be well compared with the values obtained for the equiatomic RE_2T_2X compounds.
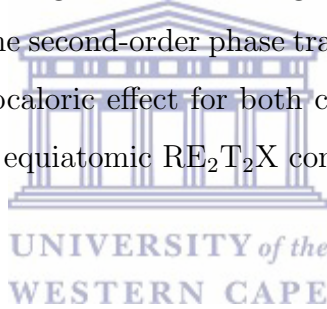
Chapter 5

Results and Discussion: $RE_8Pd_{24}Ga$ (RE = Gd, Tb, Dy)

5.1 Literature review and introduction

The intermetallic $REPd_3$, also denoted as RE_8Pd_{24} form an isostructural series with $AuCu_3$-type structure [129] corresponding to space group Pm-3m. Bulk magnetic measurements performed on this system indicate rather low ordering temperature (below 4.2 K) [130, 131, 132, 133]. In the case of RE = Ce, Tm, Yb, intermediate valence associated with hybridization with $4d$ state of Pd or Kondo hybridization are possible. The synthesis and magnetic behaviour of ternary cerium compounds with composition $Ce_8Pd_{24}M$ where M = In, Ga, In, Sn, Pb, Sb and Bi have been reported by Gordon *et al.* [134, 135]. This series of compounds form in a cubic superstructure closely related to the cubic $AuCu_3$-type structure of the parent compounds $CePd_3$. Mitra *et al.* [136] explored the superstructure formation for other RE atoms and obtained isostructural single-phase compounds $RE_8Pd_{24}M$ for RE = La, Pr, Sm, Gd, Tb, Y, Dy, Er and Lu and M = Ga and Ge. They reported first-order antiferromagnetic ordering and metamagnetic transition in $Tb_8Pd_{24}M$, (M = Ga and Ge) [136]. The group of compounds $Ce_8Pd_{24}M$, where M is *p*-block or *d*-element has been the subject of several experimental investigations due to interesting magnetic ground state properties [134, 135, 137, 138, 139]. Several investigations were reported on $Ce_8Pd_{24}Ga$ and $Tb_8Pd_{24}Ga$ in particular [134, 135, 136, 139, 140]. $Ce_8Pd_{24}Ga$ order antiferromagnetically below $T_N = 3.1$ K [139]. This compound has been investigated using neutron diffraction, inelastic neutron scattering, electrical

resistivity, magnetoresistivity, heat capacity and magnetic properties measurements [139, 140]. Inelastic neutron studies show two well-defined crystal-field excitations at 3.2 meV and 12.8 meV [139]. The heat capacity calculated from the crystal-field level scheme shows a Schottky-type anomaly at 15 K [139]. The resistivity exhibit a $-\ln(T)$ behaviour at high temperatures characteristic of incoherent single-ion Kondo scattering. This is followed by a peak at 8 K and eventually drops at T_N [139, 140]. The peak in the resistivity was attributed to the combined effect of crystal-electric-field and Kondo interaction [139]. The resistivity data below T_N was described by the antiferromagnetic spin-wave with energy gap $\Delta =$ 16.1 K in the spin-wave spectrum [139]. The magnetoresistivity was found to be positive at 1.8 K and changes to a negative sign above 3 K [139]. The magnetic susceptibility exhibits a Curie-Weiss behaviour above 20 K with an effective magnetic moment $\mu_{\mathrm{eff}} =$ 2.33 μ_B [139]. The low-temperatures of the susceptibility data of $Ce_8Pd_{24}Ga$ are distinctly different for zero-field-cooled (ZFC) sample with field-cooled (FC) sample [140, 141]. In the case of $Tb_8Pd_{24}Ga$, first-order antiferromagnetic ordering and metamagnetic transition was reported [136]. The magnetic susceptibility above 100 K follows the Curie-Weiss behaviour with μ_{eff} 9.63 μ_B and a Weiss temperature $\theta_p = -1$ K. This negative θ_p value indicates antiferromagnetic exchange interactions. The antiferromagnetic state occurs at $T_N = 5.2$ K [136]. The resistivity results exhibits hysteresis in the transition regime for this compound [136]. A sharp metamagnetic transition was observed at a field of 1.2 T below the magnetic ordering T_N [136]. Heat capacity data of $Tb_8Pd_{24}Ga$ exhibit a sharp first-order-like peak at T_N which confirms the bulk nature of the magnetic ordering [136].

Despite intense investigations on the electrical and thermal transport, magnetic and thermodynamic properties on the group of compounds $RE_8Pd_{24}M$ for the past decades, to the best of my knowledge, there has been no effort to investigate the magnetocaloric effect of this group of compounds. However, several investigations on the magnetocaloric effect were devoted to the group of compounds RE_2T_2X [126, 142, 143, 144, 145, 146] and RETX [147, 148, 149, 150], where RE = rare-earth elements, T = transition elements and X = p-block elements.

Indeed, magnetic materials with large magnetocaloric effect have potential application in magneto-refrigeration and eco-friendly cooling industry [8, 62, 151]. Magnetic refrig-

eration technology based on magnetocaloric effect shows superior application potential over conventional gas compression refrigeration technology because of its environmental friendliness, higher efficiency as well as compactness [8, 62, 152, 153, 154]. The magnetocaloric effect is an intrinsic thermal response of the application or removal of a magnetic field to a magnetic material, which can be characterized by the couple variations of two quantities such as the isothermal magnetic entropy change (ΔS_{M}) and/or the adiabatic temperature change (ΔT_{ad}). A potential magnetic refrigerant should have large/giant magnetocaloric effect and negligible hysteresis loop. It has been observed that compounds with large first-order magneto-structural transition show large magnetocaloric effect [147]. The rare-earth based alloys, which exhibit large magnetocaloric effect and refrigeration capacity with small or zero hysteresis loops, have been of great interest in the last few years [155, 156, 157, 158, 159, 160, 161]. Among the group of compounds $RE_8Pd_{24}M$ (M = p-block elements), only crystal structure, transport, magnetic properties and heat capacity have been reported. To further understand the physical properties of $RE_8Pd_{24}M$ compounds, in this chapter the crystal structure, electrical resistivity, magnetic properties, heat capacity and the magnetocaloric effect have been investigated on $RE_8Pd_{24}Ga$ with RE = Gd, Tb and Dy.
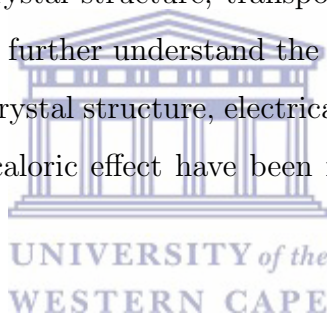
5.1.1 Crystal structure

Figures 5.1, 5.2 and 5.3 show the results obtained from the scanning electron microscope experiment at the working distance of 250 μm for all three compounds. The micrograph images are characterized by smooth surfaces with regions of slightly different darkness. Energy dispersive spectroscopy analyses indicate that the entire samples of all three compounds were homogeneous and thus the dissimilar regions should be attributed to crystallites with different crystallographic orientation. The quantitative energy dispersive spectroscopy measurements over the surface areas of each sample results in the elemental composition normalized to the RE content: $Gd_8Pd_{23.870(2)}Ga_{0.961(1)}$; $Tb_8Pd_{23.931(2)}Ga_{0.925(2)}$ and $Dy_8Pd_{23.887(2)}Ga_{0.953(2)}$, which are roughly close to the 8:24:1 composition. The small offsets of the atomic ratios result from the small weight loss that occurs during the arc-melting process (sample synthesis).

5.1.1 . Crystal structure
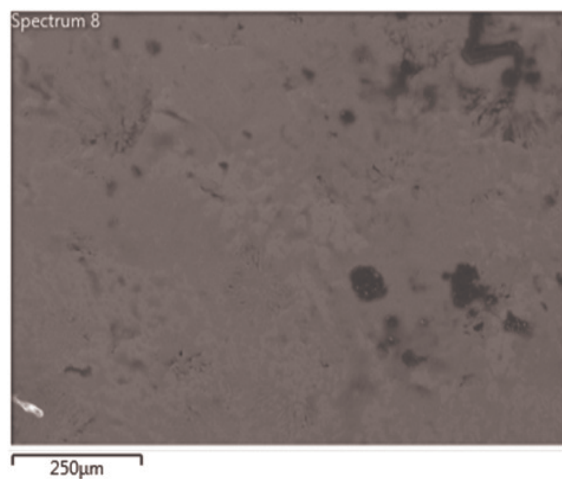
Figure 5.1: Cross section micrograph of scanning electron microscope done on $Gd_8Pd_{24}Ga$ with a scale of 250 μm.
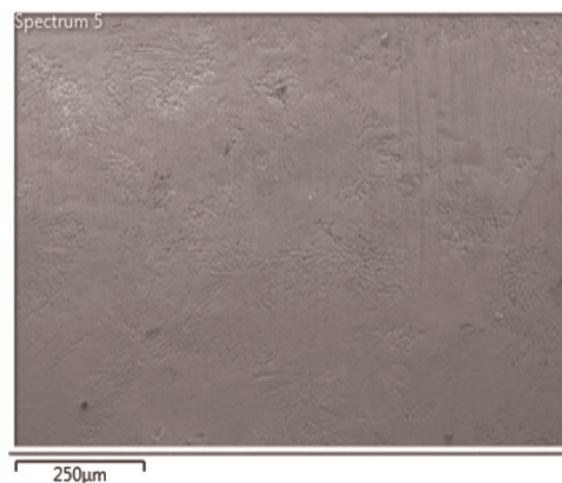
Figure 5.2: Cross section micrograph of scanning electron microscope done on $Tb_8Pd_{24}Ga$ with a scale of 250 μm.
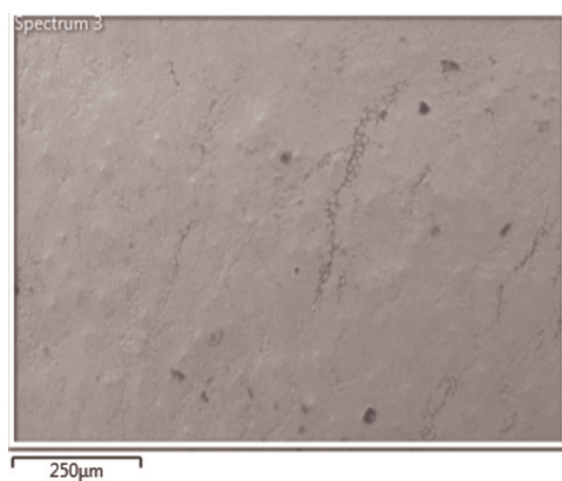
Figure 5.3: Cross section micrograph of scanning electron microscope done on $Dy_8Pd_{24}Ga$ with a scale of 250 μm.

5.1.1 . Crystal structure

X-ray diffraction patterns of the three compounds are shown in figures 5.4, 5.5 and 5.6, together with the full-profile least squares Rietveld refinement. X-ray diffraction analysis reveal that all compounds were single-phase material with no secondary phases and crystallized in the cubic structure with lattice parameters and unit-cell volumes listed in table 5.1. It is observed that the unit-cell volume satisfied the relation $V_{\mathrm{Gd_8Pd_{24}Ga}}$ $>V_{\mathrm{Tb_8Pd_{24}Ga}}$ $>V_{\mathrm{Dy_8Pd_{24}Ga}}$, consistent with the lanthanide contraction as one moves from La to Lu. It is also noted that the lattice parameters of $\mathrm{Gd_8Pd_{24}Ga}$, $\mathrm{Tb_8Pd_{24}Ga}$ and $\mathrm{Dy_8Pd_{24}Ga}$ are nearly double the lattice parameters a = 4.0813 $\mathring{A}$ of $\mathrm{GdPd_3}$, a = 4.0691 $\mathring{A}$ of $\mathrm{TbPd_3}$ and a = 4.0612 $\mathring{A}$ of $\mathrm{DyPd_3}$ [131]. This suggests the existence of a cubic supercell in all three compounds under investigation. The value of the lattice parameter obtained for $\mathrm{Tb_8Pd_{24}Ga}$ is in agreement with the value of 8.26 $\mathring{A}$ reported for the polycrystalline sample [136]. The X-ray diffraction patterns were refined using the Rietveld refinement method. The input space group setting was the cubic Pm-3m structure as proposed for $\mathrm{Ce_8Pd_{24}Sb}$ [135]. The assumed crystal structure of $\mathrm{AuCu_3}$-type is depicted in figure 5.7. In this unit cell, RE atoms occupy the crystallographic 8g sites, Pd occupy three different types of sites, Pd1 at the $6f$ sites, Pd2 at the $6e$ sites and Pd3 at the $12h$, sites and Ga atoms occupy the $1a$ sites. In the refinement process, the full occupancies were assumed and the isotropic displacement parameters of all the atoms were kept fixed, while the free atomic coordinates were varied. The calculation gives the atomic coordinates gathered in table 5.1 for all three compounds. These values are in agreement with previous reported values. The resulting phase density (PD) and final discrepancy factors of the Rietveld refinement are gathered in table 5.2. The low values obtained χ^2 and R-factors indicate the good quality of the fit. Furthermore, the low values R_{B} indicate that the structural model is correct.

5.1.1 . Crystal structure

Table 5.1: Atomic coordinates derived for $Gd_8Pd_{24}Ga$ from the Rietveld refinement. The site occupancies S.O. = 1 and the isotropic displacement parameters $B_{eq} = 1$ were assumed.

Atom	Wyckoff site	x	y	z	a(Å)	V(Å^3)
Gd	8g	0.25(4)	0.254(5)	0.254(5)	8.2704(6)	565.691(2)
Pd1	6f	0.249(9)	1/2	1/2		
Pd2	6e	0.255(9)	0	0		
Pd3	12h	0.253(8)	1/2	0		
Ga	1a	0	0	0		
Tb	8g	0.25(4)	0.254(5)	0.254(5)	8.237(6)	558.87(2)
Pd1	6f	0.249(9)	1/2	1/2		
Pd2	6e	0.255(9)	0	0		
Pd3	12h	0.253(8)	1/2	0		
Ga	1a	0	0	0		
Dy	8g	0.250(4)	0.250(5)	0.254(5)	8.2070(6)	552.781(2)
Pd1	6f	0.254(9)	1/2	1/2		
Pd2	6e	0.292(9)	0	0		
Pd3	12h	0.259(8)	1/2	0		
Ga	1a	0	0	0		

Table 5.2: R-factors obtained from the Rietveld refinement methods in X-ray powder diffraction data analysis of $RE_8Pd_{24}Ga$, with RE = Gd, Tb and Dy.

discrepancy factors-Rietveld	$Gd_8Pd_{24}Ga$	$Tb_8Pd_{24}Ga$	$Dy_8Pd_{24}Ga$
R_{wp} [%]	4.840	5.688	6.520
R_{exp} [%]	2.387	2.410	2.969
R_p [%]	3.683	4.267	4.942
χ^2	2.028	2.360	2.196
DW	0.643	0.438	0.581
R_B [%]	3.850	4.141	4.126
PD (g/cm^3)	10.964(2)	11.574(3)	11.787(3)
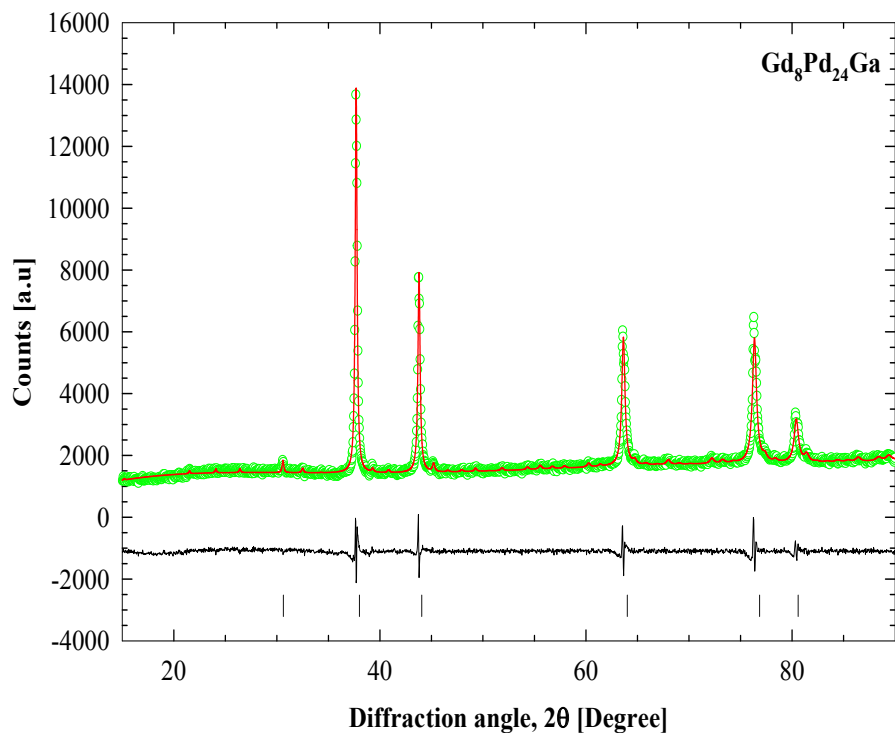
Figure 5.4: The X-ray diffraction pattern (green symbols) of $Gd_8Pd_{24}Ga$ collected at room temperature along with its Rietveld refinement (red curve). The bottom black curve is the difference between the experimental and calculated patterns. The vertical lines are the Bragg position.
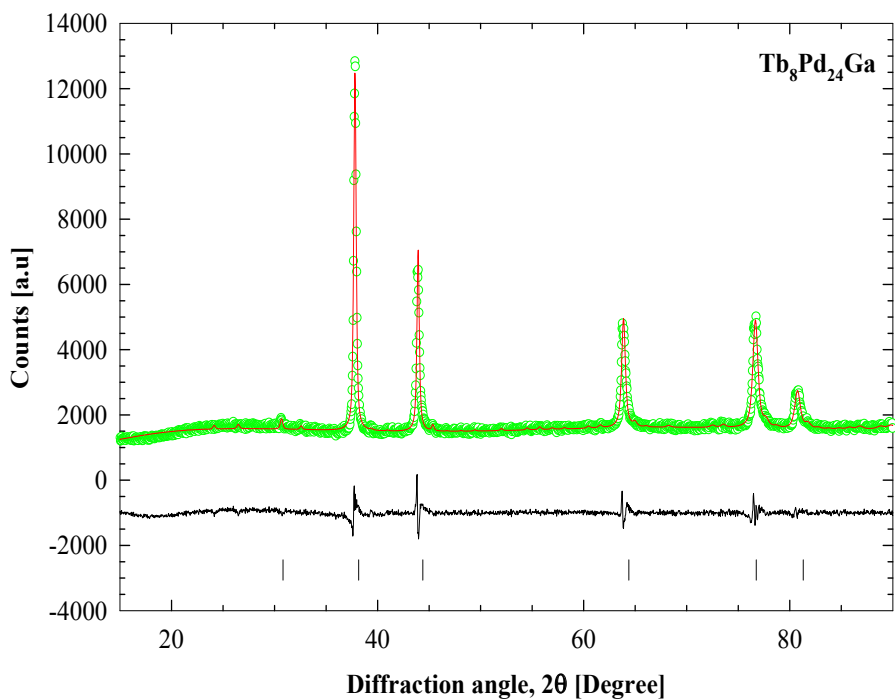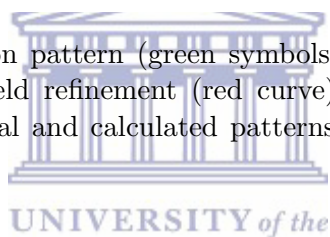
Figure . 5.5: The X-ray diffraction pattern (green symbols) of $Gd_8Pd_{24}Ga$ collected at room temperature with its Rietveld refinement (red curve). The bottom black curve is the difference between the experimental and calculated patterns. The vertical lines are the Bragg position.

118
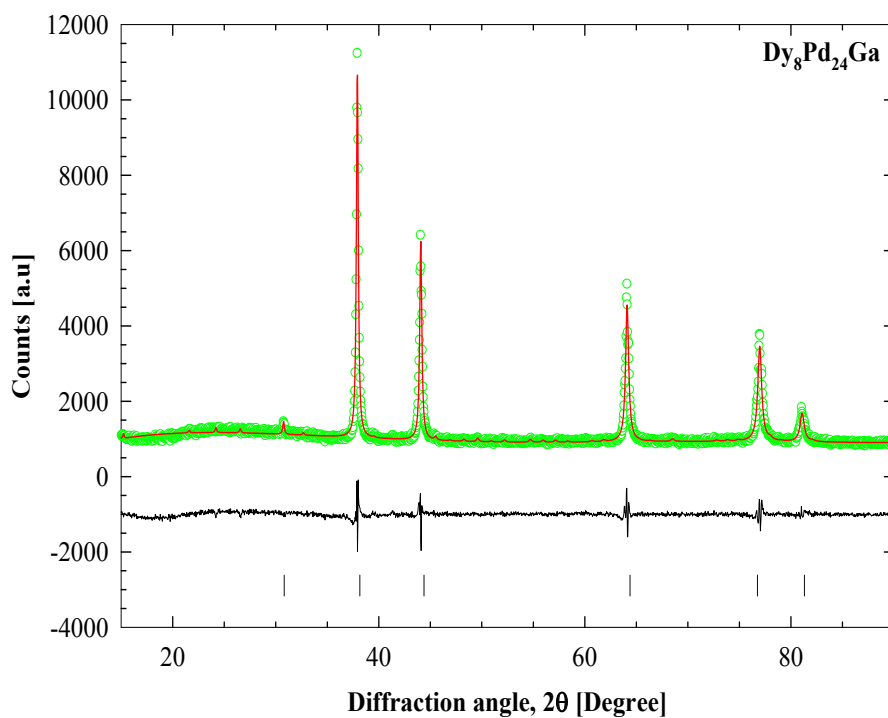
Figure 5.6: The X-ray diffraction pattern (green symbols) of $Dy_8Pd_{24}Ga$ collected at room temperature with its Rietveld refinement (red curve). The bottom black curve is the difference between the experimental and calculated patterns. The vertical lines are the Bragg position.
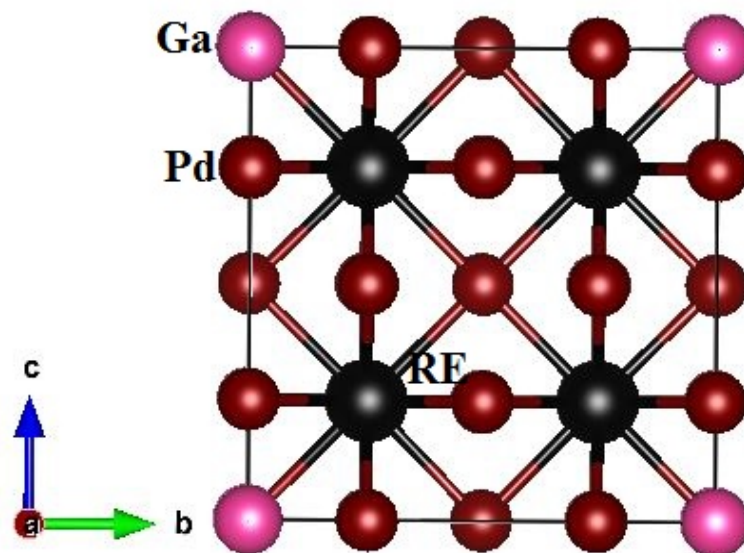
Figure 5.7: The cubic unit cell of $RE_8Pd_{24}Ga$. The pink, brown and black balls represent Ga, Pd and RE atoms, respectively.

119

5.1.2   Electrical resistivity

The temperature dependencies of electrical resistivity, $\rho(T)$ of $Gd_8Pd_{24}Ga$, $Tb_8Pd_{24}Ga$ and $Dy_8Pd_{24}Ga$ are depicted in figures 5.8a, 5.8b and 5.8c, respectively. It should be noted that the high values of $\rho(T)$ for Tb compound are due to micro cracks and voids on the resistivity sample. At high temperatures for all three compounds, $\rho(T)$ behaviour is typical of normal metals with the resistivity varying linearly with temperature. This behaviour is characteristic of electron-phonon scattering in the absence of crystal-electric-field and/or $s - d$ interband scattering.

The low-temperatures of $\rho(T)$ for the three compounds are shown as the insets in figures 5.8a, 5.8b and 5.8c. It is observed that $\rho(T)$ data for all three compounds exhibit a sudden drop due to the gradual loss of the spin-disorder induced scattering, associated with antiferromagnetic anomalies at $T_N = 9$ K, 5.8 K and 3.8 K for Gd, Tb and Dy compounds, respectively as indicated by arrows in the insets. The magnetic phase transition in these compounds manifest itself as a pronounced anomaly in the temperature derivative of the resistivity $d\rho/dT$ as shown in figures 5.10a, 5.10b and 5.10c. The values of T_N were estimated according to Sato criterion [109], which is at the midpoint of the anomaly in the $d\rho/dT$ curves as indicated by the arrows in figures 5.10a, 5.10b and 5.10c. The obtained values of T_N are agreed with the values obtained from heat capacity results (see section 5.1.3) and magnetic susceptibility (see section 5.1.4). In the ordering region ($T \leq T_N$), $\rho(T)$ for the Gd compound decreases nearly linearly with decreasing temperature. Such linear decrease has been observed in many Gd compounds such as $Gd_8Pd_{24}Al$ [162], $GdCu_4Au$ [163], $GdPd_3$ [164].
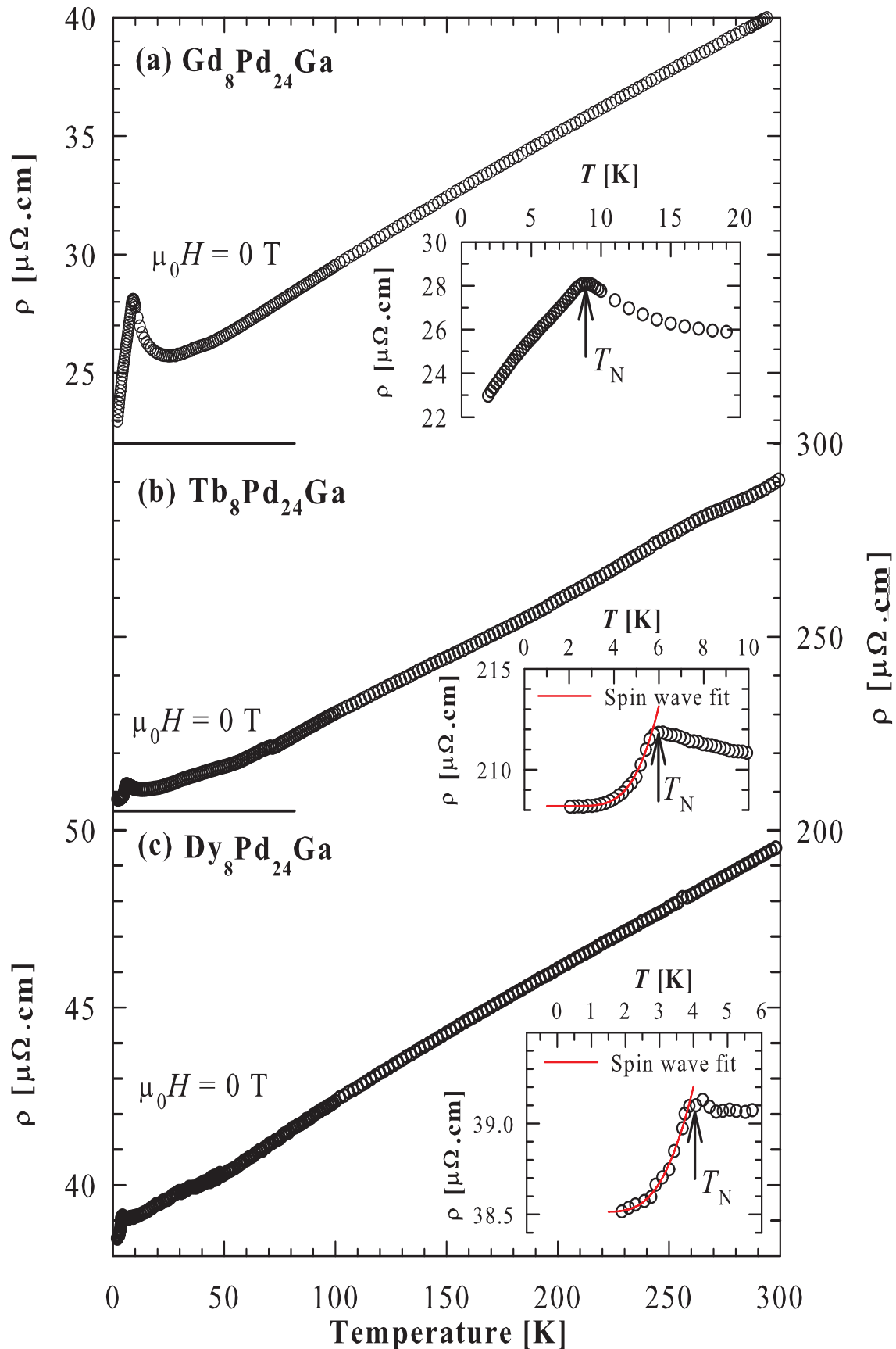
Figure 5.8: Temperature dependence of electrical resistivity, $\rho(T)$ for (a) $Gd_8Pd_{24}Ga$, (b) $Tb_8Pd_{24}Ga$ and (c) $Dy_8Pd_{24}Ga$ obtained under 0 magnetic field. The insets show the low-temperatures of $\rho(T)$ with the least squares fits (in (b) and (c), solid red curves) using the spin-wave relationship (equation 5.1). The arrows show the position of the magnetic transition.

121

5.1.2 . Electrical resistivity

For the Tb and Dy compounds, the low-temperatures ($T \leq T_\mathrm{N}$), $\rho(T)$ are governed by the scattering conduction electrons on antiferromagnetic spin-wave excitations with the energy gap (Δ_R) in the magnon spectrum, and can be described by the formula [34]:

$$\rho(T) = \rho(0) + A_\rho \Delta_\rho^{3/2} T^{1/2} exp(-\Delta_\rho/T) \left[1 + \frac{2}{3}\frac{T}{\Delta_\rho} + \frac{2}{15}\left(\frac{T}{\Delta_\rho}\right)^2 \right], \qquad (5.1)$$

where $\rho(0)$ is the residual resistivity originating from defects, Δ_ρ is the energy gap and A_ρ is a prefactor defining the stiffness of the sample. The validity of such a description is illustrated by the solid red lines in the insets of figures 5.8b and 5.8c which are the least squares fits of equation 5.1 to the $\rho(T)$ data below T_N. These yielded the parameters: ρ_0 = 208.198(3) $\mu\Omega$.cm, Δ_ρ = 29.6(1) K, A_ρ = 1.5(4) $\mu\Omega$.cm/K^2 and ρ_0 = 38.51(1) $\mu\Omega$.cm, Δ_ρ = 15(1) K, A_ρ = 0.22(6) $\mu\Omega$.cm/K^2 for Tb and Dy compounds, respectively. Below 25 K shallow resistivity minima are seen for Gd, Tb and Dy compounds. The minima are more pronounced for the Gd and Tb compounds and occurs at T_min = 25 K and 10 K respectively. The observed resistivity minimum at 10 K for the Tb compound is in good agreement with that reported for the same compound in the literature [136], however, the resistivity loop reported in reference [136] was not observed in the result shown in this thesis since the measurements were done in the cooling mode. Below T_min, $\rho(T)$ data of both Gd and Tb compounds exhibit an upturn up to T_N. Such an upturn was observed in many rare-earth compounds such as GdPd$_3$ [164], RE$_8$Pd$_{24}$Al (RE = Gd, Tb, Dy and Ho) [162]. It was reported that the observed minimum in GdPd$_3$, was likely due to the opening of antiferromagnetic superzone gap (pseudogap for $T \geq T_\mathrm{N}$ = 6.5 K and gap for $T <$ 6.5 K) at the Fermi surface, which is a manifestation of a magnetic structure whose periodicity is incommensurate with the periodicity of the crystal lattice [164]. On the other hand, Singh and Dhar [162] reported for RE$_8$Pd$_{24}$Al (RE = Gd, Tb, Dy and Ho) compounds that, since the minimum occurs at temperature below T_N, the upturn in the resistivity for the temperature range $T_\mathrm{N} < T < T_\mathrm{min}$ in the paramagnetic region can not be attributed to the magnetic-superzone-induced gap effect. Since the antiferromagnetic order is associated with large reciprocal magnetic lattice vector, typically for temperatures above T_N, the large-k (k being the wave vector) fluctuations diminish while small-k fluctuations grow [162, 165], which should lead to a decreasing resistivity in

5.1.2 . Electrical resistivity

antiferromagnetic metals above T_N. Hence the resistivity minima arise because the phonon contribution to the resistivity is increasing slower than the decrease of the critical resistivity in the paramagnetic region which results in a negative temperature coefficient for the resistivity in a certain range of temperature [162]. To further investigate the opening of an antiferromagnetic superzone pseudogap at the Fermi surface in $Gd_8Pd_{24}Ga$ and $Tb_8Pd_{24}Ga$ compounds, the plots of $\rho(T)$ data at low-temperature are shown in figures 5.9a and 5.9b and are fitted to the activated behaviour [164]:

$$\rho(T) = A + Bexp\left(\frac{\Delta}{T}\right),\qquad(5.2)$$

where A and B are constant and Δ is the superzone band gap. Least squares fits yielded the values: $A = 23.7(4)\ \mu\Omega.cm$, $B = 1.1(3)\ \mu\Omega.cm$, $\Delta = 13(2)\ K$ and $A = 208.4(9)\ \mu\Omega.cm$, $B = 1.3(7)\ \mu\Omega.cm$, $\Delta = 6(1)\ K$ for Gd and Tb compounds, respectively. The obtained values of the superzone band gap are relatively smaller compared to those obtained for $GdPd_3$ [164]. In the present case, the resistivity minimum observed in Gd and Tb compounds may or may not originate from an antiferromagnetic superzone pseudogap formation since the overall details of the Fermi surface and the magnetic structure may, however bring qualitative changes in the thermal vibration of the resistivity above T_N.
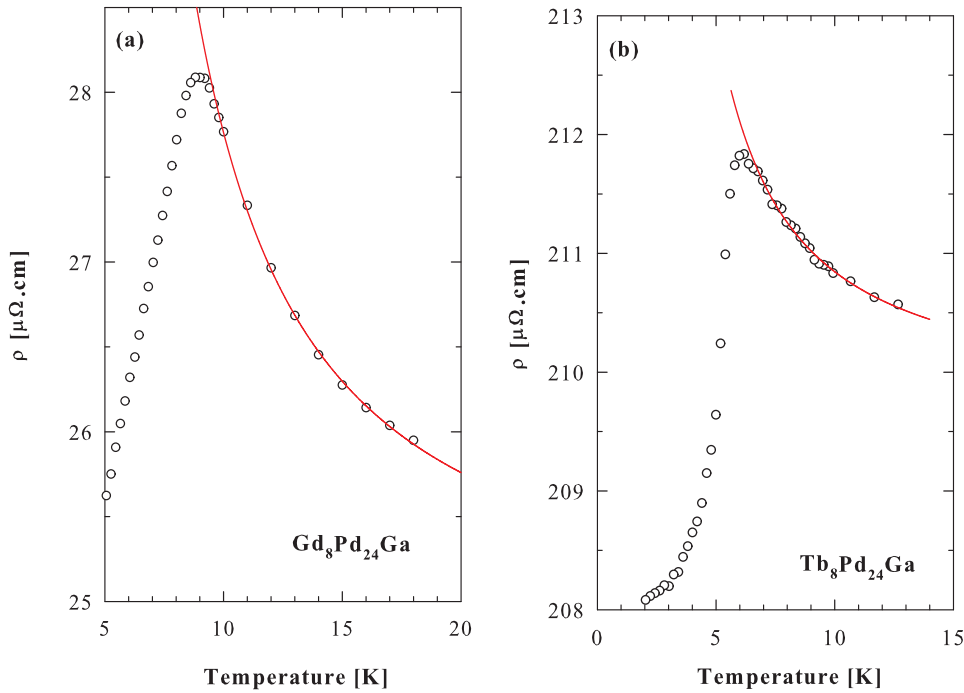
Figure 5.9: The Low-temperatures, $\rho(T)$ data of (a) $Gd_8Pd_{24}Ga$ and (b) $Tb_8Pd_{24}Ga$ depicting an expanded view of the antiferromagnetic superzone regions. The solid red curves are the least squares fits of equation 5.2.
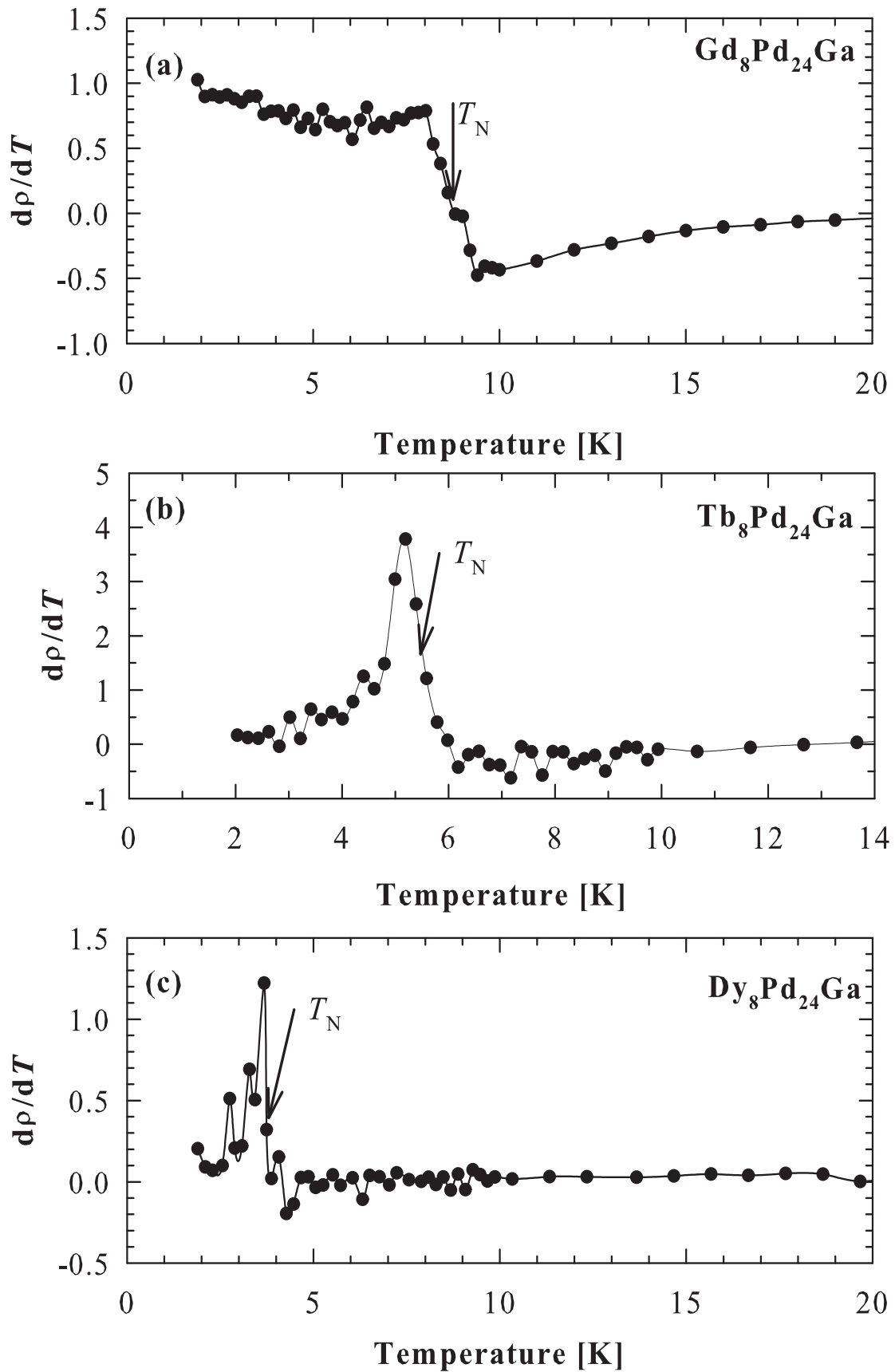
Figure 5.10: The first derivative of electrical resistivity, $d\rho(T)/dT$ data of (a) $Gd_8Pd_{24}Ga$, $Tb_8Pd_{24}Ga$ and (c) $Dy_8Pd_{24}Ga$. The arrows indicate the positions of T_N.

5.1.3 Heat Capacity

Figures 5.11a, 5.11b and 5.11c show the temperature dependent heat capacity of Gd, Tb and Dy compounds, respectively measured in 0 magnetic field in the temperature range of 1.8 K - 300 K. In the entire measured temperature range, the specific heat values of $Gd_8Pd_{24}Ga$ and $Dy_8Pd_{24}Ga$ compounds rach the Dulong-Petit limit, $3nR = 823.1$ J/mole.K (n = 33 is the number of atoms per formula unit, R stand for the gas constant) at room temperature, and at 180 K for $Tb_8Pd_{24}Ga$ compound. Well above T_N, in the paramagnetic region $C_p(T)$ data can be described by the standard Debye formula given by the equation 4.3 . The least squares fits of equation 4.3 to the experimental data (note the red solid lines in figures 5.11) yielded the parameters: $\theta_D = 238.886(7)$ K, and $\gamma = 1.386(1)$ J/mole.Gd.K^2 for $Gd_8Pd_{24}Ga$; $\theta_D = 230.26(4)$ K, and $\gamma = 3.340(4)$ J/mole.Gd.K^2 for $Tb_8Pd_{24}Ga$ and $\theta_D = 233.20(2)$ K, and $\gamma = 2.373(3)$ J/mole.Gd.K^2 for $Dy_8Pd_{24}Ga$. The obtained values of θ_D are fairly similar to those reported for the members of $RE_8Pd_{24}M$ series [136, 137, 166]. Similar to the RE_2Pt_2In (RE = Pr, Nd) compounds discussed in chapter 4, the values of θ_D for all three compounds are of the same order of magnitude, signalling the similarity of the phonon vibration in the three compounds as a result of the similarity of their atomic masses.

The low-temperature of $C_p(T)/T$ data of all three compounds are shown in the insets of figures 5.11a, 5.11b and 5.11c. Sharp peaks at 8.7 K, 5.6 K and 3.9 K are observed in the Gd, Tb and Dy compounds, respectively and confirms the bulk nature of the magnetic ordering in these compounds. These peak positions coincide nearly with T_N estimated from the resistivity data. In the inset of figure 5.11a, another maximum can be discerned at a temperature $T_t = 4$ K for Gd compound and in the inset of figure 5.11c a shoulder at $T_t = 2.2$ K for Tb compound. The temperature at which this maximum and a shoulder appear coincided with the temperature at which the magnetic susceptibility of both Gd and Dy compounds form a shoulder (see below).
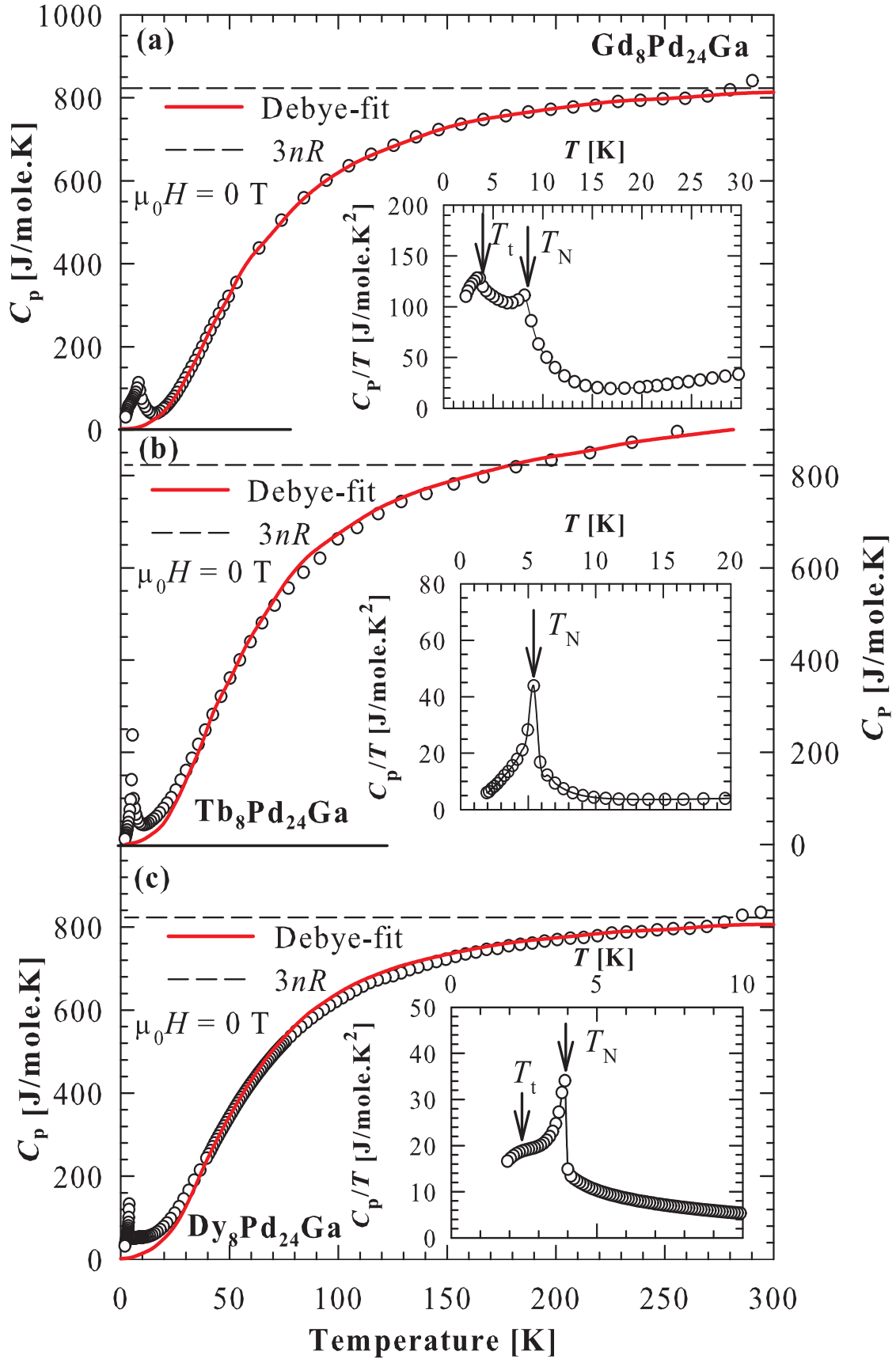
Figure 5.11: Heat capacity data of (a) Gd$_8$Pd$_{24}$Ga, Tb$_8$Pd$_{24}$Ga and (c) Dy$_8$Pd$_{24}$Ga, measured in 0 magnetic field. The red solid curves are the Debye fits to the experimental $C_p(T)$ data using equation 4.3. The horizontal dashed lines are the Dulong-petit values limit. The insets are the expanded low-temperatures region plotted as C_p/T vs. T. The arrows show the position of the magnetic transitions.

126

Based on both findings, a kind of magnetic order-order transition may be anticipated. In the case of the Tb compound, no additional peak below T_N was observed from the C_p/T data but was observed in the susceptibility data (see 5.1.4). It is worth recalling that every similar additional feature in the ordering state was observed for the equiatomic $Tb_8Pd_{24}Ge$ [136] as well as for other rare earth intermetallics, such as TbCuGe [147], GdCuSi [149], CeCuSn [167], and was attributed to spin reorientation of the rare-earth magnetic moments. The value of T_N observed from the $C_p(T)$ data of Tb compounds is in good agreement with value of 5.2 K reported for the same polycrystalline sample from the heat capacity results [136].

5.1.4   Magnetic susceptibility and magnetization

The inverse magnetic susceptibility $\chi^{-1}(T)$ measured in an applied magnetic field of 0.1 T and in the temperature range 1.7 K - 400 K are displayed in figure 5.12 for Gd, Tb and Dy compounds. Above 20 K, $\chi^{-1}(T)$ for all three compounds follows the Curie-Weiss relationship (equation 4.6). Least squares fits (red solid lines in figures 5.12a, 5.12b and 5.12c) yielded the susceptibility parameters: $\theta_p = -2.2(1)$ K, $\mu_{\text{eff}} = 8.004(2)$ μ_B for Gd compound, $\theta_p = -2.29(1)$ K, $\mu_{\text{eff}} = 9.76(2)$ μ_B for Tb and $\theta_p = -2.3(5)$ K, $\mu_{\text{eff}} = 10.756$ (8) μ_B for Dy compound. The experimental values of the effective moment are in reasonable agreement with the theoretical values $g_J[J(J+1)]^{1/2} = 7.94$ μ_B; 9.72 μ_B and 10.65 μ_B expected for the three Gd^{3+}-, Tb^{3+}- and Dy^{3+}-ions ($J = 7/2$, 6 and 15/2 for Gd, Tb and Dy, respectively). The negatives θ_p hint at the antiferromagnetic exchange interactions between the rare-earth moments. Below 20 K, $\chi^{-1}(T)$ data deviate from the Curie-Weiss linear behaviour likely due to magnetocrystalline anisotropy. As can be inferred from figures 5.13a, 5.13c and 5.13e, $\chi(T)$ data exhibit a maximum at $T_N = 8.5$ K, 5.5 K and 3.9 K for Gd, Tb and Dy compounds, respectively, characteristic of long-range antiferromagnetic phase transition also observed in $\rho(T)$ and $C_p(T)$ results. These values of T_N were accurately estimated at the maximum of the derivative of $\chi(T)$ curves (see figures 5.13b, 5.13d and 5.13f). Below T_N, for Gd and Dy, $\chi(T)$ data steeply decreases and exhibit a shoulder at $T_t = 3.5$ K and 2.9 K, while for Tb compound, below T_N, $\chi(T)$ firstly decreases and increases sharply up to a maximum. Such a feature in the ordering region of Tb compound was not previously observed in reference [136]. The temperature at which this shoulder in $\chi(T)$ occurs coincides with the temperature at with the heat capacity $C_p(T)$ forms a max-

imum for Gd and a shoulder for Tb compounds (see above). This feature in the ordering region confirms the spin reorientation of the rare-earth moments. To further investigate the magnetic structure of the Gd, Tb and Dy compounds, the values of $\varepsilon = \chi(0)/\chi(T_N)$ have been calculated at applied field of 0.1 T, where $\chi(0)$ is the value of the susceptibility taken at the lowest measured temperature of 1.7 K. It should be noted that, for a collinear antiferromagnetic structure $\varepsilon = 2/3$ [168, 169]. The calculated values of ε for the present compounds are: $\varepsilon = 0.898$, 1.162 and 0.895 for Gd, Tb and Dy, respectively. These values suggest a noncollinear antiferromagnetic spin arrangement of the rare-earth spins where the ordered moments below T_N are not aligned along the same axis. Such behaviour was reported in GdPd$_3$ [164].

Figure 5.14 shows the magnetization isotherm at 1.7 K, $M(\mu_0 H)$ of the three compounds measured in magnetic field up to 7 T. For the Gd compound, $M(\mu_0 H)$ exhibits almost a linear behaviour with field up to 7 T with value of the magnetic moment 6.35 μ_B/Gd^{3+} which is slightly smaller than theoretical value $g_J J = 7$ μ_B/Gd-atom. This shortfall is likely due to magnetic anisotropy. For the Tb and Dy compounds, $M(\mu_0 H)$ initially increase linearly up to a critical field, $(\mu_0 H)_{met}$ that can be associated with a metamagnetic-like singularity. These critical fields were accurately estimated at the maximum of the derivative of $M(\mu_0 H)$ curves (figure 5.14b and 5.14c right axis) to be $(\mu_0 H)_{met} = 1.5$ T and 0.5 T for Tb and Dy compounds, respectively. At high field, $M(\mu_0 H)$ data show a downward curvature for both compounds. In the terminal field $(\mu_0 H) = 7$ T, $M(\mu_0 H)$ data reach values of 7.7 μ_B/Tb-atom and 8.1 μ_B/Dy-atom. Both magnetic moments are smaller than the theoretical values $g_J J = 9$ μ_B/Tb-atom and 10 μ_B/Dy-atom. This discrepancy likely results from effect of crystal-electric-field and magnetic anisotropy.
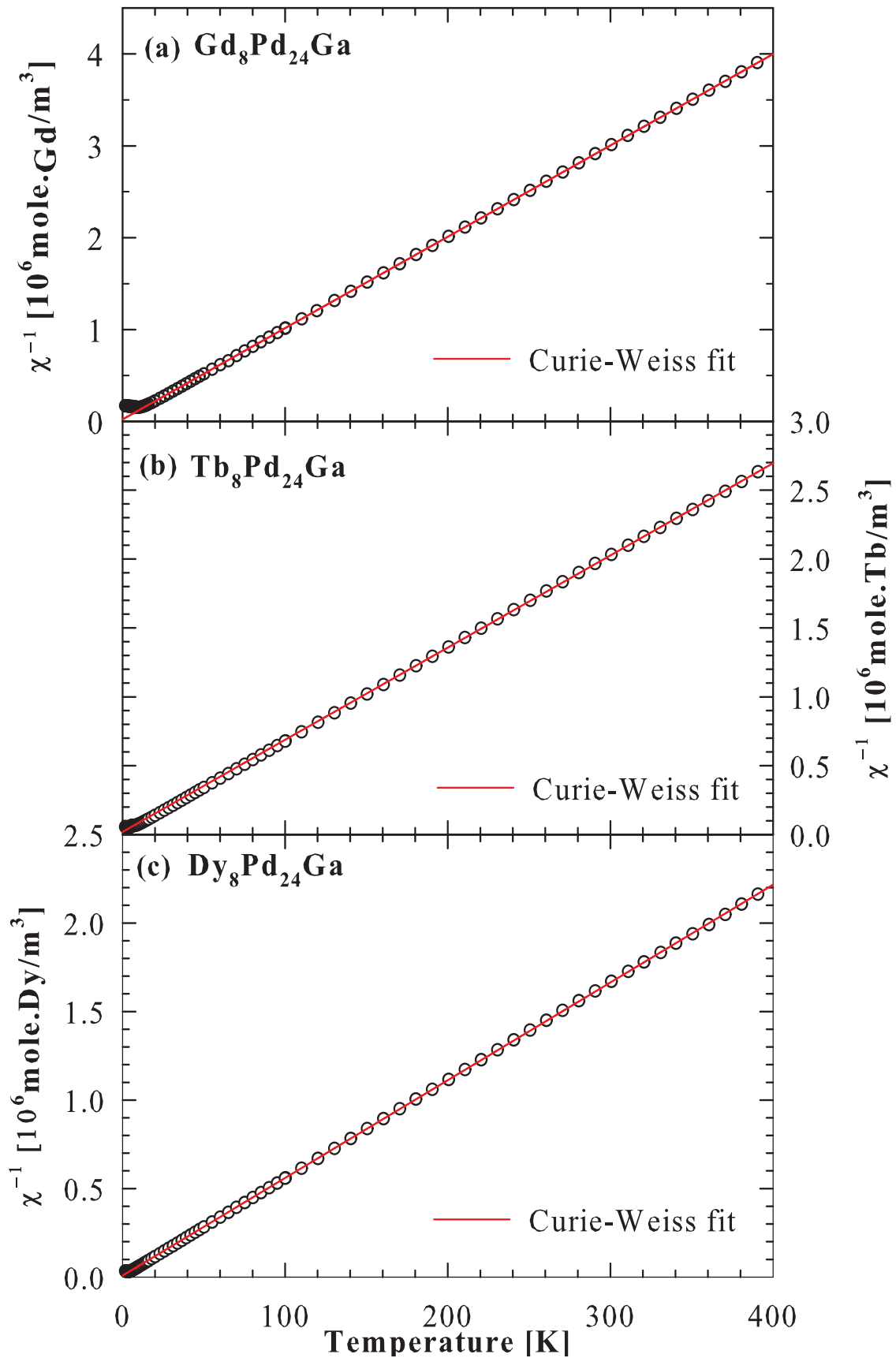
Figure 5.12: Temperature variation of the inverse magnetic susceptibility, $\chi^{-1}(T)$ of (a) Gd$_8$Pd$_{24}$Ga, (b) Tb$_8$Pd$_{24}$Ga and (c) Dy$_8$Pd$_{24}$Ga data. The red solid lines are the Curie-Weiss fits done above 20 K for all the data using equation 4.6.
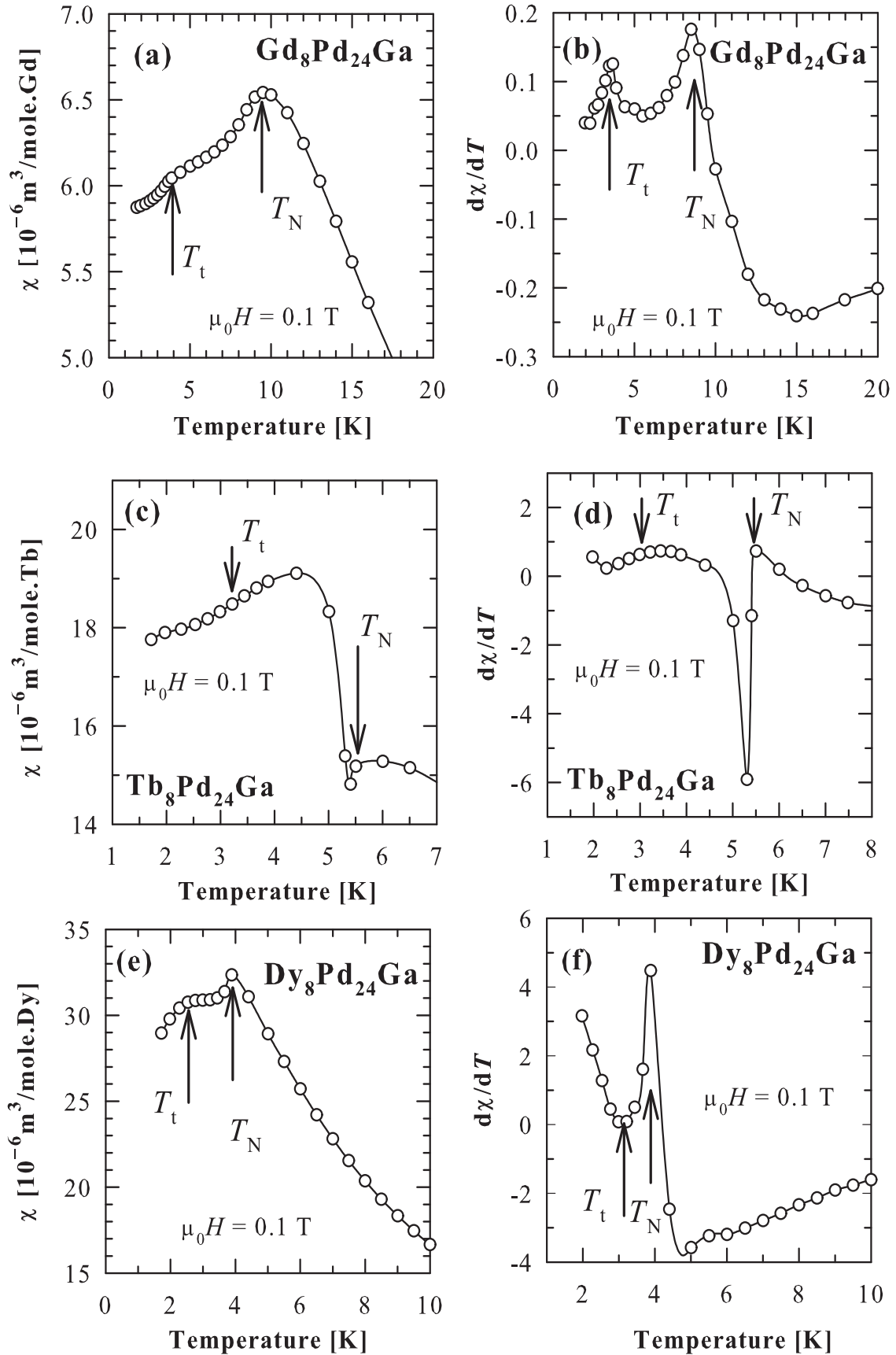
Figure 5.13: (a) Low-temperatures $\chi(T)$ data of (a) $Gd_8Pd_{24}Ga$, (c) $Tb_8Pd_{24}Ga$ and (e) $Dy_8Pd_{24}Ga$ in the antiferromagnetic region measured in a magnetic field of 0.1 T. (b), (d) and (f) display the $d\chi/dT$ calculated from $\chi(T)$ data of all three compounds. The arrows indicate the point of the transition temperature.
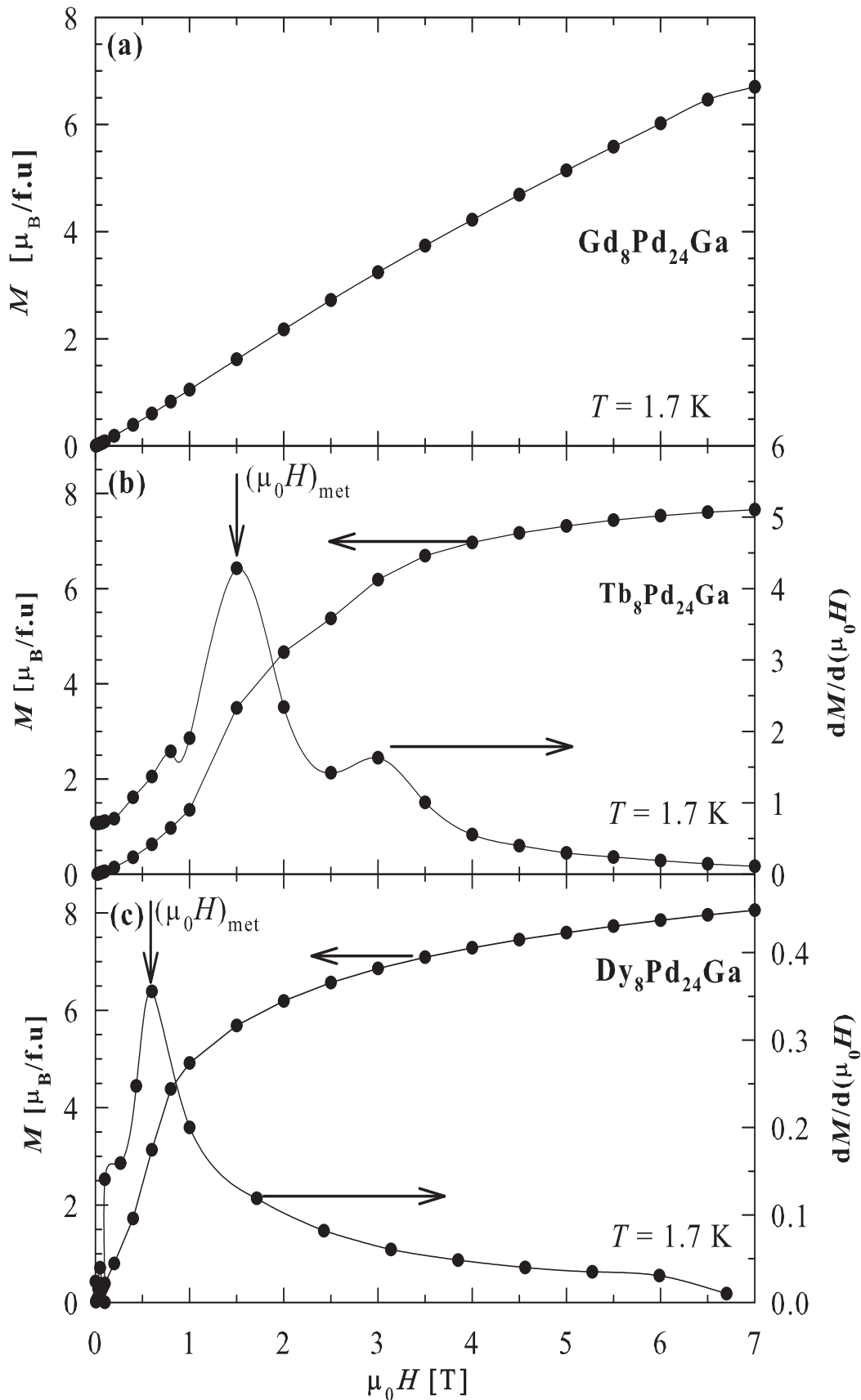
Figure .5.14: The magnetic field dependence of magnetization, $M(\mu_0 H)$, of (a) $Gd_8Pd_{24}Ga$, (b) $Tb_8Pd_{24}Ga$ (left axis) and (c) $Dy_8Pd_{24}Ga$ (left axis) measured at $T = 1.7$ K. The derivatives of magnetization are shown in (b) and (c) (right axis). The vertical arrows pointing at the maximum of $dM/d(\mu_0 H)$ show the metamagnetic point in Tb and Dy compounds.

131

5.1.5 Isothermal magnetization and magnetocaloric effect

Figure 5.15 depicted the field variations of the isothermal magnetization, $M(\mu_0 H)$ of $Tb_8Pd_{24}Ga$ and $Dy_8Pd_{24}Ga$ measured in applied field up to 7 T and 5 T, respectively, at several different temperatures in the range $2\ K \leq T \leq 10\ K$ in the step of 1 K. For both compounds, sharp metamagnetic transitions are observed in the ordering region ($T \leq T_N$) at critical fields of about 1.5 T and 0.5 T for Tb and Dy compounds, respectively. Above T_N, $M(\mu_0 H, T)$ curves exhibit a downward curvature and a tendency toward saturation above 7 T. In the terminal field $\mu_0 H = 7$ T and 5 T, the magnetization reaches values ranging from 5.33 μ_B to 4.78 μ_B and 7.13 μ_B to 6.31 μ_B, respectively at temperature from 2 to 10 K.
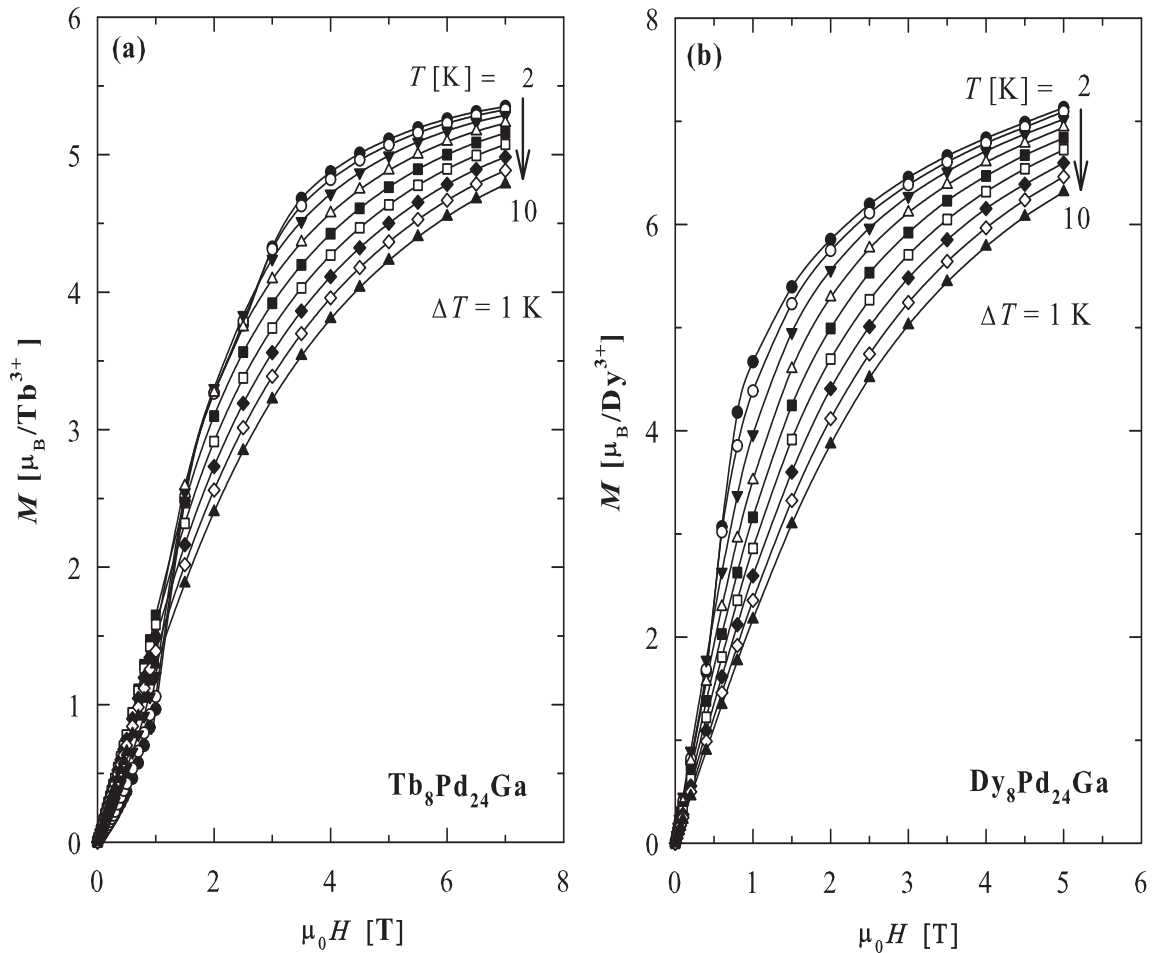
Figure 5.15: Isothermal magnetization curves, $M(\mu_0 H, T)$ of (a) $Tb_8Pd_{24}Ga$ and (b) $Dy_8Pd_{24}Ga$ measured in magnetic field up to 7 T at the vicinity of the transition temperatures (from 2 K - 10 K with a step of 1 K).

The magnetocaloric effect has been calculated from the isothermal, $M(\mu_0 H, T)$ data. The isothermal entropy change, $(-\Delta S_M)$ has been estimated from the Maxwell's relation

132

5.1.5 . Isothermal magnetization and magnetocaloric effect

(equation 4.15). The resulting temperature dependence of $-\Delta S_{\mathrm{M}}$ for various field changes are depicted in figures 5.16a for Tb and 5.17a for Dy compounds, respectively. The Tb compound shows positive magnetocaloric effect in the whole measured temperature range for $\mu_0 H \geq 4$ T and positive and negative magnetocaloric effect for $\mu_0 H \leq 3.5$ T. The negative magnetocaloric effect is observed around T_{t} and may be attributed to spin reorientation, as seen in the susceptibility data. Such behaviour was also observed in GdCuSi [149]. The negative magnetocaloric effect was not observed for Dy compound. Since the magnetocaloric was estimated in the temperature range 3 to 10 K, above T_{t} of this compound. $-\Delta S_{\mathrm{M}}$ rises into a broad maximum for the Tb compound well above T_{N} value and to a sharp peak for the Dy compound close to T_{N} value. The magnitude of this feature increases with increasing field change and reaches a maximum of $-\Delta S_{\mathrm{M}}^{max} = 14.23$ J/(kg.K) for a field change of 7 T for the Tb compound and $-\Delta S_{\mathrm{M}}^{max} = 11.20$ J/(kg.K) for a field change of 5 T. These values of $-\Delta S_{\mathrm{M}}^{max}$ may be compared to those reported for various promising rare-earth magnetic refrigerant materials in the same field changes, such as HoZn: $-\Delta S_{\mathrm{M}}^{max} = 12.1$ J/(kg.K) and 15.2 J/(kg.K) for the magnetic field change 0-5 T and 0-7 T [170]; EuAuZn: $-\Delta S_{\mathrm{M}}^{max} = 9.1$ J/(kg.K) and 11.3 J/(kg.K) for the magnetic field change 0-5 T and 0-7 T [171]; TmZnAl: $-\Delta S_{\mathrm{M}}^{max} = 9.4$ J/(kg.K) and 11.8 J/(kg.K) for the magnetic field change 0-5 T and 0-7 T [172]; Tm$_4$PtMg: $-\Delta S_{\mathrm{M}}^{max} = 13.4$ J/(kg.K) and 16.9 J/(kg.K) for the magnetic field change 0-5 T and 0-7 T; Er$_4$PdMg: $-\Delta S_{\mathrm{M}}^{max} = 15.5$ J/(kg.K) and 20.6 J/(kg.K) for the magnetic field change 0-5 T and 0-7 T; Er$_4$PtMg: $-\Delta S_{\mathrm{M}}^{max} = 17.9$ J/(kg.K) and 22.5 J/(kg.K) for the magnetic field change 0-5 T and 0-7 T [173, 174].

In order to investigate the nature of the magnetic phase transition in these compounds, the maximum value of $-\Delta S_{\mathrm{M}}$ at T_{N} was plotted as a function of the reduced field $h^{2/3}$ (with $h = (\mu_0 H \mu_{\mathrm{B}}) / (k_{\mathrm{B}} T_{\mathrm{C}})$) and displayed in figure 5.16b and 5.17b. It should be noted that for materials with second-order transition, $-\Delta S_{\mathrm{M}}^{max}$ usually follows the relation defined by equation 4.16. Least squares fits of equation 4.16 to the experimental data (solid red lines) yielded the values $S(0,0) = $ - 5.3(3) J/(kg.K) and $kM_{\mathrm{s}}(0) = 5.5(1)$ J/(kg.K) for Tb compound and $S(0,0) = $ - 1.3(2) J/(kg.K) and $kM_{\mathrm{s}}(0) = 5.0(1)$ J/(kg.K) for Dy compound. The negative sign of $S(0,0)$ corroborates with the second-order phase transition in these compounds, while the linear dependence of $-\Delta S_{\mathrm{M}}^{max}$ vs. $h^{2/3}$ indicates

strongly localized character of Tb and Dy magnetic moments [121]. The second-order phase transition observed for the Tb compound is in contracdiction with the first-order reported for the same compound [136].
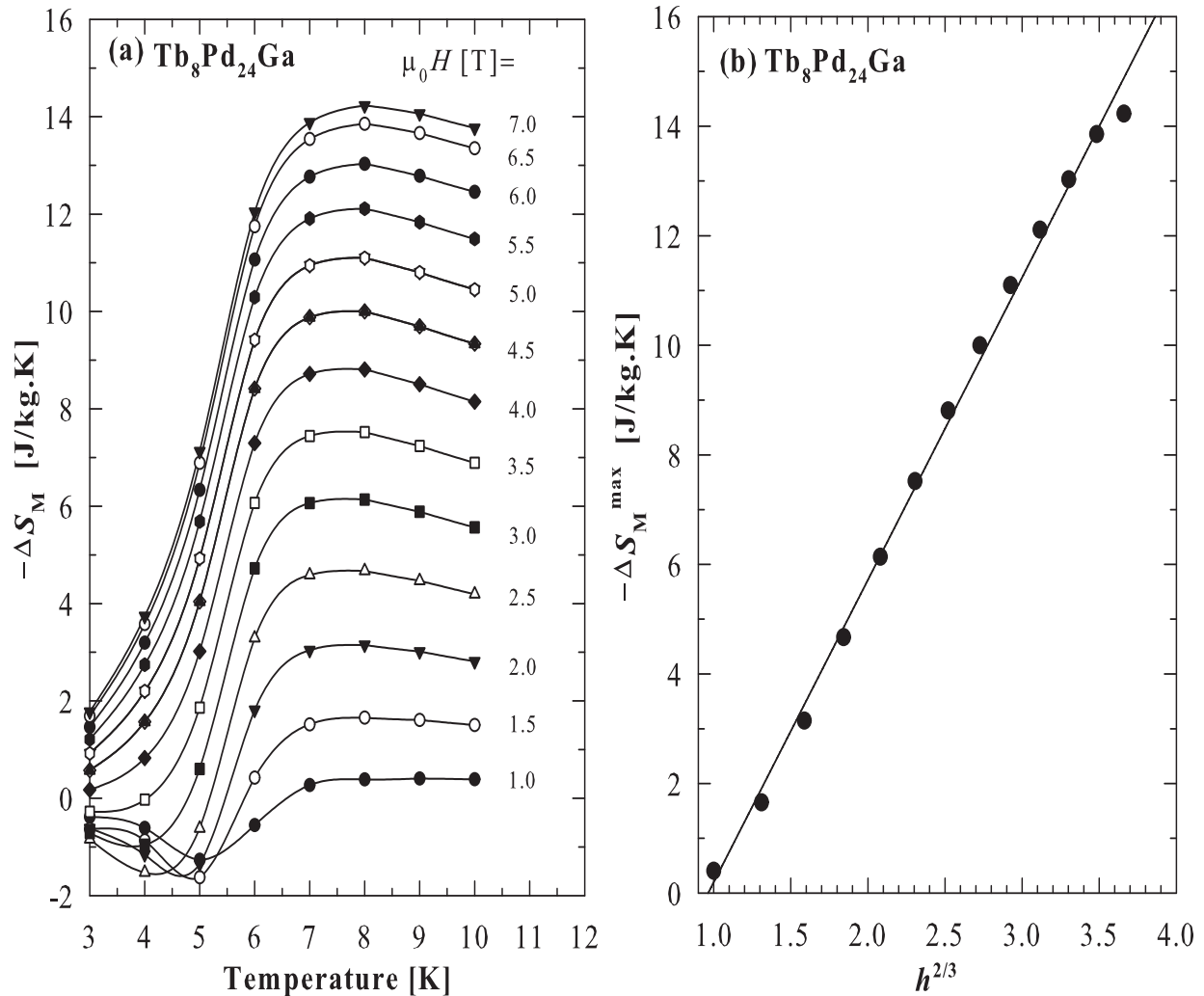
Figure 5.16: (a) Temperature dependencies of the isothermal entropy change, $-\Delta S_M(T)$ in $Tb_8Pd_{24}Ga$ measured in different magnetic fields up to 7 T in the step of 0.5 T. lines are guide to the eye. (b) The maximum isothermal magnetic entropy change $(-\Delta S_M^{max})$ around T_N as a function of reduced magnetic field $h^{2/3}$ (see test for the definition of h). The solid line is the least squares fit of equation 4.16 to the calculated $-\Delta S_M^{max}$ data.
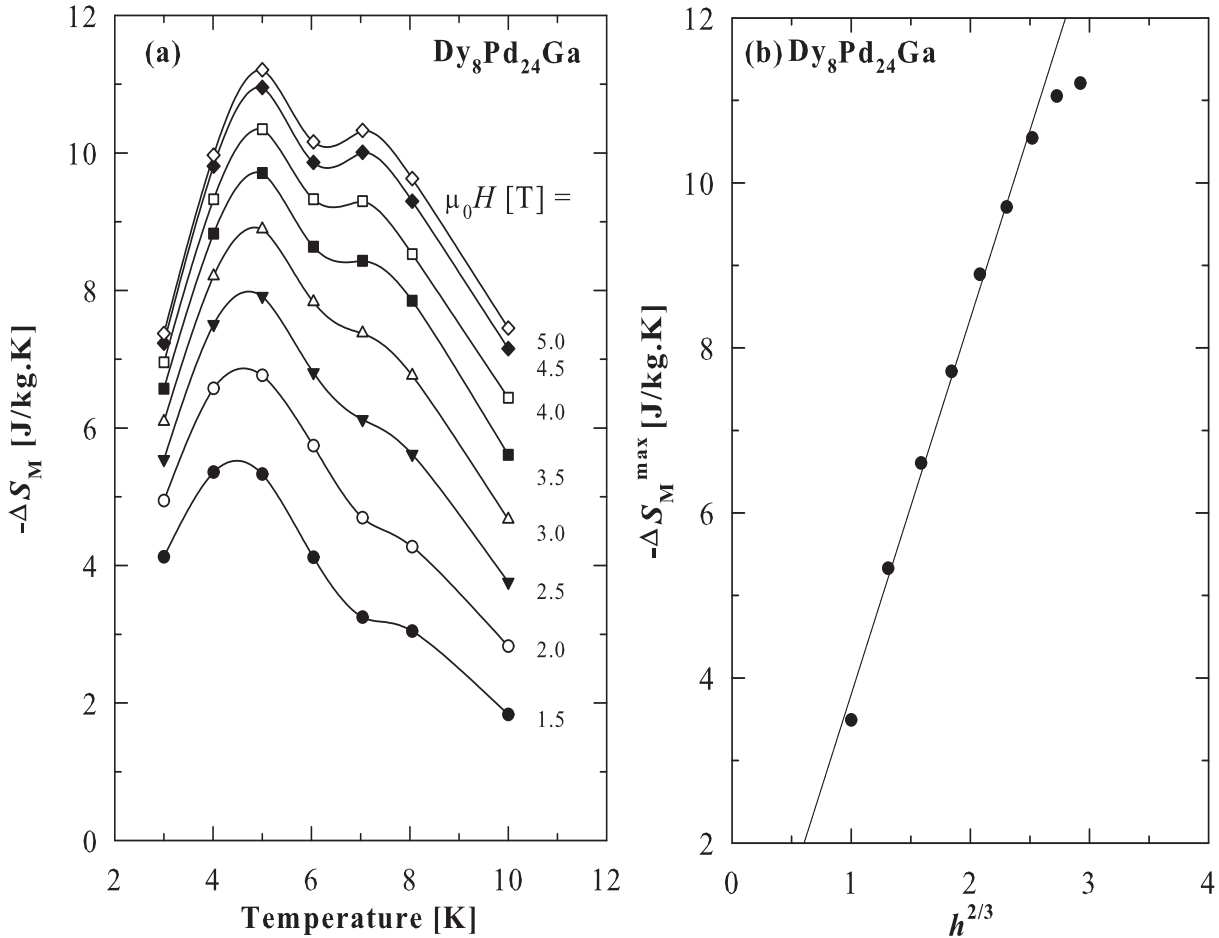
Figure 5.17: (a) Temperature dependencies of the isothermal entropy changes, $-\Delta S_\text{M}(T)$ in Dy$_8$Pd$_{24}$Ga measured with different field change in step of 0.5 T. (b) The maximum isothermal magnetic entropy change $(-\Delta S_\text{M}^{max})$ at T_N as a function of reduced magnetic field $h^{2/3}$ (see test for the definition of h). The solid line is the least squares fit of equation 4.16 to the calculated $-\Delta S_\text{M}^{max}$ data.

5.1.6 Summary

X-ray diffraction studies confirm the cubic Au$_\text{Cu}$3-type structure with space group Pm-3m, No. 221 for all compounds. Studies of $\rho(T)$, $C_\text{p}(T)$ and $\chi(T)$ indicate antiferromagnetic phase transition at $T_\text{N} = 9$ K, 5.8 K and 3.8 K for Gd, Tb and Dy respectively. Below T_N spin reorientation is observed for all compounds as confirm from $C_\text{p}(T)$ and $\chi(T)$ results. In the ordering state, $\rho(T)$ for both Tb and Dy compounds can be well described by the antiferromagnetic spin-wave spectrum with energy gap $\Delta_\rho = 29.6(1)$ K and 15(1) K for Tb and Dy compounds, respectively. $\rho(T)$ data of Gd and Tb exhibit a resistivity minimum above T_N which may due to the opening of antiferromagnetic superzone gap at the Fermi surface, with superzone energies band gap, $\Delta = 13(2)$ K and 6(1) K for Gd and

5.1.6 . Summary

Tb compounds, respectively. In the paramagnetic region $C_p(T)$ data for all compounds can be well described by the standard Debye formula. $\chi(T)$ data at high temperatures for all three compounds follow the Curie-Weiss relationship giving an effective magnetic moments close to that expected for the Gd^{3+}-, Tb^{3+}- and Dy^{3+}-ion. Magnetization data show metamagnetic transition for both Tb and Dy compounds. Large magnetocaloric effect were obtained for both Tb and Dy compounds. $-\Delta S_M$ rises into a broad maximum for the Tb compound well above T_N value and to a sharp peak for the Dy compound close to T_N value. The magnitude of this feature increases with increasing field change and reaches a maximum of $-\Delta S_M^{max} = 14.23$ J/(kg.K) for a field change of 7 T for Tb compound and $-\Delta S_M^{max} = 11.20$ J/(kg.K) for a field change of 5 T. These values of $-\Delta S_M^{max}$ may be compared to those reported for various promising rare-earth magnetic refrigerant materials in the same field changes, such as HoZn: $-\Delta S_M^{max} = 12.1$ J/(kg.K) and 15.2 J/(kg.K) for the magnetic field change 0-5 T and 0-7 T [170]; EuAuZn: $-\Delta S_M^{max} = 9.1$ J/(kg.K) and 11.3 J/(kg.K) for the magnetic field change 0-5 T and 0-7 T [171]; TmZnAl: $-\Delta S_M^{max}$ = 9.4 J/(kg.K) and 11.8 J/(kg.K) for the magnetic field change 0-5 T and 0-7 T [172]; Tm_4PtMg: $-\Delta S_M^{max} = 13.4$ J/(kg.K) and 16.9 J/(kg.K) for the magnetic field change 0-5 T and 0-7 T; Er_4PdMg: $-\Delta S_M^{max} = 15.5$ J/(kg.K) and 20.6 J/(kg.K) for the magnetic field change 0-5 T and 0-7 T; Er_4PtMg: $-\Delta S_M^{max} = 17.9$ J/(kg.K) and 22.5 J/(kg.K) for the magnetic field change 0-5 T and 0-7 T [173, 174]. This indicates that the presently studied compounds belong to a class of large magnetocaloric effect materials and are potential magnetic refrigerant materials for applications in magnetic refrigeration technology.

In order to investigate the nature of the magnetic phase transition in these compounds, the maximum value of $-\Delta S_M$ at T_N was plotted as a function of the reduced field $h^{2/3}$ (with $h = (\mu_0 H \mu_B) / (k_B T_C)$) and displayed in figure 5.16b and 5.17b. It should be noted that for materials with second-order transition, $-\Delta S_M^{max}$ usually follows the relation defined by equation 4.16. Least squares fits of equation 4.16 to the experimental data (solid red lines) yielded the values $S(0,0) = $ - 5.3(3) J/(kg.K) and $kM_s(0) = 5.5(1)$ J/(kg.K) for Tb compound and $S(0,0) = $ - 1.3(2) J/(kg.K) and $kM_s(0) = 5.0(1)$ J/(kg.K) for Dy compound. The negative sign of $S(0,0)$ corroborates with the second-order phase transition in these compounds, while the linear dependence of $-\Delta S_M^{max}$ vs. $h^{2/3}$ indicates a strongly localized character of Tb and Dy magnetic moments [121].

Chapter 6

Conclusion and future works

Magnetic refrigeration is an active field of research, with relevant activity both in the search of new magnetocaloric materials as well in the application of these materials into magnetic refrigeration devices. On the materials research side, one of the mainstream line is the discovery of new phases with significant magnetocaloric response. From a more fundamental point of view, magnetocaloric characterization has been proven to be a reliable method for the determination of the characteristics of the phase transition from which the phenomenon originates.
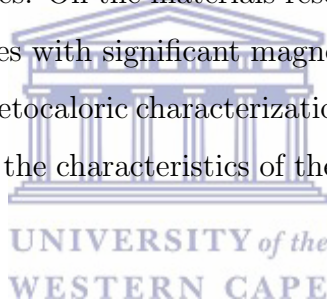
The research project investigated in this thesis involves magnetic materials as potential magnetic refrigerant materials. These investigations have been conducted successfully through measurements of electrical resistivity, heat capacity, magnetic susceptibility, magnetization, isothermal magnetization and magnetocaloric effect. Results of the isothermal magnetization have been used to investigate the critical behaviour around the para-to-ferromagnetic phase transition temperature in Pr_2Pt_2In and Nd_2Pt_2In compound and to determine the universal class to which they belong. Electrical resistivity, data have been presented as an ingredient to the magnetic properties of all the compounds investigated.

The main achievement of the research project of this thesis is summarized as follows: The compounds RE_2Pt_2In (RE = Pr, Nd) crystallize with the tetragonal Mo_2FeB_2-type crystal structure (space group P4/mbm-D_{4h}^5, No.127). Both compounds order ferromagnetically at $T_C = 9$ K and 16 K for Pr and Nd-based phase respectively as confirmed by $\rho(T)$, $C_p(T)$ and $\chi(T)$ results. In the ordered state, $\rho(T)$ and $C_{4f}(T)$ variations in

137

zero field can be well described considering a gapped ferromagnetic spin-wave spectrum with energies $\Delta_R = 8(2)$ K and $\Delta_C = 6.0(3)$ K for Pr compound and $\Delta_R = 13(1)$ K and $\Delta_C = 7.6(3)$ K for Nd compound. $C_p(T)$ data of the nonmagnetic reference compound La_2Pt_2In is featureless down to 1.8 K and can be described by the Debye-Einstein model given the Debye temperature $\Delta_D = 190.3(5)$ K and the Einstein temperature 69.8 K. In the paramagnetic state, $C_p(T)$ data of both Pr_2Pt_2In and Nd_2Pt_2In are well described by the standard Debye formula given the Debye temperature $\theta_D = 155.0(3)$ K and 152.44(2) K, respectively. In concert, the $\rho(T)$ variation in zero field of the Pr_2Pt_2In in this region can be well described by the Bloch-Grüneisen-Mott relationship given a resistivity Debye temperature $\theta_R = 193.8(6)$ K. Still in the paramagnetic region, $\chi(T)$ data of both compounds follow the Curie-Weiss relation giving effective magnetic moment values close to that expected of the free Pr^{3+}- and Nd^{3+}-ions. Positive Weiss temperature constant θ_p was obtained for both compounds reflecting the ferromagnetic exchange interactions and the ferromagnetic phase transition has a second-order character in line with the results of the magnetocaloric effect. Critical behaviour study around the ferromagnetic phase transition in Pr_2Pt_2In can be well described within the 3D-Ising, while for Nd_2Pt_2In compound in this study ascribed the compound to belong between the 3D-Heisenberg and 3D-Ising universality class. A maximum magnetocaloric effect value of 7.44 J/(kg.K) was obtained for a field change of 7 T in Pr_2Pt_2In and 6,25 J/(kg.K) in Nd_2Pt_2In for the same field change. For the Nd_2Pt_2In compound, the maximum value of the change of magnetic entropy $(-\Delta S_M^{max})$ for a field change of 5 T observed from $-\Delta S_M(T)$ calculated from the magnetization isotherm $M(\mu_0 H, T)$ is in good agreement with that obtained from $-\Delta S_M(T)$ calculated from heat capacity. For both compounds $-\Delta S_M^{max}$ was found proportional to $h^{2/3}$ with a negative intercept, indicating that the ferromagnetic phase transition in both compounds has a second-order character.

For the $RE_8Pd_{24}Ga$ (RE = Gd, Tb and Dy) compounds investigated, the studies of X-ray diffraction confirm the cubic $AuCu_3$-type crystal structure with space group Pm-3m. The resulting unit cell volumes are consistent with the lanthanide contraction as one moves from La to Lu. The resistivity results of all three compounds show normal metallic behaviour at high temperatures with evidence of crystal-electric-field or $s - d$ interband scattering. The low-temperatures resistivity data indicate the onset of magnetic

phase transition associated with antiferromagnetic ordering at $T_N = 9$ K, 5.8 K and 3.8 K for Gd, Tb and Dy compounds, respectively. These values of T_N corroborate with values obtained from the heat capacity and magnetic susceptibility results. In the ordering region, the resistivity data of Tb and Dy compounds are governed by the scattering conduction electrons on antiferromagnetic spin-wave excitations with energy gap: $\Delta_\rho = 29.6(1)$ K and 15(1) K for Tb and Dy compounds, respectively. Above T_N, the resistivity data of both Gd and Tb exhibit a resistivity minimum due to the opening of an antiferromagnetic superzone gap at the Fermi surface with the superzone band energies values of $\Delta = 13(2)$ K and 6(1) K for Gd and Tb compounds, respectively. The heat capacity data at high temperatures for all three compounds can be described well by the standard Debye formula given the Debye temperature values: $\theta_P = 238.886(7)$ K, 230.26(4) K and 233.20(2) K for Gd, Tb and Dy, respectively, which indicate a similarity of the lattice vibration in all three compounds. The heat capacity at low-temperature exhibits a peak at T_N. Below T_N, another magnetic phase transition occurs at $T_t = 4$ K and 2.2 K for the Gd and Tb compounds, respectively. This second-order phase transition is attributed to spin reorientation of the Gd and Tb moments. The magnetic susceptibility for all compounds above 20 K follows the Curie-Weiss relation, given effective magnetic moments: $\mu_{eff} = 8.004(2)\ \mu_B$, 9.76(2) μ_B and 10.65(8) μ_B for Gd, Tb and Dy compounds, respectively. These values are close to that expected for the free Gd^{3+}-, Tb^{3+}- and Dy^{3+}-ion. The magnetic susceptibility results revealed a noncollinear antiferromatic arrangement of the rare-earth spin for all three compounds. This noncollinear structure corroborates with the result of the magnetocaloric effect, showing a sign change for the Tb compound. The magnetization results indicate metamagnetic transition at 1.5 T and 0.5 T for Tb and Dy compounds, respectively. Investigation of magnetocaloric effect of both Tb and Dy compounds indicate a second-order phase transition. Both compounds exhibit an antiferromagnetic state below T_N, and process a field-induced metamagnetic transition around T_N, resulting in a large magnetocaloric effect. Particularly, the value of $-\Delta S_M^{max}$ reach 14.23 J/(kg.K) for field change of 7 T for Tb compound and 11.20 J/(kg.K) for a field change of 5 T, indicating that both Tb and Dy compounds could be a potential candidate for low-temperatures and low-magnetic field refrigeration.

For future experimental investigations, the nature of the ordered state of $RE_8Pd_{24}Ga$

compounds need to be performed through measurements of AC magnetic susceptibility. The magnetic structures of all compounds in this thesis need to be investigated through inelastic neutron scattering experiments. On the other hand, thermoelectric materials attract a lot of attention since they are key for thermoelectric power generation and thermo-electric cooling. The key to improve thermoelectric conversion efficiency of thermoelectric generation and the coefficient of performance of thermoelectric cooling lies in high dimensionless figure of merit. For these reasons, the next step of investigations are based on the thermal transport properties measurements of the compounds investigated in this thesis and other rare-earth intermetallic compounds. These investigations involve measurements of thermal conductivity, thermoelectric power, the Lorentz number and the dimensionless figure of merit. Furthermore, the new techniques for determining critical exponents, the order of phase transitions and the identification of tricritical point separating first and second-order phase transitions using magnetocaloric method are being applied in the broader scope of general characterization of magnetic materials. The succesful application of the magnetocaloric effect in magnetic refrigerators has established the seed for study of other caloric phenomena (like elasto-caloric, electro-caloric, etc.) and this will probably lead to alternative technologies for refrigeration.
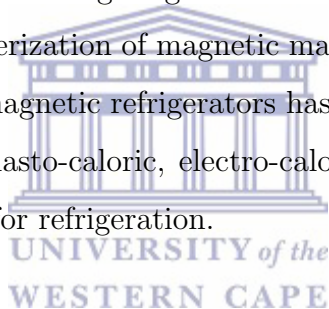
Bibliography

[1] K.H.J. Buschow, Reports on Progress in Physics **40**, 1179 (1977).

[2] A. Szytula, *Handbook of Magnetic Materials vol 6* (Elsevier, Amsterdam, 1991).

[3] A.M. Tishin and Y.I. Spichkin, *The magnetocaloric effect and its applications* (Institute of Physics Publishing, Briston, 2003).

[4] Learn About Sustainability: United States Environmental Protection Agency, https://www.epa.gov/sustainability/learn-aboutsustainability, (2016).

[5] The Magnetic Refrigeration System. Cooltech Applications., http://www.cooltech-applications.com/magneticrefrigeration-system.html, (2016).

[6] K.A. Gschneidner and V.K. Pecharsky, Journal of Rare Earths **24**, 641 (2006).

[7] C. Zimm, A. Jastrab, A. Sternberg, V. Pecharsky, K.A Gschneidner, M. Osborne, and I. Anderson, *Advances in cryogenic engineering* (Springer, New York, 1998).

[8] K.A. Gschneidner, V.K. Pecharsky, and A.O. Tsokol, Reports on Progress in Physics **68**, 1479 (2005).

[9] K. Kamiya, H. Takahashi, T. Numazawa, H. Nozawa, and T. Yanagitani, Cryocoolers **14**, 637 (2007).

[10] A.M. Tishin, *Handbook of Magnetic Materials* **12**, 395 (1999).

[11] V.K. Pecharsky, K. Vitalij, and K.A. Gschneidner, Journal of Magnetism and Magnetic Materials **200**, 44 (1999).

[12] H. Feng-Xia, S. Bao-Gen, S. Ji-Rong, and Z. Xi-Xiang, Chinese Physics **9**, 550 (2000).

[13] H. Feng-xia, S. Bao-gen, S. Ji-rong, C. Zhao-hua, R. Guang-hui, and Z. Xi-Xiang, Applied Physics Letters **78**, 3675 (2001).

Bibliography

[14] H. Wada and Y. Tanabe, Applied Physics Letters **79**, 3302 (2001).

[15] O. Tegus, E. Brück, K.H.J. Buschow, and F.R. De Boer, Nature **415**, 150 (2002).

[16] Simon Cotton, *Lanthanide and actinide chemistry* (John Wiley & Sons, England, 2013).

[17] Ferromagnetism, http://www.wikipedia.org/wiki/Ferromagnetism.

[18] K.H.J. Buschow, Reports on Progress in Physics **42**, 1373 (1979).

[19] C. Kittel, *Introduction to solid state physics* (John Wiley, New York, 2005).

[20] J. Craik, Derek, *Magnetism, Principles and Applications* (John Wiley, New York, 1995).

[21] G.I. Likhtenshtein, J. Yamauchi, S. Nakatsuji, A.I. Smirnov, and R. Tamura, *Fundamentals of magnetism* (John Wiley, Weinheim, 2008).

[22] Ferromagnetism, http://en.wikipedia.org/wiki/Diamagnetism.

[23] C. Kittel, *Introduction to solid state physics* (Wiley, New York, 1996), Vol. 8.

[24] B.D. Cullity and C.D. Graham, *Introduction to magnetic materials* (John Wiley & Sons, Menlo Park, 2011).

[25] D.D. Stancil and A. Prabhakar, *Spin waves* (Springer, New York, 2009).

[26] N. Cusack, *The electrical and magnetic properties of solids* (Longmans, Green and Company, London, 1958).

[27] H.E. Hall and J.R. Hook, *Solid state Physics* (Chichester, Wiley, Chichester, 1986).

[28] H.E. Hall and J.R. Hook, *Solid state Physics* (Wiley, Chichester, 1994).

[29] J. Stöhr and H.C. Siegmann, *Magnetism: from fundamentals to nanoscale dynamics* (Springer Science & Business Media, New York, 2007), Vol. 152.

[30] K. Wandelt, *Surface and Interface Science Properties of Elemental Surfaces* (Wiley-VCH, Germany, 2012), Vol. 2.

[31] M.A. Ruderman, Physical Review **96**, 99 (1954).

[32] C. Kittel, Solid State Physics **22**, 1 (1969).

[33] J.R. Schrieffer, Physical Review **149**, 491 (1966).

[34] M.B. Fontes, J.C. Trochez, B. Giordanengo, S.L. Bud'ko, D.R Sanchez, E.M. Baggio-Saitovitch, and M.A. Continentino, Physical Review B **60**, 6781 (1999).

[35] N.H. Andersen and H. Smith, Physical Review B **19**, 355 (1979).

[36] H. Yamada and S. Takada, Progress of Theoretical Physics **49**, 1401 (1973).

[37] S.N. de Medeiros, M.A. Continentino, M.T.D. Orlando, M.B. Fontes, E.M. Baggio-Saitovitch, A. Rosch, and A. Eichler, Physica B: Condensed Matter **281**, 340 (2000).

[38] H.E. Stanley, *Introduction to phase transitions and critical phenomena* (Clarendon Press, Oxford, New York, 1971).

[39] A. Perumal, V. Srinivas, V.V. Rao, and R.A. Dunlap, Physical Review Letters **91**, 137202 (2003).

[40] S. Srinath, S.N. Kaul, and H. Kronmüller, Physical Review B **59**, 1145 (1999).

[41] M. Dudka, R. Folk, Y. Holovatch, and D. Ivaneiko, Journal of Magnetism and Magnetic Materials **256**, 243 (2003).

[42] S.H. Simon, Lecture Notes for Solid State Physics, 3rd Year Course 6 (2012).

[43] J.M.D. Coey, *Magnetism and magnetic materials* (Cambridge University Press, Cambridge CB2 8RU, UK, 2010).

[44] D.I. Uzunov, *Introduction to the theory of critical phenomena: mean field, fluctuations and renormalization* (World Scientific, Singapore, 1993).

[45] D.C. Mattis, *The theory of magnetism I: Statics and Dynamics* (Springer Science & Business Media, Berlin, 1981), Vol. 17.

[46] J.J. Binney, N.J. Dowrick, A.J. Fisher, and M. Newman, *The theory of critical phenomena: an introduction to the renormalization group* (Oxford University Press, UK, 1992).

[47] S.N. Kaul, Journal of Magnetism and Magnetic Materials **53**, 5 (1985).

143

[48] N.W. Ashcroft, N.D. Mermin, and S. Rodriguez, *Solid state physics* (American Association of Physics Teachers, New york, 1998).

[49] D.C. Mattis, *The Theory of Magnetism II: Thermodynamics and statistical mechanics, Springer Series in Solid-State Sciences 55*, 1 ed. (Springer-Verlag, Berlin Heidelberg, 1985).

[50] B.A. Cipra, American Mathematical Monthly **94**, 937 (1987).

[51] A.K. Pramanik and A. Banerjee, Physical Review B **79**, 214426 (2009).

[52] B.M. McCoy and T.T. Wu, *The two-dimensional Ising model* (Courier Corporation, Cambridge, 2014).

[53] R.J. Baxter, *Exactly solved models in statistical mechanics* (Elsevier, San Diego, CA 92101, 2016).

[54] S. Sachdev, *Quantum phase transitions* (Wiley Online Library, Cambridge, 2007).

[55] C. Kittel, *Introduction to solid state physics* (John Wiley, New York, 2004).

[56] J.S. Smart, *Effective field theories of magnetism* (Saunders, New York, 1966).

[57] P. Papon, J. Leblond, and P.H.E. Meijer, *Physics of Phase Transitions* (Springer, Heidelberg, 2002).

[58] J.C. Toledano and P. Toledano, *The Landau theory of phase transitions: application to structural, incommensurate, magnetic and liquid crystal systems* (World Scientific Publishing Co Inc, Singapore, 1987).

[59] P. Debye, Annals of Physics. 81, **386**, 1154 (1926).

[60] W.F. Giauque, Journal of the American Chemical Society **49**, 1864 (1927).

[61] K. Yasukōchi, K. Kanematsu, and T. Ohoyama, Journal of the Physical Society of Japan **16**, 1123 (1961).

[62] A.M. Tishin and Y.I. Spichkin, *The magnetocaloric effect and its applications* (CRC Press, Bristol: Institute of Physics Publishing, 2016).

Bibliography

[63] A.H. Wilson, *The theory of metals* (Cambridge University Press, London Office: Bentley House, x.w. I, 1993).

[64] F.J. Blatt, P.A. Schroeder, C.L. Foiles, and D. Greig, *Thermoelectric power of Metals* (Plenum, New York, 1976).

[65] M.R. Ward, *Electrical Engineering Science* (McGraw-Hill Education, New York, 1971).

[66] R.J. Elliott and A.F. Gibson, *An Introduction to Solid State Physics and its Applications* (MacMillan Press LTD, London and Basingstoke, 1974).

[67] J.M. Ziman, *Electrons and Phonons: the theory of transport phenomena in solids* (Oxford university press, Oxford, 1960).

[68] F.J. Blatt, *Physics of electronic conduction in solids* (McGraw-Hill, New York, 1968).

[69] T. Kasuya, Progress of Theoretical Physics **16**, 45 (1956).

[70] P.G. De Gennes, Journal of Physics and Chemistry of Solids **4**, 71 (1958).

[71] A.J. Dekker, Journal of Applied Physics **36**, 906 (1965).

[72] S.V. Vonsovski, Zhurnal Eksperimentalnoi i Teoreticheskoi Fiziki **18**, 219 (1948).

[73] S.V. Vonsovski, Izvestiya Akademii Nauk SSR, Seriya Fizicheskaya **19**, 426 (1955).

[74] T. Kasuya, Progress of Theoretical Physics **22**, 227 (1959).

[75] I. Mannari, Progress of Theoretical Physics **22**, 335 (1959).

[76] R.J. Elliott and F.A. Wedgwood, Proceedings of the Physical Society **81**, 846 (1963).

[77] H. Miwa, Progress of Theoretical Physics **28**, 208 (1962).

[78] H. Miwa, Progress of Theoretical Physics **29**, 4466 (1963).

[79] H. Yamada and S. Takada, Progress of Theoretical Physics **52**, 1077 (1974).

[80] E.S.R. Gopal, *Specific heats at low temperatures* (Springer Science & Business Media, Plenum, New York, 1966).

[81] A.A. Coelho, Journal of Applied Crystallography **36**, 86 (2003).

[82] D.B. Wiles and R.A. Young, Journal of Applied Crystallography **14**, 149 (1981).

[83] H.M. Rietveld, Journal of Applied Crystallography **2**, 65 (1969).

[84] R.A. Young, *The Rietveld method* (International union of crystallography, Oxford University Press., 1993), Vol. 5.

[85] G. Will, *Powder diffraction: The Rietveld method and the two stage method to determine and refine crystal structures from powder diffraction data* (Springer Science & Business Media, Berlin, Germany, 2006).

[86] J. Durbin and G.S. Watson, Biometrika **58**, 1 (1971).

[87] R.J. Hill and H.D. Flack, Journal of Applied Crystallography **20**, 356 (1987).

[88] Physical Property Measurement System, User Manuel, 1988.

[89] J.C. Gallop and F. Piquemal, *The SQUID Handbook, Vol. II Applications of SQUIDS and SQUID systems* (WILEY-VCH, Weinheim, 2006).

[90] B. Chesca, R. Kleiner, D. Koelle, and A.I. Braginski, *Fundamentals and technology of SQUIDs and SQUID systems* (Wiley–VCH, Germany, 2004).

[91] J. Clarke and A.I. Braginski, *The SQUID handbook, Vol. I Applications of SQUIDs and SQUID systems* (John Wiley & Sons, Weinheim, 2004).

[92] D. Kaczorowski, P. Rogl, and K. Hiebl, Physical Review B **54**, 9891 (1996).

[93] R.A. Gordon, Y. Ijiri, C.M. Spencer, and F.J. DiSalvo, Journal of Alloys and Compounds **224**, 101 (1995).

[94] F. Hulliger, Journal of Alloys and Compounds **217**, 164 (1995).

[95] F. Hulliger and B.Z. Xue, Journal of Alloys and Compounds **215**, 267 (1994).

[96] H. Nakotte, A. Purwanto, R.A. Robinson, K. Prokes, J.C.P. Klaasse, P.F. De Chatel, F.R. de Boer, L. Havela, V. Sechovskỳ, L.C.J. Pereira, A. Seret, J. Rebizant, J.C. Spirlet, and F. Trouw, Physical Review B **53**, 3263 (1996).

[97] L. Havela, V. Sechovskỳ, P. Svoboda, H. Nakotte, K. Prokeš, F.R. de Boer, A. Seret, J.M. Winand, J. Rebizant, J.-C. Spirlet, A. Purwanto, and R.A. Robinson, Journal of Magnetism and Magnetic Materials **140**, 1367 (1995).

[98] F. Hulliger, Journal of Alloys and Compounds **221**, L11 (1995).

[99] N. Furukawa and Y.I. Motome, Applied Physics A: Materials Science & Processing **74**, s1728 (2002).

[100] R. Nirmala, A.V. Morozkin, and S.K. Malik, Pramana **84**, 977 (2015).

[101] V.K. Pecharsky and K.A. Gschneidner, Physical Review Letters **78**, 4494 (1997).

[102] S. Gama, A.A. Coelho, A. de Campos, A.M.G. Carvalho, F.C.G. Gandra, R.P.J. Von, and N.A. de Oliveira, Physical Review Letters **93**, 237202 (2004).

[103] H. Feng-xia, S. Bao-gen, and S. Ji-rong, Applied Physics Letters **76**, 3460 (2000).

[104] X.X. Zhang, F.W. Wang, and G.H. Wen, Journal of Physics: Condensed Matter **13**, L747 (2001).

[105] N.A. De Oliveira, P.J. Von Ranke, M.V.T. Costa, and A. Troper, Physical Review B **66**, 094402 (2002).

[106] Q.Y. Dong, B.G. Shen, J. Chen, J. Shen, and J.R. Sun, Journal of Applied Physics **105**, 113902 (2009).

[107] N.F. Mott and H. Jones, *The theory of the properties of metals and alloys* (Courier Corporation, London, 1958).

[108] G. Grimvall, *The electron-phonon interaction in metals* (North-Holland, Amsterdam, 1981), No. 9.

[109] N. Sato, N. Aso, K. Hirota, T. Komatsubara, Y. Endoh, S.M. Shapiro, G.H. Lander, and K. Kakurai, Physical Review B **53**, 14043 (1996).

[110] B.K. Banerjee, Physics Letters **12**, 16 (1964).

[111] A. Arrott and J.E. Noakes, Physical Review Letters **19**, 786 (1967).

[112] A. Oleaga, A. Salazar, M.C. Hatnean, and G. Balakrishnan, Journal of Alloys and Compounds **682**, 825 (2016).

[113] A. Aharoni, *Introduction to the Theory of Ferromagnetism.* (Clarendon Press, Oxford, England, 2000), Vol. 109.

[114] M.E. Fisher, M. Shang-keng, and B.G. Nickel, Physical Review Letters **29**, 917 (1972).

[115] J.S. Kouvel and M.E. Fisher, Physical Review **136**, A1626 (1964).

[116] B. Widom, The Journal of Chemical Physics **41**, 1633 (1964).

[117] B. Widom, The Journal of Chemical Physics **43**, 3898 (1965).

[118] N.H. Duc, D.T. Kim Anh, and P.E. Brommer, Physica B: Condensed Matter **319**, 1 (2002).

[119] D. Qiao-yan, Z. Hong-wei, S. Jue-lian, S. Ji-rong, and S. Bao-gen, Journal of Magnetism and Magnetic Materials **319**, 56 (2007).

[120] Q.Y. Dong, H.W. Zhang, J.R. Sun, B.G. Shen, and V. Franco, Journal of Applied Physics **103**, 116101 (2008).

[121] J. Shen, Y. Li-Qin, J. Zhang, W. Fang-Wei, S. Ji-Rong, H. Feng-Xia, R. Chuan-Bing, and L. Yang-Xian, Journal of Applied Physics **103**, 07B315 (2008).

[122] M. Falkowski, Journal of Alloys and Compounds **689**, 1059 (2016).

[123] Z. Fisk, Solid State Communications **18**, 221 (1976).

[124] Z. Kletowski, P.J. Markowski, and B. Staliński, Solid State Communications **57**, 293 (1986).

[125] A. Tari, *The Specific Heat of Matter at Low Temperatures* (Imperial College Press, London, 2003).

[126] J.J. Mboukam, B.M. Sondezi, M.B. Tchoula Tchokonté, A.K.H. Bashir, A.M. Strydom, D. Britz, and D. Kaczorowski, Physica B: Condensed Matter: **536**, 505 (2017).

Bibliography

[127] R. Pöttgena, R.K. Kremerb, S. Rayaprola, B. Heyinga, and R.D. Hoffmanna, Zeitschrift für Naturforschung B **62**, 169 (2007).

[128] M. Giovannini, H. Michor, E. Bauer, G. Hilscher, P. Rogl, T. Bonelli, F. Fauth, P. Fischer, T. Herrmannsdörfer, L. Keller, W. Sikora, A. Saccone, and R. Ferro, Physical Review B **61**, 4044 (2000).

[129] I.R. Harris, G.V. Raynor, and C.J. Winstanley, Journal of the Less Common Metals **12**, 69 (1967).

[130] W.E. Gardner, J. Penfold, and I.R. Harris, Le Journal de Physique Colloques **32**, 1139 (1971).

[131] W.E. Gardner, J. Penfold, T.F. Smith, and I.R. Harris, Journal of Physics F: Metal Physics **2**, 133 (1972).

[132] R.D. Hutchens, V.U.S. Rao, J.E. Greedan, W.E. Wallace, and R.S. Craig, Journal of Applied Physics **42**, 1293 (1971).

[133] J.M.M. da Silva, Solid State Communications **28**, 857 (1978).

[134] R.A. Gordon, C.D.W. Jones, M.G. Alexander, and F.J. DiSalvo, Physica B: Condensed Matter **225**, 23 (1996).

[135] R.A. Gordon and F.J. DiSalvo, Zeitschrift für Naturforschung B **51**, 52 (1996).

[136] C. Mitra, S.K. Dhar, and S. Ramakrishnan, Journal of Applied Physics **87**, 5146 (2000).

[137] C.D.W. Jones, R.A. Gordon, B.K. Cho, F.J. DiSalvo, J.S. Kim, and G.R. Stewart, Physica B: Condensed Matter **262**, 284 (1999).

[138] S. Singh and S.K. Dhar, Physical Review B **68**, 144433 (2003).

[139] D.T. Adroja, B.D. Rainford, K.S. Knight, and P.C. Riedi, Journal of Physics: Condensed Matter **13**, 459 (2001).

[140] M.B. Tchoula Tchokonté, P.V. Du Plessis, and D. Kaczorowski, Journal of Magnetism and Magnetic Materials **272**, E5 (2004).

[141] D. Kaczorowski, M. Koźlik, and L. Kępiński, Journal of Physics and Chemistry of Solids **60**, 521 (1999).

[142] Y. Zhang, X. Xu, Y. Yang, L. Hou, Z. Ren, X. Li, and G. Wilde, Journal of Alloys and Compounds **667**, 130 (2016).

[143] Y. Yi, L.W. Li, K.P. Su, Y. Qi, and D.X. Huo, Intermetallics **80**, 22 (2017).

[144] Y. Zhang, Y. Yang, X. Xu, L. Hou, Z. Ren, X. Li, and G. Wilde, Journal of Physics D: Applied Physics **49**, 145002 (2016).

[145] R.K. Kumar, H.S. Nair, B.N. Sahu, S. Xhakaza, and A.M. Strydom, arXiv preprint arXiv:1711.09816 (2017).

[146] M.B. Tchoula Tchokonté, J.J. Mboukam, B.M. Sondezi, A.K.H. Bashir, D. Britz, A.M. Strydom, and D. Kaczorowski, Physica B: Condensed Matter: **536**, 418 (2017).

[147] S.B. Gupta and K.G. Suresh, Journal of Magnetism and Magnetic Materials **391**, 151 (2015).

[148] S.B. Gupta and K.G. Suresh, Applied Physics Letters **102**, 022408 (2013).

[149] S.B. Gupta, K.G. Suresh, and A.V. Lukoyanov, Journal of Materials Science **50**, 5723 (2015).

[150] A.K. Bashir, M.B. Tchoula Tchokonté, B.M. Sondezi, A.M. Strydom, and D. Kaczorowski, Journal of Alloys and Compounds **699**, 7 (2017).

[151] E. Brück, Journal of Physics D: Applied Physics **38**, R381 (2005).

[152] L.W. Li, Chinese Physics B **25**, 037502 (2016).

[153] B.G. Shen, J.R. Sun, F.X. Hu, H.W. Zhang, and Z.H. Cheng, Advanced Materials **21**, 4545 (2009).

[154] V. Franco, J.S. Blázquez, B. Ingale, and A. Conde, Annual Review of Materials Research **42**, 305 (2012).

[155] L. Li, Y. Yuan, Y. Zhang, T. Namiki, K. Nishimura, R. Pöttgen, and S. Zhou, Applied Physics Letters **107**, 132401 (2015).

Bibliography

[156] Y. Zhang, G. Wilde, X. Li, Z. Ren, and L. Li, Intermetallics **65**, 61 (2015).

[157] Y.J. Ke, X.Q. Zhang, Y. Ma, and Z.H. Cheng, Scientific Reports **6**, 19775 (2016).

[158] J.C.B. Monteiro, R.D. dos Reis, and F.G. Gandra, Applied Physics Letters **106**, 194106 (2015).

[159] L. Li and K. Nishimura, Applied Physics Letters **95**, 132505 (2009).

[160] D. Jang, T. Gruner, A. Steppke, K. Mitsumoto, C. Geibel, and M. Brando, Nature Communications **6**, 8680 (2015).

[161] L. Li, K. Nishimura, W.D. Hutchison, Z. Qian, D. Huo, and T. NamiKi, Applied Physics Letters **100**, 152403 (2012).

[162] S. Singh and S.K. Dhar, Journal of Physics: Condensed Matter **14**, 11795 (2002).

[163] A.K. Bashir, M.B. Tchoula Tchokonté, and A.M. Strydom, Journal of Magnetism and Magnetic Materials **414**, 69 (2016).

[164] A. Pandey, C. Mazumdar, R. Ranganathan, and D.C. Johnston, Scientific Reports **7**, 42789 (2017).

[165] I. Balberg, Physical Review B **91**, 71 (1977).

[166] J. Sereni, G. Nieva, J.P. Kappler, M.J. Besnus, and A. Meyer, Journal of Physics F: Metal Physics **16**, 435 (1986).

[167] H. Nakotte, E. Brück, K. Prokes, J.H.V.J. Brabers, F.R. de Boer, L. Havela, K.H.J. Buschow, and Y. Fu-ming, Journal of Alloys and Compounds **207**, 245 (1994).

[168] D.C. Johnston, Physical Review Letters **109**, 077201 (2012).

[169] D.C. Johnston, Physical Review B **91**, 064427 (2015).

[170] L. Li, Y. Yuan, Y. Zhang, R. Pöttgen, and S. Zhou, Journal of Alloys and Compounds **643**, 147 (2015).

[171] L. Li, O. Niehaus, B. Gerke, and R. Pöttgen, IEEE Transactions on Magnetics **50**, 1 (2014).

[172] Y. Zhang, L. Hou, Z. Ren, X. Li, and G. Wilde, Journal of Alloys and Compounds **656**, 635 (2016).

[173] Lingwei Li, Oliver Niehaus, Marcel Kersting, and Rainer Pöttgen, Intermetallics **62**, 17 (2015).

[174] L. Li, O. Niehaus, M. Kersting, and R. Pöttgen, IEEE Transactions on Magnetics **51**, 1 (2015).